HF AURORAL BACKSCATTER FROM THE E AND F REGIONS

A THESIS

SUBMITTED TO THE COLLEGE OF GRADUATE STUDIES AND RESEARCH

IN PARTIAL FULFILLMENT OF THE REQUIREMENTS

FOR THE DEGREE OF DOCTOR OF PHILOSOPHY

IN THE DEPARTMENT OF PHYSICS AND ENGINEERING PHYSICS

UNIVERSITY OF SASKATCHEWAN, SASKATOON

BY

DONALD WILLIAM DANSKIN

PERMISSION TO USE

In presenting this thesis in partial fulfillment of the requirements for a Postgraduate degree from the University of Saskatchewan, I agree that the Libraries of this University may make it freely available for inspection. I further agree that permission for copying of this thesis in any manner, in whole or in part, for scholarly purposes may be granted by the professor who supervised my thesis work or, in their absence, by the Head of the Department or the Dean of the College in which my thesis work was done. It is understood that any copying or publication or use of this thesis or parts thereof for financial gain shall not be allowed without my written permission. It is also understood that due recognition shall be given to me and to the University of Saskatchewan in any scholarly use which may be made of any material in my thesis.

Requests for permission to copy or to make other use of material in this thesis in whole or part should be addressed to:

Head of the Department of Physics and Engineering Physics
University of Saskatchewan
Saskatoon, Saskatchewan
Canada S7N 5E2

ABSTRACT

In this thesis, several aspects of HF coherent backscatter from the high-latitude E and F regions are studied with the focus on the relationship between the echo characteristics and the parameters of the ionosphere. The Hankasalmi CUTLASS/SuperDARN radar is the primary instrument for the undertaken studies.

The starting point in the research is that coherent echo characteristics are affected by two factors: the plasma physics of magnetic field-aligned irregularity formation and the propagation conditions in that the HF radio waves need to be close to the normal of the Earth's magnetic field to detect the irregularities. Since the mechanisms of irregularity production are believed to be different at various heights, observations in the E and F regions are considered separately.

For the F-region backscatter, we first investigate the ionospheric conditions necessary for backscatter to be detected at specific latitudes and in specific time sectors. To achieve this goal, two approaches are employed. First, a long-term statistical study of diurnal, seasonal and solar cycle effects on echo occurrence is done to assess the relative importance of changes in plasma instability conditions and radio wave propagation. Next, echo occurrence is studied for an area in which ionospheric parameters are measured by EISCAT and other instruments. Both approaches indicate that F-region echoes occur if the electric field is enhanced (above 5-10 mV/m). We show that, once the electric field is above the threshold, the echo power is only slightly dependent on it. We demonstrate that the strongest echoes are received when the F-region electron density is optimal for the selected range and altitude. This optimal value is found to be about $2\mathrm{x}10^{11}$ m^{-3} for the Hankasalmi radar. The role of the conducting E region on irregularity excitation and HF radio wave absorption are discussed.

The next problem considered with respect to the F-region echoes is the relationship between the velocity of the F-region echoes and plasma convection. We give additional evidence that the observed HF line-of-sight velocity is the projection of the convection velocity on the radar beam and that the Map Potential technique (currently in use for building the global-scale convection maps) compares well with the local EISCAT convection measurements.

With respect to the E-region backscatter, two major features are studied. First, a more detailed (as compared to the standard SuperDARN approach) analysis of the spectra is performed. By employing the Burg spectrum analysis method, we show that the E-region echoes are double-peaked in ~35% of observations. Variations of the peak separation with the range and azimuth of observations are investigated. The occurrence of double-peak echoes is associated with scatter from two different heights within the E region. HF ray tracing indicates that for typical ionospheric conditions, scatter from the top and the bottom of the E region is possible at certain slant ranges. In the upper layer the plasma waves move with the velocity close to the ExB convection component. For the lower layer, the plasma wave velocity is reduced due to enhanced ion and electron collision frequencies. A second issue is how do the velocities of HF and VHF E-region echoes compare for observations along the same direction. We concluded that the velocity of E-region echoes at HF can be comparable to or below the VHF velocity and well below the ExB convection component, implying that the scatter can often come from the bottom of the electrojet layer. Other aspects of VHF velocities are also discussed.

ACKNOWLEDGEMENTS

I would like to give thanks to Dr. A.V. Koustov, my supervisor, for his constant guidance and support.

I would also like to thank the other members of the HF/VHF radar group at the University of Saskatchewan. I am grateful to Drs. G.J. Sofko, G.C. Hussey and K.A. McWilliams for many useful discussions and questions. Special acknowledgement goes to Dr. D. André for the development of the raytracing software. I would like to thank my fellow graduate students, R. Makarevitch, J. Liang and L. Benkevitch for the discussion of ideas.

The Natural Sciences and Engineering Research Council of Canada provided financial assistance that enabled my studies with research grants to A.V. Koustov and G.J. Sofko and an operating grant for the Saskatoon and Prince George radars of SuperDARN. CUTLASS Finland radar is supported by PPARC, the Swedish Institute for Space Physics, Uppsala, and the Finnish Meteorological Institute.

The EISCAT data were provided by T. Ogawa, N. Nishitani and S. Nozawa of the Solar-Terrestrial Environment Laboratory, Nagoya University, Japan. The STARE data were provided by M. Uspensky and P. Janhunen of Finnish Meteorological Institute. Data of the Sodankylä ionosonde and Finnish riometers were obtained from the Sodankylä Geophysical Observatory. Additional riometer data originated from the Imaging Riometer for Ionospheric Studies (IRIS). The geomagnetic data are from the Tromso Geophysical Observatory, University of Tromso, Norway. DMSP ion drift data were provided by F. Rich, Air Force Research Laboratory, Hanscom Air Base, Mass., USA.

I would also like to thank my family for their constant understanding and encouragement.

TABLE OF CONTENTS

LIST OF TABLES

LIST OF FIGURES

LIST OF ABBREVIATIONS

ACF	Auto-Correlation Function
CADI	Canadian Advanced Digital Ionosonde
CUTLASS	Co-ordinated UK Twin-Located Auroral Sounding System
CC	Current Convective
DMSP	Defense Meteorological Satellite Program
EISCAT	European Incoherent Scatter
FB	Farley-Buneman
FFT	Fast Fourier Transform
FoV	Field of View
IMF	Interplanetary magnetic field
IRI	International Reference Ionosphere
GD	Gradient Drift
HF	High frequency
LOS	line-of-sight
MLT	Magnetic Local Time
MLat	Magnetic Latitude
STARE	Scandinavian Twin Auroral Radar Experiment
SuperDARN	Super Dual Auroral Radar Network
UHF	Ultra high frequency
UT	Universal Time
VHF	Very high frequency

CHAPTER 1

INTRODUCTION

The Sun is known not only for the visible portion of the electromagnetic spectrum but also for a continuous stream of ejected charged particles called the solar wind. The number of particles and their associated energies in the solar wind vary cyclically with more particles being ejected during the so-called solar maximum conditions. These re-appear every eleven years. There are also random and faster periodicity events in the Sun that influence the composition of the solar wind. When a particularly strong formation of particles arrives at the near Earth environment, a spectacular space weather event may occur. These are of interest not only because of complex plasma physical processes occurring in space, but more importantly because of the potential for harm to spaceships, satellites, ground-based technological systems and humans.

In addition to the particles, the solar wind carries with it an interplanetary magnetic field (IMF). The IMF and the Earth's magnetic field interact creating a magnetic field cavity called the magnetosphere. Variations in the orientation and the magnitude of the IMF cause alterations in the shape of the magnetosphere. This in turn leads to the redistribution of particle populations between various parts of the magnetosphere, the excitation of electric fields and currents, and the development of field-aligned currents between the magnetospheric regions and the highly conducting part of the Earth's upper atmosphere, the ionosphere.

1.1 The magnetosphere

The magnetosphere is an area of the near Earth environment with a rarified, magnetically confined plasma. Fig. 1.1 shows a simplified schematic view of the Earth's magnetosphere and its major regions.

When the supersonic solar wind plasma approaches the Earth, it slows to subsonic speed in the bow shock. In the process of deceleration, the thermal energy of the fully ionized plasma of the solar wind becomes enhanced. The IMF penetrates through the bow shock without significant changes.

The combination of the IMF and Earth's magnetic field gives the magnetosphere a distinctive shape with compression of the magnetic field lines of the Earth on the dayside and elongation on the nightside. In Fig. 1.1, we illustrate the situation when the IMF is oriented opposite to the Earth's magnetic field, the so-called southward IMF condition. The IMF merges with the Earth's magnetic field in the reconnection (or merging) region of the magnetosphere earthward of the bow shock. The result of reconnection is that newly opened field lines are created. Closed field lines still exist in the inner magnetosphere. Open field lines have one end connected to the IMF and the other to the Earth's ionosphere. These open field lines drift anti-sunward with the plasma. Eventually, at the far reaches of the tail of the magnetosphere, the open field lines from the northern and southern hemispheres merge to complete the closure of the magnetosphere (tail reconnection is not shown in Fig. 1.1). The region of newly opened

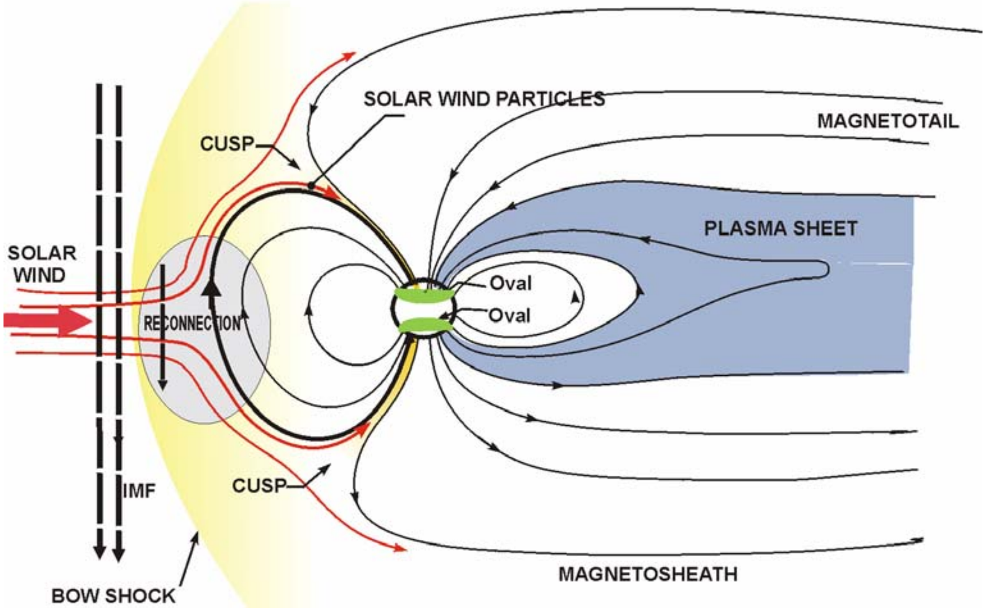

Figure 1.1 A schematic view of the Earth's magnetosphere due to the interaction of the Earth's magnetic field and the interplanetary magnetic field (adapted from original drawing by K. McWilliams).

field lines near the noon sector in the Earth's magnetosphere is called the cusp.

The cusp in the net magnetic field occurs on the dayside in both hemispheres of the Earth. This cusp can be a direct entry point for particles from the solar wind into the magnetosphere to form the dayside part of the auroral oval around the noon sector at magnetic latitudes of ~75° - 80°. At cusp latitudes, there is often an opposite process of ion upflows from the ionosphere into the magnetosphere.

Alternatively, some of the particles of the solar wind are carried past the cusp along the magnetosheath towards the magnetotail. The magnetosheath particles can diffuse inward into the plasma sheet. In the plasma sheet, particles are accelerated due magnetic field reconnection downstream from the Earth. These particles are forced towards the Earth along the magnetic field lines into the nightside auroral oval. The auroral oval is an area of most frequent auroral arc occurrences.

It is important to realize that motion of particles across the magnetic field within the magnetosphere can generate electric fields perpendicular to the magnetic field. These electric fields can be transferred along magnetic flux lines (which are highly conducting) to the electrically conducting ionosphere. In the presence of a perpendicular electric field, the ionospheric plasma is set into a motion that is often referred to as convection. In the upper part of the ionosphere the plasma convection is a mirror of the plasma motion in the magnetosphere; thus the monitoring of the magnetospheric plasma motion can be done by observing the convection in the ionosphere. The ionosphere thus is acting as a gigantic television screen whose "pictures" are the convection patterns.

A more frequently occurring situation is the one in which a large-scale magnetospheric electric field is applied across the polar cap (magnetic latitudes > ~70°) in the direction from the dawn to dusk as shown in Fig. 1.2. At the auroral zone latitudes (~65° – ~70° of magnetic latitude), in the afternoon (morning) there is typically a northward (southward) electric field. This configuration of the electric field leads to the well-known two-cell convection pattern with anti-sunward plasma convection within the central polar cap and return sunward motions in the auroral zones (westward in the evening sector and eastward in the morning sector).

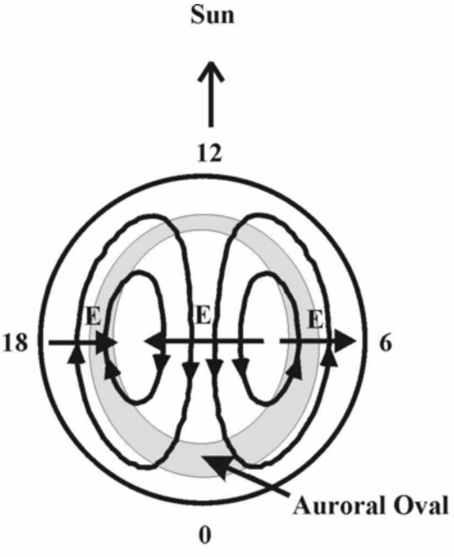

Figure 1.2 Two-cell convection pattern typical for the high-latitude ionosphere.

1.2 The ionosphere

The ionosphere is the upper part of the Earth's atmosphere where a significant charged particle component exists along with the neutrals. The ionosphere stretches from ~70 km up to ~1000-2000 km. The main sources of charged particles are solar UV radiation, electron and ion precipitation from the magnetosphere, diffusion processes and plasma convection in the crossed electric and magnetic fields. It is customary to subdivide the Earth's ionosphere into three major parts, the D, E and F regions, centered at ~80-90, 110-130 and 200-250 km, respectively. Fig. 1.3 gives example of electron density distribution at high latitudes. One can clearly recognize the D, E and F regions.

The separation of the Earth's ionosphere into three different regions, being historical in origin, has significance not only because these layers often have enhanced electron density but also because the electrons and ions move differently at these heights in the presence of external electric and magnetic fields. In the F-region, both electrons and ions are magnetic field controlled and experience the same ExB drift at all heights. At the bottom of the E region, due to the ions having frequent collisions with neutrals, they are not affected (to a first approximation) by the magnetic field; only electrons are moving in the ExB direction. At these heights, a relative motion between electrons and ions exists (electric current), and it can easily be detected by observing the magnetic effects of the electric current. In the D region, both electrons and ions are collisionally

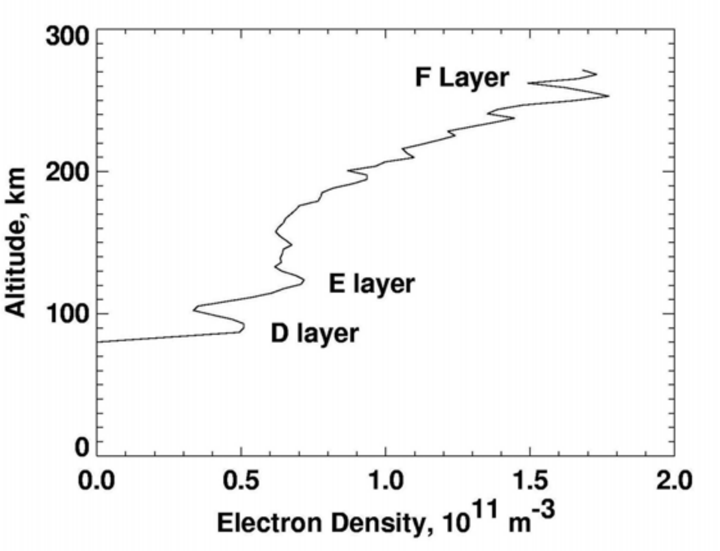

Figure 1.3 Example of an electron density profile measured with the EISCAT radar on 12 February 1999 at 1230 UT. Three different layers of the ionosphere are shown.

controlled so that there is almost no effect on their motion by the electric field.

1.3 Studies of the ionosphere

The best way to study the solar wind - Earth's magnetic field interaction is to use satellites since they provide information on plasma parameters, such as number density, ion composition, magnetic and electric fields and so on, in situ with the processes that occur. Satellites can be positioned at various regions of the magnetosphere and even in the solar wind. This is, unfortunately, still quite an expensive exercise. With only a few satellites operating at once, the big disadvantage of space measurements is their localization; data are available only along a specific orbit. Also it is difficult to distinguish spatial and temporal variations of plasma parameters.

Another approach to studying the solar wind-Earth magnetosphere interaction is to use ground-based instrumentation. The advantages of the ground-based observations are in their time continuity such that decades-long data sequences can be accumulated and in their good spatial coverage especially if arrays of instrumentation are deployed. Also, it is not so difficult to employ a much broader variety of instrumentation. Importantly, the temporal and spatial variations tend to be easier to distinguish especially if a large field of view is available. Thus networks of ground-based instruments are scientifically sound and cost-effective to monitor the processes in the magnetosphere.

Over the years, multitudes of ionospheric phenomena have been identified that manifest different effects of the interaction of solar wind with the Earth's magnetic field. In this thesis we focus only on one of these phenomena, the excitation of small-scale irregularities in the high-latitude ionosphere. These irregularities can be detected by sending HF, VHF or UHF radio waves into the ionosphere. Since the electron density in the ionosphere is low, the radio waves would travel through it into to space and never return. However, wave-like irregularities in the centimeter-decameter range elongated with the Earth’s magnetic flux lines can provide a weak “coherently” scattered signal that is detectable with low powered radars. This phenomenon is known as coherent auroral backscatter or radar (radio) aurora. Over the years, these small-scale high-latitude irregularities have also been studied in-situ by rocket- and space-based instruments. Though direct measurements have decisively proven the existence of irregularities and provided some information on their properties, the majority of our present knowledge about them has been obtained through coherent radar measurements.

An understanding of ionospheric irregularities is important for practical applications. They may affect VHF and especially HF radio wave propagation. They introduce unwanted fluctuations of the UHF signals used in the satellite communications. But more importantly, a tracing of the irregularity bulk motions in the F region allows researchers to infer the pattern of the plasma flow on a global scale which is the central issue in resolving the problem of the solar wind interaction with the Earth’s magnetosphere.

It is well established that high-latitude field-aligned irregularities are generated through various plasma instabilities. The instabilities occur when the excess energy of regular plasma motions is transferred to spontaneous thermal fluctuations of the electron density that always exist in the plasma. Because the ionospheric plasma parameters change with height, properties of excited irregularities are different at various heights. It is customary to consider separately the irregularities in the F, E and D regions.

1.4 Objective of the undertaken research

The purpose of this research is to investigate some aspects of the auroral HF backscatter at high latitudes. The main instrument for the studies is the Super Dual

Auroral Radar Network (SuperDARN) coherent HF radar. SuperDARN is a global network of HF radars observing auroral backscatter from the F and E regions. The University of Saskatchewan operates two radars, in Saskatoon and Prince George. Because of the collaborative nature of SuperDARN project, data from any radar of the network is freely accessible to the community. This thesis is based on SuperDARN observations in the European sector. This selection of radars was due to a requirement of independent ionospheric measurements within the HF radar field of view. We focus on several problems pertinent to the F and E coherent backscatter. We pursue several goals.

For the case of F-region backscatter, we first explore the relative importance of various factors that control the detection of HF echoes for the Hankasalmi radar. Ultimately, we would like to better understand the origin of such F-region irregularities. For practical purposes, we would like to know why HF coherent radars do not see echoes at specific latitudes and in specific time sectors even though one would expect them because the conditions for the irregularity excitation are apparently met. We employ two approaches. First we consider the long-term statistics on echo occurrence to assess the expected role of changes in the plasma instability conditions and radio wave propagation conditions. Then we investigate periods of HF echoes when ionospheric parameters were measured by another radar system, the European Incoherent Scatter (EISCAT) radar. We use this opportunity to relate echo occurrence with various parameters in the ionosphere.

The second issue for research with respect to the F-region echoes is the relationship between the velocity of F-region backscatter and plasma convection. This is a very important question for successful operation of the SuperDARN radars since the monitoring of plasma motion is the prime goal of the experiment. This problem has been investigated in several recent studies. We supplement those efforts with the analysis of new data sets and with the investigation of other aspects of the problem.

For the case of the E-region backscatter, we focus on the velocity of echoes and its relationship to such parameters as the electric field magnitude and direction and the electron and ion temperatures. This is also one of the central problems of auroral backscatter. Years of research have revealed significant inconsistencies between observations and theoretical predictions (e.g., Fejer and Kelley, 1980; Kelley, 1989; Sahr and Fejer, 1996). It turned out that the velocity of E-region echoes is a crucial parameter that allows us to distinguish various nonlinear effects influencing the evolution of the plasma instabilities at these heights. The goals for the E-region backscatter research are:

1) To explore the microstructure of HF spectra by employing a method of spectral analysis to resolve the SuperDARN spectra whose details are difficult to see with the standard methods.
2) To investigate the reasons for the multi-peak nature of E-region HF backscatter. We attempt to assess the role of echo height convolution in the process of coherent signal formation and plasma physics of irregularity formation.
3) To explore the relationship between HF and VHF velocities by considering near simultaneous SuperDARN HF data and 144-MHz Scandinavian Twin Auroral Radar Experiment (STARE) data.
4) To further investigate the relationship of STARE VHF velocities and SuperDARN HF velocities to the ionospheric electric field at large flow angles of observations.

1.5 Thesis outline

The outline of the thesis is as follows. We first review the major theories explaining the generation of ionospheric irregularities in the F, E and D regions (Chapter 2). In Chapter 3 we describe the capabilities, details of operation, methods of data collection and processing of all radars used in this work, namely the VHF STARE and HF SuperDARN coherent radars and UHF EISCAT incoherent scatter radar. With respect to the analysis SuperDARN data, we discuss how the spectral resolution was improved. We also explain the philosophy of convection measurements and comment on the HF propagation modes. Chapter 4 presents statistics on F-region echo occurrence and SuperDARN/EISCAT joint observations over a 4-day period in 1999. In Chapter 5 we compare line-of-sight HF velocities and convection estimates with plasma drifts measured by EISCAT. Comparison of E-region velocities at HF and VHF with EISCAT plasma drifts are presented in Chapter 6. In Chapter 7 we investigate the spectra of HF E-region echoes. The thesis concludes with suggestions for further research and conclusions in Chapter 8.

CHAPTER 2

REVIEW OF THE THEORY OF IONOSPHERIC IRREGULARITIES

In this chapter, the major theories explaining the generation of magnetic field-aligned wave-like irregularities in the electron density for the high-latitude F, E and D regions are reviewed. It is currently accepted that when small scales are concerned ($\lambda < 1$ km in the direction perpendicular to the Earth magnetic field) the irregularities are produced by various plasma instabilities (Fejer and Kelley, 1980; Kelley, 1989; Tsunoda, 1988). All these instabilities are excited primarily because of relative background drift between electrons and ions at various heights. Additional conditions need to be met. For example, for the gradient-drift instability in the E region a gradient in the electron density must exist in the direction of the electric field. We consider the threshold conditions for various instabilities since these might tell us when auroral backscatter should be observed. We also focus on the relationship between the velocity of plasma irregularities and ionospheric parameters, namely, the plasma drift. These two issues will be investigated in the experimental part of the thesis.

2.1 Plasma motion in the high-latitude ionosphere

At high-latitudes, the motion of charged particles in the ionosphere is determined by two major factors, the electric field imposed from the magnetosphere and the neutral wind established in the atmosphere due to difference in gas pressure created by the Sun between day and night.

Consider the configuration of the ambient electric and magnetic fields appropriate for the high-latitude ionosphere as displayed in Fig. 2.1. Here the electric field is directed along the x direction and the magnetic field along the –z direction. The gradient in the

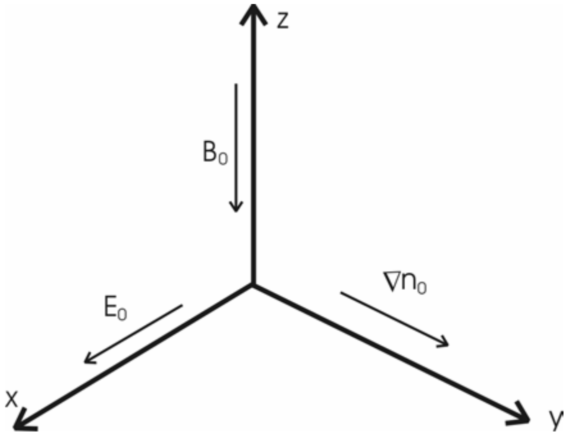

Figure 2.1 Orientation of the electric and magnetic fields, and the gradient of density adopted for the analysis.

density in the y direction will be important for the instability analysis but has little effect on the bulk plasma motions.

The general equation that govern the motion of charged particles is

$$0 = e_\alpha(\mathbf{E} + \mathbf{V}_\alpha \times \mathbf{B}) - \nu_\alpha m_\alpha (\mathbf{V}_\alpha - \mathbf{U}_n), \qquad (2.1)$$

where $e_\alpha, m_\alpha, \mathbf{V}_\alpha$, and ν_α are charge, mass, velocity, and collision frequency for either ions or electrons $(\alpha = i, e)$, and $\mathbf{U}_n$ is the velocity of neutral wind that we assume to be along the y direction; the direction of ExB plasma drift. In equation 2.1 we used the cold plasma approximation ($T_e = T_i = 0$) and neglected particle inertia effects. Equation 2.1 also describes the background motion, if one assumes that all variables refer to this state.

2.1.1. Plasma motions due to electric field

We first consider the case in which the neutral wind is neglected ($\mathbf{U}_n = 0$). By introducing $Z_e = \nu_e / |\Omega_e|$ and $Z_i = \nu_i / \Omega_i$ (where Ω_e and Ω_i are the electron and ion gyro frequencies), one can show that the electron and ion velocities are (Brekke, 1997)

$$\mathbf{V}_e = \frac{1}{1+Z_e^2}\left[-Z_e\frac{\mathbf{E}}{B} + \frac{\mathbf{E}\times\mathbf{B}}{B^2}\right], \qquad (2.2)$$

and
$$\mathbf{V}_i = \frac{1}{1+Z_i^2}\left[Z_i\frac{\mathbf{E}}{B} + \frac{\mathbf{E}\times\mathbf{B}}{B^2}\right]. \qquad (2.3)$$

We further analyze equations 2.2 and 2.3 by considering the configuration of Fig. 2.1 for different regions of the ionosphere.

a) F region

In the F region the frequency of collisions of ions and electrons is much less than the corresponding gyrofrequencies, $Z_e, Z_i << 1$, hence the components of electron and ion velocities are

$$V_{0\alpha y} = \frac{E}{B} \equiv V_E , \qquad (2.4)$$

and $$V_{0\alpha x} = Z_\alpha \frac{E}{B} = \frac{\nu_\alpha}{\Omega_\alpha} V_E . \qquad (2.5)$$

Equation 2.4 indicates that both electrons and ions move in the ExB direction. The velocity V_E is commonly called the Hall drift or plasma convection. Equation 2.5 shows that there is also plasma motion in the direction of the electric field. This motion is often called the Pedersen drift. The Pedersen drift depends on Z_α, the ratio of collision frequencies to gyrofrequencies. For typical collision and gyrofrequencies at F-region altitudes this ratio of $\nu_\alpha / \Omega_\alpha$ is ~ 10^{-3}, hence the magnitude of plasma velocity along the direction of the electric field is much less than the ExB drift. One has to keep in mind that the gyrofrequency ($\Omega_\alpha = \frac{e_\alpha B}{m_\alpha}$) of equation 2.5 is dependent on the sign of the charge. The implication is that while the ions drift along the electric field, the electrons drift in the opposite direction so that there is a relative drift between ions and electrons. Though the relative Pedersen drift of electrons and ions is small, it is essential for the creation of instabilities.

Additionally, if there is an electric field in the direction of the magnetic field, electrons and ions move along the magnetic field with the velocities

$$V_{0\alpha z} = \frac{\Omega_\alpha}{\nu_\alpha} \frac{E_z}{B} . \qquad (2.6)$$

Equation 2.6 shows that electrons are moving much faster that ions so once again there exists a relative drift (current) between electrons and ions in the F region.

b) E region

The situation is more complicated in the central and at the bottom part of the E region. Whereas the electrons behave much the same as in the F region, here the ions experience frequent collisions with neutrals and as a result they are unmagnetized ($Z_i >> 1$) meaning that their motion is much more controlled by the electric field. At these heights, the components of ion velocity are

$$V_{0ix} = \frac{1}{Z_i}\frac{E}{B} = \frac{\Omega_i}{\nu_i} V_E \,, \tag{2.7}$$

and $$V_{0iy} = \frac{1}{Z_i^2}\frac{E}{B} = \left(\frac{\Omega_i}{\nu_i}\right)^2 V_E \,. \tag{2.8}$$

One can see that the ions are mostly moving along the electric field direction. The relative importance of Hall and Pedersen drifts for ions changes drastically with height with more significant contributions from the ExB component at the top of the E region.

c) D region

In the D region, both electrons and ions are unmagnetized ($Z_\alpha >> 1$) and mostly move along the electric field direction such as

$$V_{0\alpha x} = \frac{\Omega_\alpha}{\nu_\alpha} V_E \,, \tag{2.9}$$

and $$V_{0\alpha y} = \frac{1}{Z_\alpha^2}\frac{E}{B} = \left(\frac{\Omega_\alpha}{\nu_\alpha}\right)^2 V_E \,. \tag{2.10}$$

2.1.2 Plasma motions due to neutral wind

Now if one considers the situation with no electric field but a non-zero neutral wind ($\mathbf{U}_n \neq 0$) along the y direction, from equations 2.1, one can get (Brekke, 1997)

$$\mathbf{V}_e = \frac{1}{1+Z_e^2}\left[Z_e^2 \mathbf{U}_n + Z_e \frac{\mathbf{U}_n \times \mathbf{B}}{B} \right], \tag{2.11}$$

and $$\mathbf{V}_i = \frac{1}{1+Z_i^2}\left[Z_i^2 \mathbf{U}_n - Z_i \frac{\mathbf{U}_n \times \mathbf{B}}{B} \right]. \tag{2.12}$$

One can see that at F-region heights, the electrons and ions are slightly moving along the x-axis in opposite directions. At the E-region heights, the situation is the same for electrons while ions move with the velocity of wind in the y direction. Finally, in the D region, both electrons and ions move with the velocity of neutral wind.

2.2 F-region plasma instabilities

Three major instabilities are considered to explain the plasma waves/irregularity excitation in the F-region ionosphere, the gradient-drift (GD), current convective (CC) and electrostatic ion-cyclotron (IC) instabilities with the first one believed to be the major one (Tsunoda, 1988).

2.2.1 Gradient drift instability, Pedersen mode

The generating mechanism for the GD instability implies that there is a gradient in the plasma density perpendicular to the direction of the electric field. One possible configuration of this gradient is depicted in Fig. 2.2.

Consider a sinusoidal perturbation that occurs along the x direction (direction of electric field) as in Fig. 2.2. A charge separation along the electric field is caused by the difference in the electron and ion Pedersen drifts. This leads to establishment of a varying polarization electric field E_p. The polarity of the polarization electric field is such that plasma in regions of enhanced (decreased) density, experiencing an E_pxB drift, is forced into the regions of lower (higher) electron density. In this way, the amplitude of initial perturbation increases as compared to original perturbation leading to the instability. Because the instability occurs due to relative Pedersen drift between ions and electrons, it is often referred to as the Pedersen mode of the GD instability.

Let us estimate the rate of the perturbation growth in the cold approximation. We start from equation 2.1 but in addition we neglect the effect of the neutral wind and add the continuity equation

$$\frac{\partial n_\alpha}{\partial t} + \nabla \cdot \left(n_\alpha \mathbf{V}_\alpha \right) = 0 \, . \qquad (2.13)$$

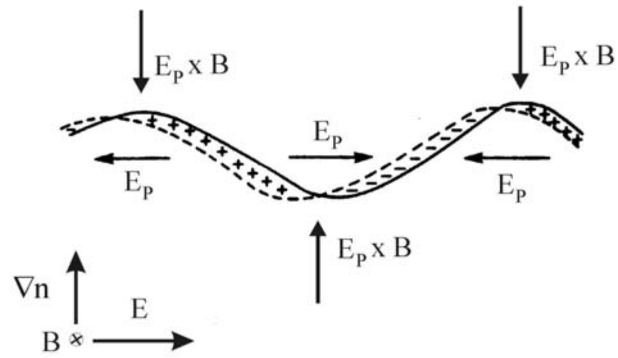

Figure 2.2 A scheme explaining the reasons for perturbation growth due to the Gradient Drift instability in the F region

Now, in accordance with the theory of small perturbations, the variables $\mathbf{E}, \mathbf{V}_\alpha$ and n_α contain a background component and a perturbed quantity, for example, $n_\alpha = n_{0\alpha} + \delta n_\alpha$ with $\delta n_\alpha << n_{0\alpha}$. From equations 2.1 and 2.13, assuming that the electric field can be represented as the gradient of an electrostatic potential ($\delta\mathbf{E} = -\nabla\delta\phi$), assuming quasi-neutrality ($\delta n_i = \delta n_e = \delta n$) and sinusoidal fluctuations for $\delta\phi$ and $\delta n \propto e^{i(k_x x + k_y y - \omega t)}$, one obtains equations for the density and potential perturbations

$$\left(-i\omega + ik_x V_{0ex} + ik_y V_{0ey}\right)\frac{\delta n}{n_0} + \left(\frac{\nu_e}{\Omega_e}(k_x^2 + k_y^2) - i\frac{k_x}{L}\right)\frac{\delta\phi}{B} = 0\,, \tag{2.14}$$

and $$\left(-i\omega + ik_x V_{0ix} + ik_y V_{0iy}\right)\frac{\delta n}{n_0} + \left(\frac{\nu_i}{\Omega_i}(k_x^2 + k_y^2) - i\frac{k_x}{L}\right)\frac{\delta\phi}{B} = 0\,. \tag{2.15}$$

Here $L^{-1} = \frac{1}{n_0}\frac{\partial n_0}{\partial y}$ is the scale length of the gradient. Making the assumption that $\omega = \omega_r + i\gamma$ ($\gamma << \omega_r$), the frequency ω_r and growth rate γ of the GD instability are

$$\omega_r = k_y V_E\,, \tag{2.16}$$

and $$\gamma = \frac{V_E}{L}\,, \tag{2.17}$$

where V_E is the Hall drift magnitude.

Equation 2.16 implies that the phase velocity of the unstable waves is equal to the component of the ExB drift in the direction of propagation. This property of GD waves is very important since it allows us to infer the plasma drift component from Doppler observations in experiments like SuperDARN.

Equation 2.17 predicts that stronger electric field (drift V_E) and stronger plasma gradient would lead to larger growth rates for the instability. The sign of the gradient is important in equation 2.17; only gradients in the direction of the Hall drift create the instability. This means that if one has a plasma density "cloud" in the ionosphere, only one side of the density structure will be unstable, as was shown in numerical simulations of the ionospheric plasma clouds done for example by Keskinen and Ossakow (1982, 1983a).

In equation 2.17 there is no scale dependence for the instability but this is the result of simplifications used in our analysis. Keskinen and Ossakow (1982) presented the general form for the growth rate of the GD instability

$$\gamma = \frac{\frac{V_E}{L}\left[\frac{\nu_e \nu_i}{|\Omega_e|\Omega_i}\right]}{\frac{k_{ll}^2}{k_x^2} + \frac{\nu_e \nu_i}{|\Omega_e|\Omega_i}} - D_\perp k_x^2 - D_{ll} k_{ll}^2, \tag{2.18}$$

where $D_\perp = \left(\frac{\nu_e}{|\Omega_e|\Omega_i}\right) c_s^2$ and $D_{ll} = \frac{c_s^2}{\nu_i}\left(1 + \frac{\left(\frac{\nu_i}{\Omega_i}\right)^2}{\frac{\nu_e \nu_i}{|\Omega_e|\Omega_i} + \frac{k_{ll}^2}{k_x^2}}\right)$ are the coefficients of diffusion perpendicular and parallel to the magnetic field and $c_s = \sqrt{\frac{k_B (T_e + T_i)}{m_i}}$ is the ion acoustic speed (k_B is the Boltzmann constant). k_{ll} and k_x are the components of the wave vector parallel and perpendicular to the magnetic field. The growth rate of the instability is strongly decreased by the presence of parallel components of the wave vector. Hence, the maximum growth occurs when the wave is generated perpendicular to the magnetic field line.

The last two terms of equation 2.18 are commonly called the diffusion terms. The presence of either parallel or perpendicular diffusion tends to decrease the growth rate of the GD instability. The inclusion of these terms also leads to a threshold for the creation of GD waves. Using typical auroral F-region plasma parameters at an altitude of 250 km, namely, $\nu_i = 1\, s^{-1}, \nu_e = 20\, s^{-1}, B = 5 \times 10^{-5} T, E = 20\, mV/m, L = 20\, km$, and $\frac{k_{ll}}{k_x} = 10^{-4}$, one obtains that the growth time of the instability is ~ 83 s which lies within the typically cited range of 50 - 250 s. When there is no parallel component of the wave vector (k_{ll} is zero), the growth rate for the simplified GD instability (equation 2.17) is recovered.

Xu (2002) performed a full analysis of the threshold conditions for the GD instability in a broad range of heights. Here we show one result of his calculations in Fig. 2.3 for the electric field of 50 mV/m and background gradient of 10 km. Four different wavelength scales were chosen (50, 40, 30 and 20 m). One can see that the GD instability is more difficult to launch at shorter scales and at the top of the F region. Importantly, the 10-m waves typically observed with the SuperDARN radars are

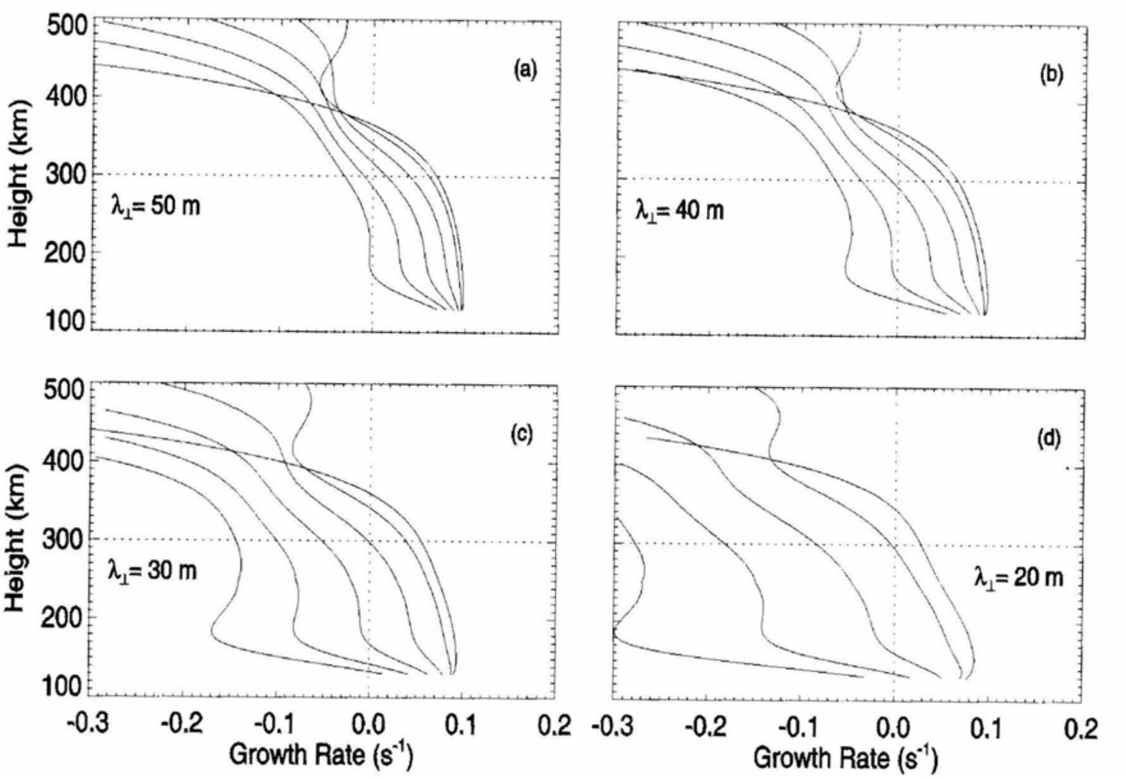

Figure 2.3 The growth rate of the gradient drift instability in the F region for the wavelengths of 50, 40, 30, and 20 m (from Xu, 2002). The curves corresponds to $k_{ll}/k_x = 0, 1, 2, 3, 4, 5 \times 10^{-4}$ with the right-most at lowest altitude being for the field-aligned condition.

impossible to generate at any height. It is expected that a non-linear energy transfer from larger-scale modes occur so that short wavelength irregularities are excited. It is believed that the mode coupling is the most likely mechanism of the GD instability saturation (Fejer and Kelley, 1980).

In the presence of the neutral wind, the magnitude of the convection velocity V_E in equation 2.17 is modified as discussed by Tsunoda (1988). Basically, collisions between molecules of the neutral wind and ions will cause the magnitude of V_E to either be increased or decreased, dependent on the orientation of the neutral wind with respect to V_E.

Expressions for the irregularity phase velocity were analyzed in detail by Xu (2002). He showed that with a high degree of accuracy, the phase velocity of GD irregularities is the cosine component of the ExB drift as equation 2.16 predicts.

2.2.2 Current convective instability

The current convective (CC) instability arises from currents parallel to the magnetic field in the presence of a gradient perpendicular to the magnetic field. Ossakow and Chaturvedi (1979) derived an expression for the growth rate of the CC instability

$$\gamma = \frac{\dfrac{V_{//}}{L}\dfrac{k_{ll}}{k_x}\dfrac{\nu_e}{|\Omega_e|}}{\dfrac{k_{ll}^2}{k_x^2}+\dfrac{\nu_e \nu_i}{|\Omega_e|\Omega_i}}, \qquad (2.19)$$

where $V_{//} = j_{ll}/n_0 e$ is the drift along the magnetic field line due to field aligned currents (j_{ll}) from the magnetosphere. Once again k_{ll} and k_x are the components of the wave vector parallel to and perpendicular to the magnetic field.

An increase in the parallel current would lead to an increase in the growth rate. Conversely, a larger gradient scale length or $\frac{k_{ll}}{k_x}$ ratio will reduce the growth, similar to the GD instability. Thus one would expect the fastest growing waves to be generated almost orthogonal (but not exactly) to the magnetic field (Keskinen et al., 1980). An increase in the electron collision frequency would enhance the growth of the instability; hence the instability would be most effective at lower altitudes.

Using typical auroral F region parameters at 250 km altitudes, namely, $\nu_i = 1\,s^{-1}$, $\nu_e = 20\,s^{-1}$, $B = 5\times10^{-5}T$, $n_0 = 2\times10^{11}m^{-3}$, $j_{ll} = 1\mu A/m^2$, $L = 20\,km$, and $\frac{k_{ll}}{k_x} = 10^{-4}$, the growth time of the instability is ~7x10^4 s, which is much larger than that of the GD instability. Also the presence of magnetic field shear, velocity shear, a finite width of the field-aligned current or a finite spatial extent of enhanced density can inhibit generation of the CC instability.

Commonly, due to the large number of similarities between the CC and GD instabilities, they are combined in description as

$$\gamma = \frac{\frac{1}{L}\left[V_E \frac{\nu_e \nu_i}{|\Omega_e|\Omega_i} + V_d \frac{k_{ll}}{k_x}\frac{\nu_e}{|\Omega_e|}\right]}{\frac{k_{ll}^2}{k_x^2} + \frac{\nu_e \nu_i}{|\Omega_e|\Omega_i}} - D_\perp k_x^2 - D_{ll} k_{ll}^2 . \tag{2.20}$$

With a strong field aligned current such that $V_d >> \frac{k_x}{k_{ll}}\frac{\nu_i}{\Omega_i}V_E$, the growth of the instability becomes independent of the electric field and dependent on the magnitude of the field-aligned current. However, these required strong field-aligned currents are seldom observed.

2.2.3 Ion cyclotron instability

The third instability potentially important for the F-region irregularity excitation is the ion cyclotron instability, which arises due to a strong parallel drift along the magnetic field. In the weakly collisional limit, Satyanarayana et al. (1985) showed from kinetic theory that the frequency of the waves is close to the ion gyrofrequency (Ω_i), as follows

$$\omega_r \approx \Omega_i \left[1 + \frac{T_e}{T_i} I_1(b_i) e^{-b_i}\right], \tag{2.21}$$

where $b_i = (k_\perp V_i / \Omega_i)^2 / 2$, and T_e, T_i, V_i and $I_1(x)$ are electron temperature, ion temperature, ion thermal speed ($\sqrt{\frac{2k_B T_i}{m_i}}$) and modified Bessel function of the first order.

The growth rate was found to be

$$\gamma \big/ \omega_r \approx -2\sqrt{\pi}\,\frac{T_e}{T_i} I_1(b_i) e^{-b_i} \frac{(\omega_r - k_{ll}V_d)}{k_{ll}V_{th}}\left[1+\sqrt{\pi}\,\frac{\nu_e}{k_{ll}V_{th}}\right]-\frac{\nu_i}{\Omega_i}\left(1+\frac{T_i}{T_e}\right), \quad (2.22)$$

where V_{th} is the electron thermal speed ($\sqrt{\frac{2k_B T_e}{m_e}}$) and V_d is the field aligned drift.

The last term in equation 2.22 shows the stabilizing effect that the ion collisions have on the instability by decreasing the growth rate. Electron collisions, on the other hand, tend to cause further destabilization. An increase in the electron thermal speed would lead to a decrease in the growth of the instability. The ratio of electron to ion temperature increases from about 1 at 100 km to about 4 at 200 km and then decreases back to about 1 at 600 km. The instability would have the best growth near 200 km where the ion collision frequency is about 1 s^{-1}. Keskinen and Ossakow (1983b) indicated that the field-aligned drift must be the order of several kilometers per second for excitation. This criterion is perhaps satisfied during periods of strong precipitation in very localized areas.

For the case of weak collisions, the growth rate was found numerically to maximize at about 400 km, whereas for the case of strong collisions, the maximum growth rate was found to be at 250 km with a diminished growth rate above and below (Satyanarayana et al., 1985).

The most important characteristic of the IC waves would be that the Doppler shift of the radio wave would be related to the ion gyrofrequency implying a high Doppler velocity of ~400-500 m/s. The variation in this shift would depend primarily on the temperature ratio.

The main controlling factor for the generation of the IC instability is that the field-aligned drift should be of the order of a few km/s.

2.3 E-region plasma instabilities

In the E region, the Farley-Buneman (FB) and gradient-drift (GD) plasma instabilities are the primary mechanisms for the generation of meter/decameter scale irregularities. The former instability occurs in a homogeneous plasma with a strong relative drift between the electrons and ions of the order of the ion-acoustic velocity of the plasma. The GD instability is essentially the same as in the F region one except it arises due to relative Hall drift between the electrons and ions. For the instability to occur, the electric field should be directed along the background plasma gradient. The instability analysis is slightly modified for the FB instability case because the ion inertia effects need to be considered.

2.3.1 Farley-Buneman instability

When ion inertia and temperature effects are to be considered, the equations of motion 2.1 need to be written as follows

$$m_\alpha \frac{d\mathbf{V}_\alpha}{dt} = e_\alpha \left(\mathbf{E} + \mathbf{V}_\alpha \times \mathbf{B}\right) - \nu_\alpha m_\alpha \mathbf{V}_\alpha - \frac{\nabla(n_\alpha T_\alpha)}{n_\alpha}. \tag{2.23}$$

The continuity equation 2.13 remains the same. By linearizing equations 2.13 and 2.23, under the assumptions of quasi-neutrality ($\delta n_i = \delta n_e = \delta n$) and that the electric field perturbations are electrostatic ($\delta\mathbf{E} = -\nabla\delta\phi$) and $\delta\phi$ and δn are sinusoidal of the form $\delta\phi$ and $\delta n \propto e^{i(k_x x - \omega t)}$, one can obtain the dispersion equation relating ω and k for the waves. Again, by assuming that the growth rate is slow ($\gamma << \omega_r$), one can obtain expressions for the phase velocity and growth rate. For the case of homogeneous plasma (FB instability)

$$\omega_r = \mathbf{k} \cdot \mathbf{V}_{ph} = \frac{\mathbf{k} \cdot (\mathbf{V}_{0e} + \psi \mathbf{V}_{0i})}{1 + \psi}, \tag{2.24}$$

and $$\gamma = \frac{1}{1+\psi}\left[\frac{\psi}{\nu_i}\left(\omega_r^2 - k^2 c_s^2\right)\right], \tag{2.25}$$

where $c_s = \sqrt{\frac{k_B\left(T_e + T_i\right)}{m_i}}$ is the ion acoustic speed for the medium, ψ is a parameter that depends on the local collision and gyro frequencies and the aspect angle between the wave propagation direction and the perpendicular to the local magnetic field (aspect angle), as

$$\psi = \frac{\nu_i \nu_e}{\Omega_i \Omega_e}\left(1 + \frac{\Omega_e^2}{\nu_e^2}\sin^2\alpha\right). \tag{2.26}$$

The growth rate of the FB instability is positive only when $\omega_r \geq kc_s$. Since for very small aspect angles ($\psi << 1$), equation 2.24 implies $\omega_r \approx kV_{0e}$ and the FB instability occurs if the magnitude of the electron drift along the wave direction is greater than c_s. In another interpretation, the instability can be excited within certain directions about the electron drift, within the so-called FB instability cone

$$\cos\theta > c_s / V_{0e}.$$

Quite often, a value of 400 m/s is used as an estimate for the c_s in the high-latitude E region. This implies that electron drift (electric field) must be in access of 400 m/s (20 mV/m) for the onset of the FB instability.

When the aspect angle is zero, the magnitude of the phase velocity of the waves is the greatest (close to V_{0e}). With deviation from zero aspect angle, ψ increases very rapidly causing a sharp decrease in both the growth rate and the phase velocity. For typical ionospheric conditions, the instability is hardly possible to generate at aspect angles more than 1°-2°. A diagram illustrating the linear theory expectation for the phase velocity decrease with aspect angle will be shown in Section 6.4.

2.3.2 Gradient drift instability, Hall mode

For the GD instability, expression for the phase velocity is the same as for the FB instability (equation 2.24) and the growth rate is usually combined with that of the FB to give

$$\gamma = \frac{1}{1+\psi}\left[\frac{\psi}{\nu_i}\left(\omega_r^2 - k^2 c_s^2\right) + \frac{\omega_r}{Lk^2}\left(\frac{\nu_i}{\Omega_i}k_y\right)\right], \qquad (2.27)$$

where $L = \left(\frac{1}{n_0}\frac{\partial n_0}{\partial y}\right)^{-1}$ is the gradient scale length. Here the GD contribution corresponds to the third term of the expression. Because the instability occurs due to relative Hall drift between electrons and ions, it is often referred to as the Hall mode of the GD instability.

Analysis of equation (2.27) shows that there is no real threshold for the GD instability onset provided that the considered wavelengths are long (>20-30 m) and the off-orthogonality angle of wave propagation is around zero. It is assumed that shorter wavelengths can be generated through the mode coupling effects.

If both terms in (2.27) are considered, the marginal growth condition ($\gamma = 0$) along the electron flow direction can be expressed as (Farley and Fejer, 1975)

$$V_{ph} = c_s \left[\left(1 + F^2\right)^{1/2} - F \right] , \tag{2.28}$$

where $F = \dfrac{\nu_i \Omega_e}{2\nu_e k^2 L c_s}$. In this case, the phase velocity can be above or below the ion-acoustic speed depending on the sign of the gradient. This effect has been used to explain a double-peak nature of auroral spectra (e.g., St-Maurice et al., 1994).

2.3.3 Contributions of ion drift to the phase velocity

Commonly in equation 2.24 most authors neglect the ion drift term when computing the phase velocity. In this section, the effect of this term will be evaluated with the aid of Fig. 2.4.

In panel a), a typical configuration of electric and magnetic fields in the northern hemisphere is shown. The electrons are predominantly drifting in the ExB direction (V_E) whereas the ions are experiencing drifts in both ExB and E-field directions. The vector

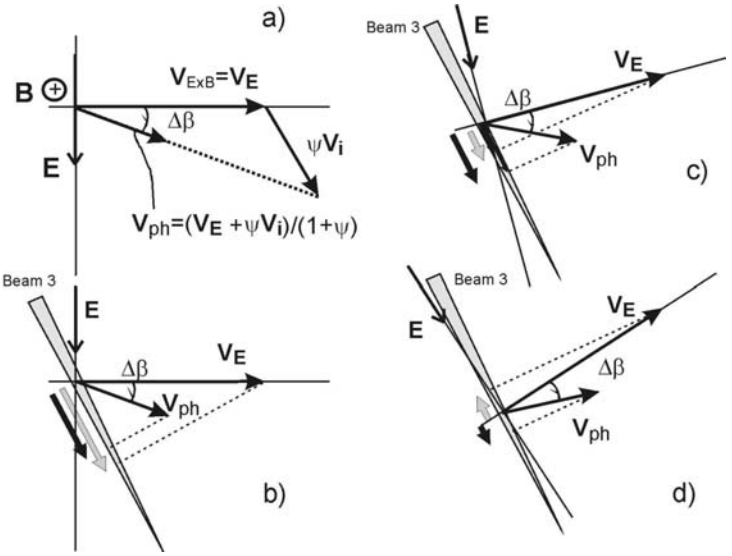

Figure 2.4 Contribution of ion motion to the phase velocity of E-region irregularities (a). (b)-(d) The apparent components of phase velocity (V_{ph}) and ExB drift (V_E) measured by a coherent radar with differing look directions.

$\psi \mathbf{V}_i$ shows the direction of the ion velocity contribution. The vector sum of the electron and ion components V_E and $\psi \mathbf{V}_i$ in equation 2.24 is directed at a certain angle $\Delta\beta$ with respect to the direction V_E as shown. The magnitude of the electron and ion contributions is reduced by the quantity $\frac{1}{1+\psi} < 1$ (often called the depression coefficient). The resultant vector of the irregularity phase velocity is shown by a heavy line on top of the dotted line in Fig. 2.4a. Clearly, the ion motions should contribute to the velocity of electrojet irregularities.

It is important to realize that the ion contribution to the irregularity phase velocity is altitude dependent since factor ψ depends strongly on the collision frequencies of electrons and ions with neutrals (changing quickly with height). In addition, the ion contribution depends on the aspect angle, α. If the aspect angle is large and considered flow angles are large so that the electron contribution in equation 2.24 is negligible, then the irregularity phase velocity may be just the ion velocity (Makarevitch et al., 2002a). In radar observations, the aspect angle changes with height so that both effects of collision frequency and the aspect angle changes must be taken into account. More general is the fact that in the lower E region the phase velocity is expected to be much less than V_E since the depression coefficient is small here. In the upper E region, the depression coefficient is close to 1 plus the ion drift is more aligned with the ExB direction and no significant velocity depresssion is expected.

The dependence of the irregularity phase velocity upon ion motions is not easy to test experimentally since the angle $\Delta\beta$ is typically less than 10° while in the course of radar measurements, the echo is a convolution of backscatter from all heights. In panels b) to d) we illustrate what might happen for observations at large flow angles when a coherent radar measures the phase velocity V_{ph} while simultaneously the velocity V_E is measured by an independent instrument. In panel b) we show a typical situation when a radar beam is oriented at a small angle with respect to the electric field but not extremely small. In this case, the ExB velocity projection onto the radar beam is larger than the irregularity phase velocity V_{ph} due to the irregularity velocity depression through the factor $\frac{1}{1+\psi}$ (equation 2.24). Panels c) and d) illustrate two more exotic situations for which the radar looks nearly along the electric field. The same ExB drift, phase velocity and relative orientation ($\Delta\beta$) is used in each case. In panel c), the phase velocity is greater than that of the ExB drift (compare the thick dark and grey arrows) meaning that the measured Doppler velocity should be larger than the ExB component. Panel d) shows an extraordinary case of the the ExB component being of opposite polarity as compared to the irregularity phase velocity.

The fact that the E-region irregularity phase velocity may be strongly affected by the ion motions gives another complication as compared to the F-region case. As was explained in Section 2.1 the ion velocity at the E-region heights depends on the neutral wind implying that under certain observational conditions, the measured phase velocity of echoes may reflect the neutral wind blowing at the heights of backscatter. This is especially true for the echoes coming from the bottom of the electrojet layer.

2.3.4 FB and GD plasma instabilities and types of auroral backscatter

The aforementioned theoretical results for the FB and GD plasma instabilities are valid only within the linear approach. The truth is that the linear analysis only describes the threshold conditions for the instability. For further analysis of any instability evolution, implementation of a nonlinear approach is required. For the sake of brevity, we will not consider this aspect of the problem here and refer the reader to excellent reviews by Fejer and Kelley (1980), Farley (1985), Kelley (1989) and Sahr and Fejer (1996). Instead, we would like to summarize the most important results of the nonlinear theories and to make a couple of points with respect to radar signatures of the FG and GD instabilities.

It is generally believed that the FB instability saturates in such a fashion that the irregularity phase velocity is somewhere close to the ion-acoustic speed (c_s). This result refers to the waves propagating within the linear instability cone; observationally this prediction is valid for radar observations along the ExB direction. Though the theories behind this result are complex, one can simply hope that the FB waves in a saturated state are close to the threshold condition $\gamma = 0$ so that $\omega = kc_s$ and $V_{ph} = c_s$ (equation 2.25). Further sophistication comes with the well-established fact that the ion-acoustic speed at the E-region heights depends indirectly the electric field magnitude. For electric fields stronger than ~50 mV/m, growing FB waves can heat the plasma and thus increase c_s. This implies that the phase velocity of the FB waves is a complex function of the ambient electric field. This conclusion is in total disagreement with the linear equation 2.24 where the irregularity phase velocity, to a first approximation, is the cosine component of the ExB plasma drift. This means that the analysis of the ion contribution to the irregularity phase velocity given in Section 2.3.3 is not applicable to the FB waves propagating along the flow. It is currently believed that the FB instability is responsible for observations of the so-called Type 1 waves, which are strong echoes with Doppler shift near the ion-acoustic speed and relatively narrow spectral line.

For observations at large flow angles, the situation is not simple as well, if one think in terms of non-linear approach. It is believed that because of the mode coupling effects the excess energy from waves within the linear instability cone can be transferred to plasma fluctuations at large flow angles so that strong enough plasma fluctuations can exist for large flow angles as well (e.g. Hamza and St-Maurice, 1995). However, what would be the irregularity phase velocity in these directions is not known. For this reason, it is customary to use the linear theory equation 2.24 to interpret radar data at large flow angles.

The evolution of the GD instability is believed to mostly governed by the mode-coupling effects (Sudan, 1983) and the irregularity phase velocity should be consistent with equation 2.24. No comprehensive assessment of the last statement has been done so far though the expectation is widely used in the radar work. The GD instability is sometimes associated with observations of weak, broad, low shifted echoes called Type 2 echoes. Though such an assumption make sense for observations at very weak electric fields, the role of the FB instability in generation of Type 2 echoes at strong electric fields is not known.

2.4 D-region instabilities and related processes

In the lower E and D regions, motion of the neutral atmosphere can be an additional source of energy for creation of ionospheric irregularities. In the past, the possibility of plasma irregularity excitation by neutral wind turbulence was hypothesized. This was reasonable to expect since both electrons and ions are collisionally coupled to the plasma component at the D-region heights (Section 2.1) and any turbulent motion of neutrals will be eventually reflected in the charged component. This idea was forwarded further recently both theoretically (Gurevitch et al., 1997) and experimentally (Schegel and Gurevitch, 1997; Ruster and Schlegel, 1999). The fundamental difference of these processes is a possibility of creation of isotropic irregularities so that auroral backscatter is not aspect sensitive. Robinson and Schlegel (2000) proposed an alternative theory of small-scale non-aspect-sensitive irregularity excitation due to strong plasma flows along the magnetic field lines. The phase velocity of these irregularities is also close to the velocity of neutral wind.

The field-aligned ionospheric irregularities responsible for aspect-sensitive auroral backscatter are more difficult to excite at the bottom side of the ionosphere due to enhanced collisions. Kagan and Kelley (1998) considered the GD instability launched by pure neutral wind and showed that the instability is possible below 100 km for the mid-latitude ionosphere. For the instability $\mathbf{U}_n \times \mathbf{B}$ drift should be parallel to the density gradient. Since stronger and quite variable winds are possible at high latitudes, one would expect this instability to be operational as well. Later Kagan and Kelley (2000) considered a thermal instability driven by neutral wind. Ion heating effects within the waves was allowed. It was shown that this instability can occur for $U_n >\sim 0.63 c_s$ implying quite strong but possible winds. The phase velocity of waves is close to the neutral wind velocity at heights between 90 and 95 km.

Dimant and Sudan (1995a, b, c; 1997) developed a kinetic theory for the current-driven instability (electric field associated) in the bottomside ionosphere for which the non-isothermal effects for the electrons were taken into account. Earlier Gurevich and Karashtin (1984) developed another type of the electron thermal diffusion instability in fluid approach. Both instabilities are fairly difficult to excite at meter scale wavelengths and much easier at decameter and longer scales. Interestingly enough, at the bottom side of the E region where the standard FB instability is not operational, the thermal instability still can produce long waves (~100 m) propagating at flow angles ~45° with respect to the electron flow.

Finally, in the D region, meteors can modify the FB instability development (Oppenheim et al., 2003a,b). Investigation of pertinent processes has just begun.

CHAPTER 3

RADAR SYSTEMS EMPLOYED: PRINCIPLES AND MODES OF OPERATION

In this chapter we consider the basic ideas of coherent radar operation and give details on the radar systems used in this thesis. In addition to the main instrument, the SuperDARN HF radar, we consider the STARE 144-MHz coherent radars and the EISCAT incoherent scatter radar. Data from both latter systems are used intensively throughout the thesis to support the HF research.

3.1 Principle of coherent radar measurements

A coherent radar transmits radio waves to the ionosphere and analyzes the information contained in the returned echo. This transmission is usually at a frequency well above the critical frequency of the ionospheric E and F regions (several MHz) so that in absence of irregularities there is no returned signal. However, if a quasi-periodic electron density structure is created in the ionosphere, multiple scatter from the wave fronts can provide a weak but detectable returned signal. For the radio wave - plasma irregularity scattering process, the momentum and the energy are conserved (Fejer and Kelly, 1980) such that

$$\mathbf{k}_{transmitted} = \mathbf{k}_{received} + \mathbf{k}_{irregularity} , \tag{3.1}$$

and $$\omega_{transmitted} = \omega_{received} + \omega_{irregularity} . \tag{3.2}$$

Hence for backscatter, the irregularity scale should be half of the radar wavelength (as follows from 3.1) and the difference in the frequency of the transmitted and received radio wave carries information on the phase velocity of the irregularity motion (as follows from 3.2). Typically, the power, Doppler velocity and spectral width of the returned echoes are investigated.

For more than five decades of radar studies, various frequencies were used. Originally, the choice of the frequency was pre-determined by the radars, which were "borrowed" by scientists for their research. For example, the Homer radar (Tsunoda et al., 1974) was originally a military installation intended to monitor approaching airplanes. With the maturing of radar experimentation as a field of research, the used frequencies became dictated by the specific desired task. Table 3.1 gives a brief summary of some recently used coherent radars.

In this thesis we focus on measurements performed with two coherent radar systems that were installed for convection studies in northern Scandinavia, Fig. 3.1. The first one is the Scandinavian Twin Auroral Radar Experiment (STARE) radars (Greenwald et al., 1978) operating since the late 1970s (with some modifications and upgrades). This is a VHF system. The second radar system is the Co-operative UK Twin

Table 3.1 Frequencies of coherent radars recently used for high-latitude research

Radar name	Radar location	Frequency (MHz)	Reference
HOMER	Alaska, USA	398	Tsunoda et al. (1974)
STARE	Northern Scandinavia	140/144	Greenwald et al. (1978)
BARS	Central Canada	48.5	McNamara et al. (1983)
SABRE	Northern Europe	150	Nielsen et al. (1983)
SAFARI	Northern Scandinavia	14.4	Villain et al. (1985)
CW-bistatic	Western Canada	50	Haldoupis et al. (1987)
CUPRI	Various (portable)	50	Providakes et al. (1988)
EISCAT	Northern Scandinavia	933	Moorcroft and Schlegel (1990)
SHERPA	Labrador, Canada	8-20	Hanuise et al. (1991)
MILLSTONE HILL	North Eastern USA	440	Foster and Tetenbaum (1991)
SAPPHIRE	Saskatchewan, Canada	50	Koehler et al. (1995)

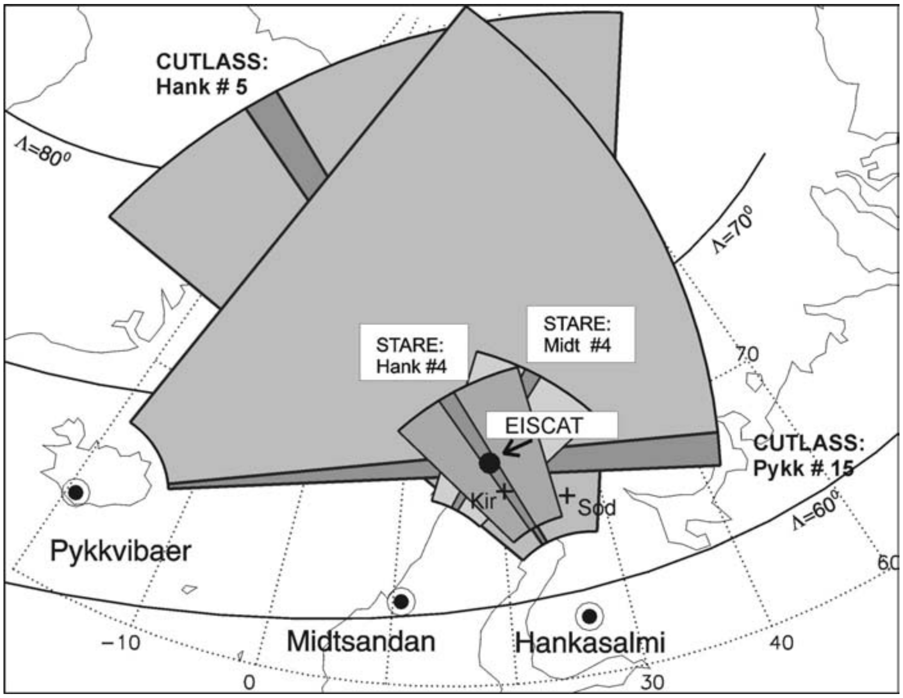

Figure 3.1 Current setup for radar observations over Northern Europe. Field of views of two coherent radar systems are shown. The larger fan-like structures represent the observational areas of the Pykkvibaer and Hankasalmi CUTLASS (SuperDARN) HF radars. The two smaller segments indicate the observational areas of the Midtsandan and Hankasalmi VHF STARE radars. The black dot shows the approximate position of the spot where ionospheric parameters are monitored by the EISCAT incoherent scatter radar whose transmitter is located at Tromso (close to the spot) and receivers are located at Kiruna (left cross) and Sodankyla (right cross). The STARE Hankasalmi and Midtsandan beams 4 cross each other in the area close to the EISCAT spot. Intersection of the CUTLASS Hankasalmi beam 5 and Pykkvibaer beam 15 is also close to the spot.

Auroral Sounding System (CUTLASS) HF radars that are part of the SuperDARN radar project. Both these radar systems were designed primarily to monitor the plasma convection over Northern Europe. However, over the years, they both have been successfully used for gaining knowledge on auroral backscatter. In fact, these two applications of the radars were progressing simultaneously.

3.2 STARE radars

The STARE experiment consists of two identical Doppler radars located at Hankasalmi, Finland (geographic latitude 62.3N, geographic longitude 26.6E) and

Midtsandan, Norway (63.7N, 10.7E, current location of the Norwegian radar). The respective field-of-views (FoV) are shown in Fig. 3.1. In the current version of the system, echoes can be detected from ranges between 495 and 1200 km with 15-km resolution. Each radar generates eight beams of 3.2° width that are separated by 3.6°. The radars operate at frequencies close to 140 MHz so that information on meter-scale irregularities is obtained. Typically, a 20-second integration time is used. Technical parameters of the STARE radars are summarized in Table 3.2.

Both radars employ a pulsed radar technique to determine the range of scatter and its associated Doppler velocity. The range and power of echoes is measured when the radar transmits single pulses. To obtain Doppler information, the transmission of a double pulse sequence is employed (Greenwald et al., 1978).

Table 3.2 Technical parameters of the STARE radars

Average power	50 kW
Frequency (Hankasalmi)	143.8 MHz
Frequency (Midtsandan)	140.0 MHz
Beam width	3.2°
Azimuthal coverage	26°
Time resolution (typical)	20 seconds
Pulse length	100 μs
Range resolution	15 km
Double Pulse separation	300 (200) μs

The backscattered power is computed from the quadrature outputs ($A(i,j)$, $B(i,j)$) for a given beam (*i*) and range (*j*) using

$$P(i,j) = A^2(i,j) + B^2(i,j) . \tag{3.3}$$

With the double-pulse information available, the quadrature samples are used to evaluate the real (*R(i,j)*) and imaginary (*I(i,j)*) parts of the double-pulse autocorrelation coefficients for each beam and range using

$$R(i,j) = A(i,j)A(i,j+N) + B(i,j)B(i,j+N) , \tag{3.4}$$

and $$I(i,j) = A(i,j+N)B(i,j) - A(i,j)B(i,j+N) . \tag{3.5}$$

Here NT is the time between the double pulses with T being the time between samples. The real and imaginary components are time averaged over the integration period to give the time-averaged phase

$$\overline{\varphi(i,j)} = \tan^{-1}[\overline{I(i,j)} / \overline{R(i,j)}], \tag{3.6}$$

which is proportional to the velocity.

For the double-pulse method, the base separation (τ) between the transmitted pulses is 300 μs. This allows unambiguous velocity measurements for 1-m irregularity wavelength (λ_{irr}) in the range of +/- 1667 m/s (${}^{\lambda_{irr}}\!/_{2\tau}$).

Since an operating frequency of ~140 MHz is utilized, the STARE radars are only sensitive to the waves in the upper D and E regions. At higher altitudes of Northern Scandinavia, the aspect angle of observations, the angle between the radar wave vector and the Earth's magnetic field, increases substantially and echo detection is problematic. As was explained in Section 2.3, the FB and GD plasma instabilities only generate plasma waves that propagate almost perpendicular to the magnetic field lines resulting in the power of off-orthogonal waves being greatly attenuated.

3.3 HF SuperDARN radars

SuperDARN (Greenwald et al., 1995) is an example of a system sensitive to ionospheric irregularities of decameter scale. The HF SuperDARN experiment was initiated to produce global-scale plasma convection maps in the F region, something that the STARE observations are not capable of doing. Over the years of operation, the SuperDARN radars proved to be extremely useful for research in various areas of space physics including auroral backscatter from the heights of the D region to the upper F region. Some expansion of SuperDARN radar applications was expected though others such as the neutral wind monitoring capabilities discussed in Hall et al. (1997) were a pleasant discovery in the course of the project development.

3.3.1 General description

The SuperDARN experiment (Fig. 3.2) currently includes 16 almost identical radar systems located in the northern and southern hemispheres. Each SuperDARN radar has one beam that is electronically steered over 16 positions separated by ~3.24°. Typically, ranges from 180 km to 3200 km are covered so that each of the SuperDARN radars monitors a significantly larger part of the high-latitude ionosphere than the STARE radars as can be seen in Fig. 3.1. The names, locations and boresight direction for the currently operating SuperDARN radars are tabulated in Table 3.3.

For most of the time the SuperDARN radars operate in a common mode, which completes one full sweep over the FoV in two minutes. Currently one minute scans are gaining popularity. The radar starts the scan at the beginning of each two (one) minutes with dwell time in each beam position of about ~7 (3) s. Echo power, Doppler velocity and spectral width are determined in 45-km range bins. The operating frequency can be chosen between 8 and 18 MHz with higher frequencies typically used during the day. Other technical parameters for the SuperDARN radars are given in Table 3.4.

Table 3.3 Radar locations and boresight directions for the SuperDARN experiment

Radar Name	Geog. Lat.	Geog. Lon.	Boresight Heading
Hankasalmi	62.32°N	26.61°E	-12.0°
Pykkvibaer	63.77°N	20.54°W	30.0°
Stokkseyri	63.86°N	22.02°W	-59.0°
Goose Bay	53.32°N	60.46°W	5.0°
Kapuskasing	49.39°N	82.32°W	-12.0°
Saskatoon	52.16°N	106.53°W	23.1°
Prince George	53.98°N	122.59°W	-5.0°
Kodiak	57.6°N	152.2°W	30.0°
King Salmon	57.0°N	157.0°W	-20.0°
Halley	75.52°S	26.63°W	165.0°
Sanae	71.68°S	2.85°W	173.0°
Syowa South	69.0°S	39.58°E	165.0°
Syowa East	69.0°S	39.61°E	106.5°
Kerguelen	49.35°S	70.26°E	168.0°
Tiger	43.38°S	147.23°E	180.0°

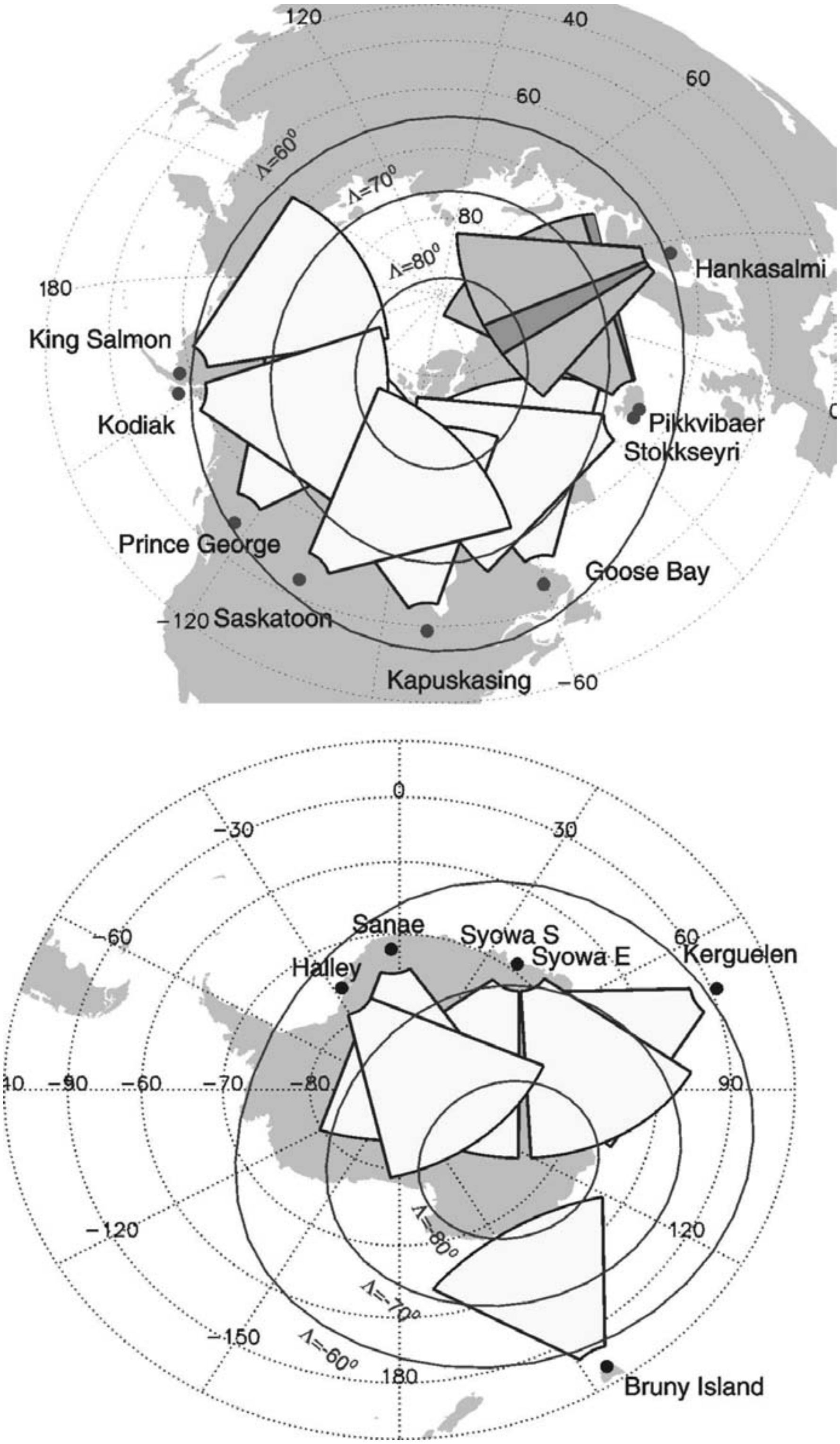

Figure 3.2 Locations of currently operating SuperDARN radars and their typical fields of view (for ranges 500-2800 km). Data of only the Hankasalmi and Pykkvibaer radars were used in this thesis.

Table 3.4 Technical parameters for a typical SuperDARN radar

Average Power	2 kW
Frequency range	8 - 20 MHz
Beam width	6^o - 2.5^o
Azimuthal coverage	~ 52^o
Scan duration	1 - 2 minute
Pulse length (typical)	100 - 300 μs
Range resolution (typical)	15 - 45 km

3.3.2 Derivation of echo parameters using FITACF approach

SuperDARN radars use a multi-pulse technique to determine the echo power, Doppler velocity, and spectral width. To achieve this, a specially designed sequence of pulses is repeatedly transmitted, and the averaged returned signal is processed into an autocorrelation function (ACF) dependent on the lag time. The pulse length and pulse pattern (including the lag time) can all be varied. The standard value for the pulse length is 300 μs, which gives the range resolution of 45 km. The lag time between samples is set to be larger than the pulse length and is currently 2400 μs. The standard pulse sequence (Fig. 3.3) consists of pulses transmitted as 0, 9, 12, 20, 22, 26 and 27 units of lag time, which results in an eighteen-lag ACF.

Fig. 3.4a illustrates the real and imaginary parts of the ACF for measurements reported by Villain et al. (1987). One can clearly recognize the decaying character of magnitude of the ACF. Importantly, for the current pulse pattern, there is only one missing lag, which makes the analysis of the ACF very convenient.

The obtained ACFs can be analyzed in several ways. The traditional way in the determination of echo parameters for SuperDARN is FITACF approach, which will be described in this section. The other two methods, the FFT method and the Burg method will be described later. All three methods of estimating the Doppler velocity are used throughout this thesis.

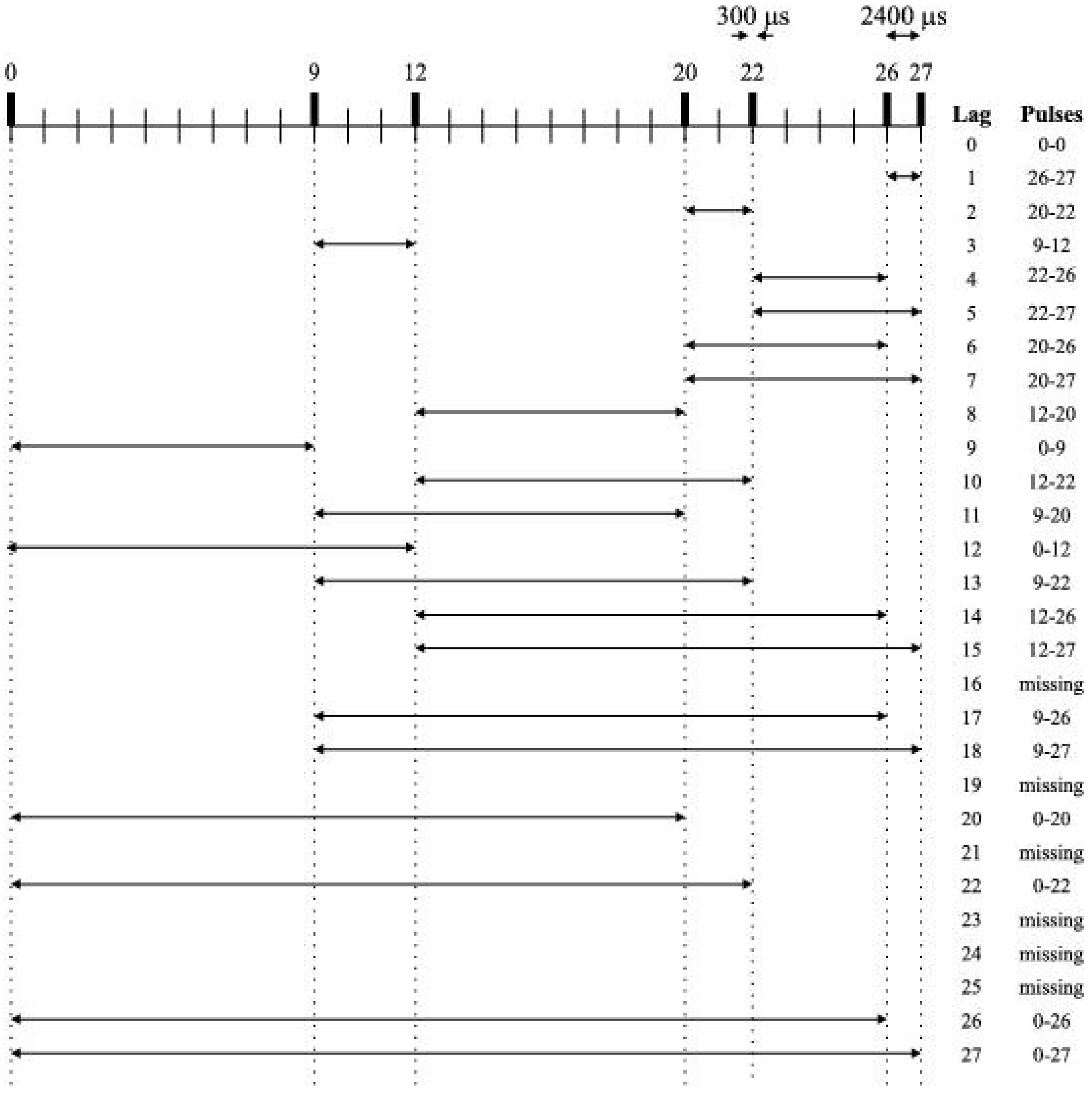

Lag	Pulses
0	0-0
1	26-27
2	20-22
3	9-12
4	22-26
5	22-27
6	20-26
7	20-27
8	12-20
9	0-9
10	12-22
11	9-20
12	0-12
13	9-22
14	12-26
15	12-27
16	missing
17	9-26
18	9-27
19	missing
20	0-20
21	missing
22	0-22
23	missing
24	missing
25	missing
26	0-26
27	0-27

Figure 3.3 The pulse sequence currently in use in SuperDARN observations (From Huber, 1999).

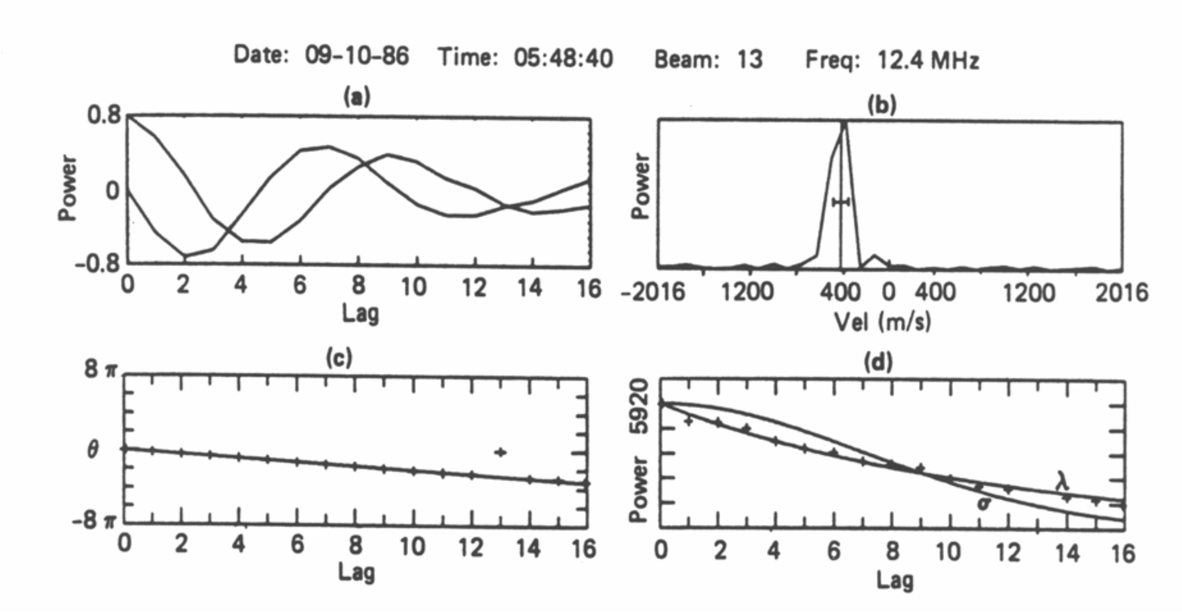

Figure 3.4 FITACF technique for analysis of SuperDARN ACFs. (a) Real and imaginary parts of the ACF. (b) FFT of the ACF and the estimates of velocity (vertical line) and width (horizontal line) obtained through FITACF. (c) Rate of change of the phase angle of the ACF with lag and the fitted velocity. (d) Decay of the power of the ACF for exponential (λ) and Gaussian (σ) fits (From Villain et al., 1987).

In the FITACF approach, one assumes that there is only one peak in the spectrum and ACF decays either exponentially or according to a Gaussian distribution law. One can plot the rate of change of the phase of the ACF versus lag number, Fig. 3.4c and find the line of best fit to the experimental points. The Doppler velocity is related to the slope (ω_d) through

$$\mathrm{v}_{Doppler} = \frac{c\omega_d}{4\pi f_{radar}}. \tag{3.7}$$

The power and the spectral width can be estimated assuming a model for the rate of the decay of the power of the ACF (Fig. 3.4d). For exponential decay, the decay of the power is modeled using

$$P(\tau) = P_\lambda e^{-\lambda\tau} \tag{3.8}$$

with the parameters P_λ and λ being evaluated. For Gaussian decay, the model equation

$$P(\tau) = P_\sigma e^{-\sigma^2\tau^2} \tag{3.9}$$

is fit to the data with the parameters P_σ and σ being determined.

The width of the spectrum is related to the decorrelation coefficients (λ and σ), using the equations for exponential and Gaussian decays, respectively,

$$width = \frac{c\lambda}{2\pi f_{radar}}, \tag{3.10}$$

and $$width = \frac{c\sigma}{\pi f_{radar}\sqrt{\ln(2)}}. \tag{3.11}$$

The power of the backscatter corresponds to the parameters P_λ and P_σ, for exponential and Gaussian decay, respectively. It can be visualized as the y-intercept of the fitted curves as in Fig. 3.4d.

3.3.3 Velocity estimates from Fast Fourier Transform spectrum

The velocity of the echo can also be estimated by analyzing the Fast Fourier transform (FFT) of the ACF, which is the power distribution for various frequencies (Fig. 3.4b). The velocity of the strongest peak of the FFT is referred to as the FFT peak velocity. The FFT method has the advantage that it gives the power spectral density (PSD) as a function of velocity, so a multiple component spectrum can easily be seen. It has two major drawbacks. First it is computationally intensive and secondly, with the current pulse pattern and lag separation, it gives a poor velocity resolution of ~100 m/s which we refer to as the usual spectral resolution.

3.3.4 Burg spectrum analysis

The third method is the Burg spectrum method (see Kay, 1988; Naidu, 1996). This is an autoregressive method that fits a statistical model to the data. This model is designed for short data sequences with the number of solutions equal to the order of the model. For the current analysis, an 8-th order Burg spectrum was calculated. The order of the model must be less than one half the number of data points in the ACF. The Fourier transform of the model can be computed to give an apparent spectrum, which is substantially smoother looking than the standard FFT of the ACF.

Schiffler (1996), Schiffler et al. (1997), Huber (1999) and Huber and Sofko (2000) have applied this method to SuperDARN data to illustrate the presence of double peaks in the cusp/cleft footprint region of the ionosphere. In general, the peaks of the Burg spectrum are the multiple velocity components in the radar data.

Velocity estimations using all three methods are demonstrated in Fig. 3.5. Here one can see the FFT spectrum (thin line), the Burg spectrum (thick line) and FITACF velocity estimate (vertical dashed line) at different cells of beam 5 for the Finland radar on 12 February 1999. For panel (a), the FFT and Burg spectrums are both single peaked,

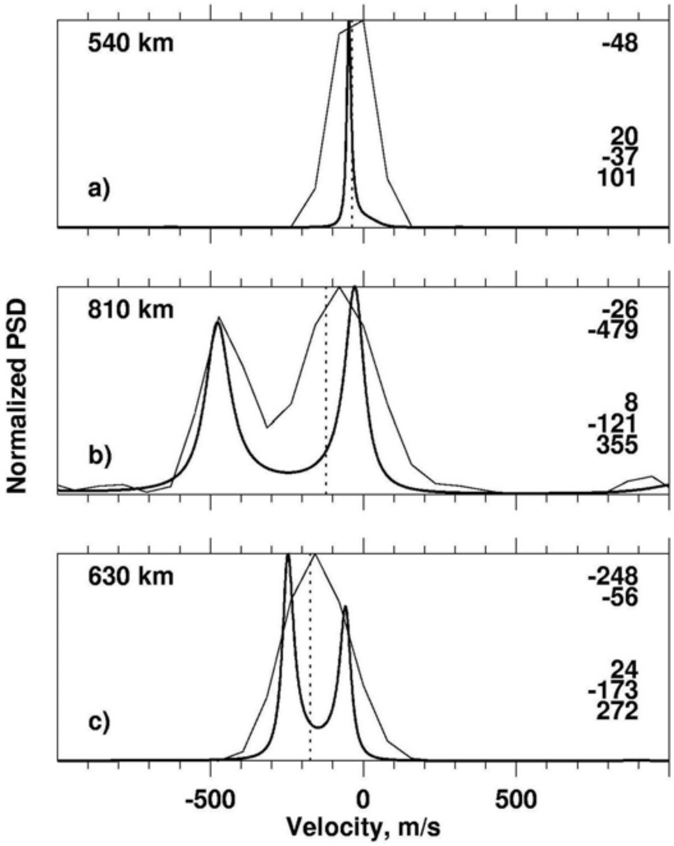

Figure 3.5 Examples of single and double peaked spectra analyzed with the Burg spectrum (thick line), FFT (thin line) and FITACF (dotted vertical line) approaches. The data were collected from beam 5 of the Hankasalmi radar on 12 February 1999. The upper panel (a) shows an example of single-peak echo observations at 14:52:33 UT with all three methods giving about the same result. Panel (b) shows results for double-peaked spectrum from 14:59:32 UT with significant separation. Panel (c) shows the spectrum at 14:58:32 UT that is seen as a single peak with the FFT method but is resolved into two components with the Burg method. Notice that for cases (b) and (c) the FITACF velocity is between the velocity peaks of the Burg spectrum.

and velocity estimates of the three methods agree quite well. For case (b) the FFT spectrum is obviously double-peaked. The Burg method shows the double peaked nature of the echo as well. Velocity estimates with these two methods agree quite well. The FITACF velocity is somewhere in between the peaks identified by the FFT and Burg methods. For panel (c), the FFT spectrum appears to be single peaked. The Burg method shows that the spectrum is actually double peaked with a small separation between the peaks. In this case, the FITACF velocity is close to the FFT mean shift while the Burg method gives information about the peaks and their separation.

3.3.5 Velocity data merging and convection maps

Both the SuperDARN and STARE systems were designed to work in radar pairs. The reason is that by combining the line-of-sight (LOS) Doppler velocities at the intersection of two beams, as shown in Fig. 3.6, one can derive the velocity of plasma drift. Repeating this procedure for all intersections of beams, a convection map of flow in the ionosphere can be inferred.

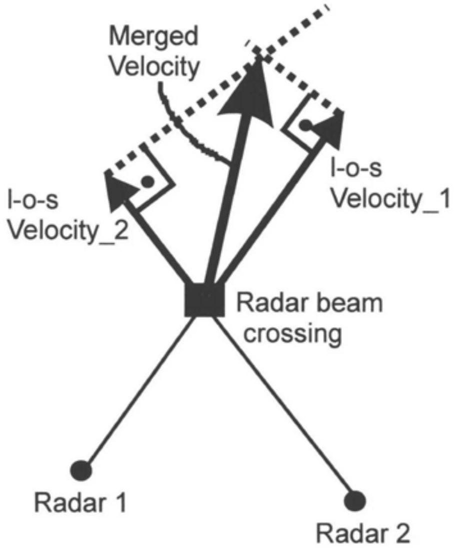

Figure 3.6 Merging of the Doppler velocities from two radars at the intersection of their beams.

Because data from two radars are not always available, other methods of convection estimation have been proposed. Out of these, the most prominent is the Map Potential approach currently in use for SuperDARN convection monitoring (Ruohoniemi and Baker, 1998). This method fits the observed LOS velocities at all available radar locations to a statistical convection pattern, which is dependent on the interplanetary magnetic field. The success of Map Potential depends on the number of data points that contribute to the solution. The more radars that have ionospheric backscatter, the more reliable the convection pattern will be. A sample convection pattern is shown in Fig. 3.7.

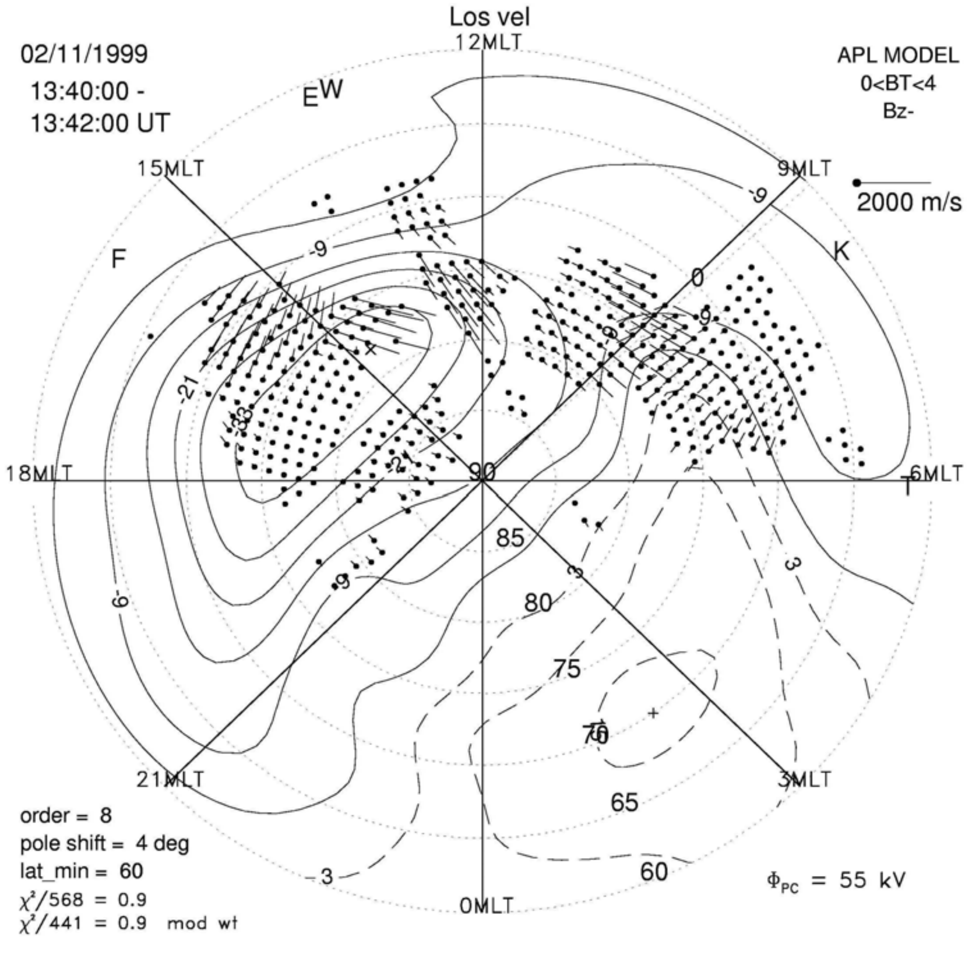

Figure 3.7 Convection pattern determined with the Map Potential technique. Data from Hankasalmi (F), Pykkvibaer (E), Stokkseri (W), Kapuskasing (K) and Saskatoon (T) were used.

3.3.6 Propagation modes

The SuperDARN radars use a lower radar frequency so that radio waves can experience significant bending and thus reach various heights in the ionosphere. Let us describe the propagation modes shown in Fig. 3.8 for SuperDARN following the nomenclature of Milan et al. (1997a). The $\frac{1}{2}$E and $\frac{1}{2}$F modes are direct ionospheric backscatter from the E and F regions, respectively. Ionospheric echoes can also be received via the $1\frac{1}{2}$F (E) modes where the radio wave is reflected by the ground before and after scattering from the F (E) region. SuperDARN can also detect ground scatter through the 1E, 1F and 2F modes where the radio wave hits the ground and is returned to the receiver. Ground scatter is easily distinguished by a near zero Doppler shift and a small width.

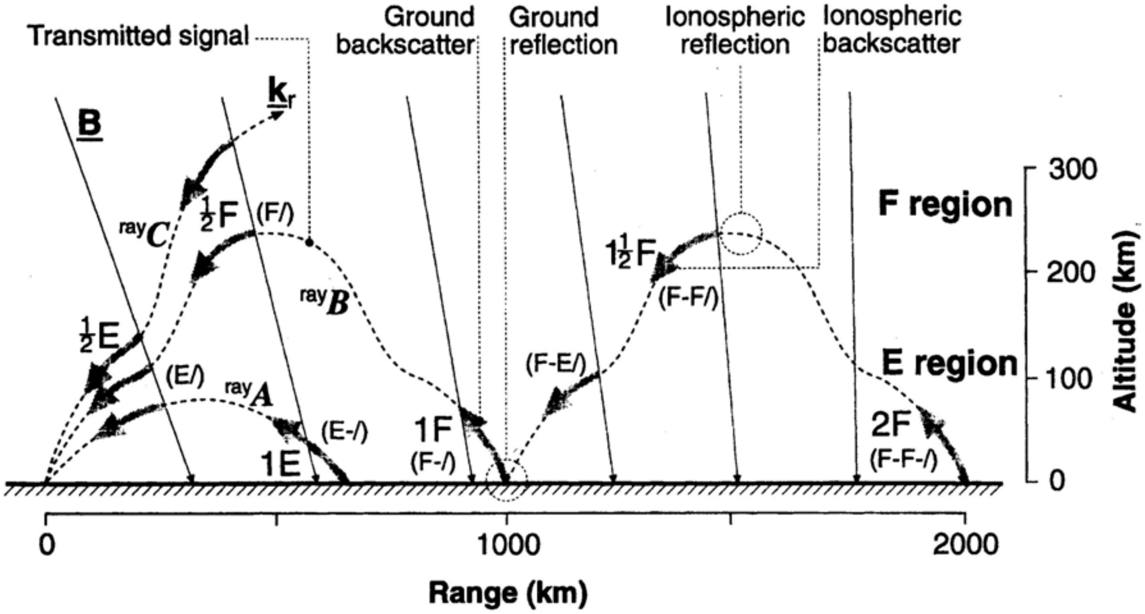

Figure 3.8 Propagation modes through the ionosphere for HF radio waves (From Milan et al., 1997a). Mode nomenclature according to Davies (1967) is shown in parentheses.

3.4 STARE and SuperDARN radars: Advantages and shortcomings

Years of coherent radar operation have shown that they are extremely useful instruments for studies of plasma irregularities. Their major advantage is the significant spatial and temporal coverage such that areas with ionospheric irregularities can be identified on a global scale. Radars operate continuously while rocket and satellite measurements that are limited to a specific trajectory, unique in time and space.

The disadvantage of coherent radar is that often echoes are missing for various reasons. Among the factors affecting radars is radio wave absorption in the D region, which is especially crucial at HF frequencies. The other factor is significant radio wave refraction that makes it more difficult to identify the area of measurements. This is alleviated by the fact that most coherent radars have rather poor, if any, resolution in altitude.

The STARE radars are superior over the SuperDARN radars in terms of range and height resolution. One knows for sure that the received echoes are coming from the E region due to aspect angle considerations while additional efforts are needed for SuperDARN.

3.5 EISCAT - Incoherent Scatter Radar

Incoherent scatter radars have been widely used in irregularity studies to supply information on the background plasma parameters in the ionosphere, such as electron density, electron and ion temperatures and electric field. A list of high-latitude incoherent scatter radar experiments is presented in Table 3.5. In this thesis, data of the

Table 3.5 Incoherent radars used for high-latitude research

Radar name	Radar location	Freq (MHz)	Reference
MILLSTONE HILL	Boston, USA	440/1290	Evans and Lowenthal (1964)
CHATANIKA	Alaska, USA later moved to Sondrestrom	1290	Leadabrand et al. (1972)
EISCAT	Northern Scandinavia	933	Risbeth and Williams (1985)
SONDRESTROM	Greenland, Denmark	1290	Kelly et al. (1995)

UHF European Incoherent Scatter Radar experiment (EISCAT) will be used. We should note that in the past some incoherent radars were successfully used for coherent echo studies by altering the orientation of the beams (Foster and Tetenbaum, 1991; Moorcroft and Schlegel, 1990).

EISCAT is a 933 MHz tri-static radar system, which can operate both in beam-scanning mode and fixed beam configuration. In the CP-1K mode, the transmitter located at Tromso (Norway) creates a narrow beam with a half power width of 0.6° along the local F-region magnetic field, see Fig. 3.9. Receivers located at Tromso and the remote sites of Kiruna (Sweden) and Sodankyla (Finland) measure the signals from the common volume at a height of ~250 km. Such an arrangement allows plasma convection measurements by combining LOS velocity measurements from three directions. Additional technical parameters for EISCAT are found in Table 3.6.

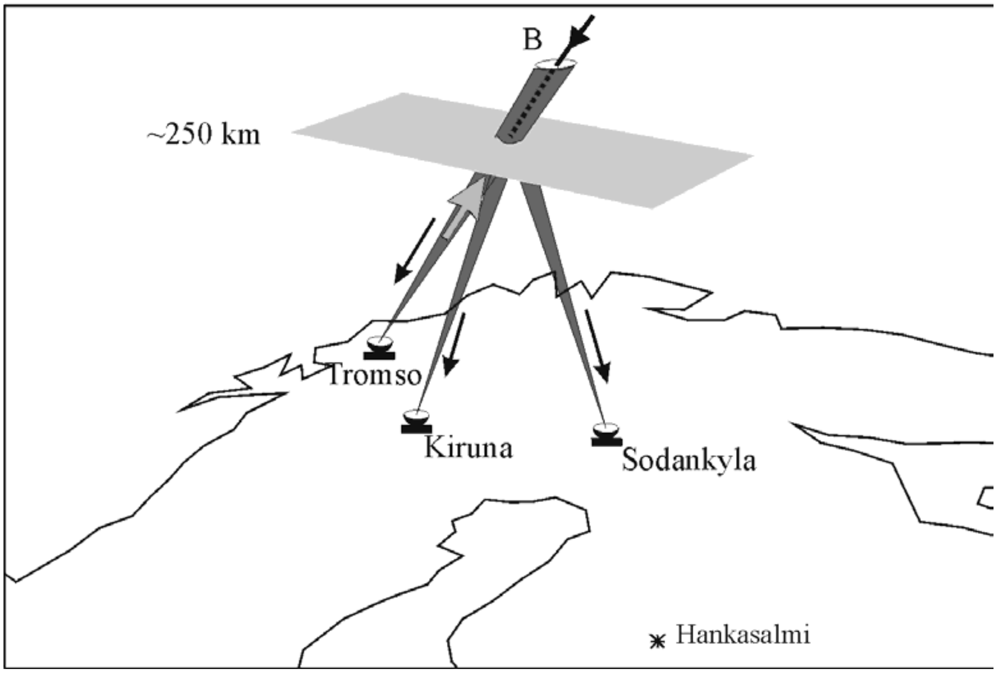

Figure 3.9 Ilustration of the function of the EISCAT radar. The Tromso antenna transmits and receives. The Kiruna and Sodankyla antennae receive only.

Table 3.6 Technical parameters of the EISCAT radar

Peak Power	1.5 MW
Frequency	933 MHz
Antenna	32m Paraboloid
Beam width	0.6^o
3 dB viewing area at 110 km	1.2 km
3 dB viewing area at 250 km	2.6 km
Observation duration (typical)	2 minute
Range resolution (typical)	3.1 or 22 km

The LOS velocity can be obtained from the Doppler shift of the scattered power spectrum with respect to the transmitted frequency, in much the same way as coherent radars. In the high-latitude F region, this LOS velocity is a component of the bulk plasma drift.

In addition to the electric field measurements, the electron density and electron and ion temperature distributions with height can be derived from the power spectrum (Fig. 3.10) of the return signals received at Tromso. The spectrum consists of two parts. The first part is the sharp resonance peaks close to the electron plasma frequency called the "plasma lines". In principle one could determine the absolute value of the electron density from these lines, but in practice they are usually weak requiring special care for their detection. The second part is the ion-dominated portion at the center of Fig. 3.10 called the "ion line". The ion part of the spectrum exhibits a double-humped shape where the humps become particularly sharp when the ratio of electron to ion temperature is much larger than one as shown by Fig. 3.11. From the shape of the spectrum, the ratio of electron to ion temperature can be determined. From the power of the backscatter, the electron density can be estimated.

The altitude resolution of the EISCAT density measurements for the periods that are considered in this thesis was 22 km for the long pulse method in the F region, and 3.1 km for the alternate code method in the E and D regions. E-region temperatures were also measured with 3.1 km resolution. We considered two-minute averaged EISCAT data. For special experiments better temporal and spatial resolutions can be achieved.

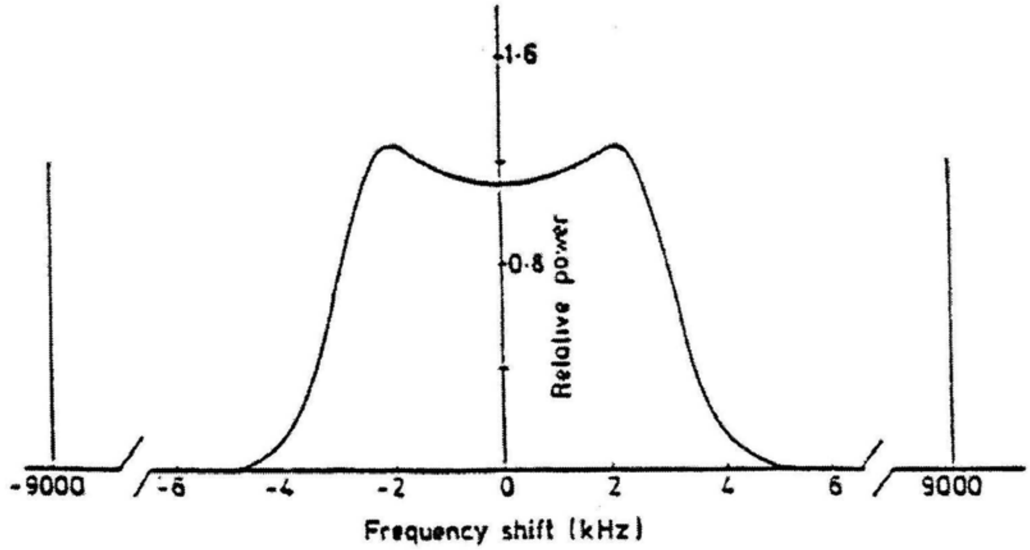

Figure 3.10 Sample power spectrum from an incoherent scatter radar. The plasma lines are the narrow lines at +/- 9000 kHz. The ion line is centered around zero shift (From Beynon and Williams, 1978).

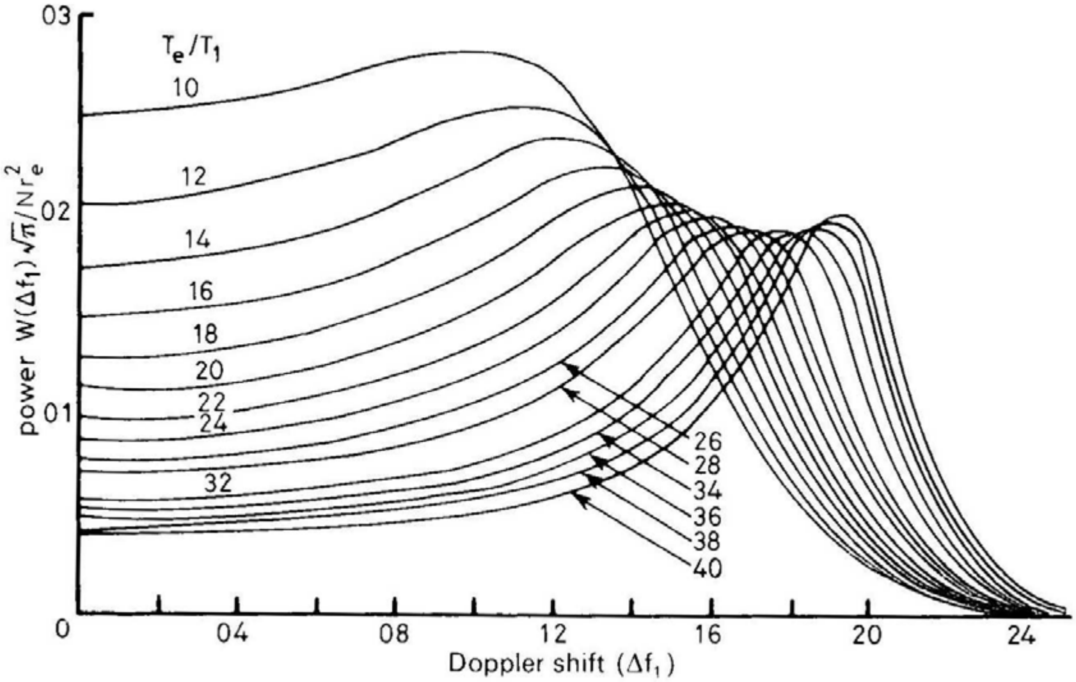

Figure 3.11 The effect of electron to ion temperature ratio on the ion line of incoherent radar spectrum (From Davies, 1990).

3.6 Summary of radar systems used

Three radar systems are used in this thesis. The primary system is the SuperDARN HF radar, which is designed to measure the power, velocity and spectral width of auroral backscatter from the D, E and F regions in a broad area of about 50 degrees in azimuth and 180–3200 km in range. Next is the VHF STARE system that is used to study the power and velocity of E-region backscatter over Northern Scandinavia. The spatial extent of the STARE radars' FoV is much less than SuperDARN, however propagation conditions are fairly stable and not a factor in their observations. Finally, EISCAT is used as a support to the other radars by measuring electron density, electric field, and electron and ion temperatures in the E and F regions. Given the highly localized viewing region, these parameters will be used as a guide in helping to unravel the properties of E- and F-region irregularities and their nature.

CHAPTER 4

OCCURRENCE OF F-REGION HF COHERENT ECHOES AT HIGH LATITUDES

Studies on the occurrence rate for auroral coherent echoes at various heights are important for two major reasons. First of all, since echoes are observed not all the time, one might associate the echo onset with the establishment of certain threshold conditions for various plasma instabilities so that times of echo occurrence might give vital information on the plasma physics associated with the ionospheric irregularity excitation. Secondly, because coherent radar systems are widely used for plasma convection monitoring, research in this area provides an assessment of system performance in terms of data coverage over time of the day, month or year. For HF radar systems, propagation conditions are important, and echo occurrence studies thus are indicative of changes in these conditions versus time. Besides practical application for radio communication purposes, these studies might shed light on the general character (trends) of the magnetosphere-ionosphere interaction.

In this chapter we first consider F-region echo occurrence for one SuperDARN radar, the Hankasalmi CUTLASS radar, for various seasons and years within the solar cycle. Such a study gives a general assessment of echo occurrence and provides insights into the factors that control F-region echo appearance. The relative role of these factors is difficult to evaluate in a statistical study of echo occurrence. We attempt to do this for specific observations for which many ionospheric parameters were monitored by the EISCAT radar. Many results of this chapter have been reported by Danskin et al. (2001a,b) and Koustov et al. (2002b, 2003) and some of them have been published in Danskin et al. (2002).

4.1 Review of previous studies

Several factors are known to control the HF echo occurrence rate. One can separate them into two groups. First of all, one has to have irregularities being excited in the ionosphere to detect them. The onset of irregularities depends on plasma physical processes involved, and in the case of the GD instability, the presence of a strong plasma gradient and an electric field is required (see Chapter 2). In the case of the current convective and ion-cyclotron instabilities, the establishment of strong field-aligned currents is required.

The second group of factors is related with the radar waves' propagation conditions since echoes can be missed even if the irregularities exist. For HF radars, an appropriate amount of refraction is essential to the reception of backscatter from the irregularities. From the linear theory for the GD and CC instabilities, one notes that the irregularities that are produced in the F region propagate orthogonal to the magnetic field; any deviation from orthogonality causes a rapid decrease in the growth rate of the instabilities.

Propagation conditions are controlled by the electron density distribution in the ionosphere and D-region radio wave absorption. An appropriate amount of density will be necessary for the radio wave to refract and reach orthogonality with the magnetic field. For excessive densities (as during midday) the radio wave can be over refracted, and ground scatter may occur. A substantial electron density in the E region may cause backscatter or ground scatter from the E region, which would inhibit the radio waves from entering the F region. Substantial absorption of the radio waves in the D region will decrease the backscattered power and may ultimately totally absorb the radio wave.

Ideally, F-region echoes should occur throughout the entire day, since the GD instability does not have a threshold value for plasma drift. Commonly the drift is caused by an electric field, however it may also be caused by motion of the neutrals/neutral winds (see Keskinen and Ossakow, 1983a) or gravity waves. In the latter case, the ions can collide with the neutral molecules resulting in motion along the direction of molecule motion. If the radar were an ideal instrument, it would observe backscatter whenever scatterers are present, but this does not appear to be so.

Typically, F-region echoes at geomagnetic latitudes less than ~75^{o} occur throughout the day with the exception of the noon sector (Ruohoniemi and Greenwald, 1997, Milan et al., 1997a). Milan et al. (1999) noticed the presence of backscatter only during times when the convection electric field was nonzero. The absence of echoes could be caused by the smoothing out of gradients due to solar illumination during the noon period (Ruohoniemi and Greenwald, 1997). Alternatively, during the daytime photoionization in the D, E and F regions substantially enhances the electron density and related conductivity of these regions. Enhanced conductivity in the E region could short out of the polarization electric field that gives rise to the irregularities in the F region. These processes have been recently discussed theoretically by Chaturvedi et al., (1994) and experimentally by Milan et al. (1997a). The increased electron densities in the D region could also lead to enhanced absorption of the HF radio wave. Perhaps a manifestation of this effect is often an echo absence near the bright auroral forms such as auroral arcs (Milan et al., 2001). There have been no studies of the level of absorption needed for HF radar echo detection with SuperDARN.

Another possibility for the absence of echoes is that large electron densities that occur during the day can cause substantial refraction of the HF radar waves (Milan et al., 1997b). In an extreme case, the ray may be returned to the ground and scattered back to the radar causing ground scatter. The presence of this ground scatter can obscure F-region scatter, because the radar may not be able to distinguish between the two. The typical operation of the radar is designed to minimize the amount of ground scatter and hence maximize the ionospheric scatter by changing the radar frequency.

Near dusk and dawn a distinct group of F-region echoes at low latitude exist. These echoes have very narrow widths and occurred within a few hours of dawn or dusk (Hosokawa et al., 2002). The dusk associated echoes are a feature of all the SuperDARN radars whereas the dawn echoes appear limited to the Canadian sector. The dusk echoes appear near the dusk meridian at magnetic latitude slightly lower than the equatorward edge of the auroral oval, which corresponds to the plasma density depleted structure known as the mid-latitude trough (Ruohoniemi et al., 1988, Mishin et al., 2003). In disturbed magnetic conditions, the dusk echoes occur at earlier local times. The dusk echoes are one of the most repeatable features whereas the dawn echoes are more rare.

Another repeatable feature of the dayside is the ionospheric footprint of the cusp which occur near magnetic local noon at about 70^{o} magnetic latitude. Ballatore et al. (2001) discovered that there is a significant correlation between the merging electric field induced by the solar wind and the rate of HF occurrence. For magnetic latitudes from 60^{o} to 67^{o} the correlation was independent of magnetic local time, whereas from 67^{o} to 74^{o} the correlation maximized near magnetic local noon. The high latitude echo occurrence near local noon may be due to cusp/cleft region of the magnetosphere.

To investigate the effects of various parameters of the high-latitude ionosphere on F-region echo occurrence, a device would be needed to measure these parameters. One of the best instruments for this purpose is EISCAT. Additionally, a riometer would be needed to ascertain the level of radio wave absorption.

4.2 Hankasalmi HF radar: Statistical study of echo occurrence

Though previous studies did point out on the preferential periods for the F-region echo occurrence, the character of these variations, for example the seasonal variation is not clear. In this section we study echo occurrence rates for the Hankasalmi HF radar. Certainly, a significant amount of data on HF echoes is available for other SuperDARN radars. The data availability varies from station to station but most radars were on the air from 1996, i.e. from the solar cycle minimum (1995/96) to maximum (2001/2002). Our restriction to just one radar originates from the concern that propagation conditions vary from one place to another so to assess their role it would be easier to deal with just one radar. One can extend consideration to other radars, and this is, in fact, what is happening while this thesis is in preparation.

As a first step, we give general ideas on echo occurrence rates for the Hankasalmi radar. We consider observations for one month during February 1999. This is the period close to the maximum of the solar activity. Our observations thus complement those by Milan (1997a) who reported data for the year of minimum solar activity. The other restriction is the consideration of only meridional beams. This is not a crucial limitation since the processed data for all beams show about the same tendencies. The restrictions is more to deal with the fact that later in this thesis, the Hankasalmi beam 5 data will be compared with EISCAT measurements, and these common observations are performed close to the magnetic meridian direction.

The echo occurrence rate was computed as a ratio of the number of registered echoes in every individual radar gate over the total number of observations in this gate for all selected beams for each month. A similar approach was undertaken by Ballatore et al. (2001). Ionospheric echoes stronger than 3 dB were only counted. Ratios were computed for every 10 minutes of observations and then arranged by 1^{o}-bins in magnetic latitude. The MLT times for echo registration at every radar gate was computed by taking into account the range and universal time. In this way, the standard "MLT-magnetic latitude (Λ)" plots of echo occurrence were obtained similar to Ruohoniemi and Greenwald (1997). We should warn that Ruohoniemi and Greenwald (1997) used different way of counting the echoes; namely, echo occurrence was assigned to specific latitude irrespective of its longitude. This resulted in higher echo occurrence rates as compared to the ones reported in this study. Though Ruohoniemi and Greenwald's (1997) approach assesses the data availability for convection studies, our way of counting is more suitable for studying the reasons for echo onset. The echo occurrence rates reported in this chapter are consistent with the data reported by others (Hosokawa et al., 2002; Villain et al., 2002; Parkinson et al., 2003).

4.2.1 Dependence on magnetic latitude and MLT time sector

The MLT-Λ plot for Hankasalmi echo occurrence in February 1999 is presented in Fig. 4.1. One can recognize three distinct areas of echo detection, the daytime (~12 MLT) echoes at magnetic latitudes 75^{o} - 80^{o}, midnight (~24 MLT) echoes at 70^{o} - 75^{o} and the evening (~18 MLT) low-latitude echoes at 62^{o} - 65^{o}.

These three ranges of echo occurrence reflect, from one side, physically different domains of space plasmas and, from the other side, the most frequently occurring radar propagation modes, see Section 3.3.6. The daytime echoes are received from the cusp area. Because electric fields are quite strong and more chaotic than in other time sectors and latitudes, echoes are typically broad (Baker et al., 1990). They are received through $1\frac{1}{2}$F propagation mode. To illustrate how the cusp echoes are received, we performed a raytracing analysis for the daytime observations (Fig. 4.2). In the panel (a) of Fig. 4.2 we

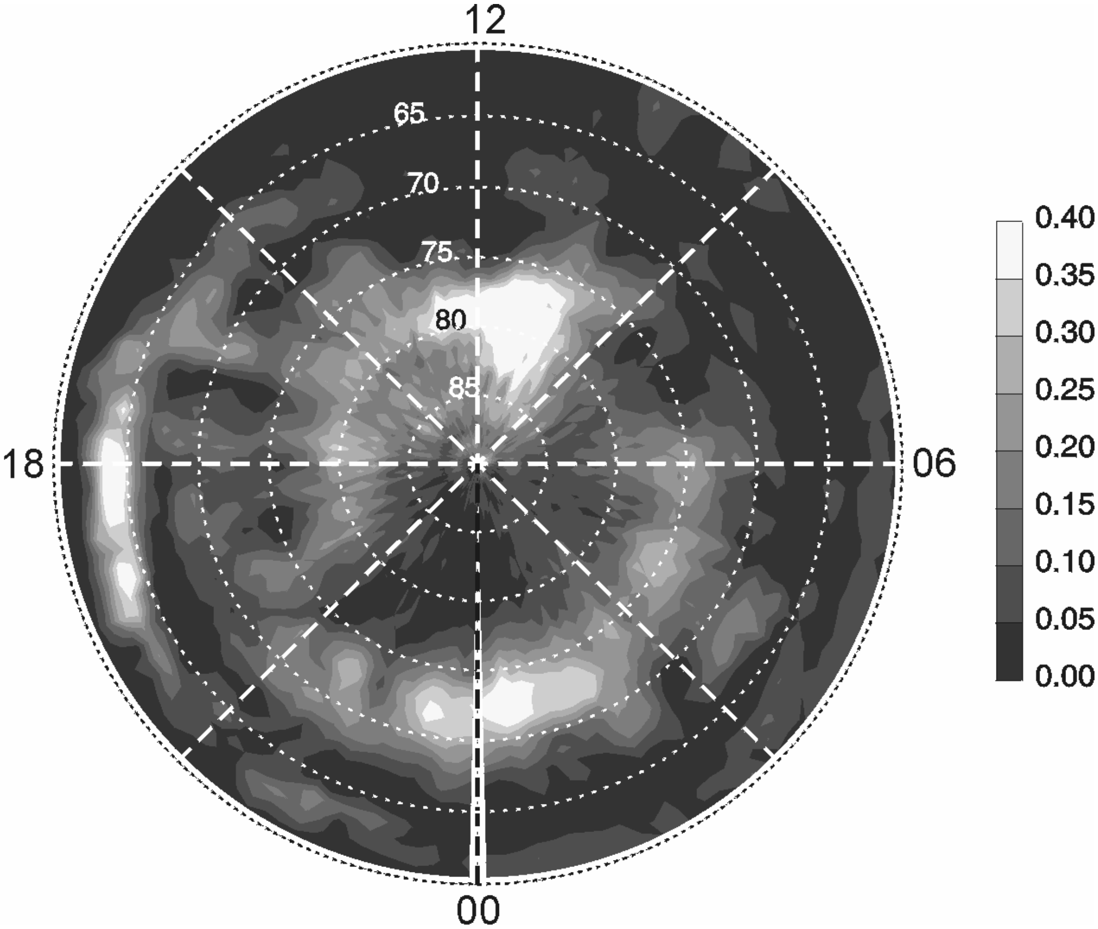

Figure 4.1 HF echo occurrence rates (normalized to 1) at various magnetic latitudes and magnetic local times for observations in February 1999 at Hankasalmi, Finland (Courtesy of D. André) in beams 5, 6 and 7 (as indicated in Figure 3.2).

show the daytime electron density profile observed at the EISCAT spot (see Fig. 3.1) on 10 February 1999 at 1230 UT (profile (*i*)). There is substantial density at the heights of ~220 km, as expected under the condition of a sunlit ionosphere. The ray tracing is shown in panel (b). The rays are 2° apart for elevation angles of 6° to 30°. Crosses indicate those parts of the trajectory where the aspect angle of observations are within ±1 degree to the magnetic field implying that backscatter could be received from these parts of the ionosphere. One can see that the radar has access to short ranges of 300-800 km (MLat = ~ 60° - 65°) and large ranges 1800-2500 km (MLat = ~ 74° - 80°). One should observe ground scatter at ranges 1200-1300 km, equatorward of the cusp echoes.

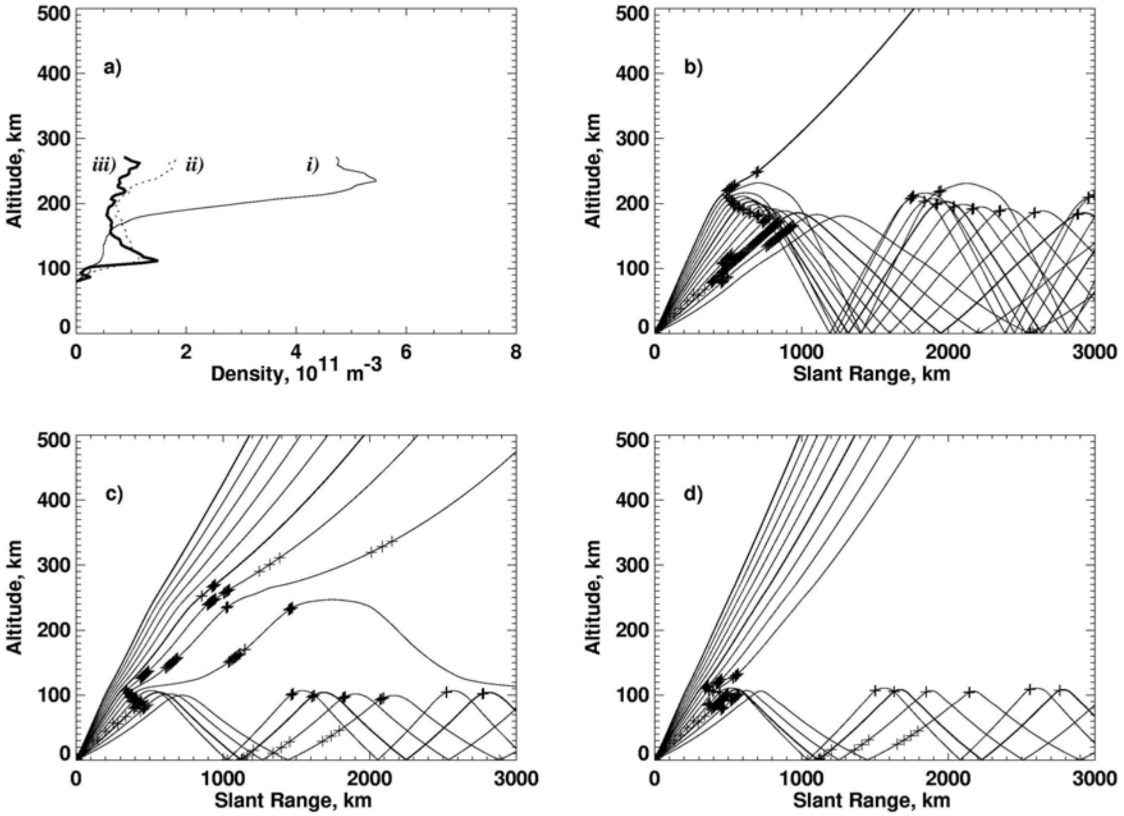

Figure 4.2 (a) The electron density distribution in the ionosphere used in ray tracings (b-d). The possible ray paths from Hankasalmi for (b) 10 February 1230 UT at 12.4 MHz using profile *i*), (c) 10 February 2210 UT at 10.0 MHz using profile *ii*), and (d) 12 February 1430 UT at 12.4 MHz using profile *iii*). Crosses indicate ranges where the ray is within ±1^{o} of orthogonality to the magnetic field.

The midnight echoes are obtained at the latitudes of the auroral oval. These are typically not as broad as the daytime echoes (Villain et al., 2002). The midnight echoes are received through $\frac{1}{2}$F mode due to the electron density decreases at night such that no significant bending of the HF radio wave can be achieved. A typical nighttime electron density profile is shown in Figure 4.2a, profile (*ii*). The E- and F-region densities of Fig. 4.2 (panel b) are of the order of 1-2 x 10^{11} m^{-3}. The ray tracing for the nighttime profile is shown on the panel (c) in the same format as for daytime observations. Calculations were performed for the radar frequency of 10 MHz because in the late evening/midnight/early morning the Hankasalmi radar usually operates at this frequency. One can see that echoes are expected to come from ranges up to ~1800 km. At short ranges one may expect E-region echoes while for ranges beyond ~800-900 km (MLat > 65°) the echoes are very likely to come from the F-region heights.

Finally, the low-latitude evening echoes are most likely coming from the E region. They are received at ranges of 300-600 km (60° - 64° magnetic latitudes) that are optimal for echo reception from ~100-120 km heights. Appropriate ray tracing for typical electron density profile (Fig. 4.2a, case (*iii*)) is shown in Fig. 4.2d. In this panel notice an absence of rays that can be backscattered from the F-region heights.

Below we consider the statistics of the midnight echo occurrence in an attempt to gain knowledge on the factors that control F-region echo occurrence. The reason for this choice is not only that midnight echoes are most frequent (see also Parkinson et al., 2003) but also because they are received through the $\frac{1}{2}$F propagation mode, the simplest possible trajectory, requiring the least electron density. We also consider separately observations in two MLT sectors, 23-24 MLT and 00-01 MLT. The motivation for doing this comes from Liou et al. (2001) who reported a significant difference in particle precipitation and auroral luminosity-background conductance relationships for these two sectors. One may expect differences in the echo occurrence as well since both the background electron density and density gradients are the factors controlling the F-region echo onset. The data presented in Fig. 4.1 indicate that echo occurrence is about the same prior to and after midnight with some tendency to prevail after midnight, but this will be explored in more detail.

4.2.2 Onset/disappearance MLT time for the midnight echoes

Data presented in Fig. 4.1 show that the midnight “blob” of enhanced echo occurrence is limited to a certain time interval. To give a quantitative description of the effect we consider the typical time for the echo onset in the evening sector and the typical time for echo disappearance in the morning sector. Fig. 4.3 shows Hankasalmi occurrence data for the year 2000 for five different latitudes and for each month of the year. A strong seasonal effect is quite obvious on this diagram with strong midnight enhancement during wintertime and much more flat distribution during summer months. The horizontal line on each panel signifies the times when echoes are seen in more than 15% of the observational time. Clearly, echoes are only seen just after midnight during

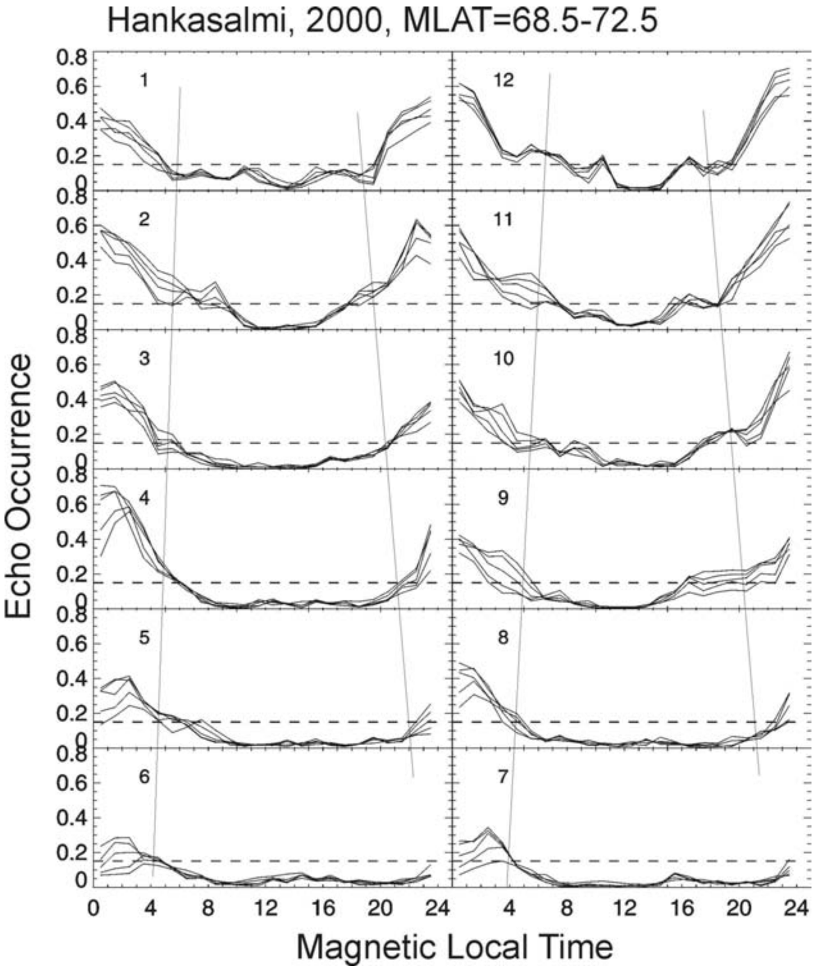

Figure 4.3 Diurnal variation of F-region echo occurrence rates at magnetic latitudes 68.5°-72.5° (each line corresponds to one latitude such as 68.5) for various months (number 1 stands for January)

summer and over much more significant time sector during equinoxes and winter. We indicate by tilted lines the periods of echo occurrence rate being more than 0.15. The slope of the lines illustrates the above effect.

4.2.3 The midnight echoes: Latitudinal location

We now explore the latitudinal location of nighttime echoes prior to and after midnight. In Fig. 4.4, the latitudinal profiles of Hankasalmi echo occurrence in two time sectors (23-24 MLT and 24-10 MLT) are presented for each month during the years of 1996 – 2001. The color-coding for the years is shown on the second panel from the top in the left column. We note that 1996 (2001) observations correspond to the solar minimum (maximum).

In Fig. 4.4 one can see that most of the echoes occur near the magnetic latitude of 70^o prior to and after midnight. In the following two sections we concentrate on observations at 70^o, a typical latitude of the auroral oval. One can notice also a tendency for the echo occurrence peaks to be not as strong during summer months.

An important feature is that the magnetic latitude for the maximum of the echo occurrence moves about $1\text{-}2^o$ equatorward during the summer. To clearly indicate this tendency we placed a large filled circle corresponding to the echo occurrence maxima for each month.

Also there is a trend within the solar cycle, namely as the solar cycle progresses, the echoes move slightly equatorward. This tendency can be seen, for example, for observations prior to midnight in January, the top left panel. It does not show up for some months of observations.

4.2.4 The midnight echoes: Seasonal and solar cycle effects

To explore in more detail the seasonal variation of echo occurrence and the solar cycle effect we consider echo occurrence rates at MLat = 70^o - 71^o. We should say that analysis for other latitudes close to the selected one show similar tendencies to the ones discussed below.

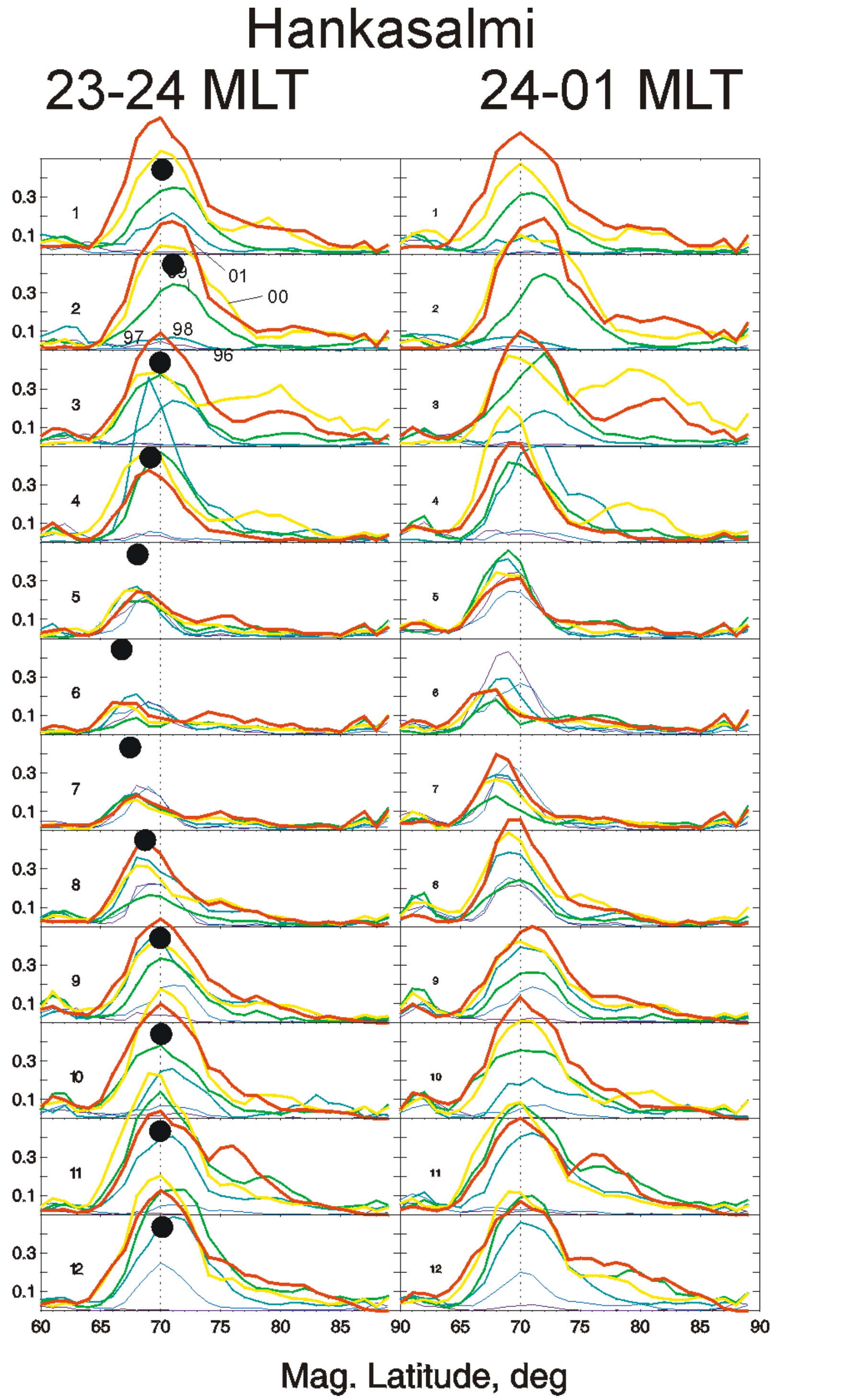

Figure 4.4 Monthly (1-12) variation of echo occurrence for the Hankasalmi radar. Left column is the pre-midnight period and the right column is the post-midnight. Colors indicate the year of observation as denoted in the second panel from the top in the left-hand column. The large filled circle indicates the approximate maximum in the latitudinal profile. Magnetic latitude of 70^o is represented by a dotted line.

In Fig. 4.5, we show data for each month in 1996-2001 again for two time sectors, one hour prior to and one hour after the midnight. One can clearly see a general trend of an increased number of echoes toward maximum of the solar cycle. The other obvious effect is a change in a character of the seasonal variation as the solar cycle progresses. In 1996 and 1997, the echoes are most common during summer and have a minimum during winter, whereas the converse happens in 2000 and 2001. For observations in 1998, corresponding roughly to the middle part of the solar cycle, there are equinoctial maxima in echo occurrence (March and September). These maxima are somewhat "washed out" by significantly increased echo occurrence for 1999-2001.

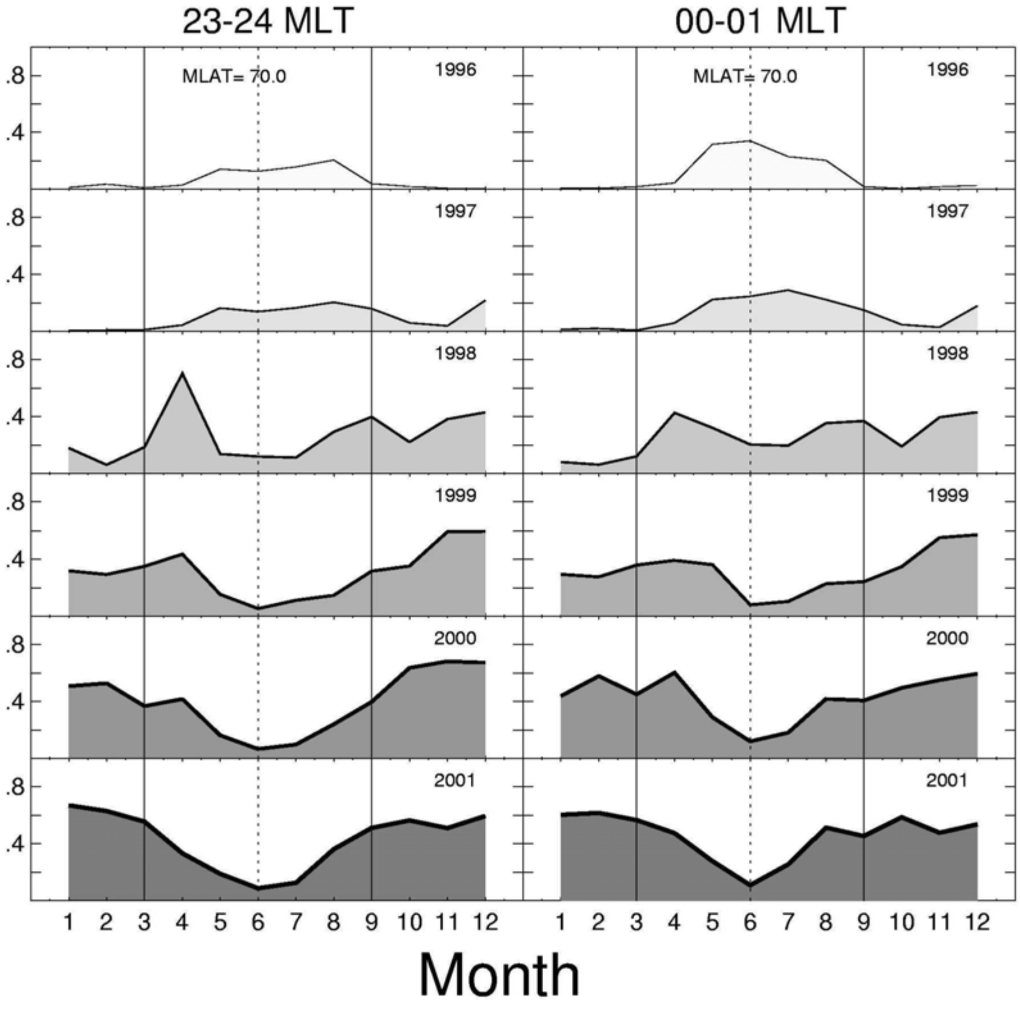

Figure 4.5 Annual variation of echo occurrence for the Hankasalmi radar at magnetic latitudes of 70-71° for the years 1996 - 2001. Left column is pre-midnight and the right column is post-midnight observations.

4.2.5 The midnight echoes: Role of electron density variations

To understand whether the presented trends in echo occurrence are the result of plasma physics of irregularity formation or change in the propagation conditions, the ray tracing analysis was undertaken. In the absence of long term electron density measurements, the International Reference Ionosphere (IRI) with its inherent seasonal and solar cycle changes of F-region electron density distribution is used to evaluate the prominent features of echo occurrence.

In Fig. 4.6, the variation of the electron density in the F region is evaluated for June and December from 1996 to 2001. There is a clear trend that the electron density increases as solar maximum is reached. The altitude of the maximum density also increases from 250 to 300 km. The lowest densities are also found to occur in December 1996 (~ 0.3 x 10^{11} m^{-3}).

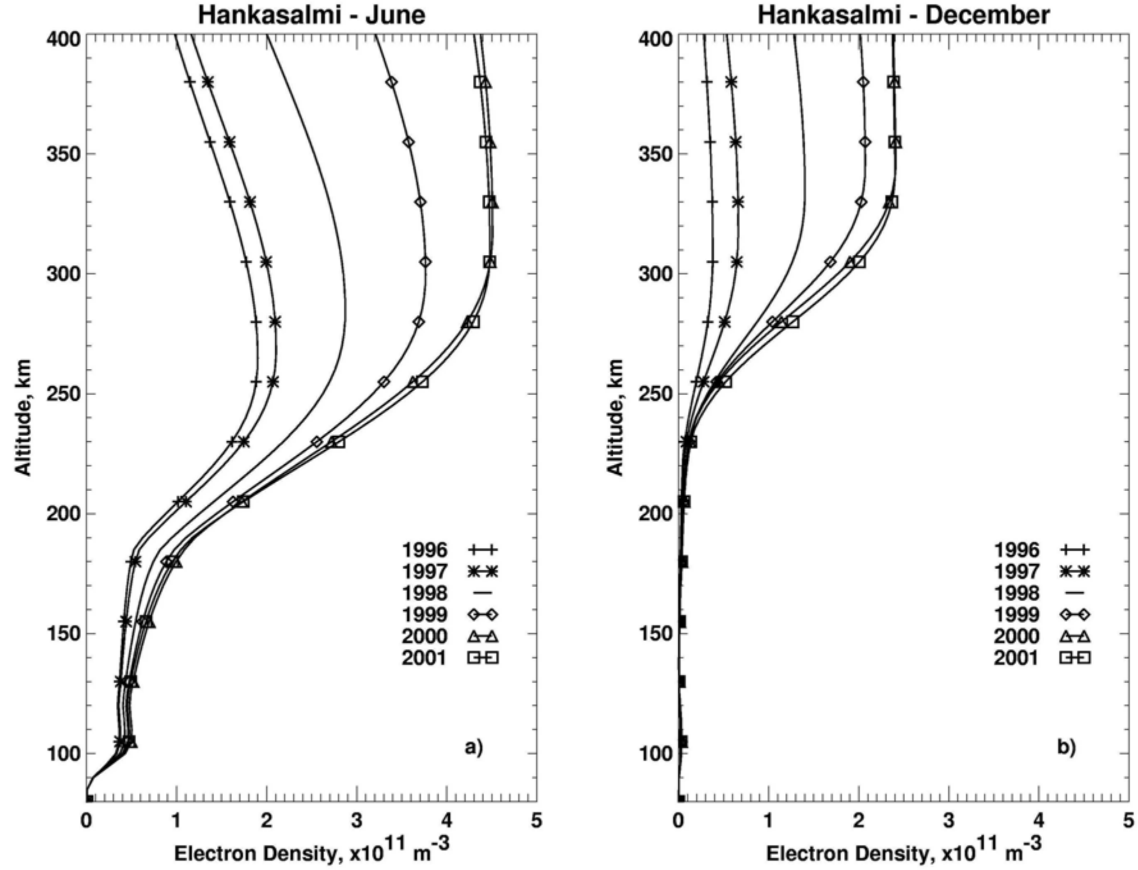

Figure 4.6 IRI electron density profiles for June (a) and December (b) for various years for the Hankasalmi field of view.

To see the effects of this change in density on the propagation of 10-MHz radio waves, a raytracing was done for 4 distinct periods from Fig. 4.6. The first two profiles come from June and December 1996 with the other profiles being their counterparts in 2001. These periods were chosen to illustrate the extreme variability of propagation conditions.

Calculations for the December 1996 profile, shown in Fig. 4.7a, indicate very little refraction for the F region (though enough bending to receive E-region echoes at altitudes of ~100 km) so that the radio wave cannot reach orthogonality to the magnetic field lines. It is not surprise then that very few echoes were observed in 1996 during the wintertime.

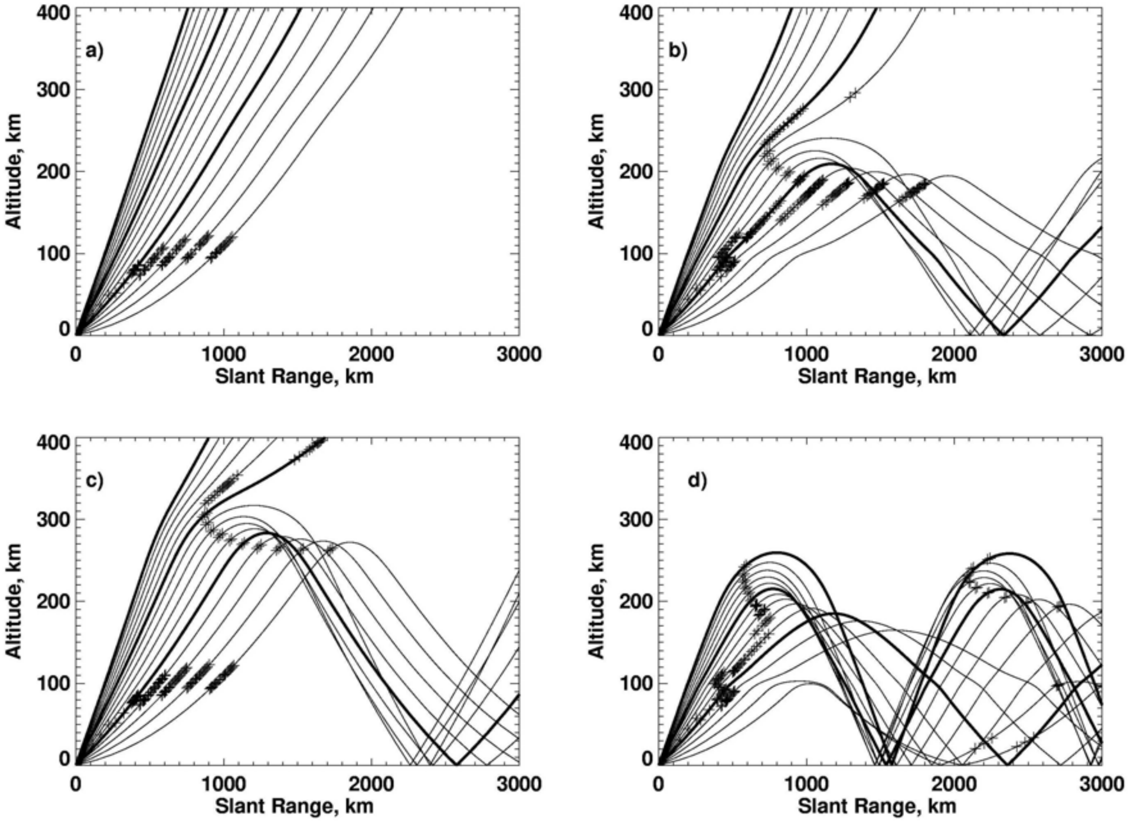

Figure 4.7 Raytracings for the Hankasalmi radar (10 MHz) with the IRI electron density profiles from Figure 4.6 for (a) December 1996, (b) June 1996, (c) December 2001, and (d) June 2001. Crosses indicate ranges where the ray is within ±1^o of orthogonality to the magnetic field. Elevation angles of 2^o-30^o are shown in 2^o steps.

In Fig. 4.7b, the results of the raytracing for the June 1996 profile (~ 2.0 x 10^{11} m^{-3} peak density) show that the propagation conditions are satisfactory in a broad range of ranges (magnetic latitudes) for echo detection during this period. F-region echoes are expected to occur between 700 - 1800 km (MLat = 64° -74°). One may observe the E-region echoes at ranges < ~700 km. Groundscatter is not expected to occur until beyond 2100 km.

The results for the December 2001 case (Fig. 4.7c) are very similar to the previous case, with the exception of F-region scatter occurring at a higher altitude. The ranges of the scatter are consistent with those of the summer of 1996, although there is a possibility of scatter from the E region at closer ranges.

In Fig. 4.7d, the propagation conditions for June 2001 indicate that there can possibly be a band of echoes close to the radar (< 800km, ~ 65° MLat). Groundscatter can be expected beyond 1500 km and $1\frac{1}{2}$ F scatter beyond 2000 km. Clearly, the diagram illustrates that it is typically not possible to get ionospheric scatter near magnetic latitude of 70° for propagation conditions of high electron density (~ 3.8 x 10^{11} m^{-3}).

Comparing these raytracings with the echo occurrence in Fig. 4.5 the absence of echoes in December 1996 at 70° MLat can be explained by the lack of necessary electron density for optimal refraction. The conditions for optimal refraction (peak electron density 2 x 10^{11} m^{-3}) are consistent with those of June 1996 or December 2001. In June 2001, the electron density is too high to give optimal scatter resulting in over-refraction at 70° MLat.

Since the electron density in the F region increases with the solar cycle, the summer echoes will be expected to decrease due to over-refraction as the electron density exceeds a value around 1.5 x 10^{11} m^{-3} (for 10-MHz nighttime echoes). We will show later that this is an optimal electron density for F-region echo detection with Hankasalmi radar at magnetic latitude of 70°. Also, it was demonstrated that the winter echoes would be expected to increase due to the electron density reaching the optimum value.

4.2.6 Comments on the factors controlling echo occurrence

The presented data demonstrate that there are clear trends in seasonal variations of the midnight HF echo occurrence for the Hankasalmi radar. Analysis showed that such consistent monthly changes over the solar cycle were seen only in the midnight sector. We believe this is the reason why previous studies (that were not focused on a specific time sector) have not identified the systematic seasonal variations in echo occurrence as we showed above. The character of the seasonal variation was found to strongly depend on the phase of the solar cycle. An increase in the number of echoes with the approach to the solar maximum was quite obvious. This conclusion is in line with previous publications (Ruohoniemi and Greenwald, 1997; Milan et al., 1997a, Parkinson et al., 2003). Winter conditions are found to be the most favorable for echo detection for the years of the solar cycle maximum and echoes were more frequent over summer during the years of low solar activity. The new feature reported here is the presence of equinoctial maxima for observations in 1998.

What do the discovered features in the seasonal variation of echo occurrence imply? Clearly, there are several factors that control echo occurrence.

First of all, the echo number increase towards the solar cycle maximum indicates, in our opinion, a more frequent occurrence of strong electric fields during these years, and thus the appearance of HF echoes due to preferential conditions for the GD plasma instability. This notion agrees with Ballatore et al. (2001) who showed that F-region echo occurrence is significantly increased during periods of negative IMF B_Z conditions when magnetospheric merging is enhanced. The discovered existence of equinoctial maxima in echo occurrence is another manifestation of enhanced electric field effect as a factor for HF echo onset. We recall that according to Russel and McPherron (1973), the equinoxes are favorable seasons for efficient interaction of the IMF and Earth's magnetic dipole.

We should note that an enhanced electric field does not mean that a HF echo would have stronger power as one might expect from the fact that the growth rate of the GD instability is proportional to the plasma drift (e.g., Tsunoda, 1988). Milan et al. (1999) presented several examples of HF echo observations from the area where electric field was monitored by the EISCAT incoherent scatter radar. It follows from these measurements that echoes occur when the electric field is somewhat larger that ~10 mV/m but there is no clear relationship between the echo power and electric field magnitude. Also Fukumoto et al. (1999, 2000) found only slight correlation of the F-region echo power and Doppler velocity, which is proportional to the E×B plasma drift.

Even though we have no doubts that the Russel-McPherron effect is the major factor for F-region echo occurrence through electric field enhancement, more processes are obviously involved since different types of seasonal variations were observed. In our opinion, the seasonal effect can be associated with changes in typical electron density profile over the season and solar cycle as we demonstrated with ray tracing. The changes in the density profiles can eventually be related to the change in the tilt of the Earth's rotation axis and changes in the solar illumination of the high-latitude ionosphere.

We should note that the solar illumination can also enhanced the electron density in the E region. Enhanced conductance of the E region can potentially influence the irregularity excitation by reducing the rate of the GD instability growth or even stabilizing it (Chaturvedi et al., 1994). As was explained in Chapter 2, this can happen because the electric field of growing perturbations in the F region can be shorted out through a highly conducting E layer. Importantly, such an effect can happen through the conducting ionosphere of the opposite hemisphere. HF radar - EISCAT comparisons by Milan et al. (1999) were inconclusive regarding the importance of this effect; echo power decreases correlated with the onset of a strongly conducting E region for some periods but not for others. More studies of the effect are thus needed and we attempt this later in the chapter. As far as the role of the opposite hemisphere is concerned, one possibility is to study the echo occurrence rate for conjugate radars, which is currently under way.

The other way the solar radiation can influence the occurrence of F-region echoes is through smoothing out the electron density gradients vital for the GD instability onset. Ruohoniemi and Greenwald (1997) related the significant echo deficiency during daytime periods to this factor. For the Hankasalmi radar, the midnight ionosphere is sunlit during May-August. Hankasalmi data do show the effect of echo reduction during summer, but only for the years of solar activity maximum (1999-2001) as shown in Fig. 4.5. The effect does not exist for 1996-1997.

We believe that seasonal changes in the propagation conditions, first of all due to changes in typical densities in the F region, contribute in some ways to the seasonal variation of echo occurrence as we showed by ray tracing. The importance of optimal electron density for echo detection is consistent with the fact that there is a significant nighttime echo occurrence increase (as compared to the daytime) in the evening and decrease in the morning (Fig. 4.3) correlated in some ways with the sunrise and sunset times. The idea is that after sunset (sunrise) the electron density in the F region would decrease (increase) to nearer the optimal value. During the daytime the density is too strong to detect echoes at $\Lambda=70^{o}$ and 75^{o}. Certainly, to some extent, the echo absence during the daytime may be associated with presence of the highly conducting E region and/or the effect of smoothing of the density gradients. An additional fact to support the importance of proper F-region electron density for the midnight echo appearance is the location of the midnight echo band in latitude (Fig. 4.4).

An important issue, as far as echo occurrence is concerned, is the role of D-region radio wave absorption. Riometer observations indicate preferential occurrence of strong absorption events prior to midnight (Hargreaves, 1992). Data for some periods (for example, the ones presented in Fig. 4.1) indicate more frequent echo occurrence after midnight, in favor of the effect, but this is rather a weak tendency. Overall, not much difference (in terms of echo occurrence) for observations prior to and after midnight was found as evidenced by the data in Fig. 4.5. The presented data were for two very close time sectors, 23-00 MLT and 00-01 MLT. Analysis of data in other time sectors showed that the discussed features in echo occurrence rate hold for much broader time sectors, 2-4 hours away from the midnight. However, as one moves significantly away from the midnight (for example, if one compares 18-19 MLT and 06-07 MLT data) the features discussed in this study fade and become barely recognizable. It is known that character of precipitation is quite different before and after midnight. The pre-midnight sector is characterized by enhanced overall luminosity with a greater chance of auroral arcs to occur (Liou et al., 2001). For this period, the overall background ionospheric conductance is decreased so that there is anticorrelation between the bright aurora and ionospheric background conductance (Shue et al., 2001). In the early morning sector, precipitation are more of diffuse type, and there is a correlation between the auroral luminosity and ionospheric conductance (Shue et al., 2001). Our observations thus indicate that the character of precipitation does not have a strong effect on F-region HF echo occurrence; we feel that this is because particle precipitation influences the echo occurrence most likely only through the formation of strong plasma gradients. Also, HF echoes do not exist in areas with very strong precipitation such as auroral arcs (Uspensky et al., 2001) perhaps due to strong radio wave refraction and/or absorption.

4.3 Electron density and electric field at the time of F-region echo detection: Hankasalmi HF radar, closely located ionosonde and EISCAT measurements

Though the analysis presented in the previous section is revealing in terms of factors controlling F-region echo occurrence, the relative importance of these factors is difficult to judge since the parameters of the high-latitude ionosphere may vary significantly over time. In this sense, our conclusions based on the IRI model might not be well substantiated. In this section we attempt to evaluate typical electric fields and F-region electron densities corresponding to the time of F-region echo occurrence. We consider HF observations of the Hankasalmi CUTLASS radar. For electric field estimates we use data collected by the EISCAT incoherent scatter radar. For the event considered EISCAT was in a scanning mode so that we obtained data at various latitudes within the area of HF echo detection. We also consider the electron density data obtained from ionosonde measurements at the Sodankyla Geophysical Observatory located not far from that part of the ionosphere where F-region echoes were observed. Even though the above three types of measurements are not collocated, the foregoing analysis gives some quantitative ideas on the conditions for F-region echo detection. We perform more detailed analysis for nearly collocated measurements in Section 4.4.

4.3.1 Experiment setup and event selection

We consider an event of 2-3 September 1997. For this day, the Hankaslami HF radar was operating in the standard mode with 2-min scans over 16 beam positions. The radar's FoV for ranges between 400 and 1500 km is shown in Fig. 4.8. We also indicate the orientation of Hankasalmi beam 5 where the echo occurrence is compared with electric field and electron density data. The beam is divided into two parts; the closer

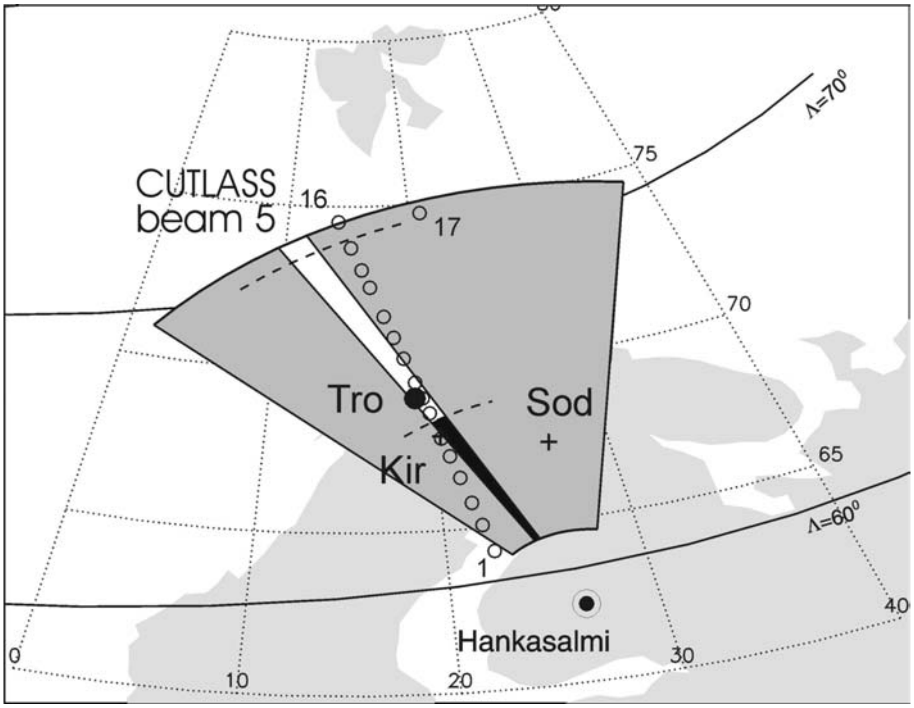

Figure 4.8 The overall CUTLASS Hankasalmi radar field of view and the location of beam 5, the sector consisting of the black and white parts. Open circles are locations where ionospheric electric field measurements were performed by the EISCAT radar.

darkened part corresponds to observations of E-region echoes while the other whitened part corresponds to ranges where F-region echoes were observed.

The EISCAT incoherent radar was working in the CP-3 mode making measurements in 17 separate positions elongated roughly with magnetic meridian. This mode is particularly beneficial to study the latitudinal distribution of the plasma convection. For every position, measurements of the electric field at ~250 km were performed by orienting all three EISCAT antennas (Tromso, Kiruna, Sodankyla) to a common volume. The measured line-of-sight velocities were combined to estimate the plasma drift component perpendicular to the magnetic field. Each scan lasted for about 30 minutes so that data for each position were averaged over ~2 minute. The Sodankyla ionosonde (shown by a cross in Fig. 4.8) provided 15-minute data of the electron density in the ionosphere.

4.3.2 Overview of the event

The Hankasalmi data for the event under investigation are overviewed in Fig. 4.9. We are concerned with observations at short ranges < 1500 km since only here the plasma convection was monitored. For these ranges, there were two periods of echo enhancement, between 1800 and 2100 UT and between 0100 and 0400 UT. For the first (second) period, echoes were received from the F (E) region as the elevation angle data indicate. One can notice that short-lived very localized echoes were also detected most of the time though more "dense" between 2300 and 0400 UT at ranges < 400 km. It is generally believed that these are meteor echoes. Some of them could be E-region echoes. One can also see that there were quite a few echoes at ranges farther than the area of interest. These echoes were seen most of the time at various ranges. The feature that stands out is a complete disappearance of far-range echoes between 0100 and 0400 UT when strong E-region echoes were observed.

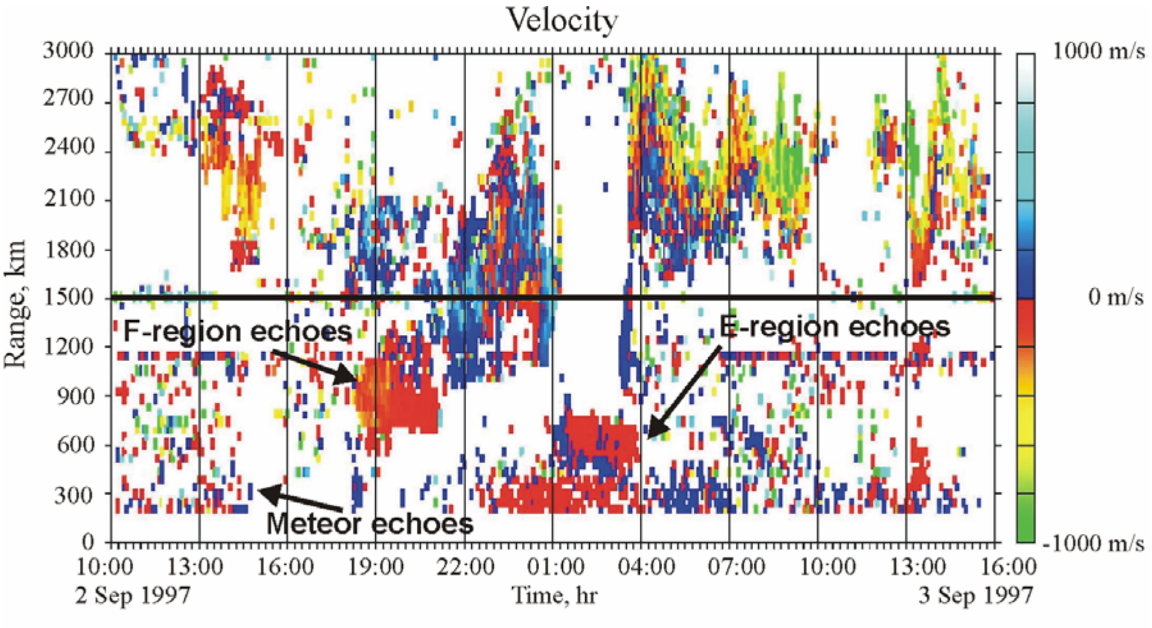

Figure 4.9 Range-time-velocity plot of Hankaslami HF radar observations on 2-3 September 1997. The observations below 1500 km were considered in this study.

4.3.3 F-region echo occurrence and electric field and electron density in the ionosphere

Fig. 4.10 shows the electron density at F (dots) and E (triangles) layer peaks, echo occurrence in beam 5 at ranges between 810 and 1485 km (F-region echoes at any range between the limits) and electric field according to EISCAT measurements in positions 7-16. Each dot on the bottom panel represents a measurement at one EISCAT spot, and the solid line shows the trends in electric field variations. One can see that echoes were detected for medium densities in the F region, 2-3 x 10^{11} m^{-3} and low E-region density, <

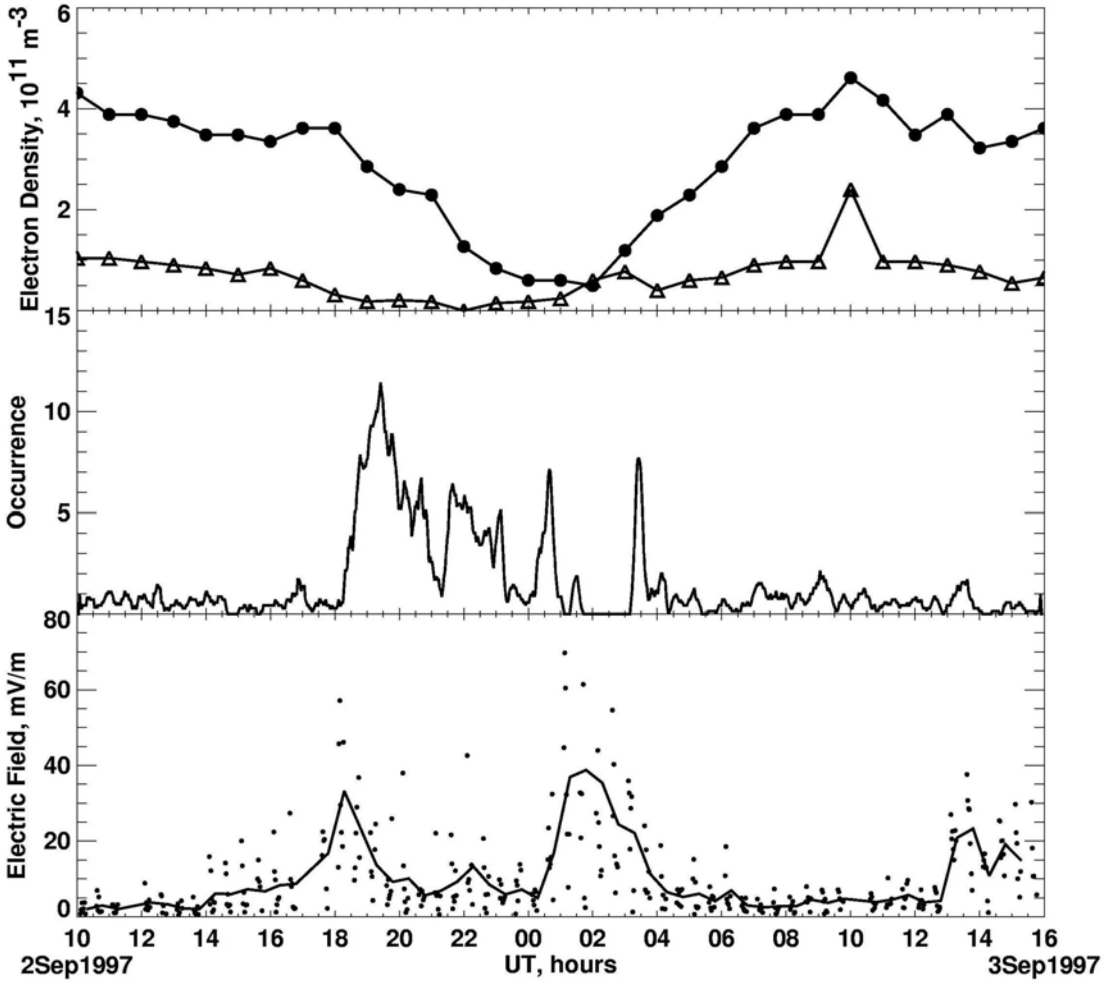

Figure 4.10 Maximum electron density in the F (circles) and E (triangles) layers, the number of Hankasalmi F-region echoes (middle panel) and averaged electric field over the latitudes of echo detection.

10^{11} m^{-3}. The electron densities in Fig. 4.10 were estimated from the observed critical frequencies of the F and E traces on ionograms. We should say that between 0100 UT and 0500UT, a sporadic E layer was observed causing the density estimates to be more uncertain. In terms of electric field, the echo onset corresponds to some enhancement, perhaps to ~5 mV/m, but as it appears, the threshold is not very rigid. The data between 0100 and 0400 UT show that despite the strong E field, no echoes were detected. This happens because the E-region electron density is too strong to allow the 10-MHz radio waves penetrate into the F region. This "propagation" limitation on the F-region echo detection illustrates that propagation conditions are very important to keep in mind when the reasons for F-region echo appearance are studied from statistics as we have done in Section 4.2.

4.3.4 E-region echo occurrence. Difference from the F-region echo case

The E-region data (Fig. 4.11) collected from ranges 200-800 km provide an opportunity to evaluate the threshold conditions for the E-region echoes. One can see two periods of enhanced echoes, but the first one, between 1800 and 2100 UT, correspond to F-region echoes detection at ranges shorter than 800 km (see Fig. 4.9). The E-region echoes observed between 0100 and 0400 UT show a more or less clear threshold of ~10 mV/m.

4.3.5 Conclusions on the reasons for the HF echo onset

The data presented in this section showed that for HF echo detection one needs some enhancement in the background electric field, perhaps more than 5 mV/m, but the threshold is not very firm. In terms of the F-region density, the typical values are between 2 - 3 x10^{11} m^{-3}. These results indicate that both factors, the electric field intensity and the electron density distribution in the ionosphere are important factors for observation of F-region HF echoes.

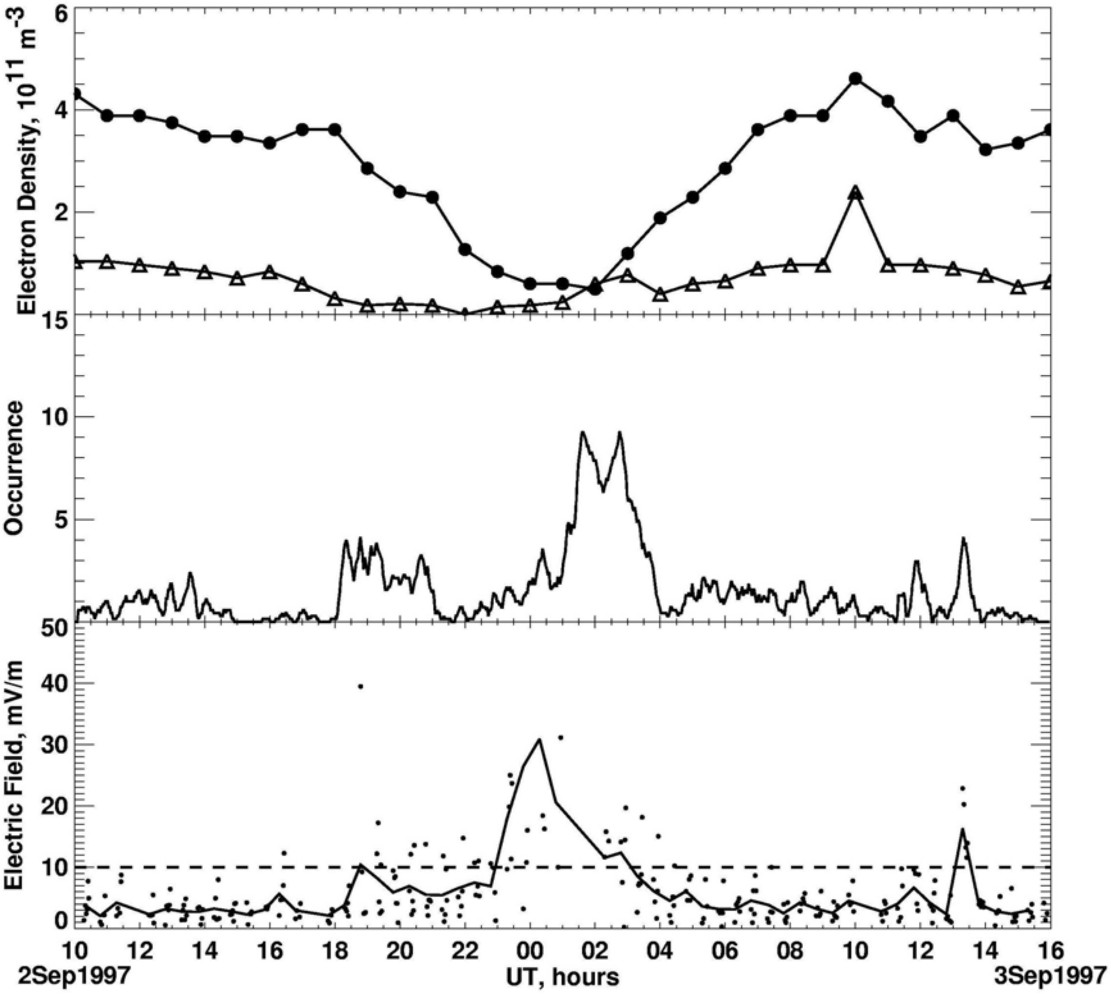

Figure 4.11 The same as in Figure 4.10 but for the E-region echo detection.

4.4 F-region echoes: Hankasalmi HF radar and EISCAT comparison for co-located observations

In this section we study the reasons for F-region echo appearance by comparing the ionospheric plasma parameters during the time of F-region echo detection in exactly the same area where HF echoes are coming from. We use observations performed simultaneously by the Hankasalmi HF radar and the EISCAT incoherent radar.

4.4.1 Experimental configuration

In Fig. 4.12 we show the location of the CUTLASS Hankasalmi HF radar (62.3^{o}N, 26.6^o E) and its viewing zone between ranges 400 and 1200 km at the height of

300 km. The radar was operated in the high time resolution mode with beam scanning through 16 positions over 1 min. We concentrate here on observations in beam 5 whose orientation is shown in Fig. 4.12 by straight lines within the overall-viewing zone. This beam was selected because it overlaps well with the region where ionospheric parameters were monitored by the incoherent scatter radar EISCAT (solid circle). The HF radar integration time was around 3 s and the range resolution was 45 km with starting range of 180 km. The operating frequency was chosen to be 10.0 MHz during nighttime and at 12.4 MHz during daytime to optimize echo occurrence rate.

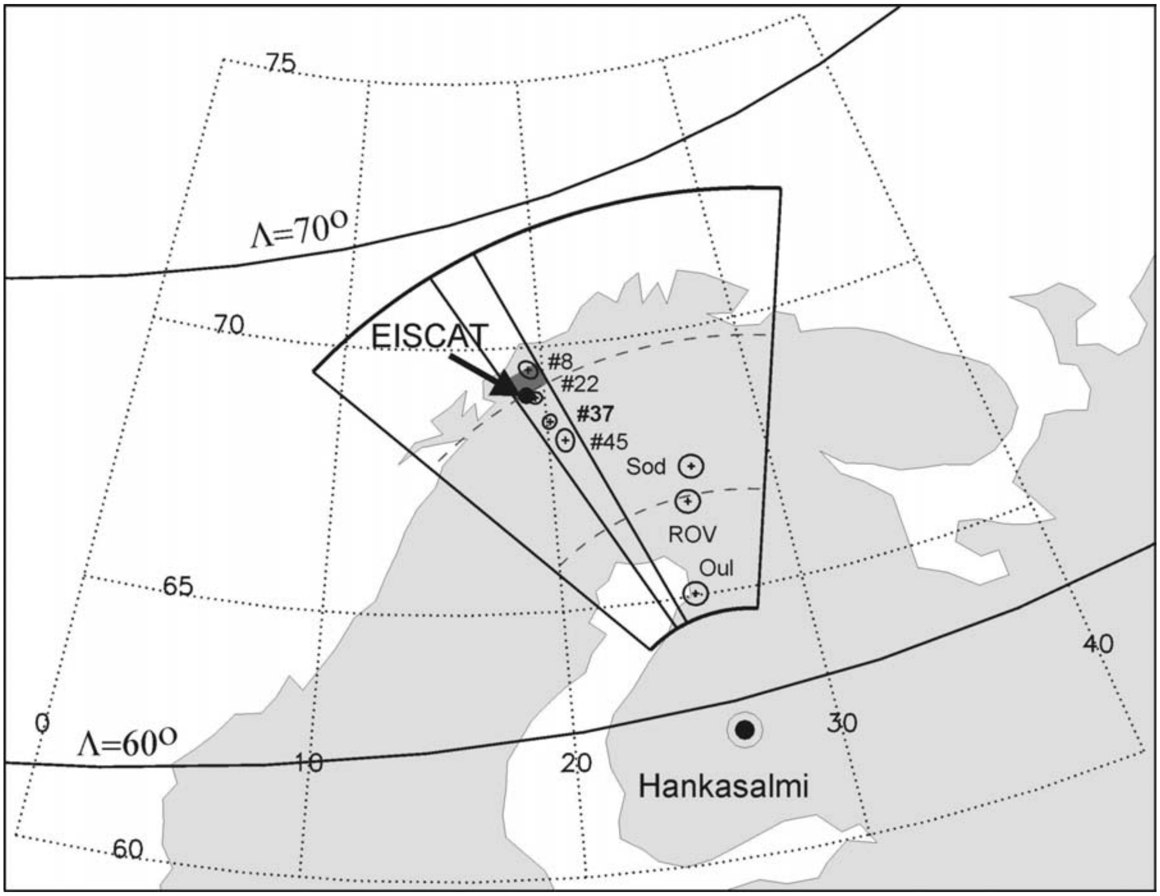

Figure 4.12 Field of view of the Hankasalmi CUTLASS HF radar for ranges in between 400 and 1200 km at the height of 300 km. Dashed lines are 600 and 900 km slant range marks. The outlined sector is the location of beam 5 with the shaded area corresponding to the range bin 16. The solid dot shows the area where ionospheric parameters were measured by the EISCAT incoherent scatter radar. Circles with pluses inside indicate the field of view for the Finnish riometers at a height of 90 km. Ellipses with pluses indicate the beam projections at 90 km for the IRIS beams as indicated. Also shown are PACE lines of equal magnetic latitudes of $\Lambda=60^o$ and $\Lambda=70^o$.

The EISCAT UHF radar worked in CP-1K mode with the remote antennas at Kiruna (Sweden) and Sodankyla (Finland) being oriented to a common area at a height of 250 km where additional Doppler velocity measurements were performed by the Tromso receiving antenna. Such an arrangement allowed tri-static electric field measurements in the area close to bin 16 (slant range of 900 km) of the CUTLASS Hankasalmi radar. In addition to the electric field measurements, the electron density distribution with height was derived from the power of the return signals at Tromso. The altitude resolution for EISCAT density measurements was 22 km for the long pulse method in the F region, and 3.1 km for the alternate code method in the E and D regions. We considered 2 min averaged EISCAT data in this study to have time resolution as close as possible to the HF radar integration time.

Finally, estimates of non-deviative D-region absorption for HF radio waves were obtained from the 38.2-MHz Imaging Riometer for Ionospheric Studies (IRIS) facility located at Kilpisjarvi, Finland (69.1^o N, 20.8^o E) and from Finnish riometer stations at Oulu, Rovaniemi and Sodankyla. The field-of-view at a height of 90 km for the Finnish riometers and four IRIS beams are indicated by circles and ellipses, respectively, with a plus sign indicating the center of the beam. The Finnish stations are located closer to the HF radio wave entry point into the D region of ionosphere where the majority of absorption occurs.

4.4.2 Overview of the observational period

We consider the 4-day period of 9-12 February 1999 as presented in Fig. 4.13. The Hankasalmi HF radar observed echoes quite often throughout this interval although many of echoes were ground scatter as indicated in gray on Fig. 4.13. Ground scatter is observed when radio waves are refracted to the ground by the ionosphere and reflected back from the ground, as was explained in Chapter 3. Ground scatter was especially strong between 0600 UT and 1800 UT, roughly from local sunrise to local sunset (MLT = UT + 2 hours). Most of the ground scatter was at slant ranges larger than the EISCAT observation spot (bin 16, range of 900 km) indicated in Fig. 4.13 by a solid line. Also, short distance meteor-like sporadic echoes were observed most of the time in the evening-midnight-morning sector.

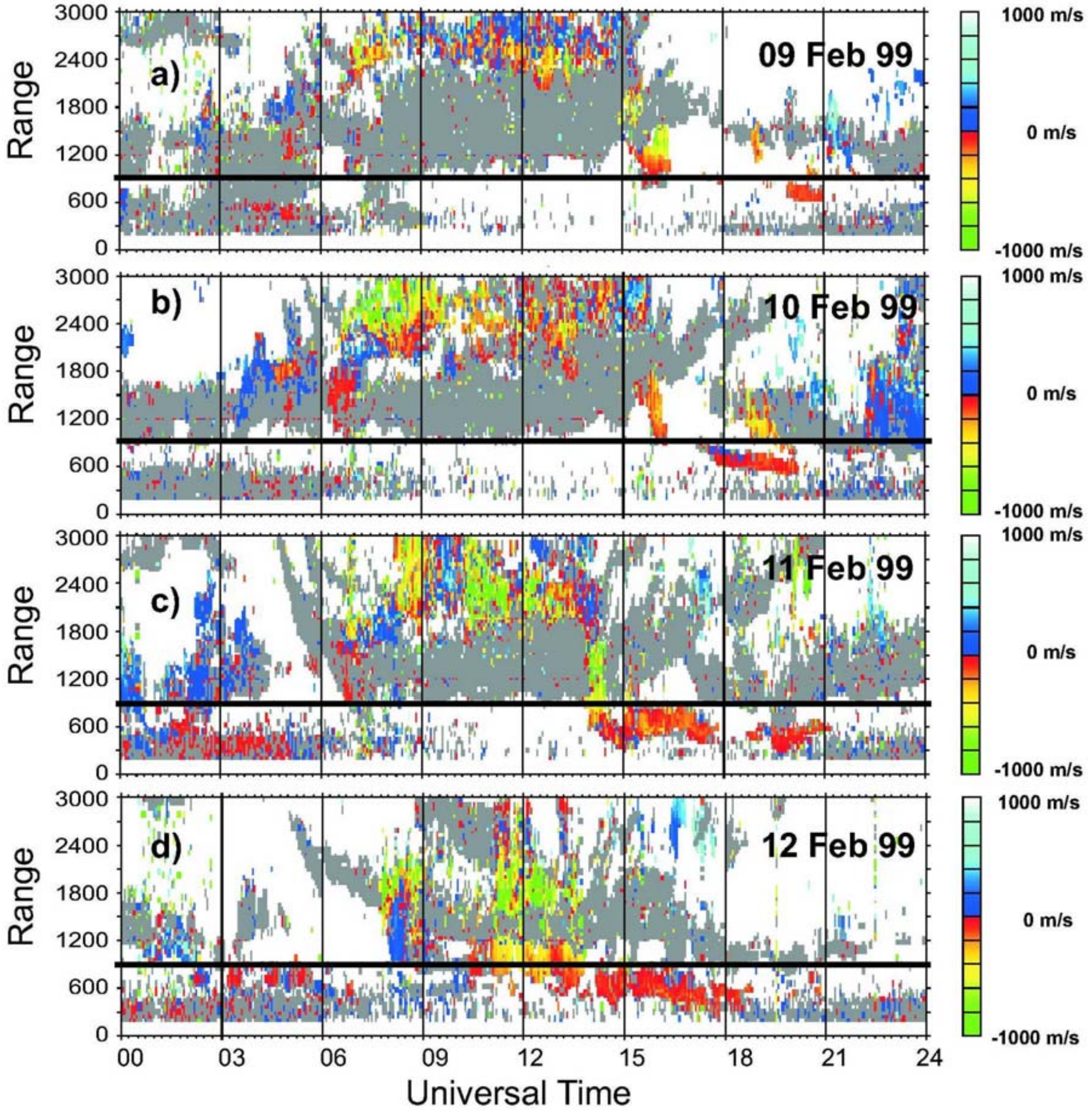

Figure 4.13 (a)-(d) Doppler velocity measured by the CUTLASS Hankasalmi radar in beam 5 on 9-12 February 1999. Horizontal solid line at 900 km shows the range corresponding to the area where measurements were made by the EISCAT incoherent scatter radar. The gray color denotes the ground scatter. MLT = UT + 2 hours.

In this study we are concerned with ionospheric scatter only. For all 4 days, such echoes were observed mostly at large ranges of 2000 - 3000 km. It is very likely that these echoes were received through the $1\frac{1}{2}$F propagation mode when the radio waves experience refraction in the F layer, ground reflection and propagation to the scatter points with return along the same path. On 9, 10 and 11 February the F-region densities between ~1000 UT and ~1500 UT were favorable for maintaining this mode as we will show later.

On 9 February, with the electron density decrease after 1500 UT, near local sunset time, echoes started to be received at shorter and shorter distance so that between 1600 and 2100 UT, the echo band was seen over the EISCAT spot. This general morphology of ionospheric and ground scatter repeated on other days. On 12 February (Fig. 4.13d), much more ionospheric scatter was detected over the EISCAT spot during noon hours.

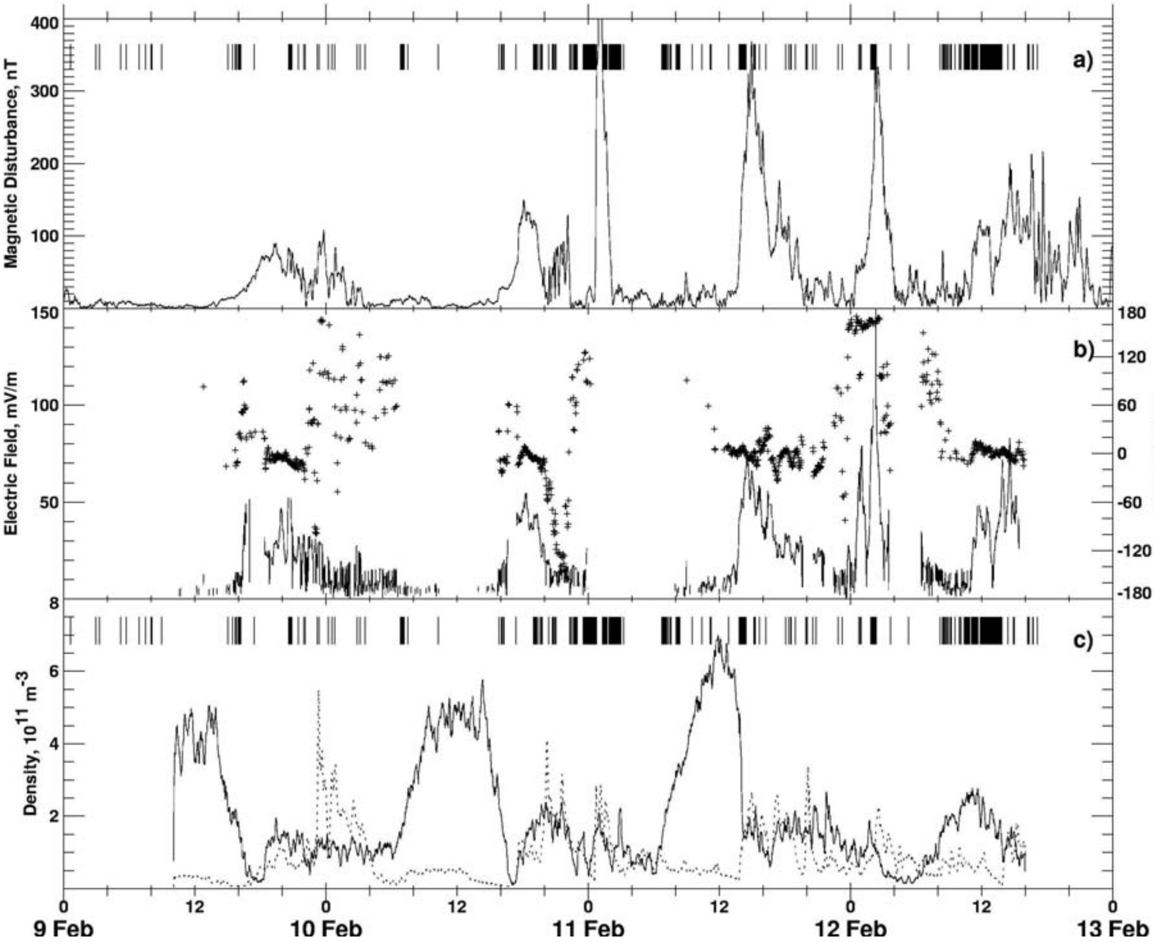

Figure 4.14 (a) Horizontal magnetic perturbations at Tromso, (b) electric field magnitude (solid line) and azimuth (crosses), and (c) electron density at 250 km (solid line) and 110 km (dots). Vertical bars in panels a) and c) indicate the times of HF echo occurrence in beam 5, bin 16.

The first 2 days were magnetically quiet with K_p indices being around 1 while the other 2 days were moderately disturbed with typical K_p indices ranging between 3 and 4 (Coffey, 1999). Total horizontal magnetic perturbations (absolute value with respect to the background lines for X and Y components) at a magnetic station near the EISCAT spot (Tromso) are presented in Fig. 4.14a. Very minor perturbations (< 100 nT) are seen on 9 and 10 February, and much more significant perturbations (up to 300 nT) in the evening and midnight MLT sectors on 11 and 12 February (for Tromso, roughly, MLT=UT+2 hours). In Figs. 4.14a and 4.14c we indicate by vertical bars the times for the ionospheric HF echo appearance over the EISCAT spot. A general trend seems to indicate that HF echoes occur during times of magnetic disturbance, however, HF echoes were detected quite often during periods of very low disturbances (10 February 1000 UT, 11 February 0600-0800 UT). Also, one can notice an absence of echoes during periods of strongest magnetic disturbances (11 February 0100 UT, 1400 UT, 12 February 0200 UT).

Throughout the considered period, the EISCAT radar was operated almost continuously. EISCAT data were available starting from 1000 UT on 9 February all the way to 1600 UT on 12 February with an 8-hour gap in electric field data on 11 February. The electric field (Fig. 4.14b) exhibited enhancements during the evening and midnight hours for all days. EISCAT measurements of the ionospheric electron density at 110 km (E region) and 250 km (F region) are presented in Fig. 4.14c. In terms of F-region electron densities, the 9, 10, and 11 February events were very much typical with densities around (5-7) x 10^{11} m^{-3} reached in the daytime sunlit ionosphere (sunrise and sunset times are around 0600 UT and 1500 UT, respectively). On 12 February, the daytime F-region densities were about 2 times smaller than the previous days. E-region densities were varying sporadically during each day. This is not a surprise since the Sodankyla ionosonde registered sporadic E-layer activity on each day, especially in the evening and midnight sectors. Clearly, the observed magnetic perturbations were related to both variations of the electric field magnitude and electron density in the E layer.

On 10 February, very few ionospheric echoes were observed at the EISCAT spot during daytime partly perhaps due to a fairly low electric field, less than 10 mV/m (often even several times smaller). With an electric field increase during evening hours, matched with a decrease in the F-region electron density (due to sunset), echoes started to appear more frequently, especially around magnetic midnight where F-region densities were favorable for direct propagation mode. Between 1700 UT and 2000 UT, a band of E-region echoes was observed at closer ranges of ~ 700 km.

For 11 February, electric field data were not available for the first 8 hours, during which there were some echoes obtained through the direct propagation mode to the EISCAT spot. Later during the day, echoes were observed again for moderate values of F-region electron density and electric field.

On 12 February, simple eye inspection shows that HF echo occurrence at the EISCAT spot correlates well with the period of moderate F-region densities of 2 x 10^{11} m^{-3}, low E-region densities of less than 1 x 10^{11} m^{-3} and occasionally enhanced electric field. With the increase of the E- region electron density after 1400 UT, echoes were observed at ranges ~600 km. Elevation angle measurements indicate that these were E-region echoes.

D-region absorption determined by the riometers near CUTLASS beam 5 is shown in Fig. 4.15. Absorption was re-calculated from the original riometer records (at frequencies 30-50 MHz) to the equivalent frequency of f = 12.4 MHz using f^{-2} dependence. Clearly, absorption is almost negligible during the first two days and there are some enhancements during the other two days, especially in the midnight sector. Also, absorption is larger at higher latitudes as expected in the auroral zone. One can notice that for some periods during the considered 4 days (e.g., 10 February, 1000-1600 UT) echoes were not detected. During these periods enhanced absorption was observed at low latitudes (e.g., Rovaniemi riometer, Fig. 4.15f) suggesting that absorption might be a factor in the echo disappearance. On the other hand, one can see that on 12 February, echoes were in abundance even though the absorption was the strongest over the four-day period. One should also note that there were extended periods when absorption was really small while echoes were not observed.

4.4.3 Relationship of echo power and various ionospheric parameters

From the above review of the period under study, one can conclude that there is no single factor that controls entirely the HF echo appearance. Below we compare echo power with each of the ionospheric parameters in order to reveal any kind of relationship.

4.4.3.1 D-region absorption

Fig. 4.16b shows echo power versus D-region two-way absorption calculated for the radar frequency of 12.4 (10) MHz at the Oulu riometer location. The histograms of occurrence of riometer absorption (Fig. 4.16a) for the entire 4 days (solid line) and

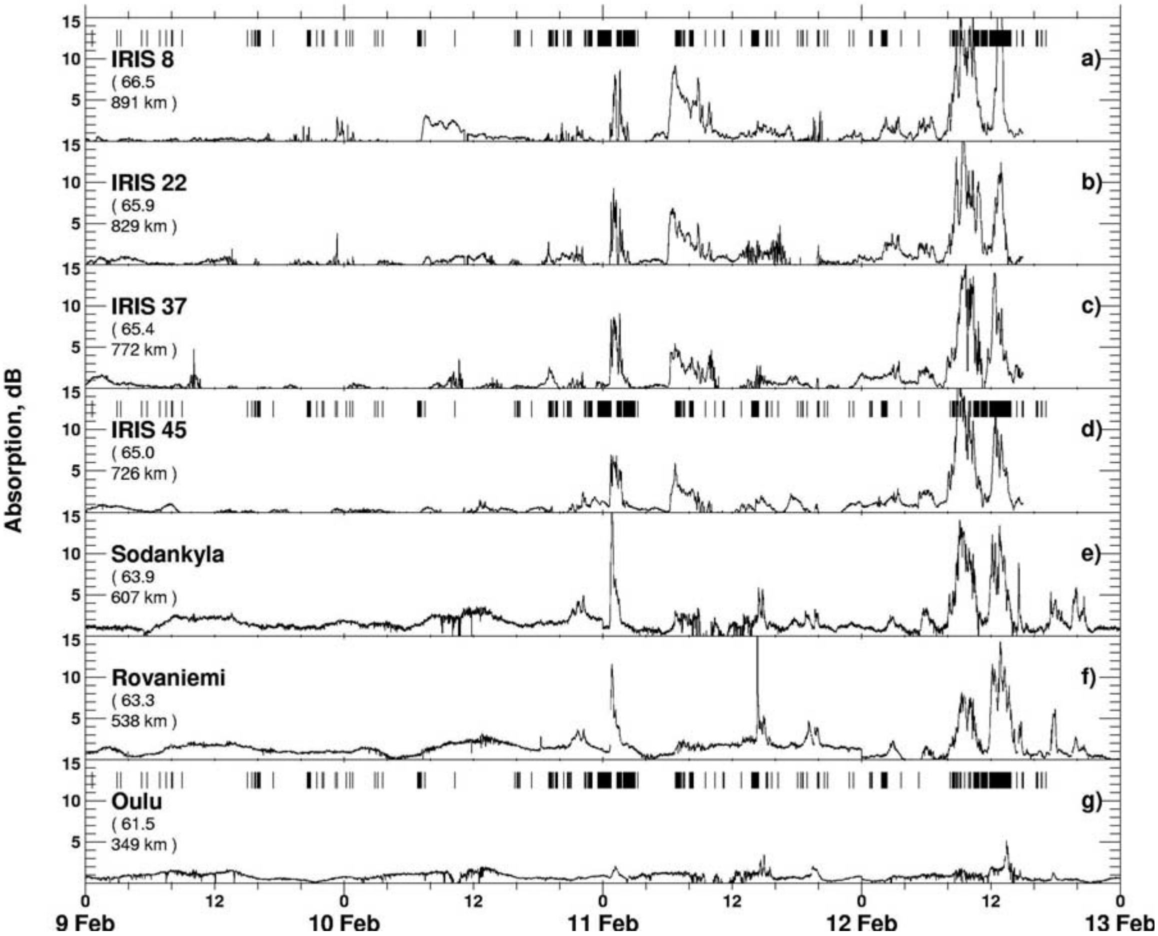

Figure 4.15 (a)-(g) Variations of D-region absorption at 12 MHz determined by riometers near CUTLASS beam 5, see Figure 4.1. Absorption was estimated from original riometer records by applying the f $^{-2}$ dependence, where f is the riometer frequency. Vertical bars in panels (a), (d) and (g) indicate the times of HF echo detection over the EISCAT spot of measurements.

riometer absorption when ionospheric scatterers were present during the 4 days (dotted line) indicate that ionospheric scatter is most likely when the absorption is of the order of 2 dB. One can see that echoes are more intense for small amounts of absorption, less than 3 dB, with the exception of "separate" cloud of 20 points at ~25 dB. These exceptional data came from observations on 12 February, around 1330 UT, see the spike in absorption on Fig 4.11g. The line in Fig 4.16b (drawn by hand) determines the limits of the echo power for various amounts of two-way absorption. This line shows a

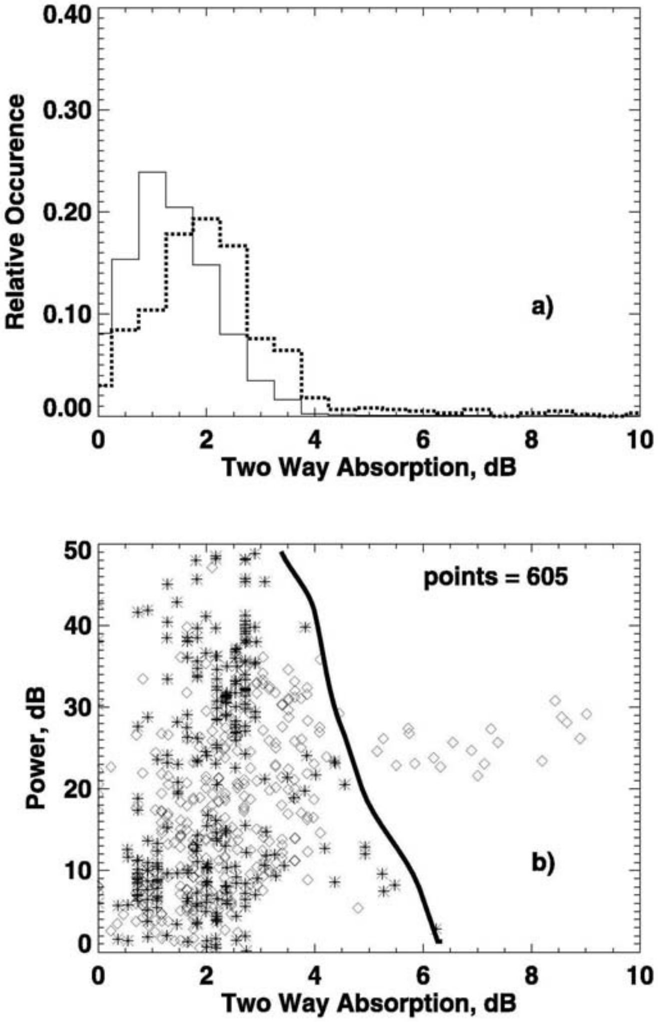

Figure 4.16 (a) Histogram of the relative occurrence of riometer absorption at Oulu for all four days (solid line) and for all times when HF ionospheric echoes were received (dotted line). (b) Scatter plot of HF echo power in bin 16 versus D-region absorption at slant range of ~350 km obtained from the original riometer records at Oulu, the closest station to the entry point of radar waves into the D region (605 points). Asterisks (diamonds) correspond to observations at 10.0 (12.4) MHz.

tendency for the echo power to decrease with absorption, which is expected. However, the majority of observed echoes correspond to small absorption values and the conclusion from this graph is that if F-region echoes occur, the amount of absorption does not substantially reduce their power nor completely absorb the radio waves. Similar conclusions were drawn from the comparison of echo power with absorption at other riometer locations.

4.4.3.2 Electron density and radio wave propagation

Previous studies have shown that both E- and F-region densities can be important for the F-region echo appearance (e.g., Milan et al., 1999). Electron density distribution in the ionosphere controls, first of all, the amount of refraction for observations at a specific range, e. g., Villain et al. (1984). In order to study the role of refraction in our measurements, we temporally assume that F-region irregularities occupy all heights, from the bottom to the top of the F region. Then the only concern is an appropriate amount of refraction for the radio waves to reach magnetic flux lines orthogonally within the scattering volume.

In Fig. 4.17, we present the power of observed echoes versus electron density at the height of 250 km. The available data were split into two sets; the top panel shows daytime observations performed at the radar frequency of 12.4 MHz while the bottom panel shows similar data for the nighttime observations at the radar frequency of 10.0 MHz. The tendency is clear; there is an optimal density that provides the greatest echo power for each radar frequency. These optimal values are around 2.0 x 10^{11} m^{-3} for at 12.4 MHz and 1.4 x 10^{11} m^{-3} at 10.0 MHz. We interpret this result as follows. At densities smaller than the optimal values, the amount of refraction is not enough to meet orthogonality condition within the expected area of scatter while for higher electron density over-refraction occurs and again the orthogonality condition is not met.

To explore what optimal density means in terms of radio wave propagation for our observations, we made a series of ray tracing modeling for the electron density profiles typically observed by EISCAT during periods of echo registration. We assume that the density only varies with altitude since two dimensional measurements of the

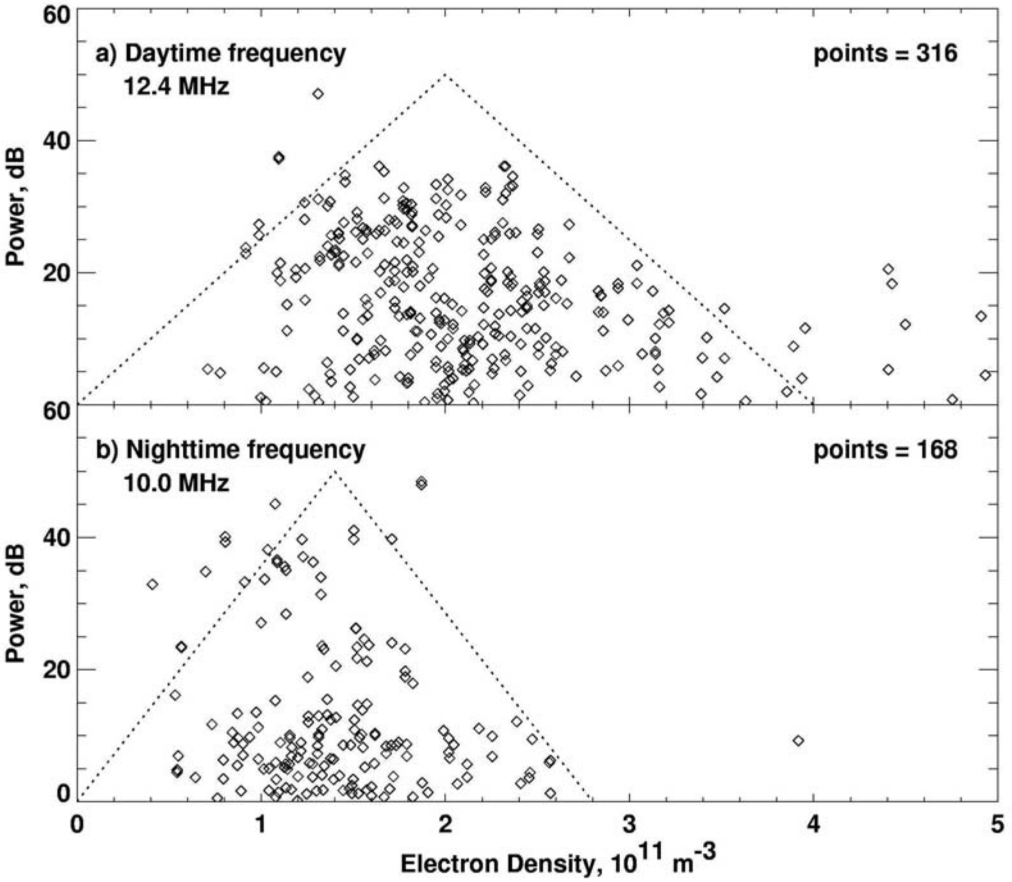

Figure 4.17 Echo power versus electron density at the height of 250 km (a) for the daytime observations at 12.4 MHz (316 points) and (b) for the nighttime observations at 10.0 MHz (168 points). Dotted lines roughly encompass the maximum power observed for each electron density.

profiles are not available in the CP1 mode. By the identification of common radar features predicted by the ray tracing, we believe this approach is a valid first order approximation. In Fig. 4.18a we show three 10-min electron density profiles, as measured by EISCAT at 1230 UT on 10 February (case (i)), and at 1230 UT (case (ii)) and 1430 UT (case (iii)) on 12 February. In Figs. 4.14b-d we show the slant ranges and altitudes of expected backscatter (with aspect angles within $\pm 1^{\circ}$ range) by crosses along specific rays. The rays correspond to elevation angles of 6°-30° in 2° steps.

In Fig. 4.18b we show that for electron densities typical for daytime observations on several days, there are no chances to receive direct F-region echoes at ~900 km but there are opportunities to receive $1\frac{1}{2}$F signals at ~2500 km. Also reception of ground scatter is very likely from 1200–2800 km. Ionospheric echoes are expected to come from

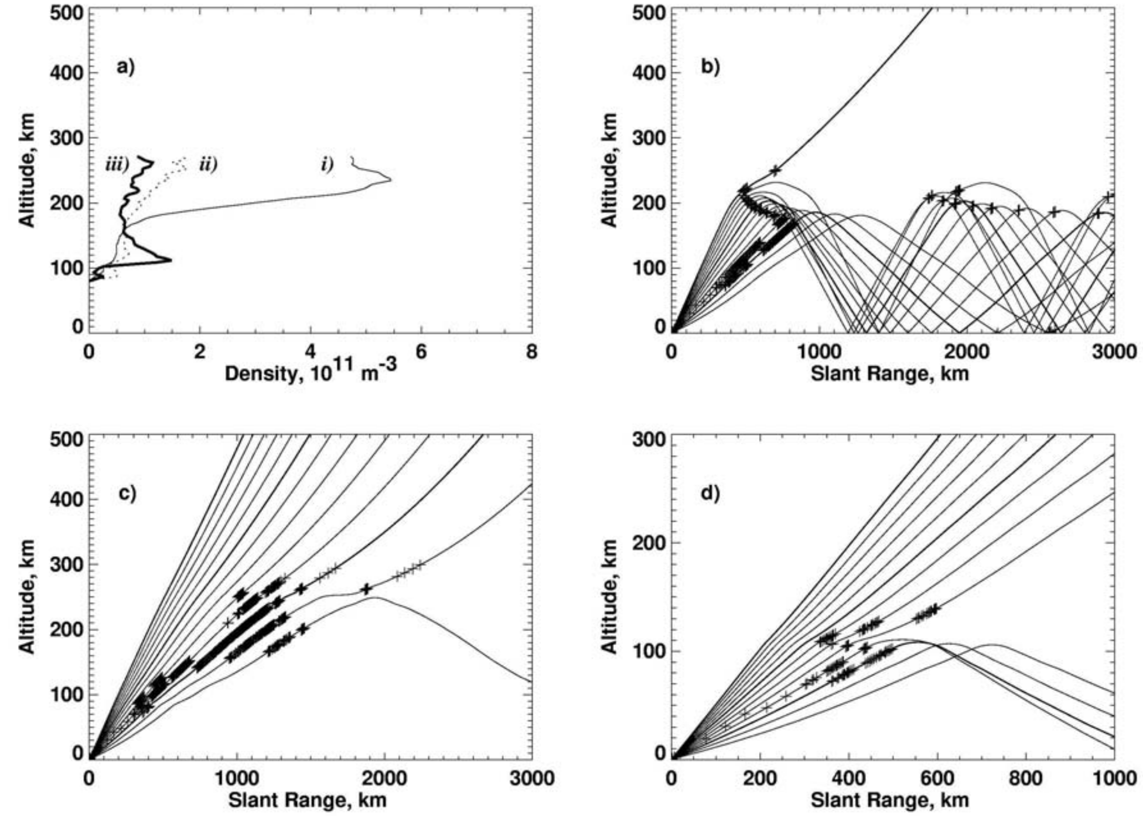

Figure 4.18 (a) The electron density distribution in the ionosphere used in ray tracings (b-d). The possible ray paths for 12.4 MHz observations from Hankasalmi for (b) 10 February 1230 UT, using profile *i*), (c) 12 February 1230 UT, using profile *ii*), and (d) 12 February 1430 UT, using profile *iii*). Crosses indicate ranges where the ray is within $\pm 1^{o}$ of orthogonality to the magnetic field.

the altitudes of 190–250 km with elevation angles of 20^{o}-30^{o}. These values of elevation angles are in reasonable agreement with radar measurements. This diagram also predicts that echoes (from both E- and bottom F-regions) can be obtained from short distances, but they were not detected according to Fig. 4.13b except of sporadic traces of echoes at near ranges of 300-600 km. We believe that the F-region echo absence is related to the low electric field observed at this time.

Fig. 4.18c shows how propagation is affected due to a substantially decreased F-region density as was typical during the daytime of 12 February. One can not see the $1\frac{1}{2}$ F propagation mode here. After 1400 UT, the E-region electron density was enhanced which caused the rays to reach orthogonality only in at E-region altitude and much shorter ranges as depicted in Fig. 4.18d. Thus ray tracing supports our conclusions on the propagation modes that were in effect during our measurements. Another way the electron density distribution can affect the appearance of F-region irregularities is through slowing down the gradient-drift (GD) instability responsible for the irregularity excitation. This happens due to shorting out the polarization electric field in growing GD modes (Vickrey and Kelley, 1982; Chaturvedi et al., 1994). We will explore this effect in the next sub-section, since it is closely related to the intensity of the electric field in the ionosphere.

4.4.3.3 Electric field intensity

The existence of ionospheric irregularities of appropriate scale size ultimately determines the appearance of auroral echoes; without the irregularities no return echo could be detected. Unfortunately, not much is known about properties of F-region irregularities of decameter scale (Fejer and Kelley, 1980; Hanuise, 1983; Tsunoda, 1988). In the auroral zone, the most likely mechanism of F-region irregularity formation is the gradient-drift instability. The positive contribution to the growth rate of the GD instability is determined by the electric field magnitude, the scale of the background gradient and their mutual orientation (Keskinen and Ossakow, 1982). Damping of the GD waves is determined by the diffusion (dependent on the temperatures and collision frequencies of charged particles). As mentioned above, diffusion can be enhanced in the presence of highly conducting E layer (Vickrey and Kelley, 1982). According to Vickrey and Kelley (1982) the effect is determined by the parameter $\zeta=1-M^{-1}$, where $M=1+\Sigma_p^F/\Sigma_p^E$ and Σ_p^E and Σ_p^F are the height integrated Pedersen conductances of the E and F layers, respectively. For a poorly conducting E layer, $\Sigma_p^E \rightarrow 0$, $M\rightarrow \infty$ and $\zeta\rightarrow 1$. For a highly conducting E layer, $M\rightarrow 1$ and $\zeta\rightarrow 0$ and the growth rate of the GD instability is greatly decreased. In this section we explore the role of both these factors in observations of F-region echoes.

Fig. 4.19 is a scatter plot of echo power versus electric field magnitude separated once again into daytime and nighttime events. There is a significant data spread here; however, during the daytime, points seem to show a power increase as indicated by the shaded circles which represent the average power in each 10 mV/m electric field bin. Overall, one can say that stronger electric field is preferred. For the nighttime, no such trend is seen. However, for the nighttime frequency there does appear to be a limit in the electric field of about 20 mV/m above which the power does not exceed 20 dB. Indeed, some echoes observed at electric fields as high as 80 mV/m were of low intensity.

In Fig. 4.20 we explore the effect of conducting E layer on the echo appearance. We plot here the height-integrated conductances of the E and F layers and the parameter M for the times that EISCAT density measurements are available. We arbitrary represented the E layer as being contained between 90 and 140 km and F layer being spread over altitudes above 140 km, similar to Milan et al. (1999). We also indicate in

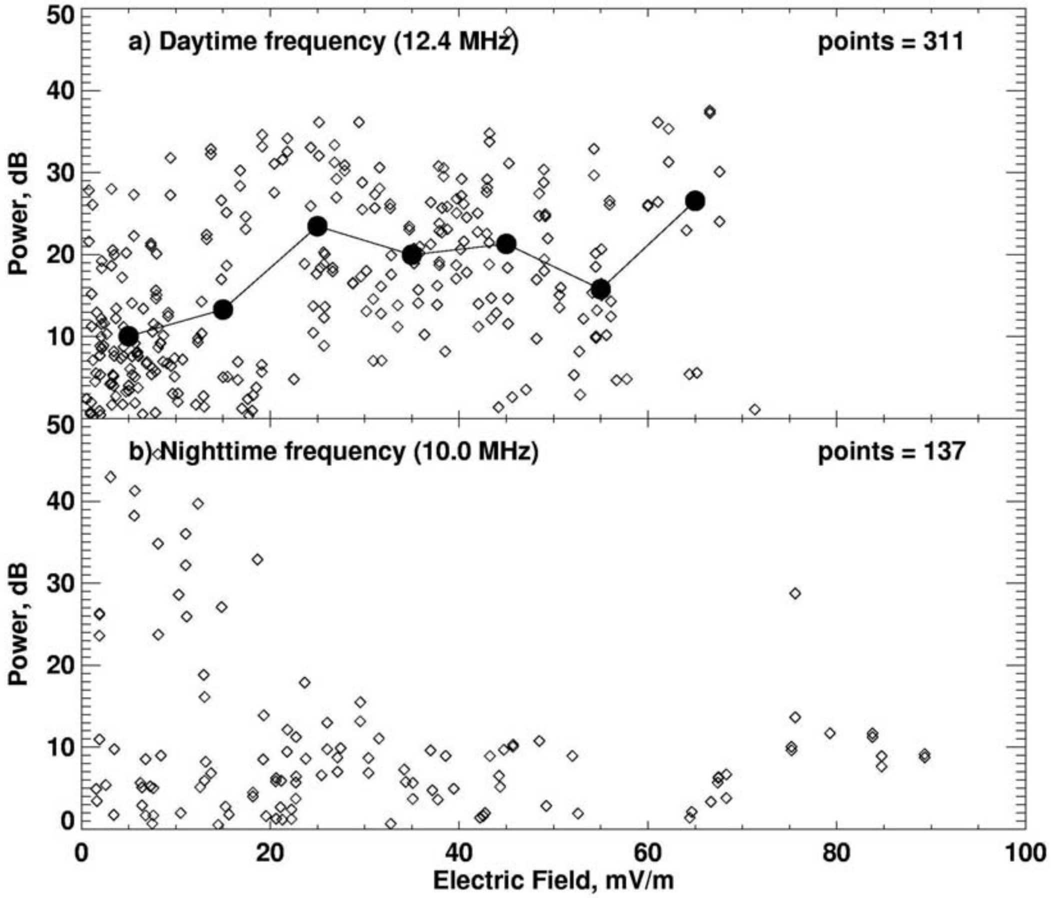

Figure 4.19 Scatter plot of echo power versus electric field magnitude for all echoes observed over 4 days (a) for daytime observations at 12.4 MHz (311 points) and (b) for nighttime observations at 10.0 MHz (137 points). Shaded circles in (a) indicate the average power in the associated 10 mV/m electric field bin.

Fig. 4.20c the times for the echo appearance over the EISCAT spot by vertical bars. The general impression from Fig. 4.20 is that echoes are mostly observed during the times of low values of the M factor. Contrary to expectation every time M was enhanced at noon, very few echoes were seen. One should note that periods of high M values typically also coincide with periods of low electric field, so the judgment on the importance of the effect is difficult to ascertain. For example, on 11 February, the echoes were seldom between 0800 UT and 1300 UT even though the M value was enhanced and the electric field was about 10 mV/m or so. On the other hand, on 12 February, at ~0200 UT, echoes were observed, as predicted, when the M values were enhanced, perhaps due to a simultaneously enhanced electric field.

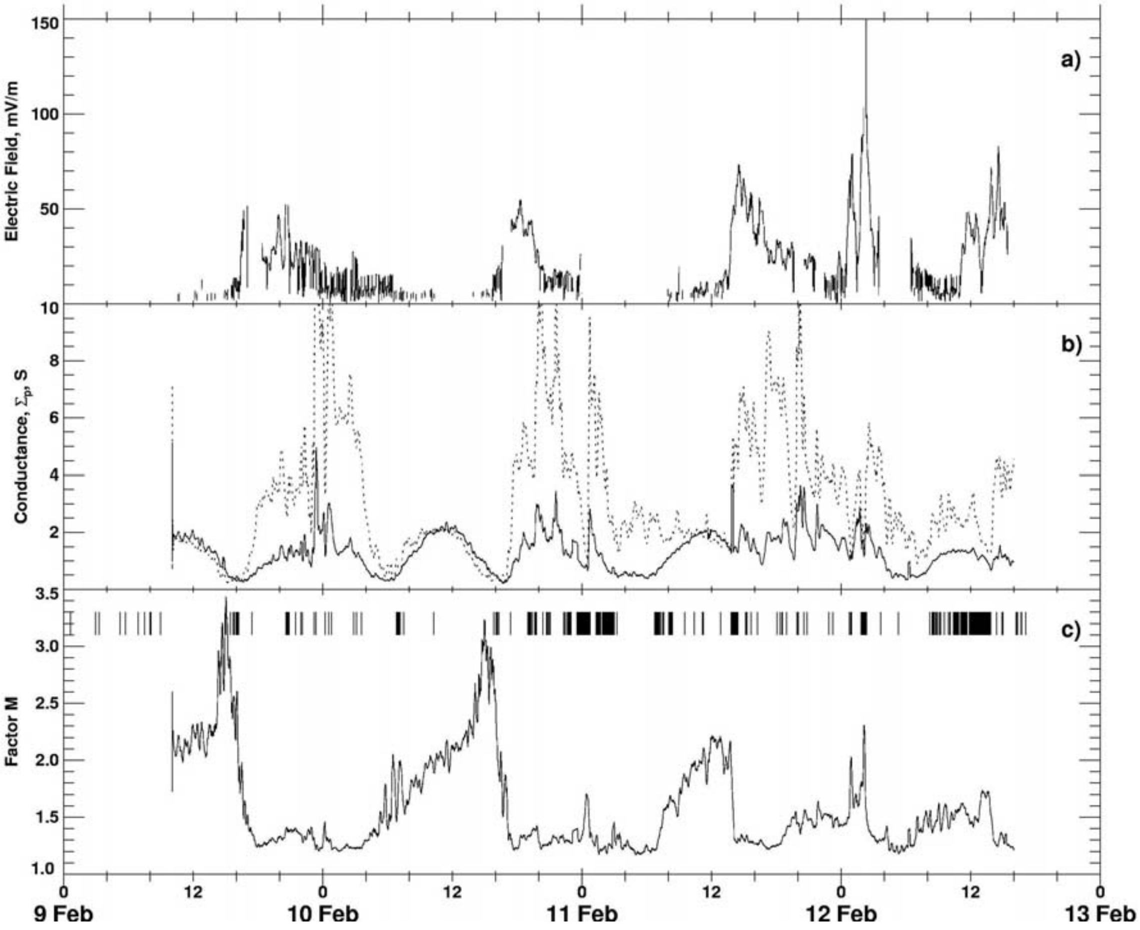

Figure 4.20 Temporal variations of (a) the electric field, (b) the height-integrated Pedersen conductances in the F and E regions (solid line and dots, respectively), (c) the parameter $M=1+\Sigma_p^F/\ \Sigma_p^E$ influencing the growth rate of the F-region gradient-drift instability in the presence of conducting E region. Vertical bars in panel (c) show the HF echo occurrence over the EISCAT spot.

One important feature of the data presented in Fig. 4.20 worth mentioning is the observations right at the end of the period, 12 February 1400-1500 UT when M values were unusually low while electric field was strong but no echoes were observed. To clarify this point, we present data for 12 February, 1000-1600 UT in Fig. 4.21 with better time resolution than data in Fig. 4.20. One can see the effect easily as the value of M approaches 1; the instability is inhibited. However, this is not the likely reason for the lack of F-region echoes at this time. As we discussed in Section 4.4.2, echo disappearance at this time is very likely due to enhanced density in the lower portion of the ionosphere so that HF radar waves are refracted to smaller heights and closer ranges (Fig. 4.18d). Another similar event is around 1140 UT on this day.

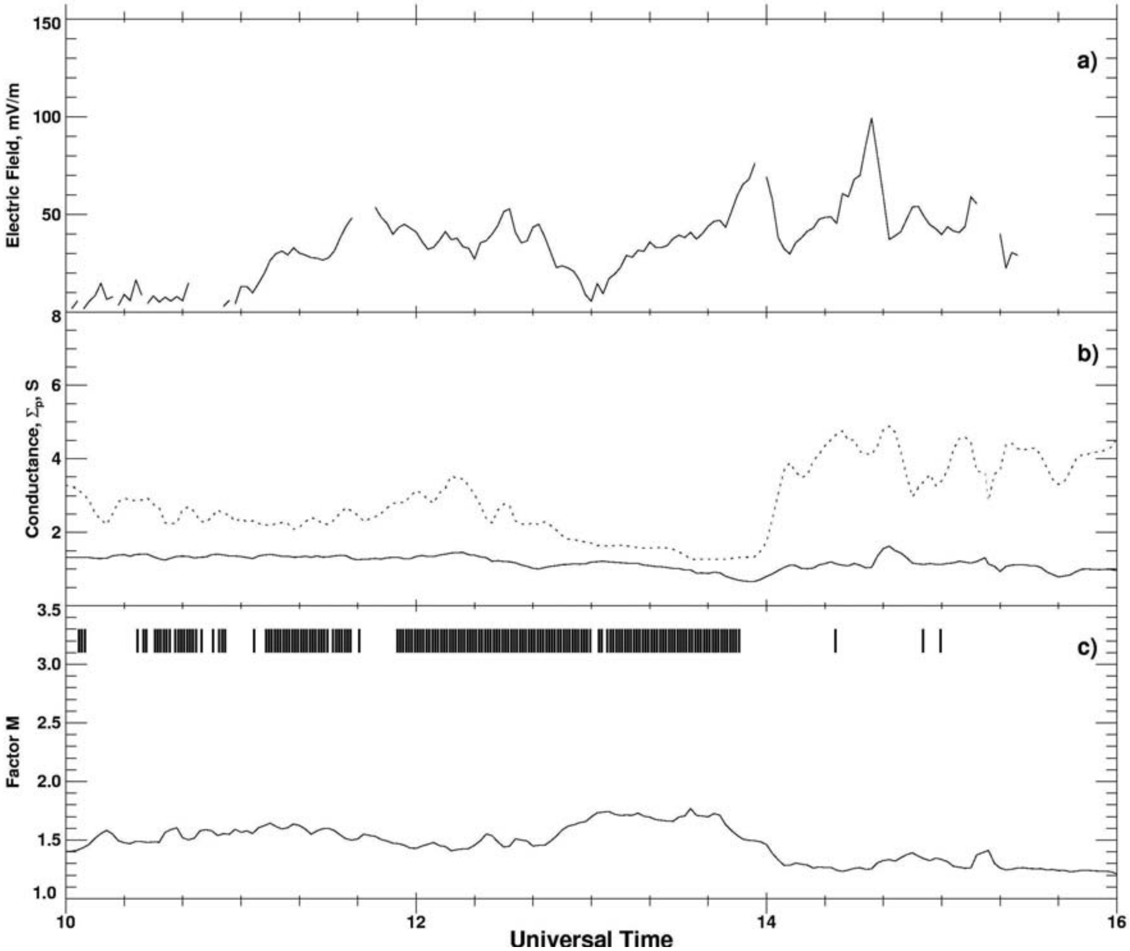

Figure 4.21 The same as in Figure 4.20, but for 12 February 1999 observations between 1000 and 1600 UT.

On the other hand, looking at Fig. 4.21 and Fig. 4.18c, one can notice that short-lived echo disappearance is not always related to propagation effects. For example, around 1300 UT there were no significant redistribution of electron density (no change in conductance) but echoes disappeared perhaps due to the decrease in electric field magnitude.

4.4.4 On the factors controlling echo occurrence: A case study perspective

As in the statistical approach, it is not easy to address question on the relative importance of various factors for F-region echo occurrence without reliable knowledge on irregularity availability and of plasma parameters all the way along the propagation path of the HF radar wave, including, of course, the scattering volume. It is important to realize that at HF several propagation modes are important so that an assessment of various factors certainly should take this circumstance into account.

We considered the simplest case when F-region echoes are received through the direct F-region propagation mode. In this case, radio waves reach F-region irregularities through an appropriate amount of refraction (this is also called $\frac{1}{2}$F mode, Milan et al., 1997a). But even for this simple situation, we had a very limited data set. Namely, we had measurements of electron densities at the scattering volume and extrapolated these measurements along the HF radar beam. One should also bear in mind that the area of EISCAT and CUTLASS effective collecting volumes are quite different for each instrument. EISCAT measures parameters in an area with the diameter of ~2.6 km at the height of 250 km while the effective area for the CUTLASS radar has dimensions of ~45 km × 150 km with no information on irregularity heights being available. Without knowing much about the thickness of the irregularity layer for the HF measurements (is it several kilometers or hundred kilometers?) the conclusions drawn from the ray tracing are not decisive. The effect of the irregularity filling the coherent radar beam has been studied by Walker et al. (1987).

For the event under consideration, we found that echo detection at the point of EISCAT observations (geomagnetic latitude of ~66.5^{o}) is strongly determined by the propagation conditions. The electron density distribution in the ionosphere must be appropriate to support radio wave propagation exactly to the expected area of joint observations as in Fig. 4.18c.

Most of the echoes at the EISCAT observational area tended to occur during evening and midnight hours, the preferential period for Hankasalmi echoes at these latitudes (Milan et al., 1997a). Echoes occurred for electron densities in between 1.0 x 10^{11} m^{-3} and 4 x 10^{11} m^{-3}, which is exactly what is needed for radio wave focusing to the F-layer heights, according to the ray tracing analysis. The derived densities are consistent with the finding of Milan et al. (1997a) that echoes typically occur for F-layer critical frequency of 4 MHz.

One should say that during daytime/early evening hours in February 1999 stronger densities in the F layer are usually achieved (according to the EISCAT measurements for 9, 10 and 11 February and according to the Sodankyla ionosonde statistics, see Milan et al. (1997a), Fig. 7). Hence the direct mode for F-region echoes should occur, if ever, at shorter distances. Hankasalmi echo occurrence rates published by Milan et al. (1997a) do not have enough spatial resolution to see the effect while Hosokawa et al. (2001) did not consider very low latitudes. Recent echo occurrence analysis performed by D. André (results are not published) confirms that maximum of echo occurrence for February 1999 is located at 2^o-3^o lower than normal latitudes, in agreement with expectations. Our observations for 9, 10, and 11 February are also in agreement with this expectation. On 12 February, echoes were observed in the noon sector, but as we demonstrated, the densities were ~2 times smaller during this day.

One would expect another desirable effect with density increase, namely a better chance to get echo detection through the $1\frac{1}{2}$F propagation mode since in this case, strong bending is more likely through refraction. Milan et al. (1997a) clearly demonstrated that Hankasalmi daytime echoes are typically cusp/cleft echoes obtained through this mode, and other reports (e.g., Ruohoniemi and Greenwald, 1997; Hosokawa et al., 2001) support this conclusion.

One should mention that Hosokawa et al. (2001) found quite a few afternoon/evening echoes being produced at the poleward edge of the mid-latitude ionospheric trough. As we mentioned in Section 4.4.2, echoes were observed more frequently right after the local sunset for the F region so the horizontal plasma gradient associated with trough might well contributed to preferential irregularity formation during these hours. In addition, Hosokawa et al. (2001) did find a second, morning peak in echo occurrence for the Canadian radars, but not for the Hankasalmi radar. In our event, quite a few echoes were observed during morning hours on 10 and 11 February and perhaps on 9 February (EISCAT measurements are not available here, but Sodankyla ionosonde data support this conclusion) prior to local sunrise. One can conclude that F-region echoes at the EISCAT spot for February can be related to the trough. For sure echoes are seen when the ionosphere experience a transition from the daytime to nighttime configuration in the evening sector and from the nighttime to the daytime in the morning sector.

Our conclusion of the primary role of refraction as a factor for the HF echo appearance refers to one specific point in the Hankasalmi radar field of view. It cannot be simply extrapolated to other areas within this radar FoV, not to say about other SuperDARN radars. Besides refraction, the issue here is whether strong F-region irregularities exist at all ionospheric heights accessible to radar waves. This is especially important for observations within the polar cap where the background density is not strong enough to support refraction as it can in the auroral zone. Polar cap patches of F-region background ionization are important in two ways; they provide enhanced refraction and, on the other hand, the gradients at their edges are the primary areas for the excitation of the GD instability (Tsunoda, 1988). These clouds are certainly limited in their horizontal extent and the height. So for the polar cap echoes the propagation conditions should be matched with the irregularity production conditions.

The prime importance of proper refraction conditions for echo appearance does not mean that other factors are not important. First of all, with respect to the D-region absorption we should mention that the events under consideration were, by chance, for quiet and moderately disturbed days. The absorption was very small at the range (~300 km), where the rays that intersect the F region at ~900 km were passing through the D region. Stronger absorption was detected at some larger ranges, which might affect scatter at ranges beyond 900 km, although this assessment is complicated due to presence of ground scatter at these ranges. We would expect more significant importance of D-region absorption during more disturbed days when the region of strong particle precipitation is shifted equatorward. It is well documented now that HF radar echoes quickly disappear at the expansive phase of a substorm developing in the local time sector of radar measurements (e.g., Voronkov et al., 1999).

The irregularity production factors are also important. For the considered events, the IMF B_z component was mostly negative so that one would expect mostly strong electric fields in the auroral zone, and the EISCAT measurements indeed show E fields in excess of 5-10 mV/m needed for the excitation of the GD instability. The daytime data presented in Fig. 4.19 indicate that echo power generally increases with electric field. This conclusion is consistent with the statistical analysis of echo power-Doppler velocity relationship performed by Fukumoto et al. (1999, 2000). These authors found that the power of echoes increases with the l-o-s velocity, clearly during daytime, and in more complicated fashion in the midnight sector. This is similar to our results, if one assumes that the l-o-s velocity increases because of electric field enhancement (power variations with the flow angle are not expected for the F-region echoes though analysis of this effect has not been done yet). One would expect the density fluctuation level to increase with electric field since the GD instability is strongly dependent on the electric field magnitude (Tsunoda, 1988).

Our analysis shows that besides a strong electric field, the conductance of the E region must be taken into account when the irregularity production is considered; this conclusion is similar to one of Milan et al. (1999). For example, on 11 February, between 1600 and 1800 UT, the propagation conditions were satisfactory, $N_e = 2 \times 10^{11}$ m^{-3}, electric field was of reasonable intensity, 20 mV/m, and as a consequence of reasonably small M values, echoes were not seen over the EISCAT spot. However, the situation was not always clear. Contrary to prediction, we showed that echoes were not always observed when M factor values were large.

Several other effects can explain echo absence over the EISCAT spot. One of these is that propagation conditions might have been such that one would need irregularities to be intense below 200 km. It well might be that irregularities simply were not generated at these heights. It is expected that the GD instability is efficient at the edges of plasma clouds in the F region, and it might be that ionospheric gradients were not strong enough to generate the irregularities, although with the current experiment, the horizontal gradient could not be measured. Further study should be carried out to ascertain the effects of horizontal gradients on the production of F-region irregularities.

4.5 Summary on F-region echo occurrence

In this chapter we attempted to evaluate the factors influencing the F-region echo appearance at the high latitude ionosphere. Data from only one HF radar, the CUTLASS Hankasalmi radar, were considered. We considered observations in that part of radar's FoV where echoes can be detected through the direct propagation mode. Three different approaches were undertaken. First, we looked at the long-term data on echo occurrence to infer the solar cycle, seasonal and diurnal trends in echo occurrence. In this approach we analyzed the occurrence with the generally accepted model estimates of the electric fields and electron densities in the ionosphere. We then compared echo appearance times with the electric field magnitude measured over significant part of the ionosphere and with the electron density measured in the middle part of the radar's FoV. Finally, we compared electric field and electron density data in one localized area with echo occurrence exactly at this point. In this approach we also monitored D-region radio wave absorption along the radar beam considered.

All three types of work indicated that HF echoes occur more frequently and they are more intense for stronger electric field though often only a marginal enhancement to 5-10 mV/m was observed. The statistical study hinted that the presence of plasma gradients is crucial for the echo appearance; with the Sun rising the echoes were seen more rarely. We thus provided experimental support to the notion that proper conditions for the GD plasma instability onset needs to be established in the ionosphere to detect F-region HF echoes.

In addition, we found that the electron density distribution in the ionosphere, both in the E and F regions, is an extremely important factor for the echo detection. We concluded that there is an "optimal" F-region density to see echoes; one needed a density in between 0.5×10^{11} m^{-3} and 4×10^{11} m^{-3}. For densities outside the above interval, there is either under- or over-refraction of radio waves resulted in the absence of scatter. This is especially evident for observations during winter months in solar minimum and during summer months in solar maximum, respectively. E-region density, besides supporting or prohibiting the propagation mode, may perhaps influence the wave electric field of F-region irregularities so that in a case of very dense E region the instability is slowed down or even prevented by the enhanced conductance. We found that D-region absorption is a minor factor for the echo detection though all considered cases correspond to low magnetic activity. This factor becomes crucial once observations during periods of strong auroral activity are considered.

The performed analysis, unfortunately, did not give a quantitative estimate on the role of various factors controlling F-region HF echo occurrence. Obviously the problem is complex, and certainly there is a need for a work that integrates HF observations with the data on the background conditions in the ionosphere.

CHAPTER 5

DOPPLER VELOCITY OF HF COHERENT ECHOES FROM THE F REGION AND PLASMA CONVECTION

The relatively frequent occurrence of HF coherent echoes at high latitudes is a well-known fact from 1960s (Bates, 1965; Hanuise et al., 1981; Greenwald et al., 1983; Baker et al., 1983). In spite of this, various properties of such echoes are not well studied. Perhaps part of the reason is that HF coherent radars were not as popular as VHF systems that are easier to construct and operate. The situation has changed over the last decade with the introduction of the SuperDARN HF radars. Operation of the radars has instigated further research into the nature of the F-region echoes and their properties.

In the previous chapter we considered the question why F-region echoes occur at any specific location. This is certainly a vital issue for the SuperDARN experiment. But to successfully fulfill the task of convection monitoring one needs not only to have F-region echoes but one also has to be sure that the measured Doppler velocity of echoes is the line-of-sight component of the ExB plasma drift (projection of the ExB drift on a radar beam). We now investigate the relationship between Doppler velocity of F-region echoes and the plasma convection.

The results presented in the chapter were reported by Danskin et al. (2001c).

5.1 Review of previous comparisons

In the past, several attempts have been made to assess the relationship between the Doppler velocity of F-region echoes (F-region irregularities) and the ExB bulk plasma drift. For these comparisons, independent plasma convection measurements were performed by incoherent scatter radars, DMSP satellites and CADI ionosondes.

Comparing HF data with incoherent scatter radar measurements, Villian et al. (1985), Ruohoniemi et al. (1987) and Davies et al. (1999, 2000) provided evidence that

HF Doppler velocity is close to the ExB (V_E) drift projected along the line of site of the HF radar. Ruohoniemi et al. (1987) showed remarkably good agreement in temporal behavior between the ion drift component as determined by the Sondrestrom incoherent scatter radar and the Doppler velocity measured by the Goose Bay HF radar. Though for most of the points agreement in velocities' magnitude was reasonably good, the HF velocity was actually larger than the drift V_E by a factor of 30%. Measurements by Davies et al. (1999), comprised of 4 hours of coincident data from ~1000 hours of joint experimental time between EISCAT and Hankasalmi HF radar, generally supported the idea that the HF velocity corresponds to V_E. Surprisingly for large plasma drifts the HF velocities were consistently less than V_E, up to 0.70 of V_E values, in an apparent contradiction to Ruohoniemi et al. (1987) results. In addition, the authors reported that the E-region HF velocities were smaller than V_E by a much stronger margin, up to 0.57 of V_E. Good agreement with a best-fit line slope of 0.68 between EISCAT drift measurements and CUTLASS HF Doppler velocity (for EISCAT drifts components < 300 m/s) were reported by Milan et al. (1999). Comparisons with incoherent scatter data were continued by Xu et al. (2001) who utilized data from the Sondrestrom incoherent radar and Goose Bay and Stokkseyri SuperDARN radars. These authors showed that for low plasma drifts of less than 500 m/s the HF Doppler velocity is ~30% over estimation of V_E and it is ~30% under estimation for the higher velocities of > 500 m/s.

Baker et al. (1990) compared HF velocities with ion drift measured over one pass of the DMSP satellite and found good correspondence between the data sets up to velocities of ~1500 m/s. Large variations in the ion drift occurred near the cusp latitudes, but the smoothed DMSP values were consistent with the HF measurements. Later Xu (2002) made more comprehensive DMSP-SuperDARN comparison and found that the DMSP drifts are larger that the HF convection component. The effect was found to exist in a broad range of latitudes.

By comparing the motion of F-region patches of density, Grant et al. (1995), ascertained that the drifts determined by the Canadian Advanced Digital Ionosonde (CADI) were in good agreement with those of SuperDARN with a discrepancy of +/-30% in speed. Furthermore, they found no tendency for the drift speed measured by either device to be larger. These conclusions are in some disagreement with later comparison performed by Xu (2002) who presented two events (of ~2 hours in duration for each) for which SuperDARN inferred convection was ~0.70 of the convection inferred from CADI measurements in co-located areas. It was also shown that SuperDARN merge convection vectors are quite often larger than the convection vectors determined by the Map Potential technique.

To continue the story on the relationship between the HF Doppler velocity and ExB plasma drift, André et al. (2000) reported the occasional occurrence of velocity divergent structures, for which HF velocity does not appear to correspond to V_E. The authors believe that an increase in the ion collision frequency may cause the anomalous transport and ion demagnetization. The ions hence may have a tendency to drift along the electric field and not with the Hall drifting electrons resulting in a motion different from V_E.

Furthermore, not all of the echoes that the HF radars detect occur in the F region. It is generally believed that scatter at ranges less than 600 km are from the E or even D regions. Those beyond 900 km are mostly caused by F-region irregularities as discussed in Section 4.4.2 reached by either direct or $1\frac{1}{2}$F propagation modes. Milan et al. (1997a) mused that some scatter at ranges greater than normal radio horizon for the E region (1200 km) could actually come from the E region. These authors believe that such E-region echoes can be received when HF radio wave is refracted to the ground and reflected to the E region (the $1\frac{1}{2}$E propagation mode). The discovery was based on a statistical look at the velocity distribution which showed that there was a small percentage of echoes that had a phase velocity of ~ C_s, typical of scattering from E-region irregularities. The idea was advanced further by Lacroix and Moorcroft (2001).

To summarize the previously performed comparisons of the HF Doppler velocity and plasma convection, one can say that most of publications indicate that, to a first approximation, the HF radars measure the component of the ExB drift if F-region echoes are received. Clearly, there was occasional violation of this relationship and its nature is not well understood. It is fortunate that the SuperDARN community is currently undergoing the process of selecting a new pulse transmission sequence to enable the radars to detect higher-velocity flows that are seldom seen with the present setup but observed by other instruments.

5.2 Event selection and approaches to comparison

To further investigate the relationship between Doppler velocity of F-region echoes and plasma convection we consider joint SuperDARN and EISCAT incoherent scatter data. In addition to a classical comparison of a single HF radar with an incoherent scatter radar, we will study the local data obtained by using information collected by the entire SuperDARN network. Two periods are focused on (11 and 12 February 1999) because reasonable SuperDARN data coverage was achieved. For both periods EISCAT was operating in the standard CP-1 mode with data averaging over 2-minute intervals (see Chapter 4).

For both events, the convection pattern consisted of two cells most of the time as illustrated in Fig. 5.1 for one frame of the 11 February 1999 event. The convection pattern is consistent with the IMF conditions of negative B_z and positive B_y. The equipotential contours are shown with negative (positive) potential being represented as solid (dotted) lines. The cross polar cap potential is estimated to be 88 kV.

To assess SuperDARN and EISCAT velocity data, we first compare the ionospheric electric field inferred from SuperDARN global convection maps at the spot close to the EISCAT observations with the EISCAT electric field data. We recall that all previous comparisons except Xu (2002) dealt with local observations for just one HF radar while here we use data from Saskatoon, Kapuskasing, Stokkseri, Pykkvibaer and Hankasalmi. In our second approach, we compare the LOS velocities observed at Hankasalmi and Pykkvibaer with ExB components (V_E) according to EISCAT, again at coincident locations.

5.3 SuperDARN global convection maps and EISCAT ExB drift

The map potential convection estimates for the area close to the EISCAT spot are compared with EISCAT measurements in Figs. 5.2 and 5.3. For the area of interest, only Hankasalmi data were typically available with some exceptions of 11 February1999

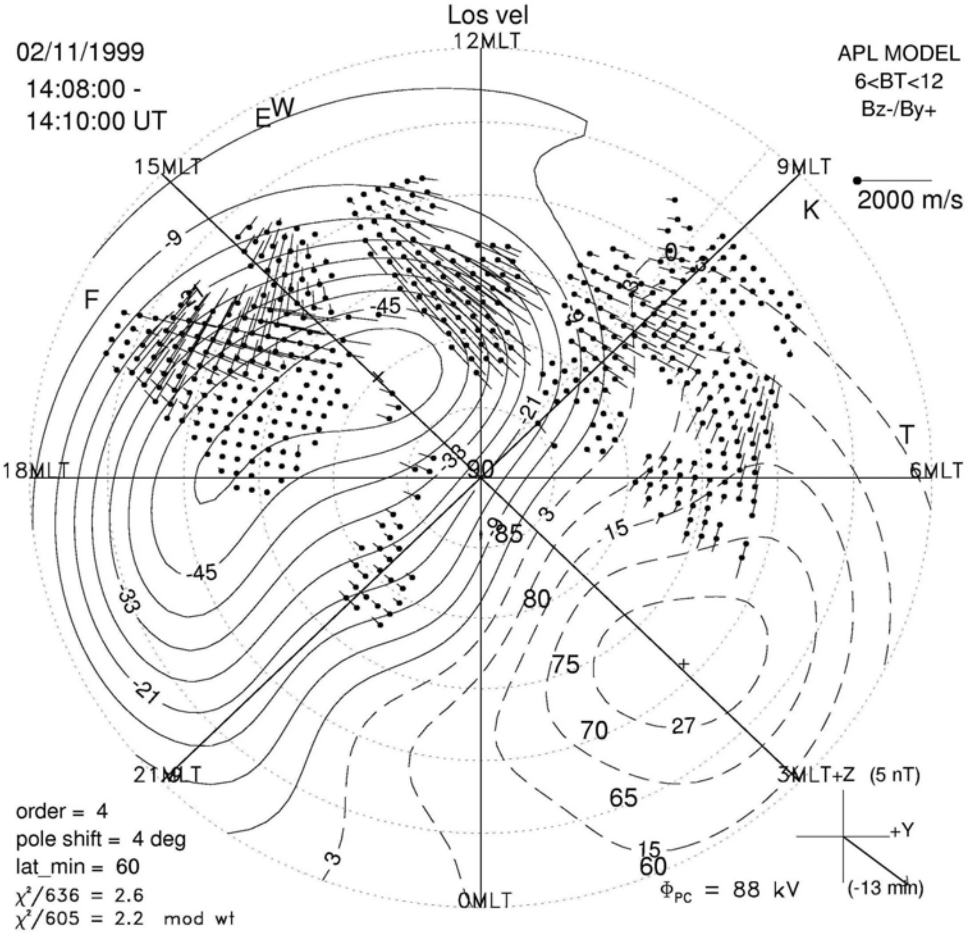

Figure 5.1 A sample convection pattern determined from the Map Potential routine. Data from Saskatoon, Kapuskasing, Stokkseyri, Pykkvibaer and Hankasalmi radar were used to construct.

observations for which the Pykkvibaer radar contributed as well, as one can see in Fig. 5.1. EISCAT data were available for longer periods (see Chapter 4) but SuperDARN echoes were seldom detected outside the shown intervals.

One of the most startling features is how well both devices exhibit similar temporal behavior. The direction of the predominantly northward electric field is quite stable from 1015 UT to the end of the interval. Prior to 1015 UT, the magnitude of the electric field is of the order of ~10 mV/m and the direction had a high degree of variability, still the agreement is remarkably good.

The magnitude of the electric field according to SuperDARN is fairly consistent with that measured with EISCAT, although there tends to be a slight underestimation.

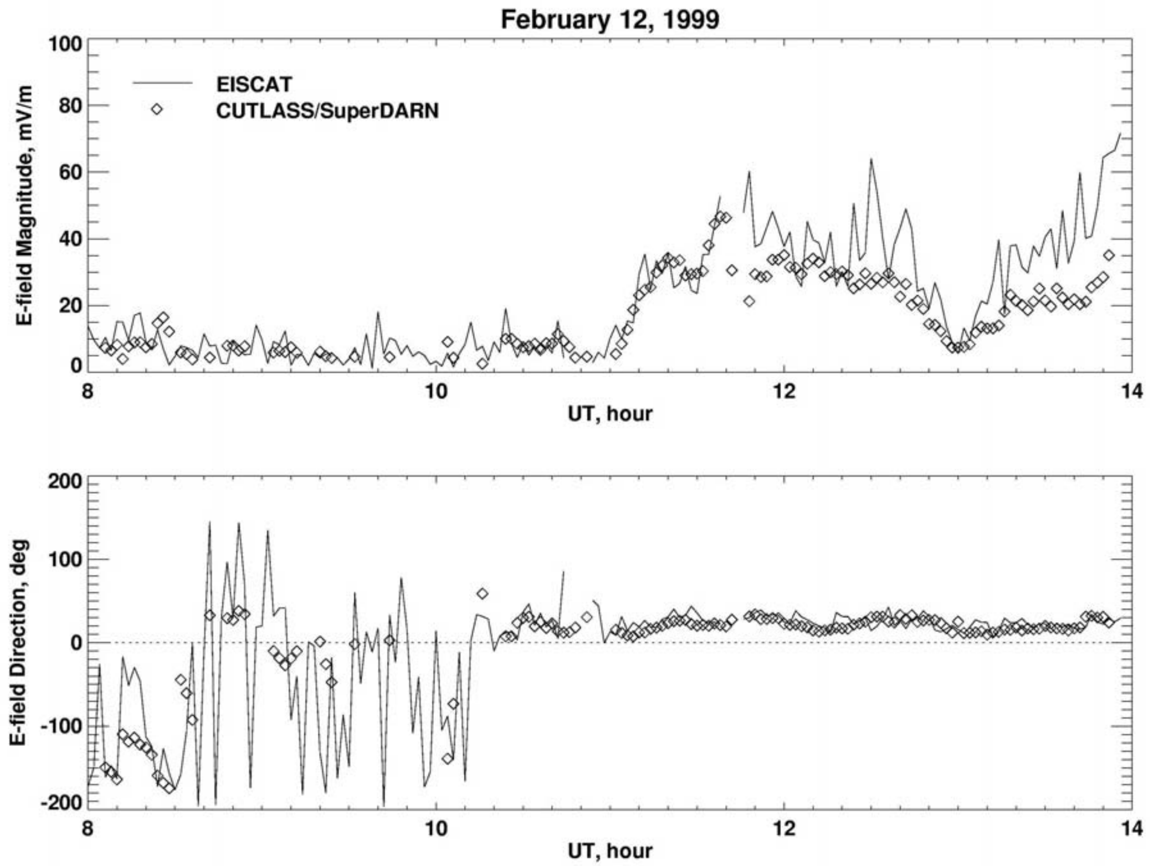

Figure 5.2 The electric field magnitude and direction as determined by EISCAT (solid line) and by SuperDARN/CUTLASS (diamonds) using the Map Potential routine for 12 February 1999.

Prior to ~1130 UT, both devices give very consistent estimates for the magnitude. After this period, the electric field values determined from SuperDARN are less than the EISCAT ones. Also the EISCAT magnitude seems to be more variable though never less than that of SuperDARN. The less variability in the SuperDARN magnitudes may be related to the global nature of Map Potential technique. EISCAT may be seeing much more localized effects.

For observations on 11 February 1999, Fig. 5.3, once again, the electric field directions measured by the two instruments are very consistent and stable being predominantly northward. The magnitude of the SuperDARN electric field is always less than that measured by EISCAT. Significant variations in the magnitude of EISCAT may be due to small-scale local convection anomalies that cannot be seen by SuperDARN.

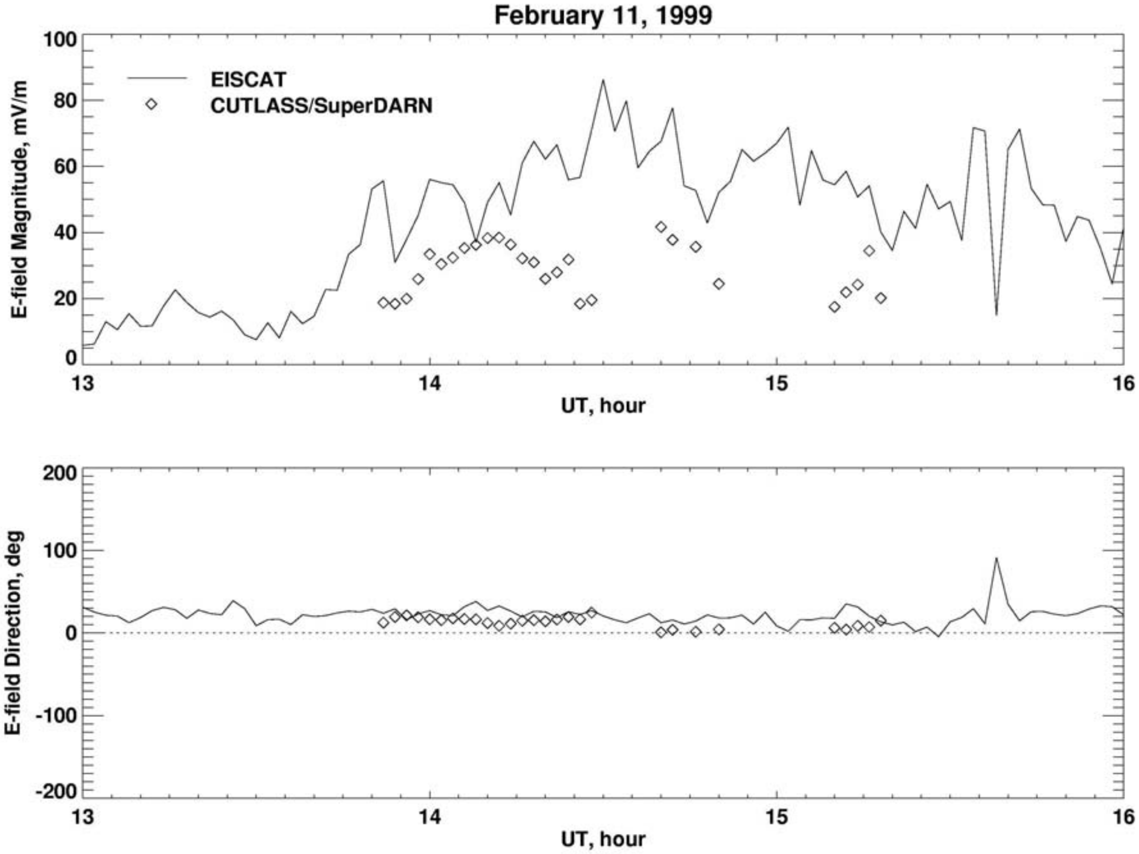

Figure 5.3 Same as in Figure 5.2 except for 11 February 1999.

5.4 Hankasalmi: LOS velocity comparison with EISCAT

Now we employ second approach for an assessment of EISCAT and HF data, namely we compare LOS velocity of Hankasalmi (Pykkvibaer) radar and the component of ExB drift measured by EISCAT. We recall from Fig. 3.1 that the EISCAT spot in CP-1 measurements corresponds to the range of 900 km (range gate 16) for the beam 5 of the Hankasalmi CUTLASS radar and to the range of ~1935 km (range gate 39) for the Pykkvibaer CUTLASS radar beam 15.

The results for the comparison are presented in Figs. 5.4 and 5.5. For 12 February 1999 event, Fig. 5.4, the temporal correspondence of the LOS velocity with component of the ExB drift is quite remarkable. Once again one can note a slight underestimation in the magnitude of the drift measured by SuperDARN. The scatter plot comparing the

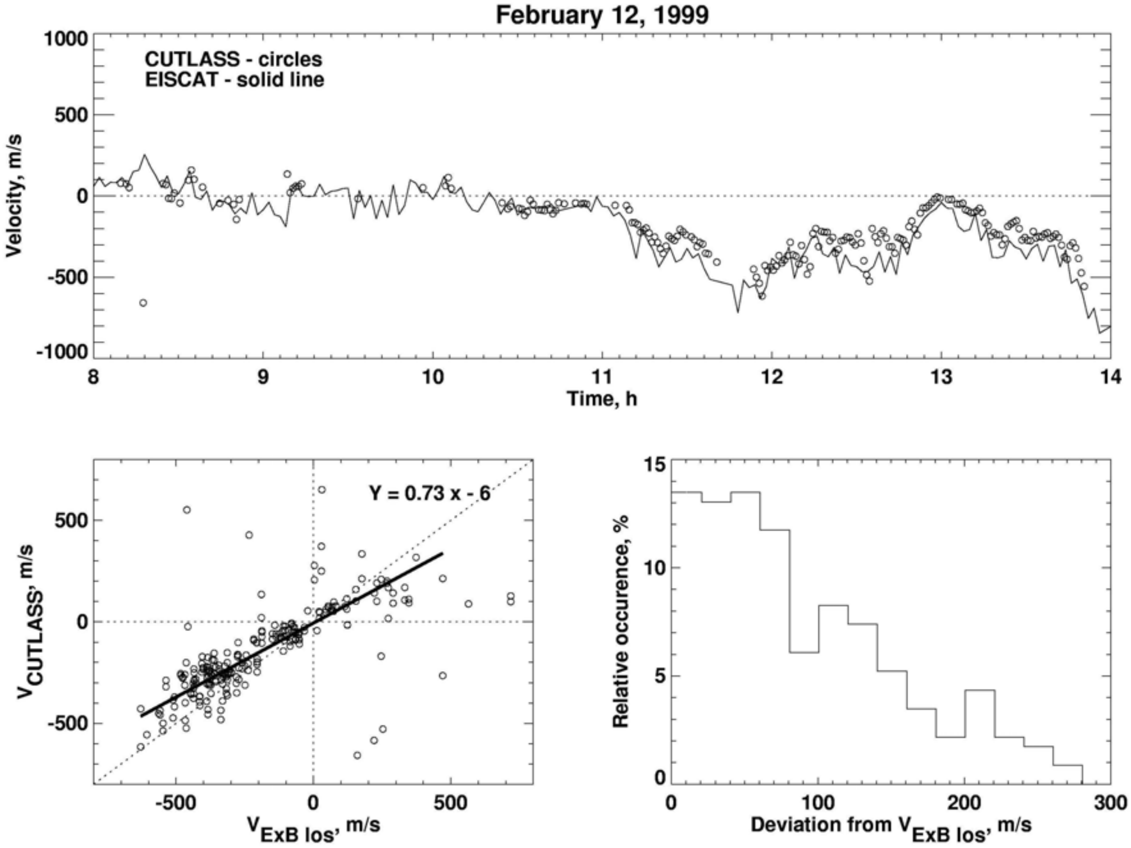

Figure 5.4 Comparison of the Hankasalmi beam 5 LOS velocity (diamonds) with the expected component of the ExB drift as ascertained from EISCAT for 12 February 1999. Lower left is the scatter plot of time matched events. Lower right is the histogram of deviation of LOS velocity from the expected component of the ExB drift.

above velocities shows a general linear trend with a slope of 0.73. The histogram shows that more than 50% of the data has a deviation less than 100 m/s from the expected drift as determined by EISCAT. Only in 10% of the cases the deviation in drift was more than 200 m/s.

For the 11 February event presented in Fig. 5.5, the data are noisier. The overall agreement seems to be better with the slope being 0.89. There are a few events when the Hankaslami LOS velocity was greater than the EISCAT component.

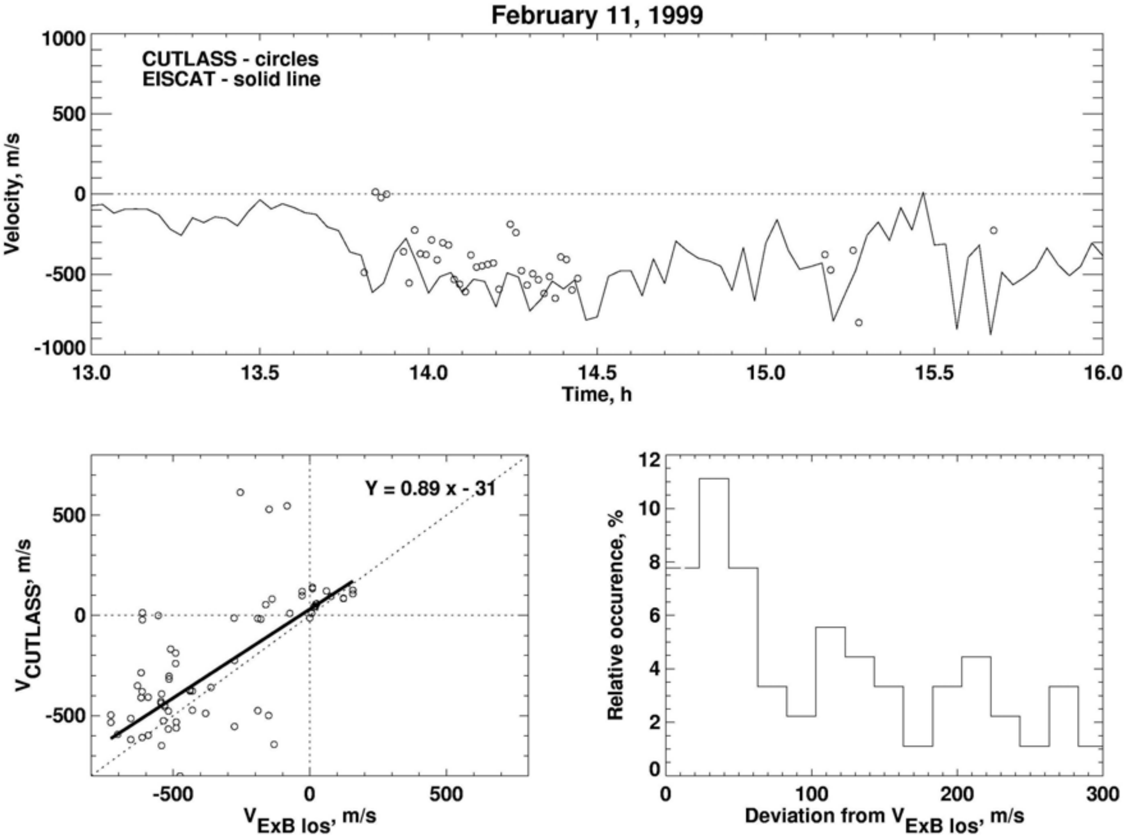

Figure 5.5 Same as in Figure 5.4 except for 11 February 1999.

5.5 Pykkvibaer: LOS velocity comparison with EISCAT

With the Hankasalmi radar, the look direction is predominantly perpendicular to the ExB drift direction for the northward electric field. In this respect, the Pykkvibaer radar looks more along the flow, Fig. 3.1. The Pykkvibaer/EISCAT velocity comparison thus refers to different flow direction. In addition, the Pykkvibaer echoes at the range gate 39 (1935 km) are most likely obtained throught the $1\frac{1}{2}$ F propagation mode. This sort of comparison provides an opportunity for checking the idea of Milan et al. (1997a) that some far-range Pykkvibaer echoes are received from the E and not from the F region, as usually assumed.

The data for 11 February 1999 event are presented in Fig. 5.6 (unfortunately, there were no echoes at required ranges for the 12 February 1999 event). The data are

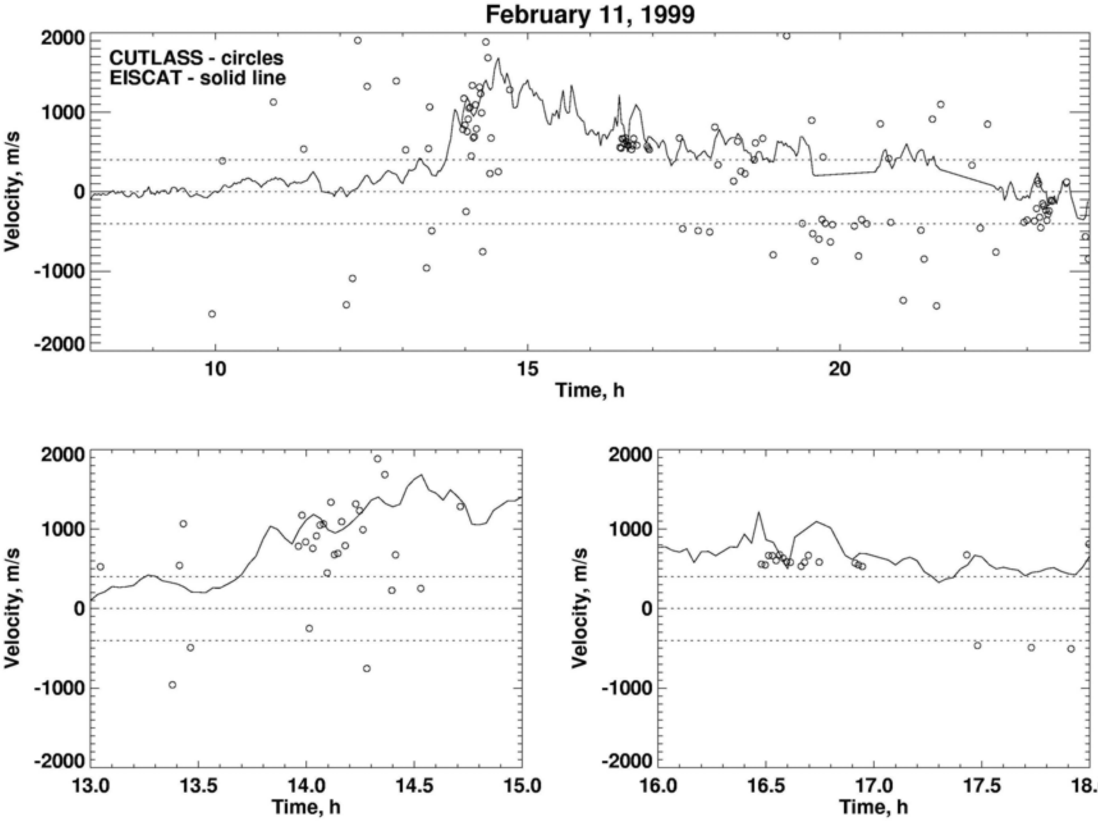

Figure 5.6 Comparison of the LOS velocity of the Pykkvibaer radar (diamonds) with the expected component of the ExB drift as ascertained from EISCAT for 11 February 1999.

very scattered. A good agreement is obtained for the intervals 1400 - 1415 UT and 1600 - 1700 UT. Poor agreement is observed between 18-22 UT where the SuperDARN velocity is of opposite polarity with the EISCAT drift. No trend for the velocity saturation at c_s can be inferred.

5.6 On the reasons for EISCAT/SuperDARN velocity disagreements

The data presented in this section once again support the general opinion that the SuperDARN radars measure the plasma convection component quite accurately. In fact, the presented results show agreement better than any data previously published. One could have been stopped at this point. Instead, we would like to go further and try to analyze the reasons for the velocity differences that still were observed in some instances.

Our major concern is with the fact that our data show again and again that HF velocities are slightly smaller than they are expected to be on a basis of EISCAT measurements, the conclusion made by Xu (2002).

5.6.1 Range counting effect

One potential problem with the comparisons could be an error in mapping of F-region echo location. It is well known that HF radio waves propagating through the ionosphere are slowed down (see Davies, 1990). This effect is not taken into account in the routine SuperDARN mapping procedures though estimates show that range overestimation as strong as 150 km can occur at far ranges (Hanuise, 2003).

To investigate this effect a comparison with the LOS velocities for several consecutive range bins with the EISCAT (expected) drift was done. Fig. 5.7 presents the

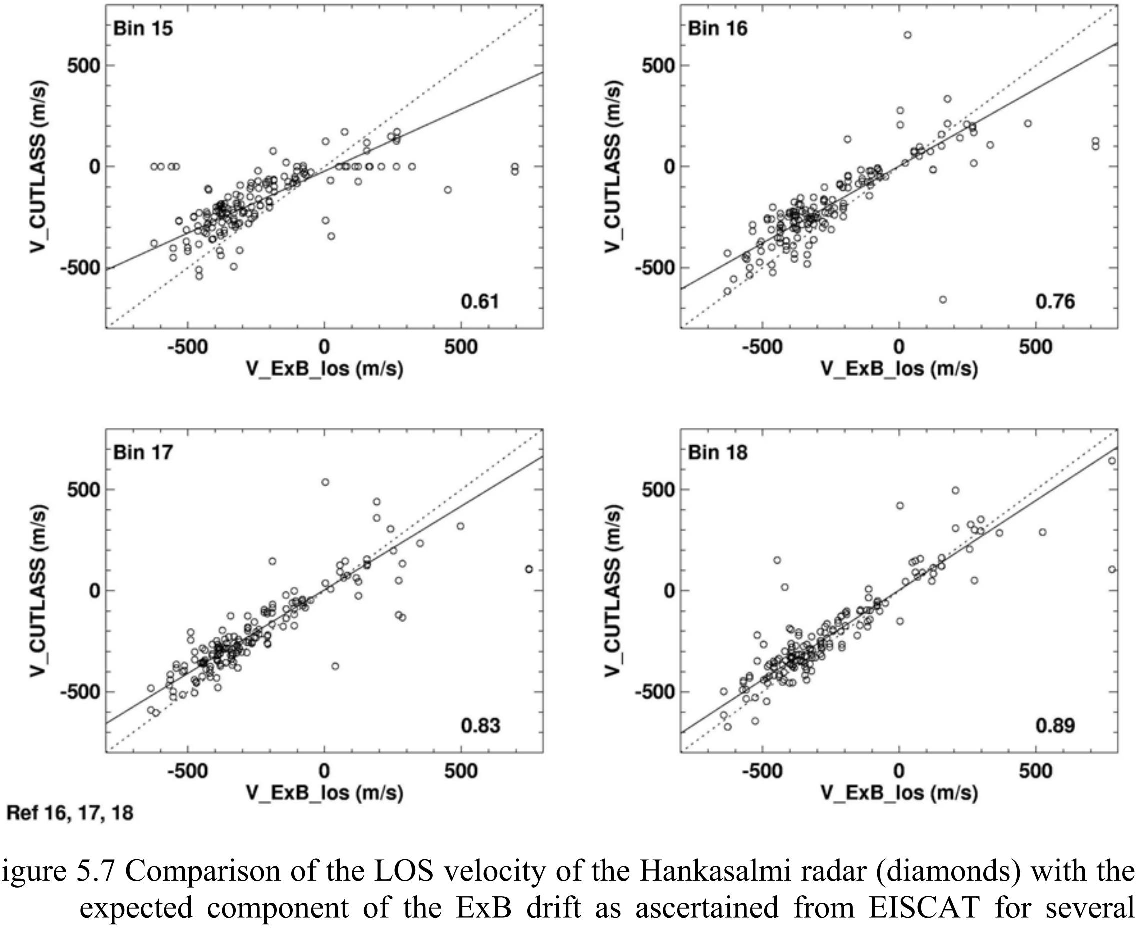

Figure 5.7 Comparison of the LOS velocity of the Hankasalmi radar (diamonds) with the expected component of the ExB drift as ascertained from EISCAT for several different range bins as noted in the upper left hand corner. The number in the lower right hand corner of each panel is the slope of the best-fit line.

comparison for Hankasalmi range bins of 15 - 18. Only events when scatter was available in bins 16, 17 and 18 were considered to give a common electric field reference. The numbers at the lower right of each panel indicate the slope of the best-fit line.

The slope of the best-fit line varies from 0.61 in bin 15 to 0.89 in bin 18 for a range increase of 180 km. The slight improvement in fit with the increase in range indicates that the range counting effect can play some role but cannot completely account for the underestimation of the LOS velocity of SuperDARN.

5.6.2 Lateral refraction of the radar beam

Another potential reason for the disagreement between the Hankasalmi LOS velocity and the ExB drift component could be lateral refraction of the HF radar waves and a change in the assumed orientation of the beam with respect to the convection.

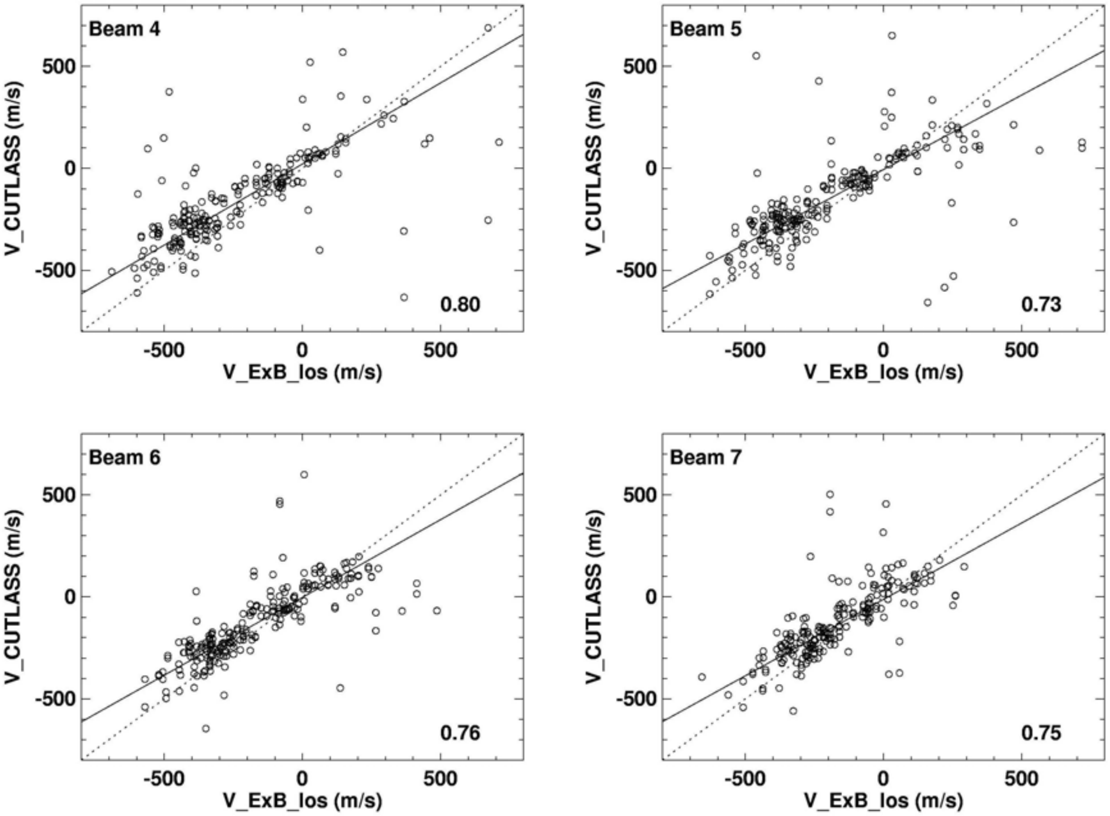

Figure 5.8 Comparison of the LOS velocity of the Hankasalmi radar (diamonds) with the expected component of the ExB drift as ascertained from EISCAT for several beam directions.

We looked at the HF velocity in several beams in the vicinity of beam 5. The velocities in beams 4-7 are compared with the component of the electron drift from EISCAT (projected onto the assumed beam 5) in Fig. 5.8. The rationale behind this comparison is that if other beams are closer to the true direction of plasma flow than beam 5, then the Hankasalmi-EISCAT data would be more consistent for one specific beam. Fig. 5.9 indicates that there is not a significant increase nor decrease when looking at different beams.

5.6.3 Error in the EISCAT azimuth

Next we try to ascertain what would be the effect of a slight error in the direction of the electric field measured by EISCAT. For the experiment under consideration, the total electric field was quite strong plus Hankasalmi observations were performed almost

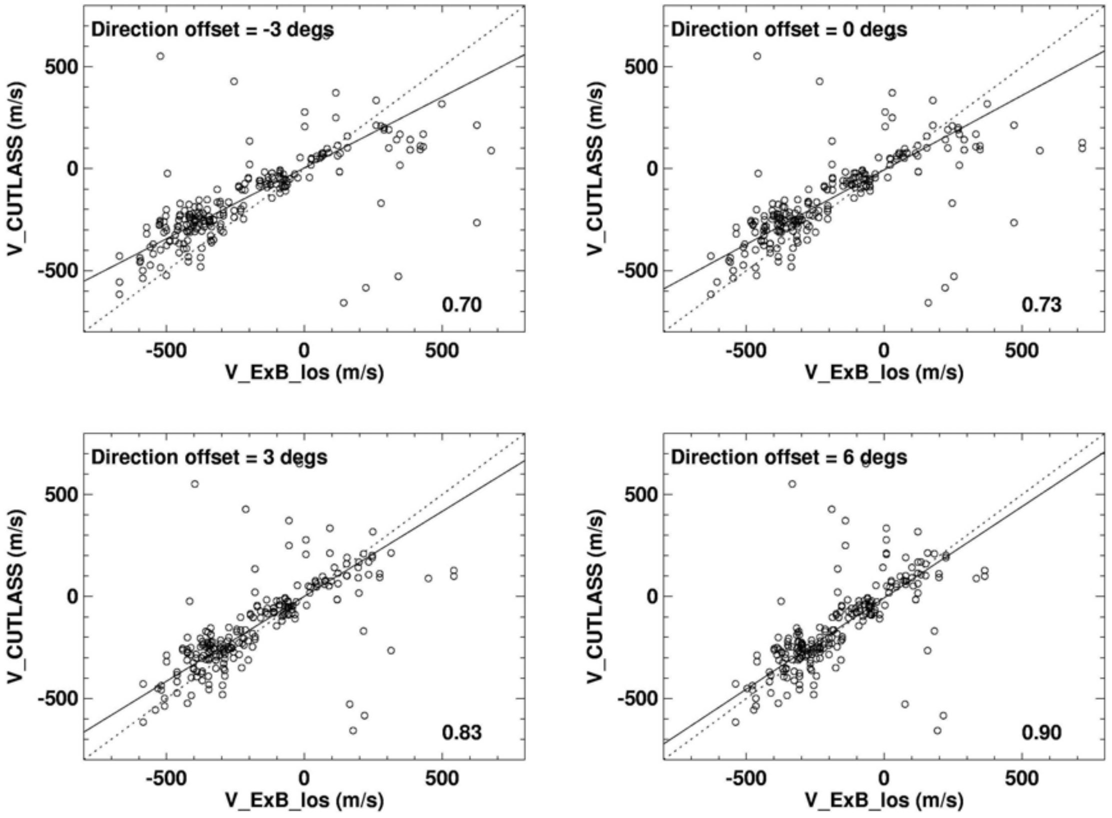

Figure 5.9 Comparison of the LOS velocity of the Hankasalmi radar (diamonds) with the expected component of the ExB drift as ascertained from EISCAT. The electric field direction is offset as indicated. The slope of the best-fit line is shown in the lower right corner.

perpendicular to the plasma flow. This means that even minor error in the EISCAT azimuth determination might result in a major difference in EISCAT ExB component and Hankasalmi velocity.

In Fig. 5.9, the SuperDARN data from beam 5, bin 16 are compared with the estimate of the electric field component based on an offset to the electric field direction. The numbers at the bottom of each panel indicate the slope for the line of best fit. One can see an increase in the slope of the best-fit line. For stronger offsets the agreement between EISCAT and Hankasalmi data increases. The variability of the data remains similar for each offset indicating not a substantially better fit. This could indicate the presence of electric field rotation or an error in the determination of the electric field azimuth.

5.6.4 Significance of micro structure of plasma flows

The two events considered above are of exemplary type; they demonstrate the agreement between the SuperDARN and EISCAT convection estimates quite clearly. This is in some contrast with the data presented by others, especially the ones reported by Xu (2002). One may ask why do we have such a difference? In our opinion, this happens because the resolutions of coherent and incoherent radars are different while the electric field distribution in the high-latitude ionosphere can be quite homogeneous for one event and very inhomogeneous for other. We recall that EISCAT measures convection in very small region of ~ 2.6 km in diameter. It integrates the signal over two minutes. The SuperDARN spatial resolution is more that one cell of measurements which is ~ 45x100 km (the last number depends on the range). In terms of time, even though we say that SuperDARN produces 2-minute convection maps, the data from each beam position are lumped together assuming that there is no change in the convection within the 2-minute time interval. Thus, micro-structure of plasma flow could lead to differences between EISCAT and SuperDARN convection estimates.

Xu (2002) showed examples of daytime and nighttime coherent/incoherent data comparisons. It was pointed out that the scatter of points is stronger for the nighttime comparison. We believe that the data discussed in this chapter on 11 and 12 February 1999 were collected during periods when ionospheric flows were fairly uniform and for

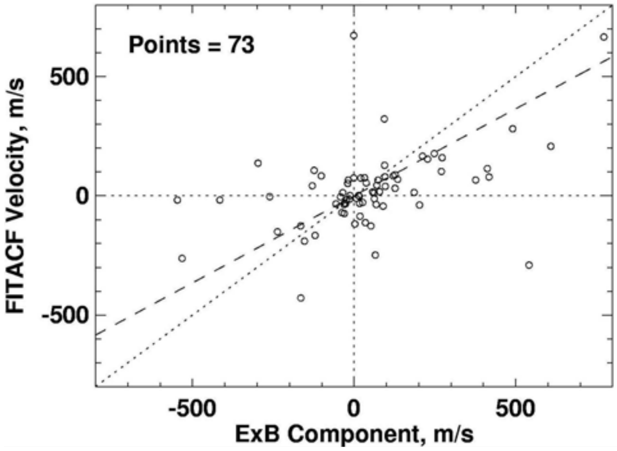

Figure 5.10 Comparison of the Hankasalmi LOS velocity with the expected component of the ExB drift as ascertained from EISCAT for 2-3 September 1997.

this reason the data consistency was excellent. As an example of observations when the flow was highly non-uniform we present here results of Hankasalmi HF radar/EISCAT comparison on 2-3 September 1997. We described the experiment and the data in previous chapter. Here we recall that EISCAT was performing 30-minute meridional scans to measure electric field at latitudes from 60° - 70° in 16 distinct positions. Analysis of data showed that electric field was changing quite strongly along the meridian, from one point of measurements to another. For some points, when there were co-located CUTLASS measurements at close times we were able to compare the EISCAT ExB component along the appropriate Hankasalmi beam. Only F-region scatter was considered. The results are presented in Fig. 5.10. Substantial scatter of points is observed so that one cannot determine the character of the velocity relationship easily; for sure one can see that points tend to be in the first and third quadrants. For a comparison, we show by the dashed line the best-fit line for the data presented by Davies et al. (1999). With this line being present, one can say that our points scatter around the Davies et al.'s (1999) line, but no stronger statement can be made.

5.7 Summary

The data presented in this chapter are consistent with the general conclusion of previous studies that the observed HF velocity of F-region echoes corresponds, to a first approximation, to the LOS component of the ExB plasma drift measured by incoherent scatter radar EISCAT. The data thus provide additional support to the SuperDARN approach of convection estimation. More specifically, for the first time of SuperDARN research we showed that currently used map potential technique worked well for the situation when in the area of interest data for only one radar were available (so that regular merging would have not been possible). Quantitatively, we showed that in terms of azimuth, the SuperDARN estimates agreed with the EISCAT measurements within 20 degrees. For the velocity magnitude, the Map Potential technique provided reasonable convection estimate though there was a minor tendency for underestimation for one of the events. The comparison of EISCAT convection along the Hankasalmi radar beam (in a traditional way accepted in other publications) showed the best-fit line slope of 0.73 with the SuperDARN velocities being smaller than expected on the basis of EISCAT measurements. We also showed reasonable agreement of EISCAT and SuperDARN velocities when $1\frac{1}{2}$F signals were considered (the Pykkvibaer case of 11 February 1999), which had not been done before.

In an attempt to understand the reasons for some differences in convection measurements by the two instruments, we analyzed the possibility of errors in SuperDARN echo region mapping (overestimation of the range, rotation of the beam orientation due to lateral refraction) and error in EISCAT azimuth. We found that these errors cannot explain in full the observed inconsistencies though some of them can have a partial success. No definitive reason for the fact that SuperDARN velocities were slightly smaller than the ones measured by EISCAT was found. Further research in this area is needed.

The fact that the velocity of the F-region echoes is close to the component of the ExB motion is in agreement with the conclusions of the linear theory of the GD plasma instability.

CHAPTER 6

DOPPLER VELOCITY OF E-REGION HF ECHOES: A COMPARISON WITH VHF (STARE) VELOCITY

The SuperDARN radars regularly detect E-region echoes at short ranges of < 700-800 km as shown in Chapter 4. With the data available many features of such echoes can be studied. In this chapter we concentrate only on the velocity. We would like to know the relationship between the Doppler velocity of echoes/ionospheric irregularities and the velocity of the bulk plasma flow. The same question was considered for F-region echoes in Chapter 5. For the E-region case, this is also a fundamental issue, for practical operation of the SuperDARN radars from one side, and for understanding the mechanisms of ionospheric irregularity formation, on the other. As far as the operational aspect is concerned, the fact is that with the Map Potential technique, the velocity of E-region echoes is included into the database for estimates of the convection pattern. Though widely believed that this is a valid procedure, no actual comparisons between the HF velocity of E-region echoes and the LOS component of the ExB drift has been done so far. There are, however, facts that raise concerns in this regard. For example, according to Milan and Lester (1998) there are several types of E-region HF echoes including the notoriously known Type 1 echoes for which the observed velocity is "saturated" at the ion-acoustic speed and does vary as the cosine of the flow angle, as the Map Potential approach assumes. The situation is reminiscent the STARE (VHF) case for which the problems with the convection derivation for observations along the flow are well known (Nielsen and Schlegel, 1985). There are indications that the HF velocity varies with the flow angle in a more complicated fashion than the generally excepted cosine rule (e.g., Makarevitch et al., 2002b).

To achieve the goal, we consider joint measurements of STARE and CUTLASS velocities. It is important to realize that comparison of 144- and 12-MHz echoes has not been done so far even though the systems are operational in common area for a number of years. In the past, Koustov et al. (2001a,b) and Makarevitch et al. (2002b) considered 50- and 12-MHz velocities. Their conclusions, however, are subject to uncertain amount of refraction at 50 MHz. In this respect, the choice of 140-MHz STARE data is superior since at this frequency refraction is not a concern.

We should state clearly that it would be more beneficial to have joint CUTLASS and EISCAT data for the selected task. Our search through the joint database showed that there is currently no simultaneous data, and for this reason to evaluate the relationship between the E-region HF velocity and convection we use the knowledge on the relationship of the STARE velocity and plasma convection. Finally, we should note that for the considered event, the EISCAT data in CP-1 mode were available, but the CUTLASS echoes over the EISCAT spot were coming from the F region as discussed in Chapter 5.

Though our primary goal in this section is to study the velocity of HF echoes, the data on STARE velocities allows us to address the question on the velocity-plasma drift relationship at VHF. This is the central issue for the STARE experiment. It has been explored in a number of previous papers but the conclusions are controversial in many respects. Results presented in this chapter were published in Koustov et al. (2002a).

6.1 Experiment setup

Fig. 6.1 shows the experiment configuration. We basically use the same configuration as in Chapters 4 and 5 except we add the STARE radars. In Fig. 6.1 the broad fan-like zone is the CUTLASS radar field-of-view (FoV) for slant ranges between 300 and 1200 km assuming the height of 110 km. Dashed lines indicate the ranges of 600 and 900 km from Hankasalmi. The lightly shaded area within the CUTLASS FoV is the location of the CUTLASS beam 5 (assuming the width of 5^{o}, the actual beam width can be slightly different depending on radar frequency), and the darker shading is the STARE beam 4 that is 3.2^{o} in width. The Finland STARE beam is slightly shifted to the west of the CUTLASS beam 5. For the analysis, these Hankasalmi beams were selected since they reasonably overlap and also there is an area where joint measurements with

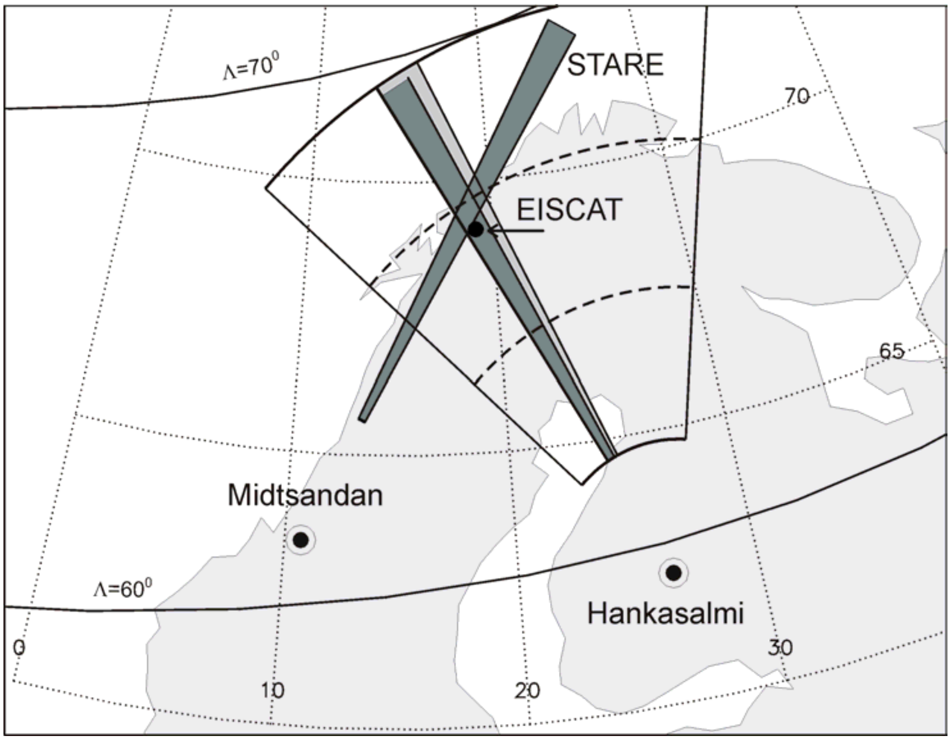

Figure 6.1 Field of view of the Hankasalmi CUTLASS HF radar for ranges between 300 and 1200 km at the height of 110 km. Dashed lines are slant ranges of 600 and 900 km. The lightly shaded sector is location of CUTLASS beam 5. The darker beam-like sectors are the location of the Finland STARE radar beam 4 and the Norway STARE radar beam 4. Solid dot denotes the area where ionospheric parameters were monitored by the EISCAT incoherent scatter radar. Also shown are PACE lines of equal magnetic latitudes $\Lambda=60^o$ and $\Lambda=70^o$.

EISCAT are possible. The solid circle in Fig. 6.1 represents the location of EISCAT area of measurements (at 300 km) in CP-1K mode. The distance from Hankasalmi to the EISCAT collecting area is around 900 km (for the height of ~300 km). We also show the location of beam 4 of the second STARE radar (140 MHz) operated at Midtsandan (Norway) by the Max-Plank-Institute, Lindau. The intersection of the chosen STARE radar beams is very close to the area of the EISCAT measurements. The distance from Midtsandan to the EISCAT spot is about 750 km. In Fig. 6.1 the PACE magnetic latitudes of 60^o and 70^o are presented for reader's convenience.

We focus in this study on the event of 12 February 1999, 1000-1800 UT. During this period, all radars were in their standard modes. The HF CUTLASS radar (12.4 MHz) was operated in the fast common mode, which completes one full sweep over the FoV in one minute. The STARE VHF radars also operated in the standard single-to-double pulse pattern (Greenwald et al., 1978) to resolve the power and Doppler velocity profiles.

The EISCAT radar was in CP-1K mode. We used 2 min averaged data to ensure the averaging was as close as possible to the integration time of coherent radars. Since the three radar systems did not coordinate the timing of the measurements, there were some differences in time between data records, but these differences were less than 1 min.

6.2 Event overview

Some information on the event was given in Chapter 4. Here we add that 12 February 1999 was a moderately disturbed day (Coffey, 1999) with low local magnetic activity over Scandinavia seen by the IMAGE magnetometer network between 1000 UT and 1300 UT (magnetic perturbations <+100 nT) and some activity afterwards. A smooth enhancement of eastward electrojet (perturbations <+250 nT) was observed between 1430 UT and 1500 UT followed by another intensification between 1500 and 1530 UT. A third activation after 1600 UT was followed by 2 short-lived intrusions of westward electrojet (magnetic perturbations stronger than -250 nT) at latitudes poleward of Tromso.

CUTLASS echoes were detected during almost the whole period under discussion but in two quite different bands of ranges, Fig. 6.2. Prior 1400 UT, echoes were located at large ranges of 700-1100 km. Interferometer measurements showed that these were F-region echoes. By employing ray tracing, we showed in Section 4.4.3 that for the period under consideration, one would expect presence of F-region echoes at 800-1200 km and E-region echoes at shorter ranges. There were seen only a few short-lived echoes at close ranges (Fig. 6.2). One of the possible reasons for the absence of these short-range echoes is an electric field decrease with latitude; we demonstrate the effect later by showing that the CULTASS velocity decreases at shorter ranges.

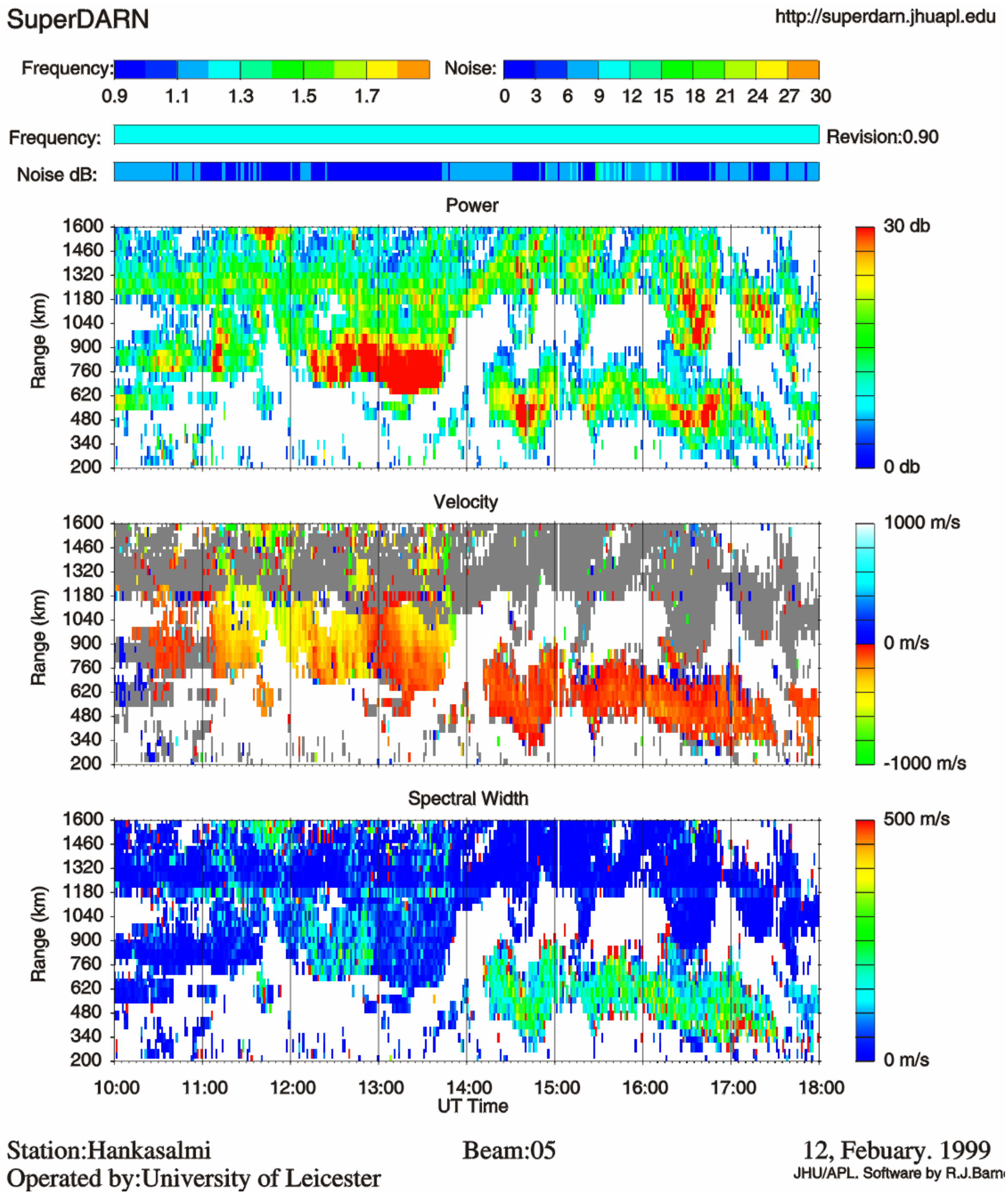

Figure 6.2 Plots of CUTLASS HF echo power, Doppler velocity and spectral width versus time in beam 5 for the event of 12 February 1999, 1000-1800 UT.

After 1400 UT, echoes were continuously seen at much shorter ranges, typically 400-700 km with some slow displacements of the echo band in the north-south direction. According to the interferometer measurements, these were E-region echoes. Generally, one can expect F-region echoes at farther ranges at these times since according to EISCAT, the electric field was quite significant at that part of the ionosphere and one would expect the decameter irregularities being present at the F-region heights. However, no F-region echoes were detected. By employing ray tracing, we show later (see Fig. 6.13 in the Section 6.5) that because of quite dense E region at these times, the F-region decameter irregularities were simply not accessible to HF radio waves. During the periods of F-and E-region HF echo observations, measured HF velocities were quite different, large, up to 200-600 m/s in the first case and low, 100-200 m/s, in the second case.

STARE registered echoes between about 1100 UT and 1800 UT in a broad band of ranges starting from about 500-600 km all the way to the radio horizon of 1200 km, Fig. 6.3. STARE velocities for both radars were quite variable with lower velocities at near distances and larger velocities at far distances. This trend was perhaps partially associated with a general decrease of electric field with latitude.

A more detailed presentation of the data is given in Figs. 6.4a-c and 6.5a-c. In Fig. 6.4a we show power of Hankasalmi and Midtsandan echoes at ranges close to the EISCAT spot (bin 27 for Hankasalmi and bin 17 for Midtsandan) for the whole event. The Norway echoes are obviously stronger. One observes quite synchronous temporal variations of the power. In Fig. 6.4a we also show the electron density at the height of 110 km, roughly at the center of the electrojet layer. According to the EISCAT measurements, the density profiles most of the time exhibited a broad maximum near 110-120 km. One notices the correlation between the STARE echo power increases (for both radars) and the electron density enhancements, a well-known effect at VHF (Starkov et al., 1983; Williams et al., 1999).

Fig. 6.4b shows the electron drift magnitude and direction (solid line) as observed by EISCAT (the data were smoothed with 5 point sliding window). The direction is measured from geographic north, positive to the east. The electron flow is quite fast, in excess of 400 m/s for the majority of the time (see horizontal dashed line). This means that the threshold condition for the FB plasma instability excitation is met most of the time. The flow is predominantly westward (eastward electrojet). One can clearly see a correlation between decrease in STARE power in Fig. 6.4a (no echoes before 1100 UT

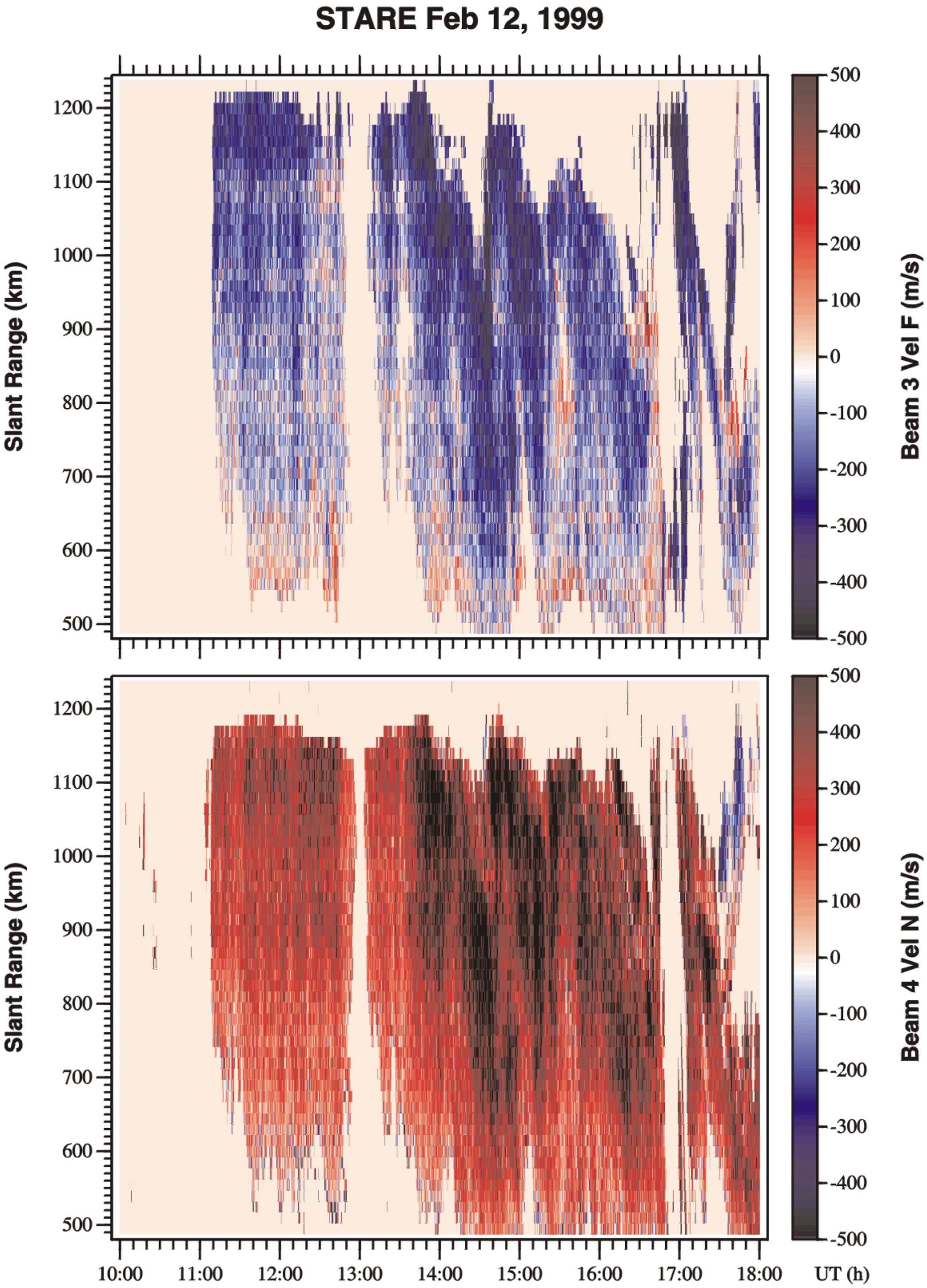

Figure 6.3 Plots of STARE VHF echo Doppler velocity versus time in beam 4 for the Finland radar and beam 4 for the Norway radar for the event of 12 February 1999, 1000-1800 UT.

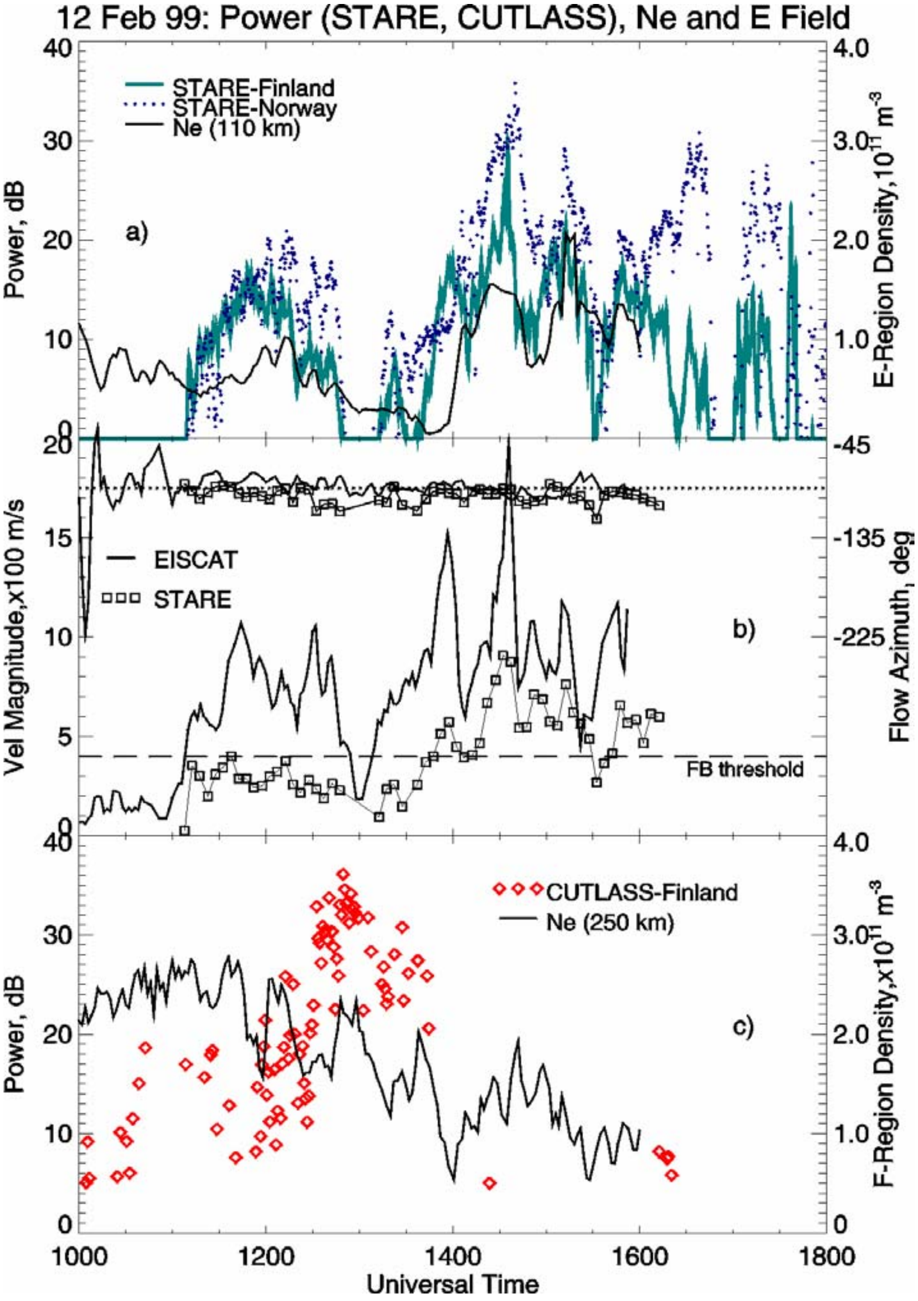

Figure 6.4 (a) Temporal variations of Finland STARE (green dots) and Norway STARE (blue dots) echo power in bins 27 and 17, respectively. Power of the Norway radar was scaled down by 2.4 dB to take into account shorter distance to the scattering volume. Solid line shows the electron density at 110 km according to EISCAT measurements. (b) Plasma convection velocity magnitude and azimuth according to EISCAT tri-static measurements at 250 km (solid line) and according to STARE merge predictions (squares). (c) The Hankasalmi CUTLASS echo power in bin 16 (red diamonds) versus time and the electron density at 250 km according to EISCAT measurements.

and around 1300 UT, low power near 1530 UT) and the decrease in electric field. We also show in Fig. 6.4b the azimuth and magnitude of the electron flow as derived from the standard STARE merging procedure (squares). One can see reasonable agreement in the STARE and EISCAT azimuths and significant STARE underestimation of the flow magnitude, in agreement with earlier results by Nielsen and Schlegel (1985).

In Fig. 6.4c, we show EISCAT electron density at 250 km. In the F region, density profiles were fairly flat between heights of 220 and 270 km (though sometimes with quite a variability from one height to the next one) exhibiting a broad maximum around 250 km. We also present in this diagram the CUTLASS echo power as measured near the EISCAT spot, red diamonds. One can see that the HF echoes are received for F-region densities around 2.0×10^{11} m^{-3}. Such electron density is sufficient to provide the radio wave orthogonality at the height of 180-230 km (Section 4.4.3) thus confirming that the CUTLASS echoes between 1200 UT and 1400 UT were indeed coming from the F-region heights.

An overview of the velocity measurements of all radars is presented in Figs. 6.5a-c. In Fig. 6.5a we show the EISCAT velocity component (solid line) projected along the direction of the STARE-Finland radar beam 4 (as expected under the assumption that the VHF Doppler velocity is a cosine component of the total drift). We superimpose the Doppler velocity (green points) measured by the STARE-Finland radar in beam 4, bin 27. Since the spread of points is significant, we indicate the smoothed temporal variation of the Doppler velocity by a solid green line. One can see some general agreement in temporal variations of the velocities although the STARE velocity is typically smaller than the EISCAT velocity by a factor of 2-3. Also shown in Fig. 6.5a is the ion-acoustic speed (we assigned negative sign for the convenience of presentation) at ~111 km according to EISCAT measurements. We assumed both electrons and ions being isothermal and the ion mass being 31 amu. One can see that most of the time the EISCAT velocity component along the Finland radar beam 4 (and the Finland radar Doppler velocity as well) was below the ion-acoustic speed meaning that the Finland STARE radar was observing electrojet irregularities outside the FB instability cone.

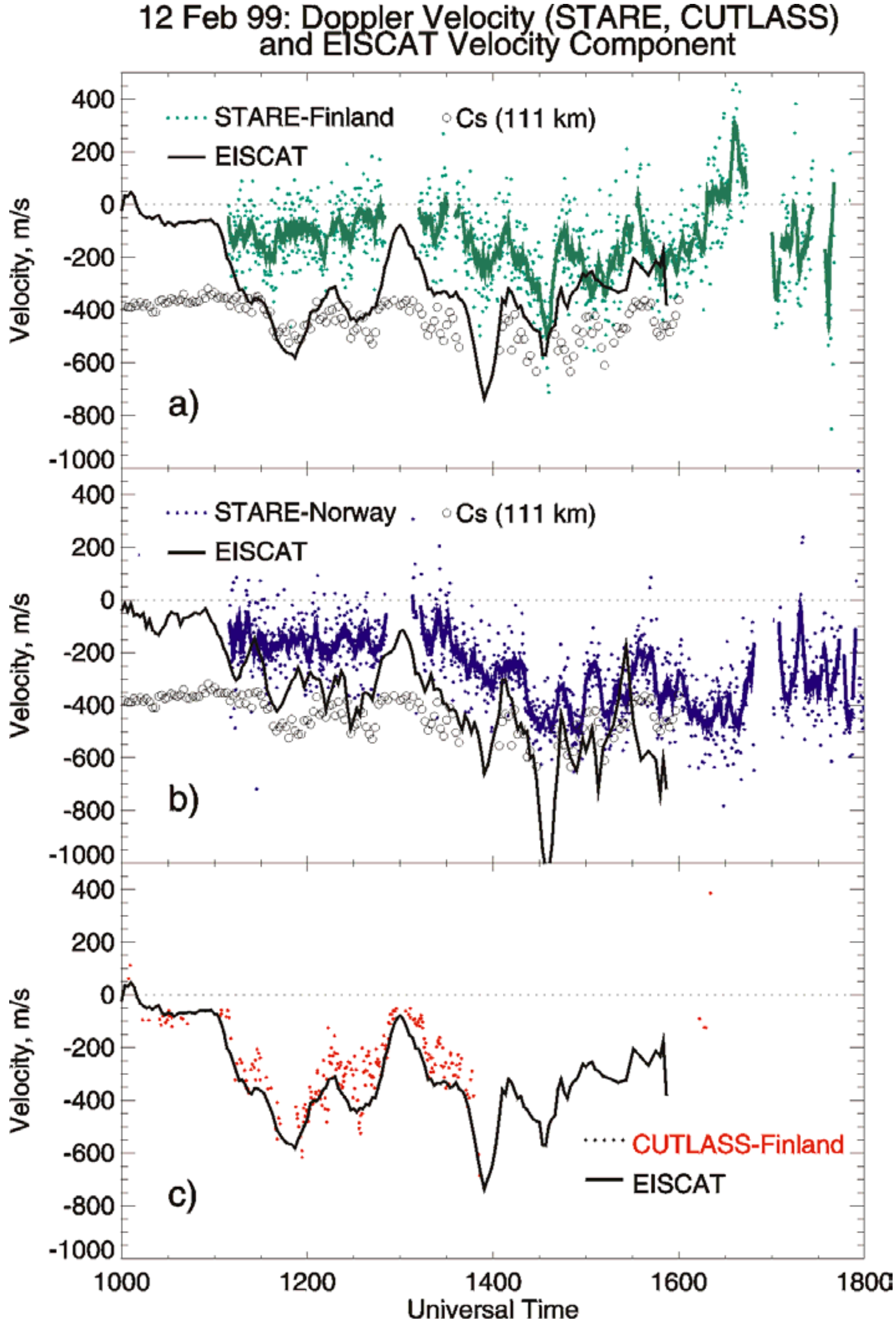

Figure 6.5 (a) Finland STARE (green dots) beam 4 Doppler velocity in bin 27 and the EISCAT convection component (solid line) along beam 4 versus time. The solid green line represents smoothed behavior of the STARE velocity. (b) Norway STARE (blue dots) beam 4 Doppler velocity in bin 17 versus time and the EISCAT convection component (solid line) along beam 4. The blue solid line represents smoothed behavior of the STARE velocity. (c) Hankasalmi CUTLASS beam 5 Doppler velocity (red dots) in bin 16 and the EISCAT convection component (solid line) along this beam versus time.

Fig. 6.5b shows similar data for the EISCAT velocity along the STARE-Norway radar beam 4, the STARE-Norway Doppler velocity in bin 17 (plotted with the opposite sign for the convenience of presentation) and the ion-acoustic speed at ~111 km (we also assigned negative sign for it). Here the STARE/EISCAT agreement is slightly better though the STARE velocity is still almost always smaller than the EISCAT velocity. Both the EISCAT velocity component along the Norway beam 4 and the Norway Doppler velocity have smaller magnitudes than the ion-acoustic speed most of the time meaning that this radar was also observing irregularities outside the FB instability cone.

Fig. 6.5c compares the EISCAT velocity component along the CUTLASS beam 5 and the CUTLASS Doppler velocity at ~900 km. Contrary to the STARE case, agreement is much better though there is a tendency for the CUTLASS velocity to be slightly smaller. One can notice a lack of CUTLASS echoes after 1400 UT; at this time the echo band was located at shorter ranges, see Fig. 6.2.

6.3 Aspect angle conditions for coherent radars

We show in this study that the aspect angle conditions of measurements are important for understanding obtained results. For this reason, we consider them in detail in this section. Fig. 6.6a shows the aspect angle (at various heights) versus slant range for both HF and VHF Hankasalmi radars and the azimuth of -20.8° (beam 4 of STARE). Simple geometric-optics approach was employed, similar to Uspensky et al. (1994). The uniform electron density of $5\text{x}10^{10}$ m^{-3} has been adopted though the STARE aspect angles do not change much for electron densities typically observed in the auroral ionosphere.

One can see that the STARE-Finland aspect angles are negative at all slant ranges. Negative aspect angles mean that additional refraction of radio waves is required to meet magnetic flux lines orthogonally. At the height of 110 km, the aspect angles are of the order of -0.8° at ranges 800-1000 km and they go down fairly quickly at shorter ranges. The STARE aspect angles are better at lower heights. Calculations show that in the F region (250 km), the aspect angles range from –25° at short distances to –8° near the radio horizon. The STARE-Norway aspect angles, presented in Fig. 6b, show variations

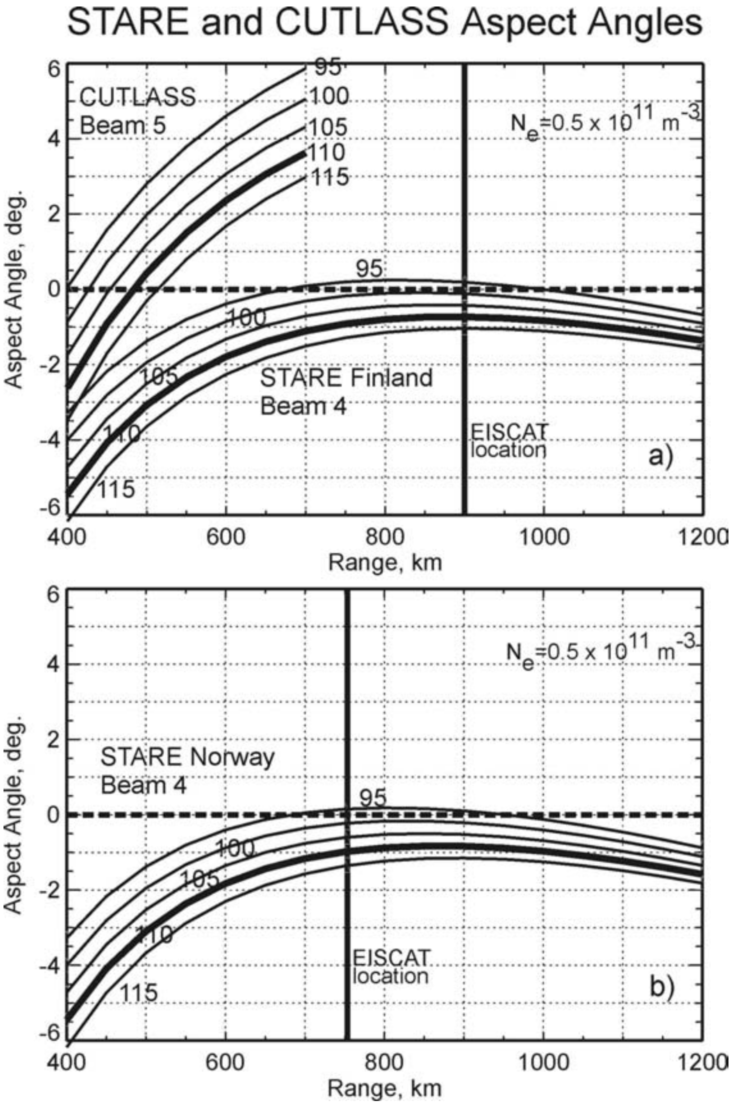

Figure 6.6 Aspect angles versus slant range at various heights for (a) STARE Finland radar beam 4 and CUTLASS Hankasalmi radar beam 5, and (b) STARE Norway radar beam 4. An electron density of 5x10^{10} m^{-3} was assumed.

similar to the ones by the STARE-Finland radar with aspect angles at the EISCAT spot of about -1° at the height of 110 km.

The CUTLASS aspect angles exhibit a more dramatic change with range. They are strongly negative at distances of less than 400-500 km and positive at distances beyond ~500-600 km. The location of the point with zero aspect angle (at every height) is very sensitive to the choice of the electron density; this point is located farther (closer) away (towards) from the radar with density decrease (increase). More thorough full ray tracing analysis for the most recent AAGCM magnetic field model shows that the range of near zero aspect angles at HF is in between 450 and 550 km, depending on height. The fact that the aspect angles presented in Fig. 6.6a are not extremely precise is not so important for this study because there is much more serious uncertainty in the electron density profile and its latitudinal variation. In the F region (250 km), the CUTLASS aspect angles are several degrees better than at 140 MHz, but still quite large for chosen electron density. An important conclusion of these calculations is that the aspect angles for both STARE radars are almost nowhere perfect. The aspect conditions quickly deteriorate at distances of less than 600-700 km whereas near perfect aspect conditions for the CUTLASS radar can be met in a broad band of ranges, from 400 km to 1200 km, depending on the electron density in the E and F regions.

6.4 Details of the velocity relationship for Hankasalmi observations

One of the goals in this study is to compare HF and VHF velocities. We do this in two different ways. First we consider averaged slant range profiles of the velocity with averaging over 10-min intervals (we consider periods during which 1-min comparison shows reasonable agreement). Our second approach is to compare VHF and HF velocity data at similar ranges and for the time separation of less than 1 min. We explore then the relationship of HF/VHF velocities and plasma convection monitored by EISCAT at a range of 900 km.

6.4.1 F/E comparison

The first half of the considered period corresponded to the case when the CUTLASS radar observed F-region scatter while both STARE radars, as always, observed E-region scatter. We call such situation the F/E case.

6.4.1.1 Range profiles

Typical examples of power and velocity range distributions for two 10-min intervals during this period are presented in Figs. 6.7a-d. Here the data are averaged for each range of observations; thin and thick lines show STARE (Finland) and CUTLASS measurements, respectively. Vertical bars indicate the standard deviations of the parameters at each range. No range corrections were applied for the power of both radars. Ranges with less than 5 points for CUTLASS and 13 points for STARE (less than half of potentially possible measurements) are not considered. Typically for each range, there were 6-8 points for CUTLASS and more than 20 points for STARE. In Figs. 6.7a,c we also show at 900 km the averaged densities as measured by EISCAT at 110 km (open diamond) and 250 km (square). In Figs. 6.7b,d we show by asterisk the averaged velocity component at 900 km as measured by EISCAT.

One can see that the range coverage for CUTLASS is smaller than for STARE. In terms of power, CUTLASS shows fairly clear maxima at ranges ~ 750 km while STARE shows much more uniform distributions with steady power decreases at short distances. This decrease is consistent with the deterioration of aspect conditions and perhaps some electric field decrease at short ranges. Also, the CUTLASS power profile in Fig. 6.7c is shifted slightly towards larger ranges than in Fig. 6.7a most likely due to a decrease in the F-region electron density. STARE and CUTLASS velocities are different at all ranges, from 700 to 1100 km, with the velocity ratio of the order of 0.5. At the point of EISCAT measurements, the CUTLASS velocity is close to the EISCAT velocity component on Fig. 6.7b and slightly smaller on Fig. 6.7d, consistent with the data presented in Fig. 6.5c. Magnitudes of HF velocity are smaller at shorter ranges. This happens, most likely, due to electric field decrease at lower latitudes, a commonly seen effect in the afternoon sector (Rich and Hairston, 1994).

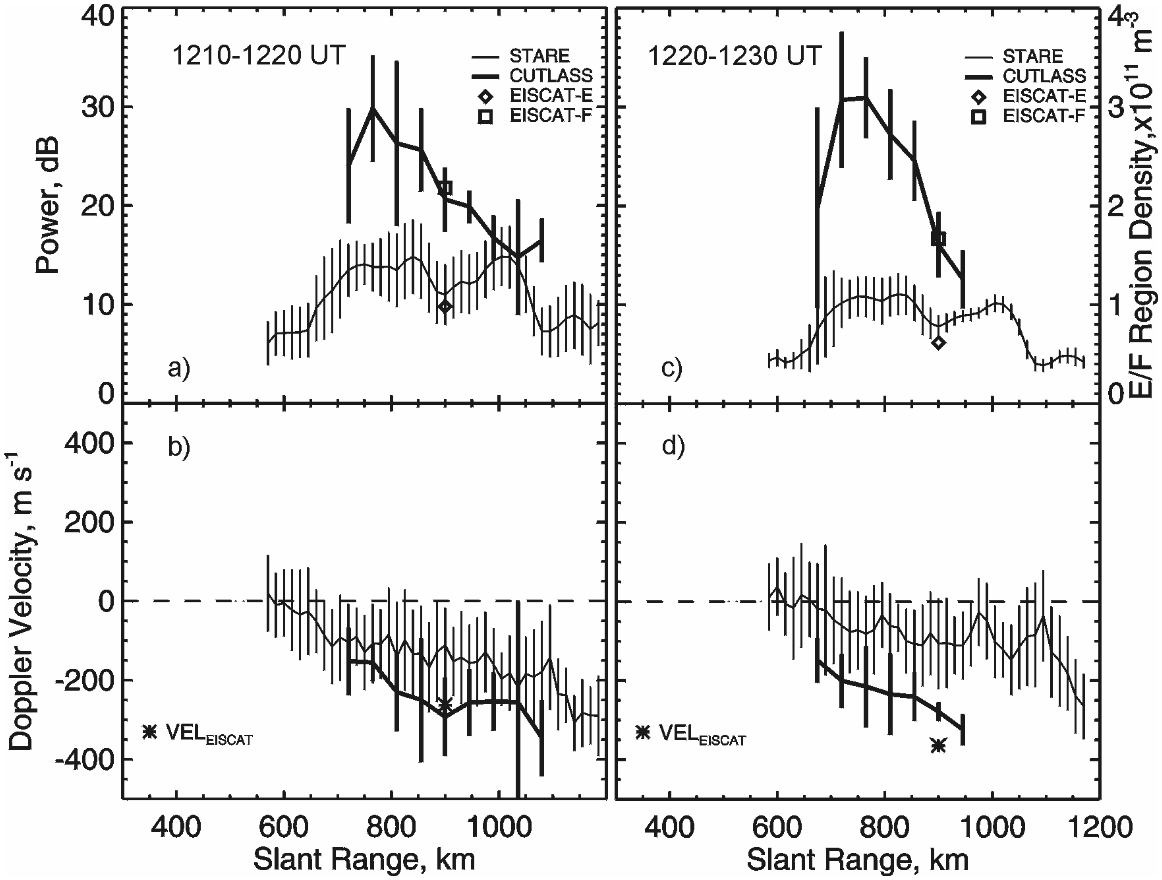

Figure 6.7 Averaged slant range profiles of echo power (a, c) and Doppler velocity (b, d) for two 10-min periods of joint STARE/CUTLASS Hankasalmi observations when CUTLASS observed F-region echoes and STARE observed E-region echoes. An asterisk (in b, d) shows EISCAT convection component along the direction of observations at the range of 900 km. Square and open diamond (in a, c) show the average electron density at the heights of 250 and 110 km, respectively. Scale for the densities is shown to the right of panel (c).

In Fig. 6.8 we compare Finland STARE and CUTLASS velocities for measurements with time separation of less than a minute. We use STARE data averaged over three successive 15-km bins (to match 45-km bins of CUTLASS). One can see that the STARE velocities are systematically smaller than the CUTLASS velocities at all ranges including the range of the EISCAT measurements.

To give more a quantitative assessment of the VHF velocity with respect to the HF velocity and thus with respect to the E×B (convection) component along the HF

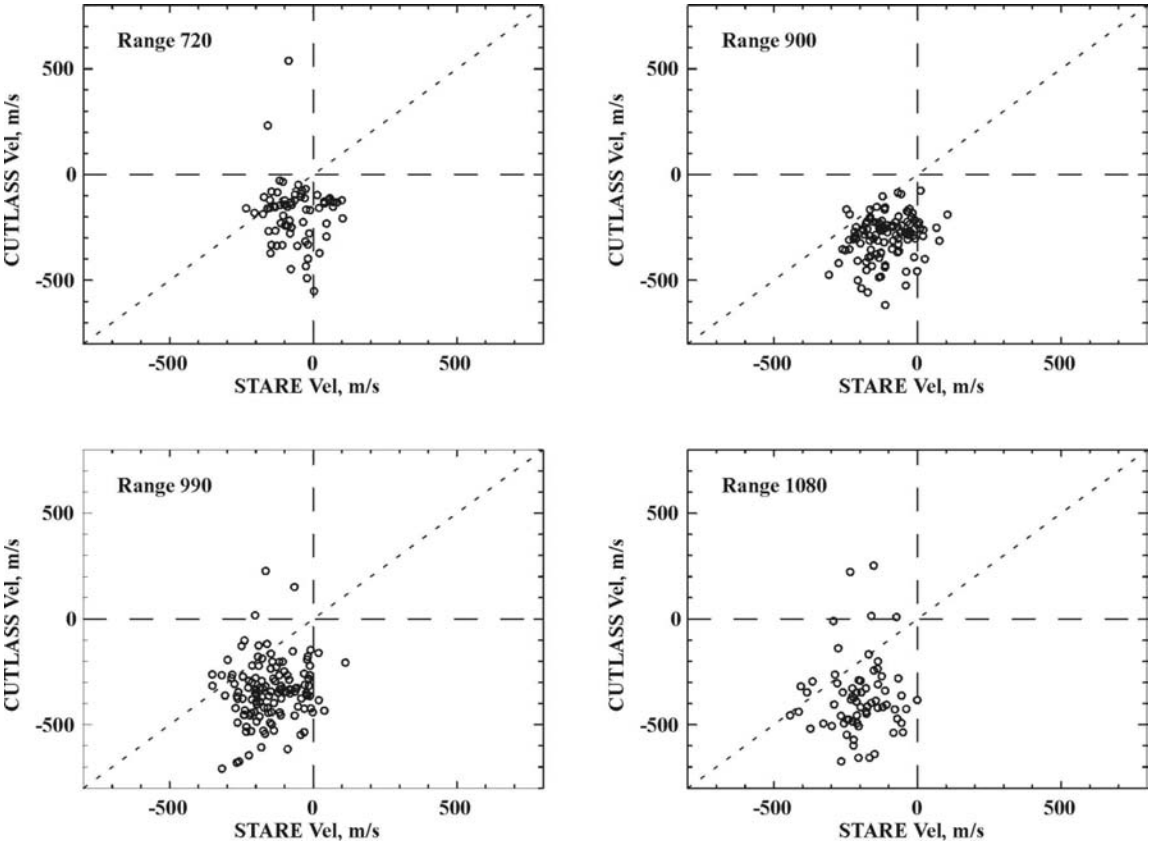

Figure 6.8 Scatter plot of Hankasalmi CUTLASS velocity versus Finland STARE velocity at several slant ranges for the period of 1100-1400 UT when CUTLASS (STARE) radar observed echoes from the F (E) region.

beam, we consider range profiles of the ratio R = $V_{STARE}/V_{CUTLASS}$. We recall that the CUTLASS Doppler velocities agreed well with the EISCAT convection measurements at one point (for the range of 900 km, Fig. 6.5c), and thus one can treat the CUTLASS velocity range profile as the range profile of the convection component. Since the aspect angles of STARE measurements are progressively larger at shorter ranges, the expectation is that R should be smaller at shorter ranges. In Fig. 6.9 we present several range profiles for the ratio R, including two profiles for the data shown in Fig. 6.7. Three profiles out of four demonstrate the expected effect. We should note that such tendency was not always clear due to significant data spread for both radar systems. Obviously a statistical study of this effect is required, and this work is currently under way for the events with more stable coherent radar data.

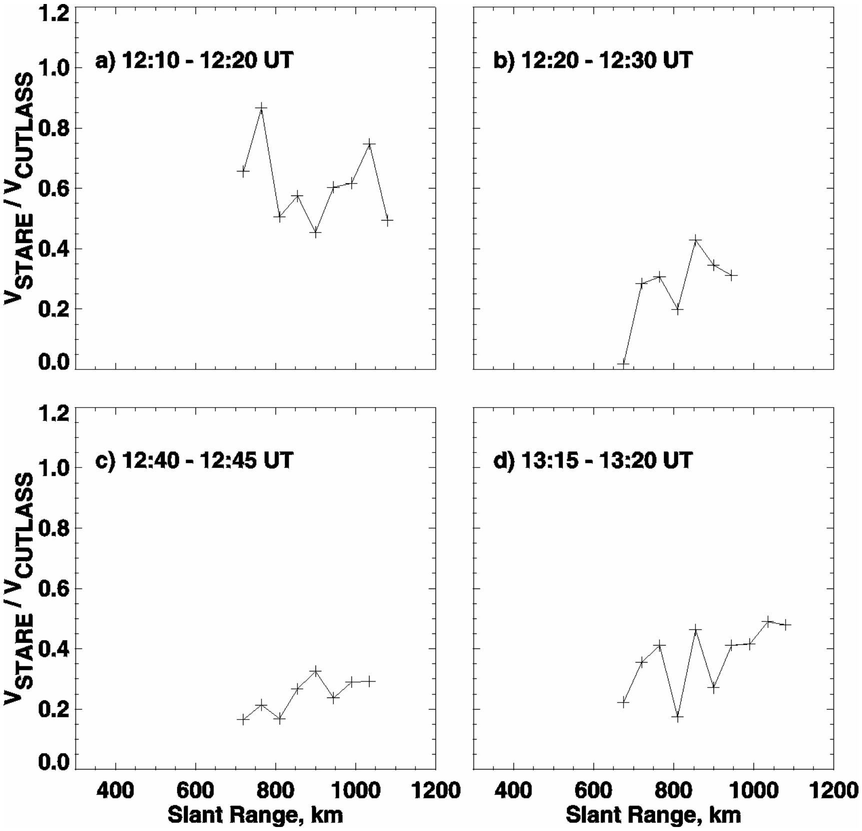

Figure 6.9 Range profiles of the velocity ratio R=$V_{STARE}/V_{CUTLASS}$ for several periods of measurements at Hankasalmi.

6.4.1.2 Comparison at the EISCAT spot

VHF measurements at the EISCAT spot allow us to assess these velocities with respect to the E×B velocity component measured by the EISCAT radar (V_{EISCAT}). We show in Fig. 6.10a the ratio $R_l = V_{STARE}/V_{EISCAT}$ for the whole period under study. Here we used the data of Fig. 6.5a that we averaged over 2-min intervals. Fig. 6.10b gives the distribution of R_l values. The more frequently occurring R_l is ~0.2 though all values between 0.1 and 1.0 are possible. Fig. 6.10c shows R_l versus V_{EISCAT}. Though the data spread is significant, one can recognize that R_l tends to decrease with the velocity (electric field), something one would expect from the kinetic theory of the FB instability (Schlegel, 1983). Fig. 6.10d shows expected values for the ratio of the irregularity phase velocity and the E×B component (V_{ph}/V_E) for various aspect angles and at different ionospheric heights according to the linear theory of the FB and GD instabilities (95-130 km, step in height is 5 km). The standard formula (Equation 2.24) was used with the ion term contribution being neglected, similar to Kustov et al. (1990) and Uspensky et al. (1994). The electron-neutral and ion-neutral collision frequencies, used in calculations, were computed similarly to Schlegel (1983) by selecting the MSIS-90 atmospheric model for the latitude, longitude and period under study. One can see from Fig. 6.10c that at the aspect angle of 1^o the irregularity phase velocity can be smaller than the convection component by a factor of 2-3, depending on the height in the ionosphere, in rough agreement with observations.

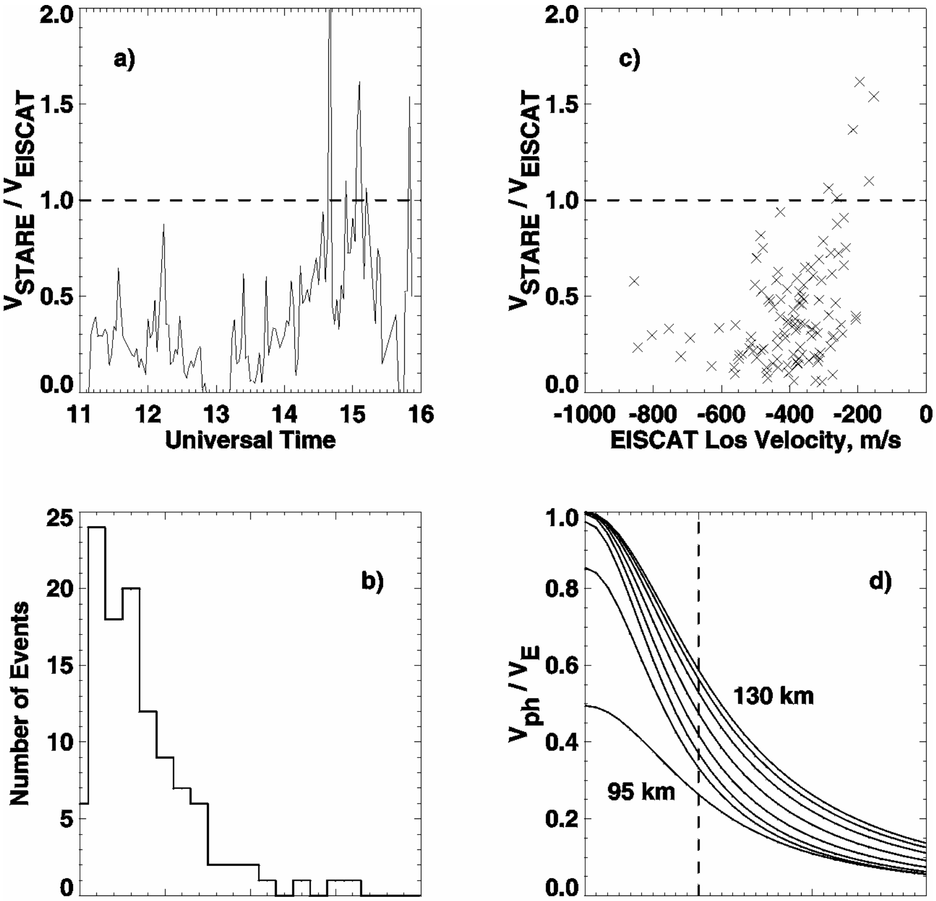

Figure 6.10 The observed STARE Finland radar velocities and linear theory expectations. (a) Ratio of the Doppler velocity to the EISCAT convection component $R_l=V_{STARE}/V_{EISCAT}$ for the whole period of observations at the EISCAT spot. (b) Statistics of R_l values. (c) Ratio R_l as a function of the convection component magnitude. (d) Ratio of the irregularity phase velocity (according to the linear fluid theory of electrojet irregularities) to the convection component as a function of the aspect angle. Curves are given for heights 95-130 km with 5-km step.

6.4.2 E/E comparison, range profiles

For the second period between 1400 and 1800 UT both STARE and CUTLASS echoes were received from the E region, and we explore these data in this section. Figs. 6.11a-d show data in the same format as in the F/E case of Figs. 6.7a-d. Again the STARE range coverage is more significant than the CUTLASS coverage. One can see that this time the CUTLASS echo regions are shifted more towards the radar than the STARE echo regions in agreement with enhanced E-region density in this case, compare with Fig. 6.4a. Interestingly enough, the maxima of the STARE power profiles are shifted (e.g., in Fig. 6.11a) to shorter ranges, where the geometric aspect angle conditions are not the best. This may indicate that a localized region with enhanced density was set up at these ranges. One can also notice a shift of the HF echo power maximum in Fig. 6.11a to slightly larger ranges in Fig. 6.11c which is consistent with the decrease in E-region electron density.

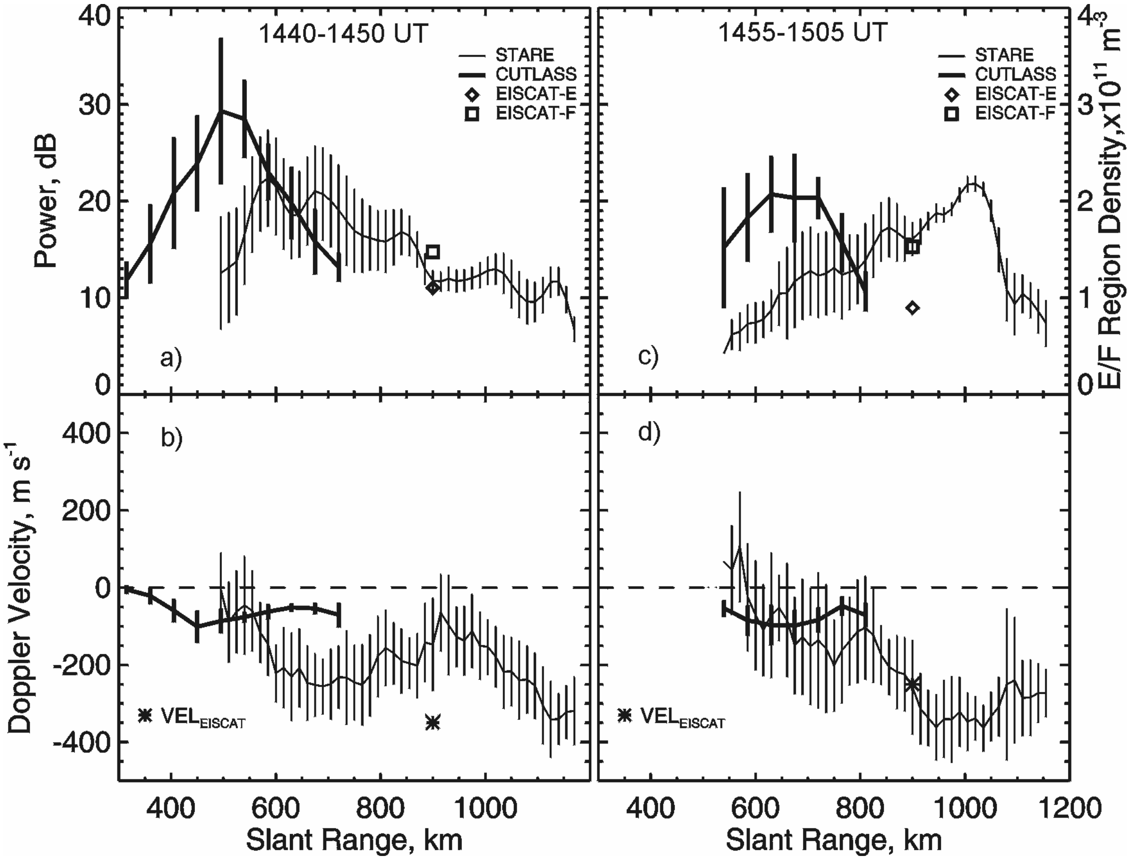

Figure 6.11 Similar to Figure 6.7 except for periods when both CUTLASS and STARE observed E-region echoes.

The STARE velocity profiles are very much similar to the previous case (Figs. 6.7b and 6.7d) in that the velocity decreases as the range decreases. The velocity magnitudes are small at short ranges, less than 100 m/s, but they exceed 200 m/sat farther ranges of ~700-800 km. At the range of the EISCAT measurements, the STARE velocity is smaller than the EISCAT convection component in the case of Fig. 6.11b and velocities are close to each other in the case of Fig. 6.11d. Contrary to the more or less monotonic decrease of STARE velocities at shorter ranges, CUTLASS velocities exhibit a clear maximum in Figs. 6.11b and 6.11d, and this maximum is located near the ranges of the CUTLASS power maximum. The CUTLASS velocities are roughly the same as the STARE velocities at the range of the CUTLASS power maxima. In Fig. 6.11d, the CUTLASS velocities are larger than the STARE velocities at several short ranges and smaller at large ranges.

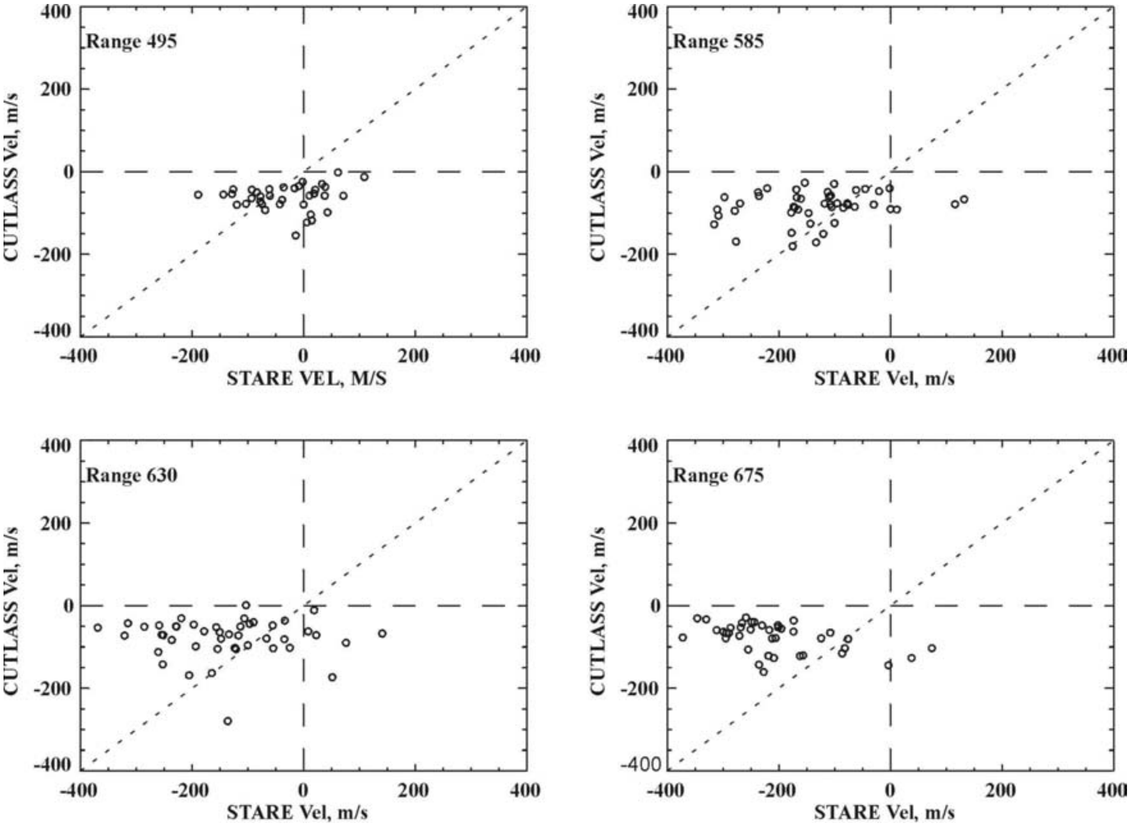

Figure 6.12 Scatter plot of Hankasalmi CUTLASS velocity versus Finland STARE velocity at several slant ranges for the period of 1400-1800 UT when both CUTLASS and STARE radars observed echoes from the E region.

Scatter plots of CUTLASS versus STARE velocities for some slant ranges are given in Fig. 6.12. One can see that points cluster around the bisector of perfect agreement, and departures both ways are possible. However, for most ranges (exceptions are shortest ranges, e.g. 495 km) the predominant trend is CUTLASS velocity to be smaller than STARE velocity.

6.5 Discussion

In this chapter we compared velocity data from CUTLASS (12.4 MHz) and STARE (144 MHz) coherent radar systems collected at Hankasalmi. We were able to check how the observed velocities are related with the plasma convection at one slant range where the EISCAT data were available.

6.5.1 Is STARE velocity a cosine component of convection?

Two distinctly different situations were encountered. First we considered the case for which the HF radar was observing echoes from the F region while the VHF radar was monitoring backscatter from the E region. For this situation, we had simultaneous EISCAT convection and electron density data, though at only one range of 900 km. Observed HF Doppler velocities were found to match reasonably well the EISCAT plasma convection component along the HF radar beam as discussed in Chapter 5. This result allowed us to assume that the observed CUTLASS velocity range profiles (for F-region echoes) corresponded to the range profiles of the convection component along this beam.

The central issue for the F/E comparison was by how much the VHF velocity differed from the "cosine" convection component. For observations along the electrojet (inside the FB instability cone), this question has been studied in a number of papers (e.g., Providakes et al., 1988; Haldoupis and Schlegel, 1990). There has not been so much focus on observations outside the FB instability cone. Up to now, the prevailing notion is that there is not much difference between these two velocities (Nielsen and Schlegel, 1985; Reinleitner and Nielsen, 1985; Nielsen et al., 2002) although Robinson (1993) seriously questioned the validity of the "cosine rule" for the STARE measurements. One should note that recent velocity statistics by Nielsen et al. (2002)

shows significant departures from the cosine law for some individual points (see their Fig.4, flow angle of +10^o) though the authors still make a conclusion that the VHF velocity varies according to the cosine law.

We employed two approaches to the problem, by comparing VHF and HF velocities at various ranges and by comparing VHF velocities with the EISCAT convection data at one range. In both cases we found that VHF velocities were considerably smaller that the convection component. Differences by a factor of ~3 were observed, especially at short ranges of ~700 km. One might expect this result on a basis of earlier studies (e.g., Kustov and Haldoupis, 1992; Kohl et al., 1992). We found that the velocity differences in our case were considerably larger than in Kustov and Haldoupis (1992) and comparable to the ones reported by Kohl et al. (1992) for several short periods of a rocket flight in the ROSE campaign.

One should mention that the F/E velocity comparison (for various ranges) has been made by neglecting the fact that HF and VHF scatter was actually coming from different heights. This means that there are some errors in a relative positioning of the STARE and CUTLASS echoes with range in Figs. 6.7a-d. The errors are of the order of one radar bin (André et al., 1996), i.e. 45 km. Inspection of range profiles given in Figs. 6.7a-d shows that this uncertainly does not change the above conclusion; the STARE velocities are smaller than the EISCAT plasma convection component in all close radar bins. To explore a potential impact of this effect on the data presented in Fig. 6.8, we compared VHF and HF velocities by considering HF data at one range bin farther than VHF data. For this comparison (appropriate diagrams are not shown here) again VHF velocities are smaller than HF velocities.

The reasons for the stronger VHF velocity depression effect in our case are not clear. One possibility is that, for our event, the double-pulse technique used in STARE measurements was not adequately describing the phase velocity of electrojet irregularities. Schlegel and Thomas (1988) reported on occasional significant differences between double-pulse and full spectrum methods of velocity determination. More study is needed on this issue.

Potential reasons for generally smaller VHF velocity as compared to the E×B velocity component outside the FB instability cone was discussed by Kustov et al.

(1990), Kustov and Haldoupis (1992) and Kohl et al. (1992). The first two papers proceeded from the idea that the auroral radar signal is collected from various electrojet heights, and at every height the irregularity phase velocity has a reduced value determined by the aspect angle of backscatter. The aspect angle variation for the irregularity velocity was taken into account by involving the liner fluid theory of the FB and GD instabilities. We illustrated the range of expected effect in Figure 6.10d and found it to be comparable with measurements. One should mention that kinetic effects (Schlegel, 1983) would further decrease values of the velocity ratio R_1 and thus provide even better agreement between the theory and measurements. For this reason, we believe that in our event the VHF velocity decrease (relatively to the EISCAT plasma convection component) for the directions outside the FB instability cone was associated with non-zero aspect angles ($>0.5^o$) of the STARE measurements.

Kohl et al. (1992) attempted to explain small STARE velocities outside the FB instability cone by involving the neutral wind that modifies the irregularity phase velocity, as predicted by the linear theory (described in Section 2.3) for the FB and GD instabilities. However, the required wind speeds were found to be several hundred meters per second, i.e. well above the typically measured ones so that this explanation needed further examination. For our event, between 1200 UT and 1400UT, MF radar measurements at Tromso (C. Meek, personal communication) showed wind drifts below ~80 m/s and quite variable in time so that application of this idea to the STARE data does not look promising.

One should mention that our conclusion on the agreement between the linear theory and measurements is in some contradiction with an earlier study by Nielsen (1986) who reported a much slower rate of velocity decrease with the aspect angle. However, one should bear in mind that Nielsen (1986) considered observations mostly along the electrojet where plasma turbulence might play strong role in setting up enhanced electron collisions. Ogawa et al. (1982) reported a slower rate of velocity decrease not only along the flow but at large flow angles as well though these authors related the latter effect to the latitudinal variations of the background electric field. Kustov et al. (1994) considered observations at large flow angles but at aspect angles of several degrees and also found slower rates of decrease.

An alternative explanation of the too small VHF velocities outside the FB instability cone is the violation of the cosine rule the irregularity phase velocity (i.e., one might question whether the cos θ term in the linear theory formula is applicable to STARE observations). To date, there are not much data in the literature that would support this notion. In the past, Reinleitner and Nielsen (1985), Nielsen and Schlegel (1985) and Nielsen et al. (2002) reported on reasonable performance of the cosine rule for the STARE drift velocity directions while Kustov et al. (1997) drew a similar conclusion for the Canadian observations at very large aspect angles. We showed that for our event (Fig. 6.4b), that STARE convection azimuth (inferred through merging of Finland and Norway velocities by the standard "stereoscopic" technique (Greenwald et al., 1978; Nielsen, 1989)) agrees well with the EISCAT observations. Though this result is expected on the basis of previous observations mentioned earlier (e.g., Nielsen and Schlegel, 1985), in our case it is still a surprise since a much stronger, than usual, velocity decrease with respect to the plasma convection was observed by the individual STARE radars. A reasonable agreement between the total STARE irregularity drift velocity directions and the EISCAT measurements in our event perhaps indicates that VHF velocity is proportional to the cosine of the flow angle and the observed small velocities are related to other factors, most likely due to the aspect angle effects, as we explained above.

If one interprets smaller VHF velocities as the aspect angle effect, then our measurements indicate that the VHF velocity decrease with the aspect angle for irregularities propagating outside the FB instability cone is significant for quite a range of aspect angles since decreased STARE velocities were seen at all ranges along beam 4. This means that the convection estimates by the standard merging technique and by the IAA technique of Nielsen and Schlegel (1985) (this method also assumes that Doppler velocity outside the FB cone is simply the cosine component of the flow angle) should deteriorate as one considers measurements at the equatorward and westward portions of the STARE field of view where the aspect angles can be as large as -2°.

6.5.2 Why are the STARE and CUTLASS E-region velocity profiles so different?

The second case in our event was when both VHF and HF echoes were received from the E region. In this case, the HF echoes occurred only at short ranges where, unfortunately, no EISCAT convection measurements were available. For the E/E comparison, results were quite complicated. The HF echoes were typically observed at shorter distances, by as much as 150-200 km, and at some moments, the HF and VHF echoes were spatially located at so different ranges that comparison of their parameters was impossible. One unfortunate situation was when the electron density (according to the EISCAT measurements) was enhanced, the HF echo band was centered at distances of 500 km or less where no STARE measurements were carried out (first range is 495 km). The STARE range profiles were not as sensitive to density changes. Such contrast between VHF and HF response to these electron density variations is expected (Uspensky et al., 1994).

For the cases with reasonable spatial overlap of STARE and CUTLASS echo bands, we found that generally velocity relationship depended on a relative position of the HF and VHF echo power maxima so that the VHF and HF velocities can either be comparable or quite different. At shorter distances usually VHF velocity was smaller than HF velocity while at larger distances it was the other way around, HF velocity was smaller than VHF velocity (here and below when we say velocity we mean the velocity magnitude). It is then not a surprise that when HF and VHF velocities were compared for the same ranges and time, Fig. 6.12, there were point deviations both ways, VHF velocity was larger than HF velocity for some measurements and less than HF for other measurements. One should note that Davies et al. (1999) reported that the CUTLASS velocities were typically smaller than the E×B component along the HF radar beam (their Fig. 5). This result agrees with our finding. Koustov et al. (2001a,b) and Makarevitch et al. (2001) also reported smaller HF velocities as compared to 50-MHz velocities for large flow angles. They typically had the situation with HF/VHF data overlapped at far HF ranges (in the present study for such a situation we also had smaller HF velocities).

To explain VHF and HF velocity relationship, one has to keep in mind several circumstances. First of all, the range profile of the VHF velocity is determined by two major factors, variation due to aspect angle and a change of the background electric field with latitude (range). The aspect angles are worse at shorter ranges leading to a VHF velocity decrease as explained above. One might expect additional decrease of the VHF velocity because of, perhaps, the lower heights (than usual 110 km) of VHF echoes at shorter ranges since the aspect angles are better at the bottom of the electrojet layer. At lower heights, collisional effects might decrease the irregularity phase velocity (Uspensky et al., 1994). We should note that the EISCAT measurements showed low electron densities below ~105 km minimizing the chance for this effect to happen. In addition to the above plasma physics' decrease of the VHF velocity at short ranges, one might expect that electric field also decreases equatorward of the auroral oval (Rich and Hairston, 1994).

For the HF velocity, the range profiles are more difficult to explain. As a starting point, one can follow Uspensky et al. (1994) who assumed that the observed HF velocity can be described by the linear theory formula and assumed that received HF signal comes from a wide range of heights. Then the range profiles should have a maximum of the power matched with the maximum of the velocity. These maxima correspond to that part of the ionosphere where the aspect angles are around zero roughly at the center of the electrojet. At distances shorter and farther away from this range of the power and velocity maximum, the HF velocity decreases, especially quickly at shorter ranges, due to the aspect angle effect.

In this way, one can explain the relative variations of the HF velocity with range, but there is still a problem with absolute values of expected velocities (unless special electron density profiles are assumed). At the range of the velocity maximum, Uspensky et al.'s (1994) model predicts only small difference between HF velocity and the convection velocity ($V_{HF} \cong 0.8\ V_E$). In observations, the differences were probably stronger; we concluded that the VHF velocity was greatly reduced by more than a factor of 2 with respect to the convection velocity at the range of the HF velocity maximum ($V_{VHF} < 0.5V_E$ at the EISCAT spot). Since VHF velocity is about the same as HF velocity at the maximum, one has to conclude that the HF velocity magnitudes were more than 3 times smaller than the convection velocity ($V_{HF} < 0.3\ V_E$). This implies that the simple approach, proposed by Uspensky et al. (1994), does not work in our case. We suggest that perhaps the linear theory formula does describe properly the aspect variation (trend) of the HF velocity, but not the absolute values. If this statement is correct, then one can explain the larger (smaller) HF (VHF) velocities at short (far) distances as a result of the aspect angle effect, similar to Uspensky et al. (1994). We should note that smaller HF E-region velocity as compared to the E×B velocity was explained in the past by using the idea that the irregularity velocity can be modified by the background plasma gradients (e.g., Hanuise et al., 1991). This explanation is not applicable to our observations since the coherent radar measurements were carried out outside the FB instability cone.

One might think that neutral winds modified seriously the observed HF and VHF velocities, as Kohl et al. (1992) stipulated. Neutral wind might affect both HF and VHF velocity as discussed in Section 2.1. Since at the range of HF echo power maxima the aspect angles of VHF echoes are worse, the neutral wind is expected to affect VHF velocities strongest since the neutral wind effect in velocity is significant for irregularities propagating/observed at large aspect angles (Makarevitch et al., 2002a). For the period 1400-1500 UT in our event the predominantly westward neutral wind of ~ 80 m/s was observed at the electrojet heights of ~106 km (C. Meek, personal communication, MF radar observations at Tromso). Such a wind would provide an additional component (less than 80 m/s) to the VHF velocity on a top of the component provided by the electric field-related particle motions (consider the ion contribution to the irregularity phase velocity according to the linear theory formula, Section 2.3.3). This would mean that the observed VHF velocities corresponded actually to a smaller V_E (some Doppler shift is due to neutral wind) and consequently the difference between observed HF velocities and V_E is not as large as we just concluded.

Another effect potentially contributing to low HF velocities (as compared to V_E) can be the HF echo contamination by low-height scatter. We performed ray tracing analysis for some intervals of the 12 February 1999 event and showed that echo reception from the D-region heights is very likely for the period under discussion. Here we make a more elaborate ray tracing analysis. In Fig. 6.13 we show three electron density profiles measured by EISCAT during the period of E/E comparison and corresponding ray-tracing diagrams. Here two neighboring ray paths differ in 2^o of elevation angle with overall range of angles between 6° and 30°. For ray tracing calculations, the EISCAT electron densities were scaled down by a factor of 2 for the following reasons. First, for smaller densities, there is a reasonable agreement between prediction of the E-region echo ranges and measurements. Second, the Sodankyla ionosonde observing at similar magnetic latitude as the location of echoes showed about 2 times smaller densities. Also, an electron density decrease equatorward the auroral oval is well expected (e.g., Rino et al., 1983). One can conclude from Fig. 6.13 that low-height echoes are very likely.

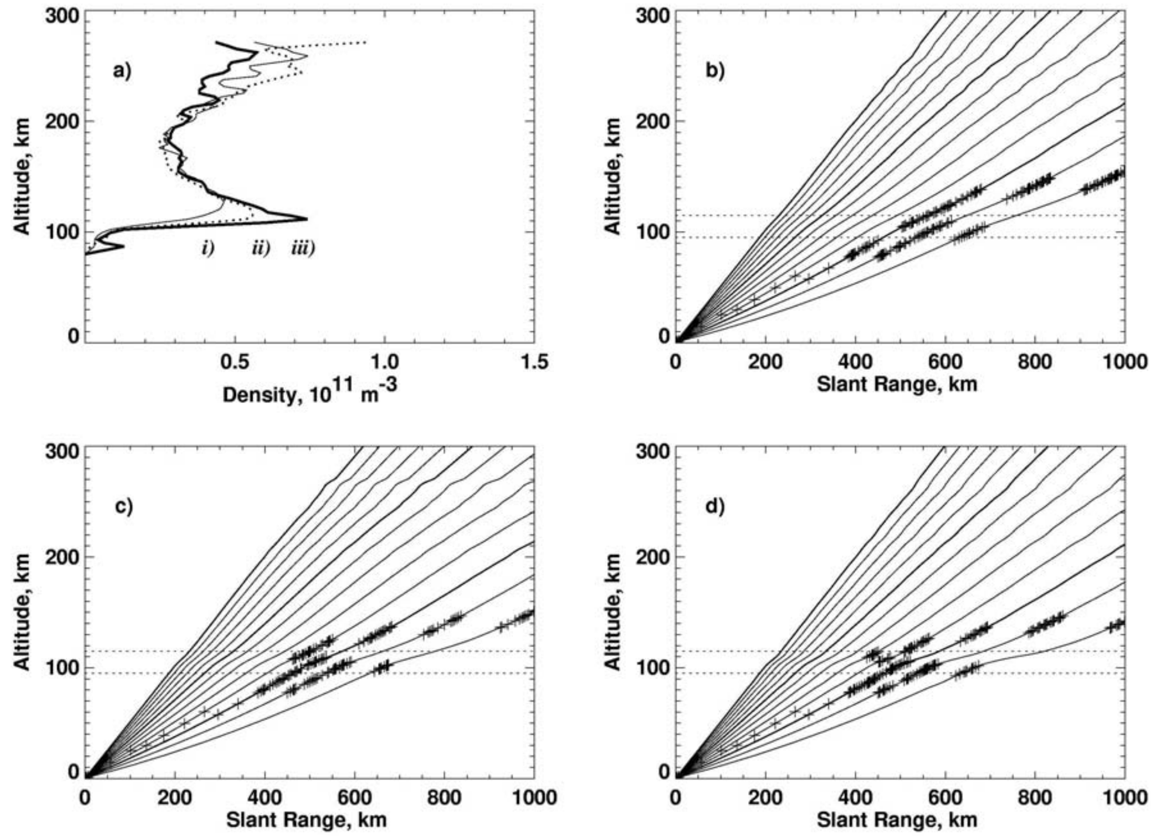

Figure 6.13 (a) Three electron density profiles measured by EISCAT at 1450 UT (case (i)), 1410 UT (case (ii)) and 1430 UT (case (iii)) and (b) –(d) possible ray paths for 12.4-MHz radar waves at Hankasalmi, Finland. The ray paths are shown in elevation angle step of 2° for the elevations between 6° and 30°. Crosses indicate ranges where the aspect angle of the ray with the Earth magnetic flux line is less than 1°. Horizontal dotted lines indicate the electrojet irregularity layer between 95 and 115 km.

If HF echoes were indeed strongly affected by scatter from the bottom of the electrojet layer, or even from the D region, then one might expect two effects. First, there could be some wind contribution to the observed HF velocity. For the event under study, a south-east wind of up to 50 m/s was observed below ~100 km over Tromso. If the electric field were oriented northward (as it was at near Tromso) then one would expect the neutral wind contribution to the irregularity phase velocity to be of opposite polarity than the electric field contribution. Thus the neutral wind can decrease the HF velocity by perhaps ~20-30 m/s. This is an additional factor in decreasing of HF velocities (with respect to V_E). The other effect is a possibility of decameter irregularities formation due to wind-related plasma instabilities (Kagan and Kelley, 1998; 2000). For such instabilities the irregularity phase velocity is not so strongly controlled by the electric and magnetic fields as in the case of pure FB or GD waves. The thermal instability considered by Dimant and Sudan (1995a,b,c, 1997) might be of importance as well. A further check on feasibility of both above explanations requires detailed information on the electric field magnitude and orientation plus the wind distribution in the D region /bottom E region which are not available.

Finally, we would like to mention that a seemingly easy task of VHF-HF comparison is quite difficult in practice. In searching for appropriate events, we noticed that quite often only either CUTLASS or STARE echoes were observed, but not both. This effect is evident even for the data presented in this study. In Fig. 6.4c one can see that strongest HF echoes occurred around 1300 UT. At this time, the VHF echoes almost completely disappeared, Fig. 6.4a, probably in response to general decrease of both the ambient electric field and electron density, but perhaps other factors are involved. Chaturvedi et al. (1994), by analyzing excitation of the GD irregularities in electrically coupled E and F layers, concluded that there might be inter-relation between excitation processes in the E and F regions, when one of the layers is strongly inhomogeneous. In our case, E layer was undergoing quick changes (around 1300 UT), which might have been boosted the GD instability in the F layer. Such processes might affect the phase velocity of irregularities, but more data are needed to discuss these issues.

6.6 Summary

In this chapter we obtained several new results. The comparison of the CUTLASS (HF) and STARE (VHF) velocities for observations in the E region showed that the HF velocity can be smaller than, equal to or larger than the VHF velocity, depending on the range of the comparison. At short (far) ranges, the HF (VHF) velocity magnitude is typically larger than the VHF (HF) velocity magnitude. For intermediate ranges, where the HF power and velocity magnitude are at maxima, the HF and VHF velocities are comparable. The observed velocity differences can be explained by different amounts of radio wave refraction at VHF and HF, so that at short (far) ranges the aspect angles of STARE (CUTLASS) observations are worse. In such an explanation it is assumed that STARE echoes originate from irregularities produced by the FB and GD plasma instabilities in a broad range of electrojet heights. Contrary to pure electrojet nature of the VHF echoes, the HF echoes are perhaps strongly contaminated by scatter from heights of less than 100 km, where the neutral wind might be contributing to irregularity excitation and HF velocity modification. We also consider a possibility of decameter irregularity generation by purely neutral wind related instabilities (that should give irregularities with low phase velocities), though no data are presented to substantiate this suggestion.

We showed that the STARE Finland double-pulse velocities, for observations outside the FB instability cone, can be 2-3 times smaller than the E×B convection along a radar beam for significant periods of time (1-2 hours). The effect is expected to be more pronounced for short slant ranges of <700-800 km where the aspect angles of measurements are the worst possible. Strongly reduced double-pulse velocities outside the FB instability cone were also observed by the STARE Norway radar at the range of the EISCAT CP-1 spot. In spite of significantly decreased double-pulsed STARE velocities as compared to the convection magnitude (measured by EISCAT), application of the standard STARE merging procedure gives reasonable estimate of the convection azimuth, the property known for the periods when the velocity outside the FB instability cone is a cosine component of the convection (e.g., Reinleitner and Nielsen, 1985). This perhaps means that the phase velocity of meter-scale irregularities outside the FB cone is proportional to the cosine component of the convection velocity, as predicted by the fluid linear theory of the FB and GD instabilities. The effect of strong velocity decrease (as compared to the convection component) can be explained by the non-zero aspect angles of STARE radar measurements, especially for the Finland radar measurements at short ranges of observations. The above results mean that STARE double-pulse convection estimates using not only standard merging technique but also the IAA approach (Nielsen and Schlegel, 1985) can deviate significantly from the true convection, especially for predictions at the equatorial and western edges of the STARE field of view. The expected deterioration of the quality of STARE convection estimates still needs verification by independent measurements.

CHAPTER 7

DOUBLE-PEAK NATURE OF E-REGION HF ECHOES

By looking at joint 12-MHz HF and 50-MHz VHF data, Makarevitch et al. (2002b) showed that HF echoes could be of two types, the high- and low-velocity echoes. For the high-velocity echoes, the HF Doppler velocity was close to the simultaneously observed 50-MHz velocity, which is believed to be a cosine component of the ExB drift (e.g., Ecklund et al., 1977). For the low-velocity echoes, the HF Doppler velocity was two and more times less than the 50-MHz velocity. The data presented in Chapter 6 indicated that the velocity of HF echoes is less than the ExB drift component. These observations perhaps correspond to the case of low velocity HF echoes of Makarevitch et al. (2002b). Since two distinctly different types of HF echoes can occur, at least at different times and locations, one generally might expect their occasional simultaneous occurrence, especially in view that the high- and low-velocity echoes were interpreted as scatter from different ionospheric heights but due to the same source (the FB and GD plasma instabilities). Signatures of backscatter from different heights can be found in the shape of Doppler spectrum, as known from VHF research (e.g., Whitehead et al., 1983).

In this chapter, we study the spectra of E-region HF echoes using data gathered by the Hankasalmi HF radar. To achieve better resolution, we employ the Burg spectral method described in Chapter 3. We concentrate on several periods of E-region scatter.

Results presented in this chapter were reported by Danskin et al. (2002, 2003) and submitted for publication in Radio Science.

7.1 Experiment setup and event description

We consider CUTLASS Hankasalmi radar observations on 12 February 1999 (1400-1600 UT), 11 February 1999 (1400-1800 UT) and 3 September 1997 (0200-0400

UT) with the first two periods being our main focus. For the first period the data were explored in the two previous chapters where we compared HF velocities, VHF velocities and the EISCAT convection measurement and concluded that HF velocities were much smaller than the cosine component of ExB plasma convection. We suggested that perhaps HF echoes were significantly affected by the scatter from the bottom of the electrojet where the decameter irregularity velocity can be significantly depressed by collisions and, in addition, we anticipated a possibility of other neutral wind related instabilities. Our analysis of 11 February 1999 period in a manner similar to the previous chapter confirmed its major conclusions. For both events no additional evidence on the importance of the lower ionosphere were found. It is natural to take a closer look at the HF Doppler spectra for these specific events. The third event was chosen just to have significantly different period of observations.

Details of the experiment for the first two events can be found in Chapters 4, 5 and 6 with the layout of the experiment being presented in Fig. 6.1. Data from beam 5 were mostly explored in this study, since it overlooks the region (at a range of 900 km from the HF radar site) where the EISCAT electron density and electric field measurements were performed. Even though the typical ranges of E-region echoes were ~ 600 km, the EISCAT information is valuable for various estimates. We concentrate in this study on observations between 1400 and 1800 UT, equivalent to 16 - 20 MLT at the location of EISCAT. On 3 September 1997 the CUTLASS Finland radar worked in the standard 2-min scan mode.

To give an example of typical slant-range distribution of short-range CUTLASS echoes, we show by dots in Fig. 7.1 the times when ionospheric echoes were observed for the 12 February 1999 event, beam 5. Fig. 7.1 is another form of presenting the CUTLASS occurrence data of Fig. 6.2. In Fig. 7.1, the echoes are seen almost all the time although in quite different bands. Between 1000 and 1400 UT two echo bands are evident, one around 1000 km (band I) and the other one at 1800-2000 km (band II). These are F-region echoes received through direct and $1\frac{1}{2}$F propagation paths, respectively (Chapter 4). This mode identification is supported by general echo statistics (Milan et al., 1997a), by the angles of echo arrival estimates, and by ray tracing based on electron densities profiles measured by EISCAT (Section 4.4.3). Band II corresponds to scatter near the cusp/cleft region. After 1400 UT, a band (III) of E-region echoes was predominantly seen at much shorter ranges, typically 400-700 km with a slow displacements of the echo band in the north-south direction. According to the interferometer measurements, these were E-region echoes (Chapter 6). Similar mode identification has been performed for two other events.

In Fig. 7.1, we indicate the times for detection of multi-peak spectra by small vertical lines. The length of the lines reflects the separation between 2 major peaks in each spectrum (note the scale at the bottom of the diagram). Consistent with Schiffler et

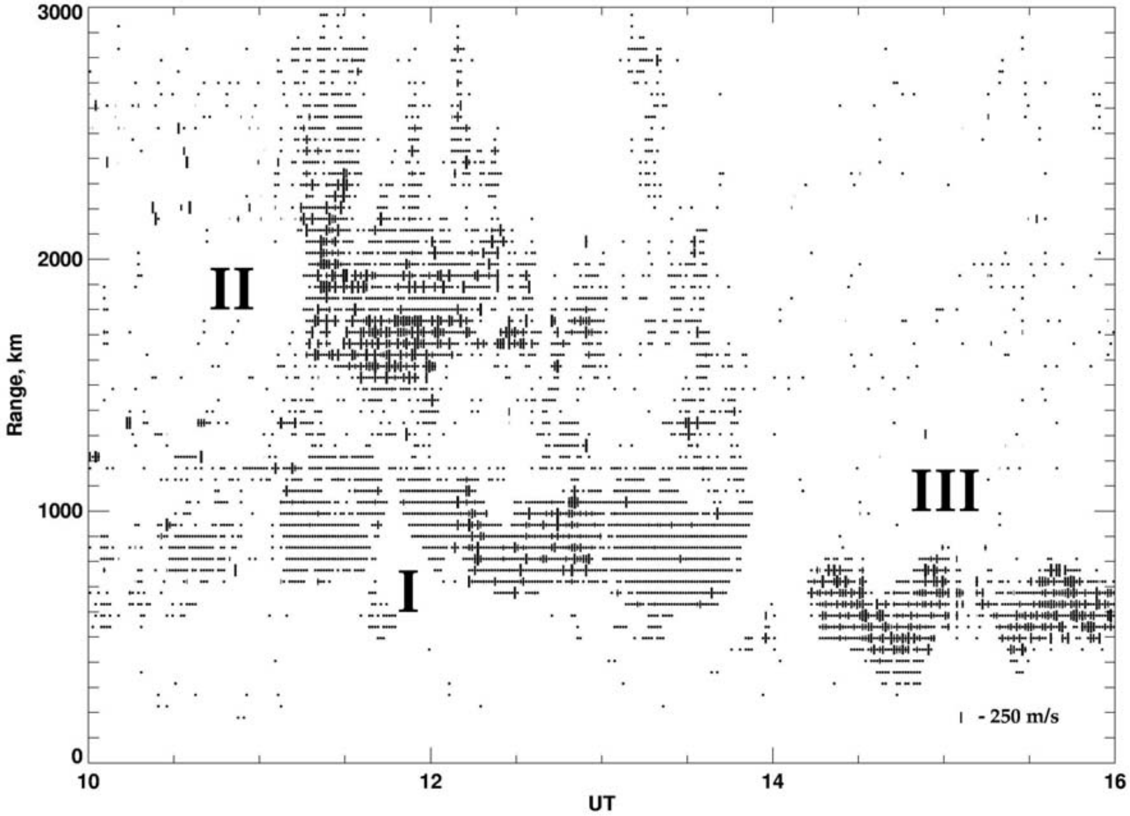

Figure 7.1 Range-time plot of ionospheric echo occurrence for the CUTLASS Finland radar beam 5 on 12 February 1999. Each dot corresponds to an event at the specified range gate. Labels I, II, and III indicate the echo bands of the direct F-region, $1\frac{1}{2}$ F and direct E-region echoes, respectively. Vertical lines denote times and ranges of double-peak echo detection. The length of the line reflects the separation between the peaks according to the scale in the lower right corner.

al. (1997) and Huber and Sofko (2000), the far-range cusp/cleft related echoes (band II) have a significant number of double-peaks. There were some, not significant, double peak presence within the band I of the F-region echoes. For band III, E-region echoes after 1400 UT, the most remarkable feature is double-peak nature of many of these echoes, and this feature is the main goal of the present study.

7.2 Range variation of HF spectra (12 February 1999 event)

Fig. 7.2 gives an example of spectra observed at 1430 UT in several range gates of beam 5. The thin line shows the standard FFT spectra while the smoother heavier line represents the Burg spectra. The vertical dotted line is the velocity estimate from FITACF. The spectra are normalized so that the maximum peak has a value of one. In the upper left corner of each panel the range of the gate is given. In the bottom right corner from top to bottom are the power in dB, the Doppler velocity in m/s and the spectral width in m/s from FITACF. In the upper right corner, the Doppler velocities for either the single- or double-peaked Burg spectrum are given.

Looking at the spectra at various gates, one can see that they are single-peaked at the near ranges of 450, 495, and 540 km. Their mean Doppler shift increases with range with all three methods giving consistent results. The spectra at the next three ranges are distinctly double peaked. Clearly, the low-velocity (high-velocity) peaks have a velocity below (above) the typical mean velocity of shorter-range single-peak spectra and below (above) the mean Doppler velocity determined through the FITACF method (FITACF velocity). The shifts of both the low- and high-velocity component changes with range; the shift of the high-velocity component increases while the shift of the low-velocity component does not have a clear trend. The double-peaked structure of the spectra is not recognizable at 720 km, although two velocity values are given in the top right hand corner of the relevant panel. The spectrum is single-peaked at far range of 765 km. The Doppler shift of this spectrum is of the order of the low-velocity components detected at shorter ranges.

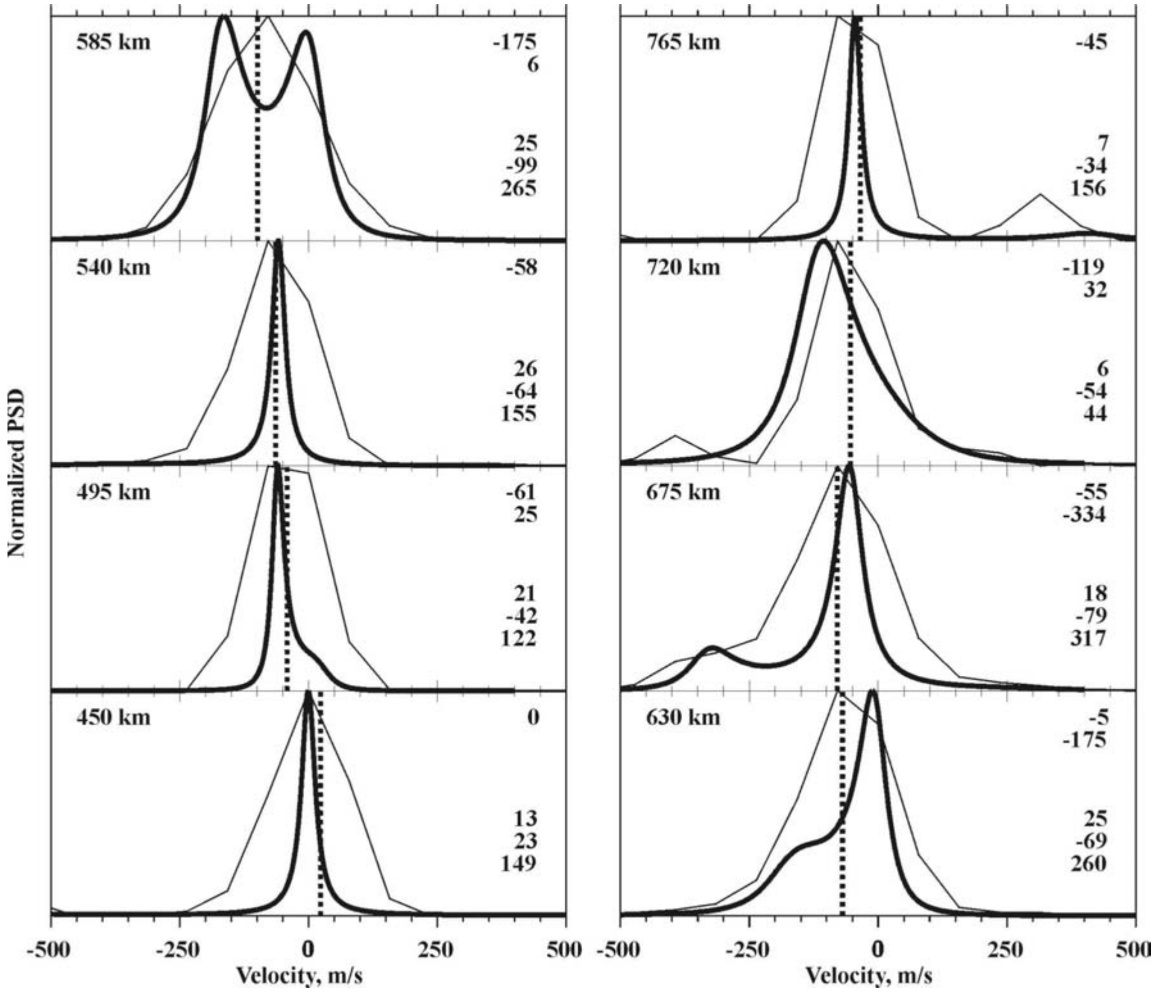

Figure 7.2 Standard normalized power spectral density for various range gates along beam 5 by FFT (thin line) and Burg spectrum (heavy line) methods at 1430 UT on 12 February 1999. The vertical dotted line is the FITACF velocity estimate. The numbers in the lower right corner of each panel are (from top to the bottom) power in dB, FITACF velocity in m/s and width in m/s. The numbers in the upper right are the one or two velocity estimates as estimated by Burg's method.

Fig. 7.3 presents further examples of the spectra, on this occasion observed at 1450 UT. For this period, the echoes were seen at larger ranges and the power of echoes maximized around 630 km as opposed to 540 km in the case of Fig. 7.2. The morphology of the spectra change with range is very similar to the data presented in Fig. 7.2. One can see single-peak spectra at short ranges of 540 and 585 km, followed by double-peak spectra at 630-765 km. The very last spectrum at 810 km also has 2 peaks, but the second one is of low intensity and is way off typical velocities one would expect

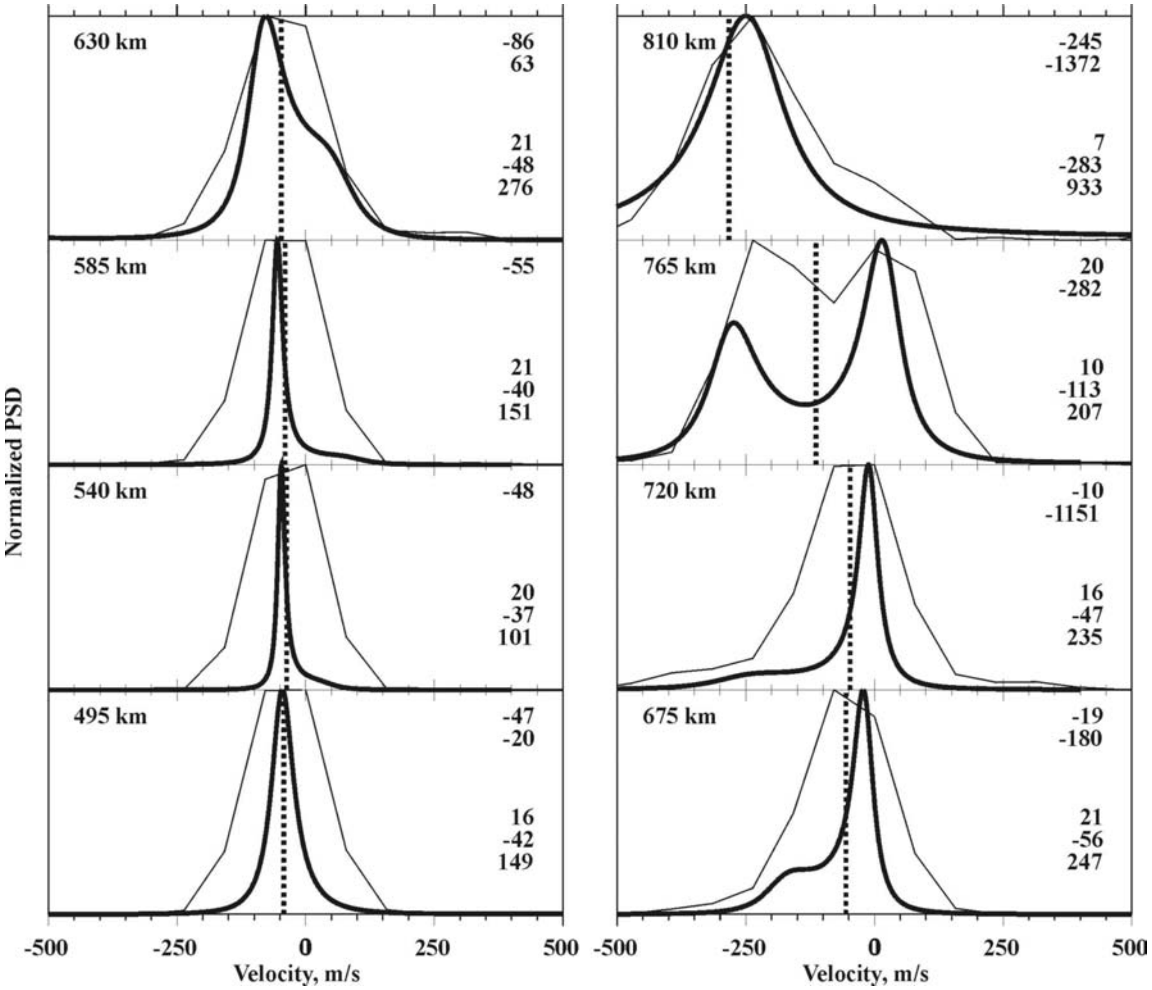

Figure 7.3 Same as in Figure 7.2 but for 1450 UT on 12 February 1999.

for the period under study. Again the Doppler shift of the low-velocity (high-velocity) components is below (above) the FITACF shift and below (above) the Doppler shifts of short-range echoes.

Other spectra observed between 1400 and 1600 UT show very much similar pattern of the double-peak spectra onset (though not always). Close inspection of band III in Fig. 7.1 shows that double-peak spectra occur typically in the middle part of the echo band and quite often they may be seen at the farthest ranges as well.

7.3 Azimuthal distribution of double-peak echo occurrence

The data presented in Figs. 7.2 and 7.3 refer to one beam/direction of observations. A natural question is whether the above morphology of double peak occurrence is typical for other directions. In Fig. 7.4 we present data for several Hankasalmi radar scans. Panel (a) shows the scan whose data from beam 5 were reported in Fig. 7.2. Panels (b) and (c) show data from 11 February 1999. Panel (d) presents data for the 3 September 1997 event. All 4 diagrams indicate that double-peak echoes occur predominantly in the middle part of the echo band in all beams; echoes are typically single-peaked at the closest and farthest ranges of the bands. In panel (a), most of the echoes are within the ranges of 450-620 km with an absence of double peaks in the western corner of the echo band at farthest ranges. In panel (b) the echo band stretches in

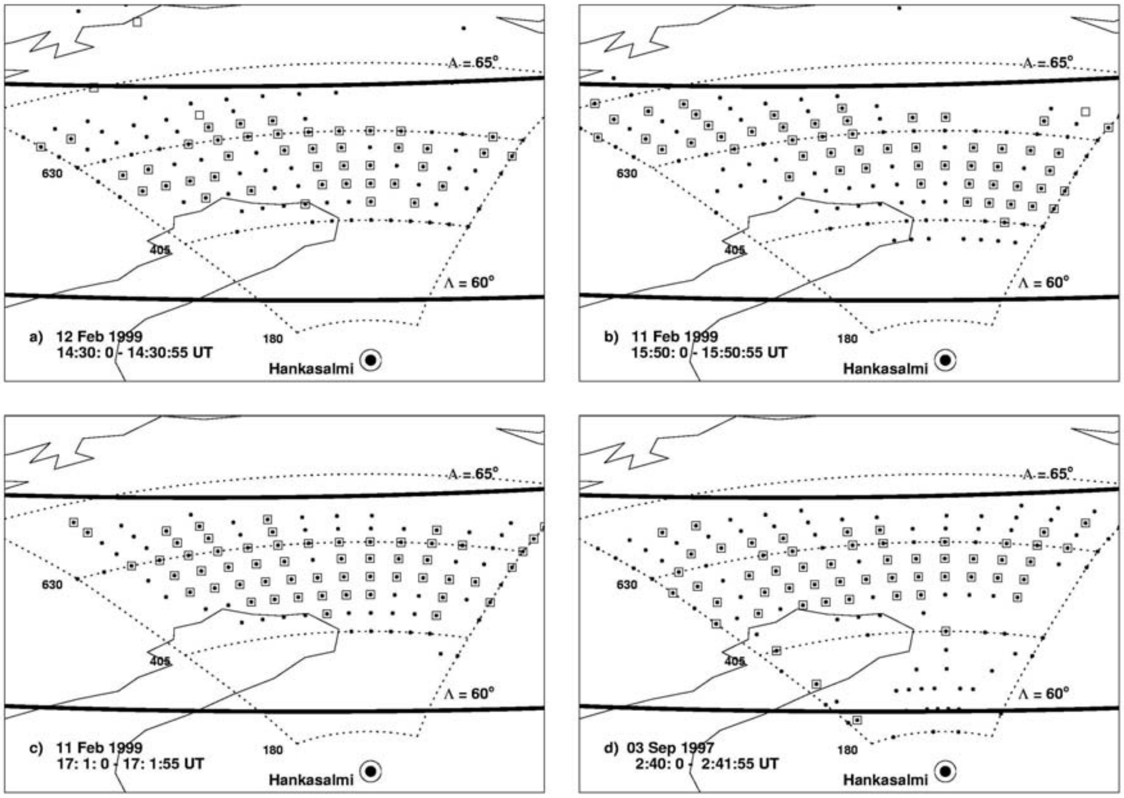

Figure 7.4 Radar scans showing the occurrence of echoes (dots) and the presence of double peaked echoes (squares). Times as noted. Also shown are the PACE lines of equal magnetic latitudes of Λ = 60° and Λ = 65°.

the southeast direction with double peaks at far ranges of the most western beams and at lower ranges in the eastern part of the scan. In our opinion, such a pattern in echo occurrence is formed because of the non-uniform electron density distribution over the scanned area so that the density is enhanced in the eastern part of the radar's field of view. If one looks at ranges ~585 km one can see that single-peak echoes in the western part of the scan are changed to double-peak echoes in the eastern part of the scan. Both panels (a) and (b) seem to hint on the absence of L-shell alignment for double-peak occurrence. The effect is more obvious in panels (c) and (d) where as one goes in the clockwise direction for the farthest ranges, the double peaks occurrence in western beams is changed to the single peaks occurrence in central beams.

To assess how often the double-peak spectra occur, we examined the data in all beams for all three events of 11 and 12 February 1999 and 3 September 1997. A total of ~50,000 spectra for echoes at ranges below 855 km were considered. We found that double-peak spectra present in about 35% of cases. This value varies from one radar beam to another, see Table 7.1. Clearly, double-peak spectra are more frequent in central beams with slightly stronger decrease for lower beams.

7.4 Some statistics for the velocity of peaks

In terms of the velocity separation between the peaks, Fig. 7.1 has minor deficiency in that one cannot recognize cases with small peak separation. This diagram also does not indicate the exact velocities associated with double peaks. Data in Figs. 7.2 and 7.3 have this information but present only two individual events for one beam. To give more quantitative ideas on what is typical for double-peak spectra in terms of the velocity, we present some statistics.

One important issue is the typical mean (FITACF) velocities for the double-peak spectra. Fig. 7.5 shows statistics of FITACF velocities corresponding to double-peak spectra in all three E-region events. Data in all beams and ranges < 855 km were considered. One can see that for beam 1, closest to the L-shell direction, typical velocity magnitudes are 100-200 m/s. The velocity magnitudes are obviously smaller for beams 5

Table 7.1 Percentage occurrence of double-peaked echoes for different beam directions.

Beam	E-Region Events	Double Peaks Occurrence
0	2524	21%
1	2664	26%
2	2731	32%
3	2933	35%
4	3056	37%
5	3186	39%
6	3301	39%
7	3255	39%
8	3287	39%
9	3316	38%
10	3310	37%
11	3299	36%
12	3247	34%
13	3220	35%
14	3179	33%
15	3159	33%
All	49667	35%

and 10, and there are quite a few echoes with positive velocities in beam 14, in the eastern part of the radar field-of-view. This feature perhaps reflects the fact that FITACF velocity changes with flow angle, as reported in other studies, e.g. Jayachandran et al. (2000).

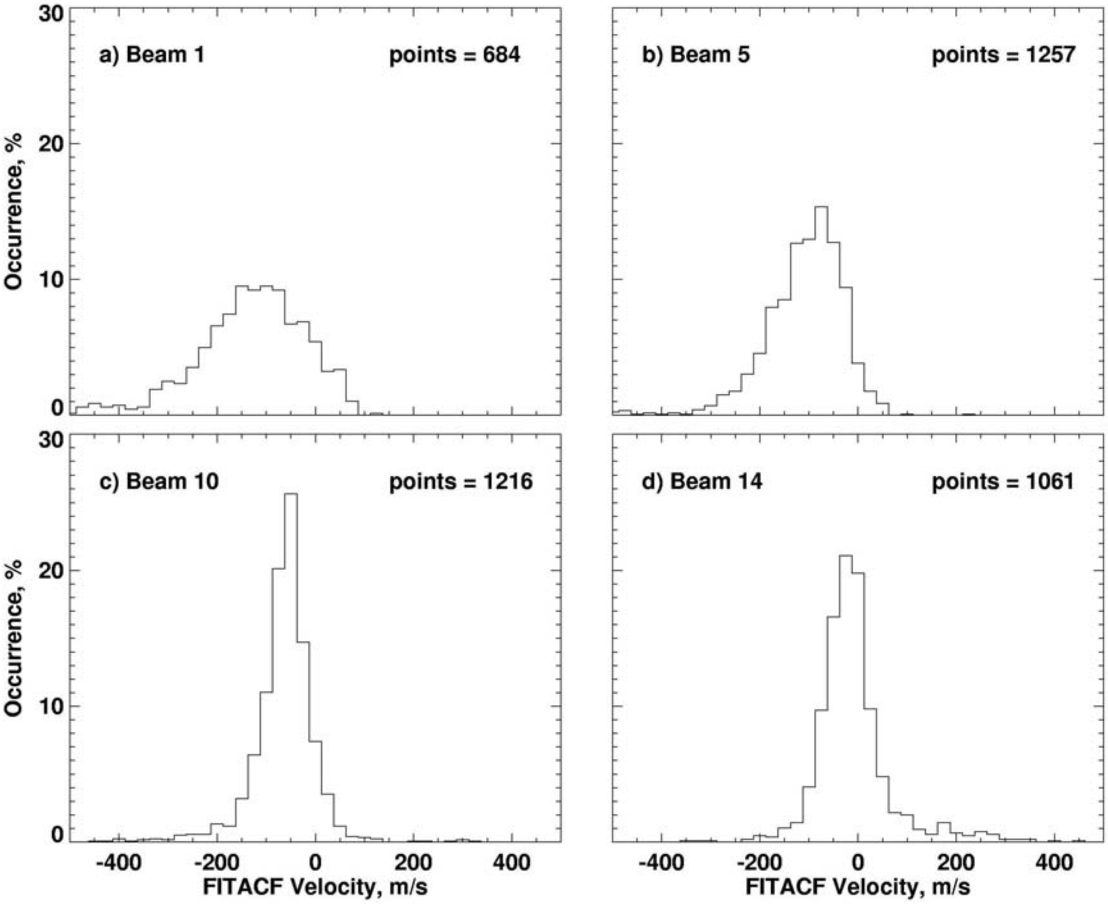

Figure 7.5 Distribution of FITACF velocities for beams 1 (a), 5 (b), 10 (c) and 14 (d) for the three periods of study when double peaked spectra were detected.

The next issue is about the typical peak separation. Fig. 7.6 gives the distribution of the peak separation for spectra detected in beams 1, 5, 10 and 14. Those peaks that were separated by more than 400 m/s were not included in the statistics. (beyond a separation of 400 m/s, the standard FITACF method would easily resolve one of these peaks). One can see the typical spectral component separations are between 120 and 180 m/s although the maximum is not pronounced. There is a tendency for the peak of the distributions to be clearer for observations in beams 10 and 14. Also, a comparison of overall velocity possible for low- and high-velocity components (velocity spread) did not show significant differences. The low-velocity components were within the range of –200 to +200 m/s. The high-velocity components occupied the range of –400 to –50 m/s.

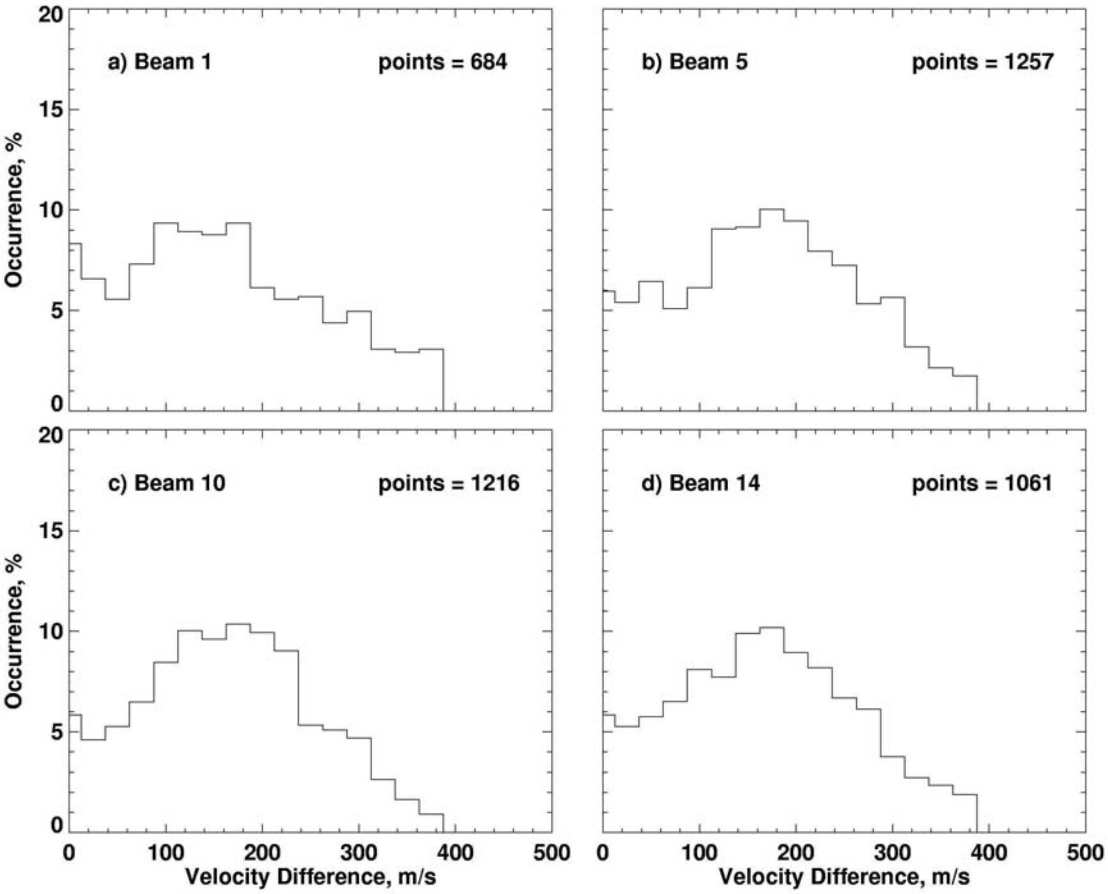

Figure 7.6 Statistics for the velocity difference of peak separation for double peaked spectra from beams 1 (a), 5 (b), 10 (c) and 14 (d).

An important question is how the velocities of the peaks are related to the FITACF velocity since the FITACF velocity is used for plasma convection estimates (Ruohoniemi and Baker, 1998). Fig. 7.7 gives the distribution of low- (blue crosses) and high-velocity (red diamonds) Doppler shifts versus the corresponding FITACF Doppler shift. Fig. 7.7b confirms statistically for beam 5 that the “resolved” components of the spectra have shifts above and below Doppler shifts of unresolved spectrum. Figs. 7.7a, c, and d show data for radar beams 1, 10 and 14 (other orientations) in the same format.

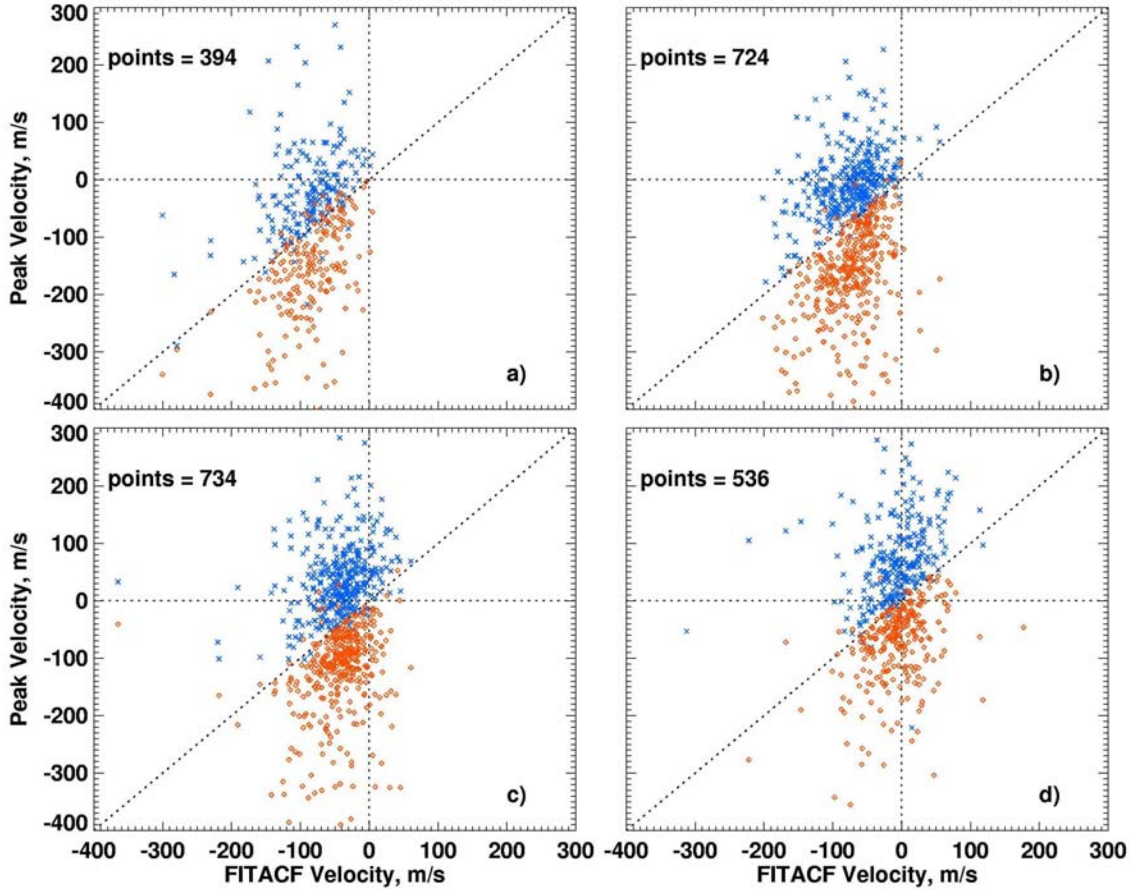

Figure 7.7 Doppler shifts in m/s of low- (blue crosses) and high-velocity (red diamonds) components of the double-peak spectra versus unresolved FITACF velocity for the CUTLASS Finland radar beams 1 (a), 5 (b), 10 (c) and 14 (d). Numbers indicate the volume of statistics.

The low- and high-velocity components change in accord with a general decrease of the FITACF velocity as the beam number increases. The FITACF velocity decrease is expected due to the orientation of the beam being more perpendicular to the direction of the electrojet. With increase in beam number the low-shifted components assume more frequently an opposite polarity as compared to the high-velocity components.

7.5 Double peaks and spectral width

The presence of two peaks in the spectrum of coherent echoes should be seen in the FITACF width. In Fig. 7.8 we check this prediction by plotting measured width (determined from the FITACF technique) of unresolved double-peak spectra versus

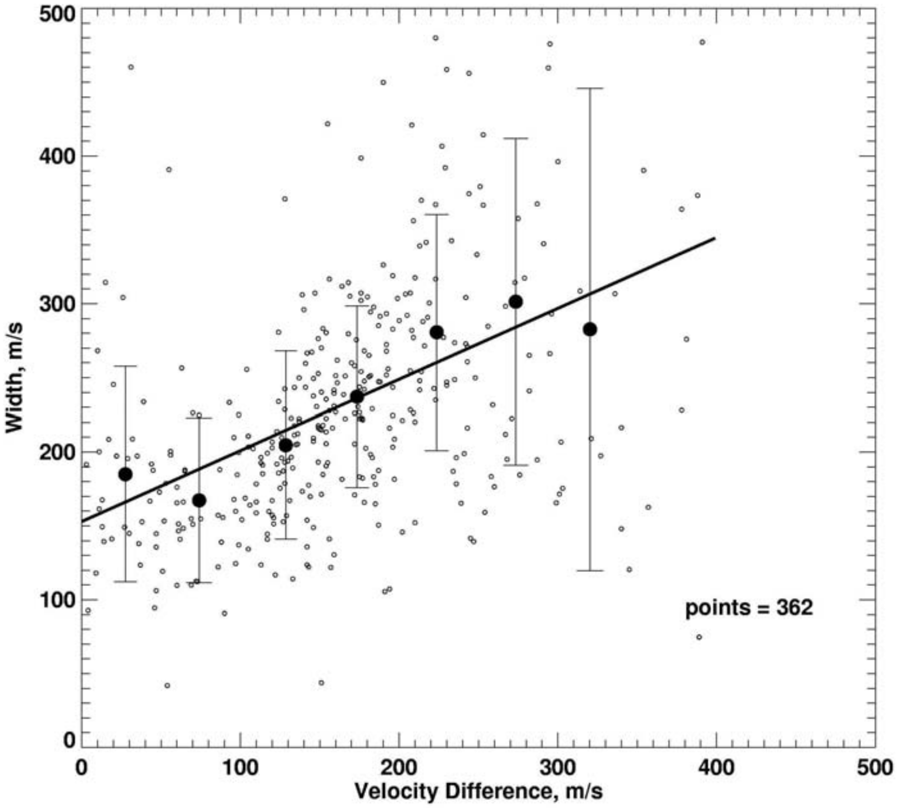

Figure 7.8 Spectral width of the CUTLASS Finland beam 5 echoes, derived from the standard FITACF procedure, versus velocity difference between the double peaks. 362 individual spectra were considered.

velocity difference between peaks for 12 February 1999 event (beam 5 only). A clear correlation between the increased width and separation of peak velocities is evident.

Another expectation with respect to the width is that it should increase with range. This effect is evident for the data presented in Figs. 7.2 and 7.3. Importantly, the spectral width enhancement should be the largest at ranges near and slightly farther than the range of the echo power maximum. To illustrate further, in a more statistical fashion, we looked at spectral width distribution versus range for all CUTLASS Finland radar beams on 12 February 1999.

Fig. 7.9 presents range distributions for the averaged echo power (a) and spectral width (b) for the period of 1430-1440 UT for all beams as determined by the FITACF technique. We focus on ranges from 180 to 945 km. The width and power are represented by colored contours with the respective scales shown on the left. The red

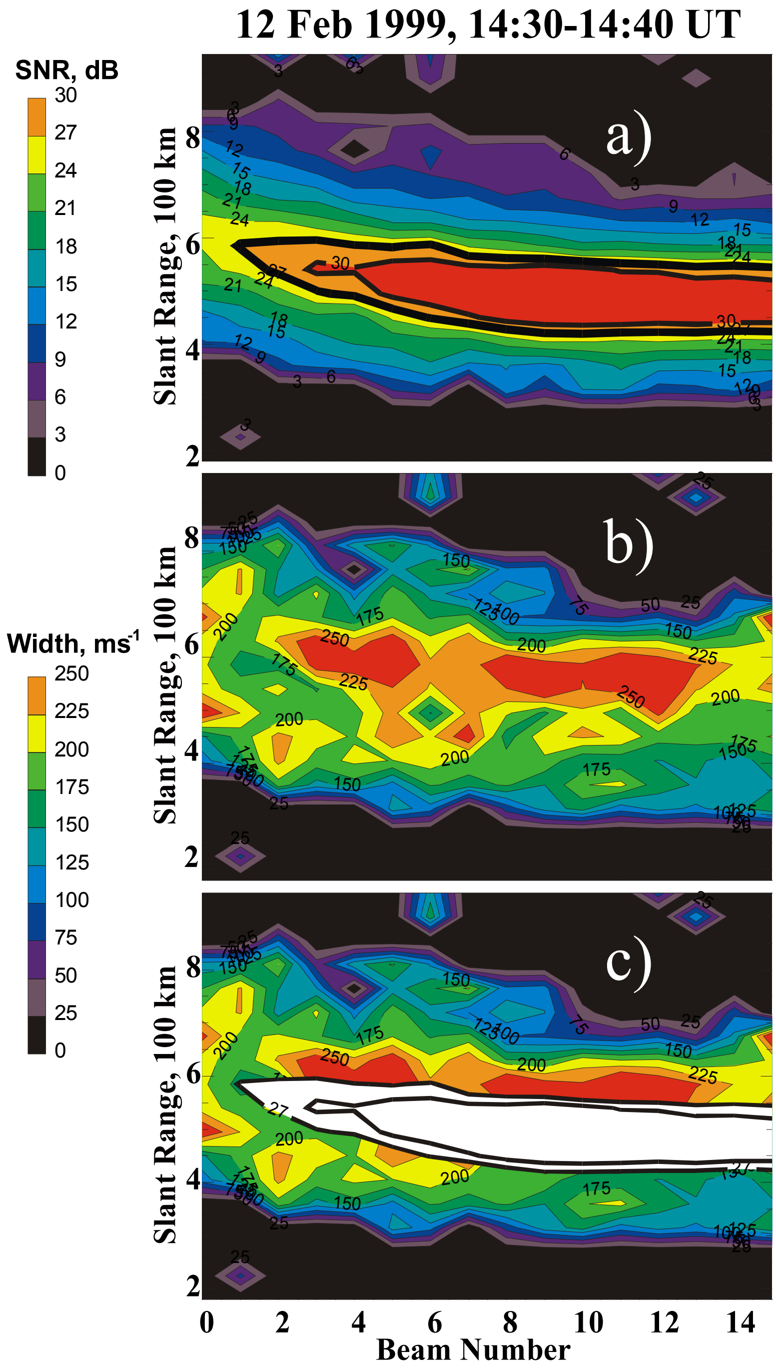

Figure 7.9 Average spectral power (a) and width (b) for various beams of the CUTLASS Finland HF radar and slant ranges. The color bars for spectral power and width are shown on the left. The red color indicates that power (width) is larger than 30 dB (250 m/s). In panel (c) the two largest power contours from panel (a) have been superimposed over the width diagram (b).

color in Fig. 7.9 indicates that echo power and width were above the highest level, 30 dB or 250 m/s, respectively. In panel (c) we superimpose on the width contour plot (b), the two highest contours of the power emphasized in (a) by thick black solid lines.

Fig. 7.9a shows a very smooth variation of power with both beam number (azimuth of observations) and slant range. The stripe of E-region echoes covers almost the entire field-of-view with the slant ranges for the echoes shifted closer to the radar at larger beam numbers. For beams 0 and 15, the echo range spans are 360-810 km and 315-720 km, respectively. Similarly, the slant range of power maximum along each radar beam is smaller at larger beam numbers (495 km for beam 0 versus 630 km for beam 15). One should note also that the intensity of the power maximum increases with the beam number from ~25 dB for beam 0 to >30 dB for beam 15.

The width distribution (Fig. 7.9b) also shows a stripe–like structure although a bit more "ragged". One can clearly see that the width maximizes at ranges 550-650 km. Unlike the power, there is no width maximum increase toward high-number beams; instead width seems to have a maximum somewhere between beams 3 and 12. The other prominent and important feature of Fig. 7.9 is that width maxima along radar beam are shifted farther from the radar than the power maxima. This feature is illustrated in panel (c) where we have superimposed power contours over the background of width contour plot. The white areas corresponding to maximum power contours do not cover red areas where width is at maximum; power maxima are closer to the radar by ~100 km.

7.6 Double-peak echoes and types of HF scatter

The double-peak nature of HF echoes can be related to two mechanisms of irregularity formation, the Farley-Buneman and the gradient-drift plasma instabilities, as was done in a number of VHF studies, e.g. Greenwald et al. (1975). In this scenario, one believes that the double-peaked spectra are resulted from azimuthal convolution of Type 1 and Type 2 scatter. Milan and Lester (1999, 2001) considered a large number of E-region HF CUTLASS echoes and sorted them according to their characteristics, including azimuthal variation of the velocity. These authors found more than just classical Type 1 and Type 2 scatter in the body of HF echoes. Only FITACF velocities were considered, so that the double-peak nature of many of the echoes was not taken into account.

One may wonder whether the idea of Type 1 and Type 2 convolution can be used as an explanation of the double-peak echoes presented in this study. Unfortunately, there is no definitive answer to this question. First of all, the standard spectral resolution of the SuperDARN measurements is not good enough to make analogies with the previous VHF measurements. One of the problems is that the width parameter for CUTLASS echoes is about the same for Type 1 and Type 2 scatter (Milan and Lester, 2001). One can attempt to look statistically at the azimuthal characteristics of the spectra. Unfortunately, the data-processing technique with the Burg method that we used in this study cannot be easily employed for mass processing of the data and studying the flow angle/azimuthal variations of double-peak echoes. For this reason, we leave such comprehensive analysis for future work.

The considered events were limited to observations at large flow angles, as known from the electric field measurements over EISCAT (or STARE convection estimates in closer areas) for two events. It is not a surprise that among considered spectra there were very few events with a high velocity component in them. As we mentioned, the high-shifted component of double peaks was below 400 m/s, a typical ion-acoustic speed in the auroral E region.

In Figure 7.10 we present an example of rare CUTLASS-Finland observations when high velocity component was observed in low number beams. Panel (a) shows the FITACF velocity map for the scan of 15:59 UT on 11 February 1999 and panel (b) shows the Burg spectra in beams 0-14 at a range of 630 km. The velocity map shows a clear and consistent velocity variation with the azimuth with strongest velocities in beams 0-1, as one would expect for westward convection. In panel (a) we show the EISCAT convection vector at the top. One can fit the velocity azimuthal variation with a cosine curve with a maximum of ~600-700 m/s. These values are less than the convection magnitude observed by EISCAT (800 m/s). One might expect such a reduction in the convection magnitude for the area ~300 km equatorward the EISCAT spot located in the auroral zone.

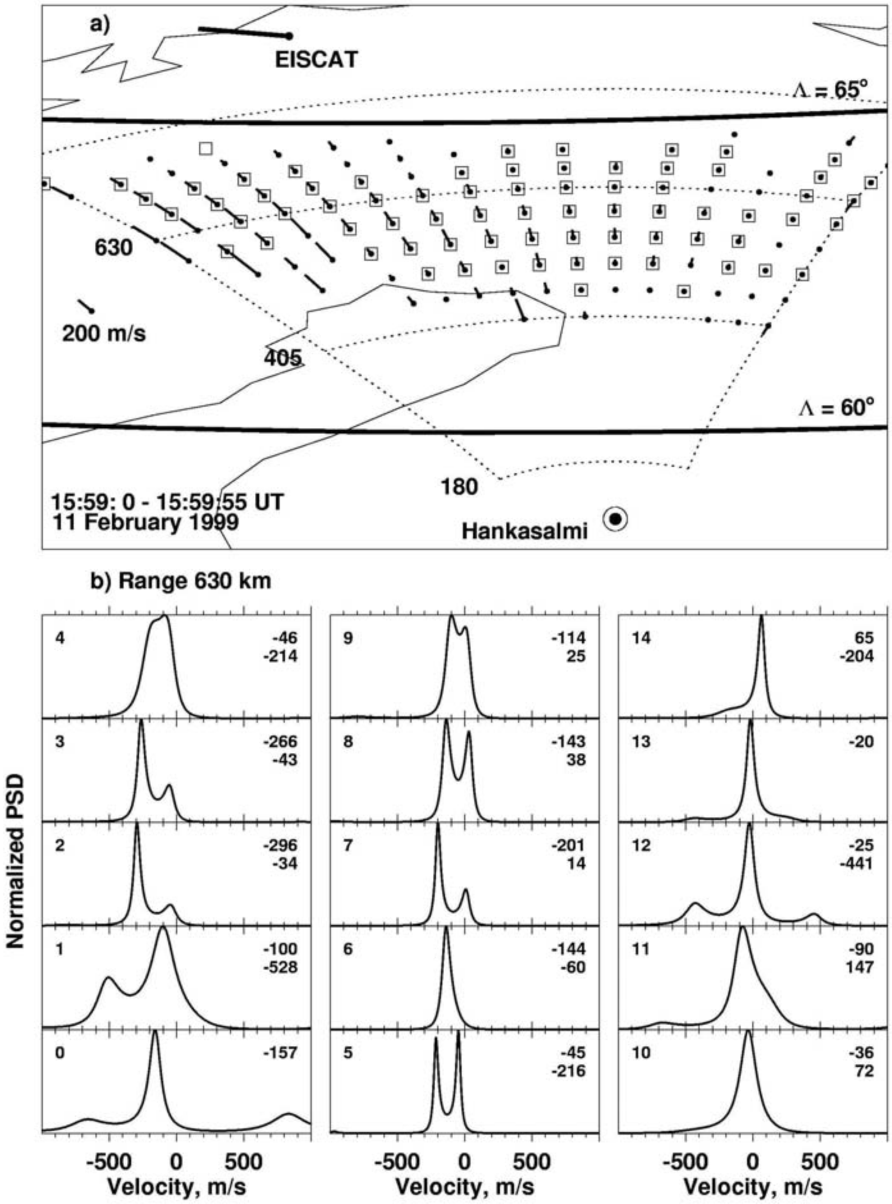

Figure 7.10 (a) Radar velocity map showing the occurrence of echoes (dots) and the presence of double-peak echoes (squares) for 11 February 1999 15:59 UT. The heavy vector indicates the ion drift measured by EISCAT. Also shown are the PACE lines of equal magnetic latitudes of Λ = 60° and Λ = 65°. Panels (b) and (c) show Burg spectra for beams 2 and 11, respectively. Ranges are noted in the upper left hand corner. The velocities of the peaks are indicated in the upper right hand corner.

Data in beam 1, panel (b), show presence of a high velocity component; the Doppler velocity is of the order of -500 m/s. Such a peak is not seen in the higher number beams. Simultaneously with the high-velocity component one can see the low-velocity component for this spectrum so that it is double-peaked. However, the separation between the peaks here is 428 m/s, well above the typical values that we reported for the double-peak structures (Fig. 7.6). The beam 0 spectrum also indicates additional energy around velocities of -600 m/s, but this enhancement was of low intensity so that the software did not identify the spectrum as double (perhaps even triple)-peaked. For the spectrum in beam 2, the high velocity component has a shift of only –300 m/s, the spectrum is double-peaked with the peak separation of 262 m/s, close to the typical separation between the double peaks reported in Figs. 7.2, 7.3 and 7.6. The spectra in beams 3-14 are also similar to the ones reported in Figs. 7.2 and 7.3 with peak separation of the order of 150-200 m/s. One cannot see a certain trend in the peak separation with the beam number (azimuth) change; this result is consistent with the statistics of Fig. 7.6.

It is important to realize that the high-velocity component existed in the beam closest to the direction of the plasma flow. For this reason and because of unusually strong velocity of the peak we think that this component of the spectrum corresponds to radar detection of the Type 1 echo. This means that, generally speaking, some double-peaks reported in this study could actually be interpreted in terms of the azimuthal convolution of Type 1 and Type 2 scatter. However, the number of such events is low, especially if one would like to have a distinctly larger separation between the peaks than the typical values. Certainly more work is needed on this aspect by involving SuperDARN radars observing along the L shells where Type 1 echo detection is more likely.

7.7 Discussion

We have shown in this study several new peculiar features of the microstructure of the E-region HF spectra observed by the CUTLASS Finland radar. To explain them one might try a purely plasmaphysical approach, for example similar to St-Maurice et al. (1994). Not denying this possibility, we attempt here to check an alternative “radiophysical” explanation by Uspensky et al. (1994) who assumed that an HF radar can receive scatter from two layers located at the top and the bottom of the E region somewhere along the beam. In some ways a similar idea of altitude convolution was theoretically considered by St-Maurice and Schelgel (1983).

In our opinion, most of the discovered features are in agreement with Uspensky’s et al. (1994) model of HF signal formation. To illustrate how this scenario can be realized we repeated the ray tracing modeling of Fig. 6.13 with a better elevation angle resolution for the specific periods studied in Section 7.4. Figs. 7.11a,c show two electron density profiles (10-min averaged) relevant to the observations presented in Fig. 7.2 and Fig. 7.3, respectively. These profiles are averaged EISCAT electron density scaled by a factor of 1/2. There is some uncertainly as to whether one can use these profiles for proper modeling since the profiles were obtained ~500 km poleward of the HF radar waves entry point into the ionosphere. The scaled profiles are consistent with the Sodankyla ionosonde measurements made ~300 km equatorward of EISCAT. Also, the predicted ranges of echoes from the ray tracing agree with the observations. We also tried ray tracing with the IRI model selected for the periods under study (the 20 minute time separation between the events does not give much difference in the IRI model), Fig. 7.11e. The IRI model shows about 2 times smaller densities and lower height of the profile maximum than the ones in Fig. 7.11a,c. There are similar discrepancies between the model profiles and the actual measurements at the EISCAT spot.

Figs. 7.11b, 7.11d, and 7.11f show the corresponding ray tracing solutions. Only 4 rays corresponding to the elevation angles of 5, 10, 15, and 20 degrees are shown. The dots indicate those ranges (including the rays that are not shown here) for which the aspect angle is within the +/-1 degree of orthogonality with the magnetic field.

For case (a) with somewhat stronger electron density, one can see that the electrojet-related echoes (in the height range of 95-125 km, horizontal dash lines in panel (b)) can be received from ranges between 400 and 650 km. Panel (b) clearly shows that for the first 50 km of the scatter band, there is only one scattering layer. At farther ranges, between 450 and 600 km, scatter from two distinct layers is possible. We note that with an increase in range, the separation between the scattering layers increases.

There is a possibility of echo reception from above the electrojet layer at ranges > 600 km simultaneously with echoes from the bottom of the electrojet. For ranges >700 km echoes can only be received from above the electrojet.

For case (c) where there is a less dense ionosphere, the electrojet-related echoes can be received from ranges of 500-750 km (see panel (d)), about 100 km farther than in the case (b). One can recognize the similar crescent-like structure in the height profile of possible scatter but it is more "diffuse" so that the echo region is expected to be more extended. One can get electrojet echoes simultaneously from two completely separated layers at 600-650 km. There is a chance to get echoes from the above the electrojet and simultaneously from the bottom of the electrojet at ranges 650-750 km.

For case (e) of an even less dense and lower (in height) ionospheric E layer, the echoes can be received from about the same ranges as in cases (a) and (c). The lower scattering layer in this case is centered below the typical electrojet boundary heights so that scatter from the bottom layer is expected to be of different origin than from the top layer.

After illustrating a possibility of echo detection from two electrojet heights, we now attempt to stress those experimental findings that support the effect. If one compares the above expectations of the ray tracing analysis and measurements reported in Section 7.4, the general agreement is observed. First of all, echoes occurred at larger ranges for the second case at 1450 UT. In both cases, echoes at nearest ranges were single peaked, double peaked at intermediate ranges and again single peaked at farthest ranges. The splitting of the spectra was slightly stronger in the second case. For the first case of 1430 UT, the low velocity peak was present all the way to the farthest ranges where signal was still available, consistent with the ray tracing predictions. The high-velocity peak was quite clear at several range gates but strongest only at one gate indicating perhaps that the electrojet irregularities were not strong everywhere at the top of the electrojet layer. The high-velocity peak had a Doppler shift of –334 m/s, which is below the ExB component of ~ 500 m/s measured by EISCAT. This peak can not for sure be associated with scatter from above the electrojet as was suggested by Milan and Lester (1998). There would need to be an electric field decrease with latitude for this

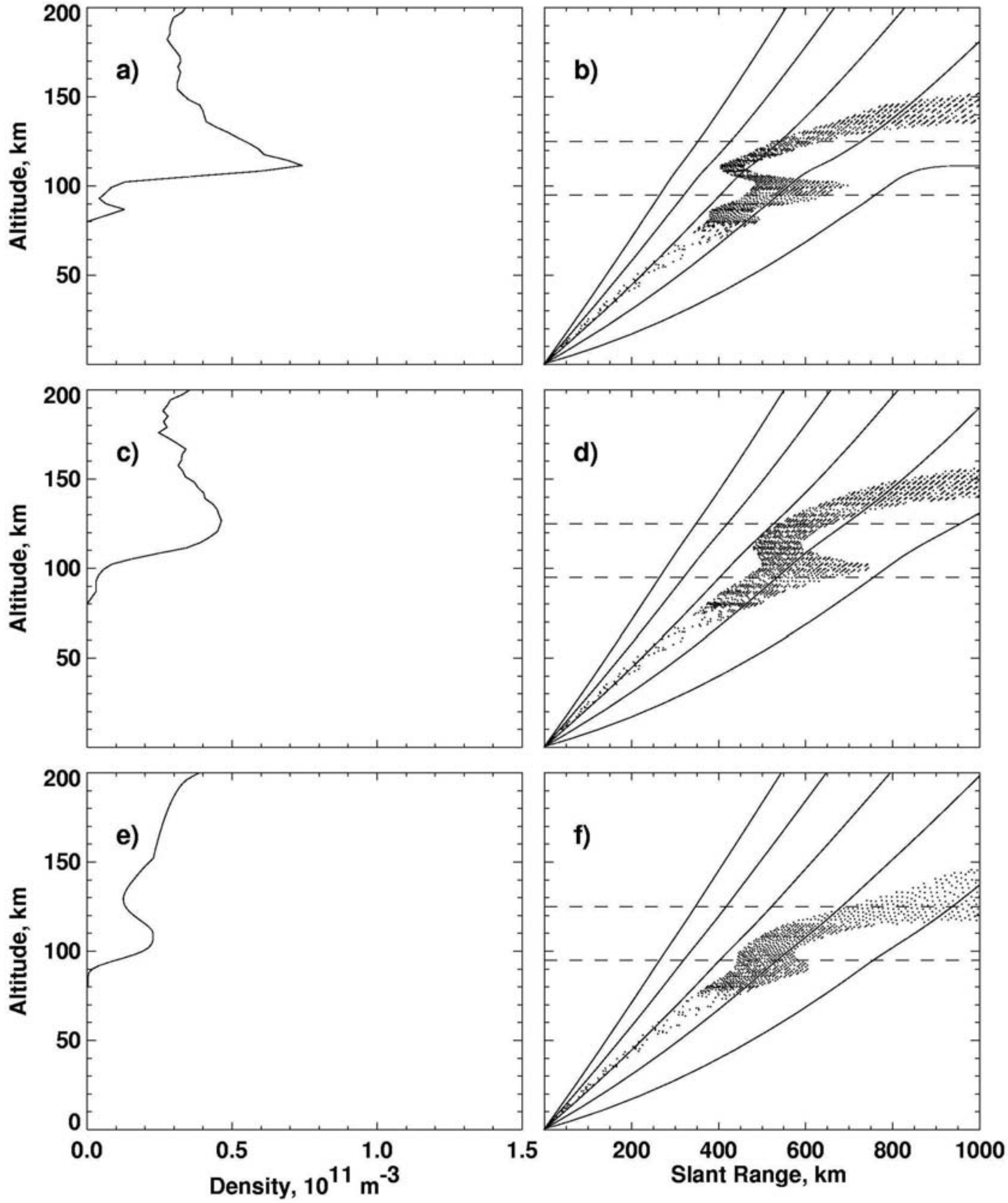

Figure 7.11 EISCAT electron density profiles observed on 12 February 1999 at 1430 and 1450 UT and the IRI model profile, panels (a), (c) and (e), respectively. Panels (b), (d) and (f) show the results of ray tracing analysis. Only 5^o, 10^o, 15^o, and 20^o elevation angle ray paths are depicted. Dots indicate those parts of the ray paths (including the ones that are not shown) for which the aspect angle of the ray is within $\pm 1^o$.

peak velocity to be consistent with the ExB component. The far range peaks at 630-765 km were of low velocity hinting that the scatter was very likely coming from the bottom of the electrojet (where the velocity depression is expected to be strongest). For the second case of 1450 UT, the far-range echo at 810 km had the Doppler shift of –245 m/s. The ExB velocity component measured by EISCAT at this time was about –250 m/s so this peak was very likely due to scatter from above the electrojet layer. This interpretation agrees with the raytracing diagram, panel (d) of Fig. 7.11.

The other feature in the data that agrees with the interpretation of double-peak echoes as scatter from the bottom and top of the electrojet layer is not L-shell alignment in these echo occurrence, Section 7.5. Since the electrojet is more or less L-shell aligned, one would expect that double-peak spectra to occur stretched along the L shell direction if they are originated from pure plasma physical effects.

We also demonstrated that the HF spectra are broader at ranges near the echo power maxima and slightly farther than that, as expected. This feature is not always present for understandable reasons; one needs nearly uniform density distribution to detect it clearly. Diagrams similar to Fig. 7.9 were obtained for a number of other events and similar feature is quite often evident. A statistically more frequent occurrence of broad E-region echoes at ranges slightly farther that the range of the echo power maximum was reported by Koustov et al. (2001b) for the Syowa SuperDARN radar.

Another important expectation of the Uspensky et al. (1994) model is that the velocity of both peaks should be below the ExB component (owing of collisions) and the velocities of the peaks and their separation should vary in accord with temporal variations of the electric field.

In regards to the velocities of the peaks, Uspensky et al. (2003) put forward an idea that HF velocity should always be below ExB due to the radar detecting signals not only from the height of perfect aspect angle but also from the nearby heights where the aspect angles are poorer and the irregularity velocity is depressed. The depressed velocities are also in agreement with theoretical model of St-Maurice and Schlegel (1983). EISCAT/CUTLASS E-region data presented by Davies et al. (1999) clearly demonstrate the effect (their Fig. 5) though the statistics is not large. In Section 7.8 we argued that the effect might be present in our data as well. Certainly more experimental work is needed for thorough assessment of this prediction.

As for the relationship of the peak velocity and the electric field variations, we attempted to assess the situation by comparing the EISCAT and CUTLASS beam 5 data for 12 February 1999 event, 14-16 UT, Fig. 7.12. Here at the top panel (a) we show the EISCAT ExB component (scaled by a factor of ½ for convenience) and the CUTLASS FITACF velocity. We understand that the EISCAT electric field data were gathered about ~300 km poleward of the HF scatter and so the electric field was somewhat different at closer ranges (most likely smaller). However, we expect that the electric field temporal variations at the ranges of HF echo detection to be more or less in accord with electric field variations at the EISCAT spot. Fig. 7.12a shows that FITACF velocity at 630 km (being below the ExB component as expected) changes in some agreement with convection variations at the beginning of the interval; one can notice "a response" to rapid EISCAT velocity change around 1430 UT. After 1445 UT, there was no correlation between FITACF and ExB velocity. Fig. 7.12b shows temporal variations of the peak separation and ExB component. One can see overall larger separations at the beginning and overall smaller separations during the second half of the event in agreement with stronger convection during the first half of the event. The drastic changes of ExB around 1430 UT are accompanied by changes in the peak separation, as expected.

In Fig. 7.12c we explore another aspect of Uspensky et al. (1994) model, namely the density effect in the observed velocity. Density involvement in observed velocity of HF auroral echoes seems to be strange since velocity is traditionally related to the phase velocity of irregularities. However, within the Uspensky et al. (1994) model, the observed velocity is a combination of scatter from various heights and the contribution from an individual height is density dependent. It is clear that stronger density (within a certain range) can increase a chance of enhanced wave over-refraction in the central part of the scattering layer so that the height (and velocity) separation between the peaks can be larger. In Fig. 7.12c, one can see that many density enhancements are accompanied by the peak separation increases.

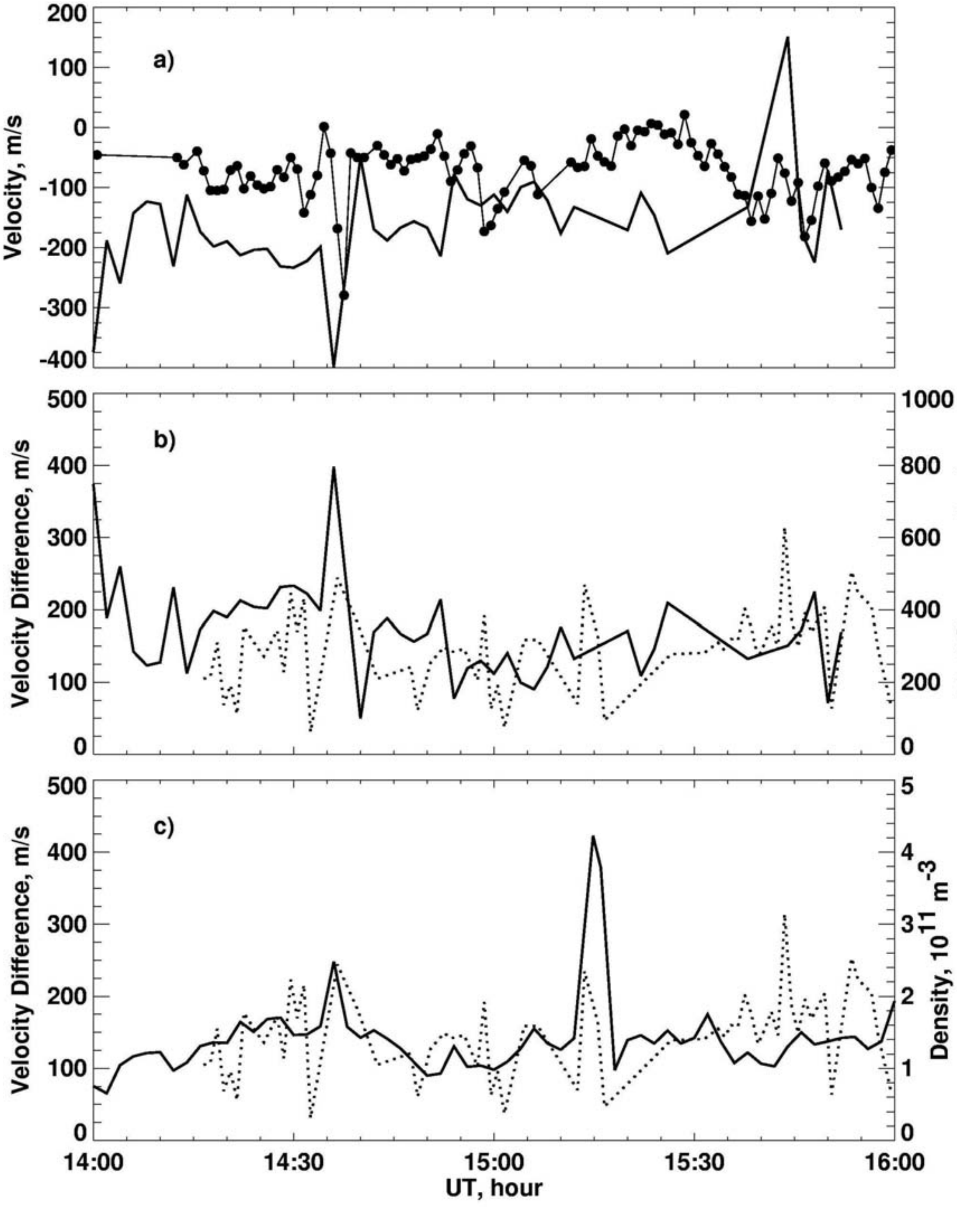

Figure 7.12 (a) FITACF velocity (filled circles) and projected ExB (solid line) component for beam 5 on 12 February 1999 at a range of 630 km. (b) The temporal variation of peak separation (dotted line) and the projected ExB component (solid line). (c) The temporal variation of peak separation (dotted line) and the E-region electron density (solid line).

Though we found many features in the data that support the Uspensky et al. (1994) model, some experimental facts are not easy to account for within this approach. In this respect, an important result is that the separation between the peaks is about the same for all the beams, Figs. 7.6 and 7.7, and the magnitude of separation is about 150 m/s. Within the model, the magnitude of separation reflects the difference in the irregularity phase velocity at the top and at the bottom of the electrojet. Since for the considered events the electric field was quite strong, the magnitude of the difference does not seem unreasonable but it should depend on the electric field magnitude and the azimuth of measurements. We illustrated that a correlation with the electric field variations was not always present, though this might be caused by difference in the locations of the areas for the HF and EISCAT measurements and, in addition, by the electron density effect, Fig. 7.12c.

As for the azimuth of observations, one expects that with the direction of observations approaching perpendicularity with the L shells, the velocity of both peaks should be approaching zero so is the peak separation. Experimentally, this is not the case, at least statistically, Figs. 7.6 and 7.7, and for one individual event of Fig. 7.10. We should say that even though the simple approach by Uspensky et al. (1994) does not work in explaining this result, the situation could be improved if the ion motion is considered as suggested by Uspensky et al. (2003). Other effects might be of importance. For example, ray tracing shows a possibility that echo reception maybe from the bottom of the E region where the irregularity production and their properties can be influenced by the neutral wind. This effect can be important for the low velocity peaks, especially for directions close to the perpendicular to the L shells. Makarevitch et al. (2002b), by considering near range 50- and 12-MHz echo statistics at the Syowa Antarctic station, showed that HF echoes occur more frequently not along the electrojet flow, unlike the VHF echoes, but some tens of degrees off the flow. They also showed that HF echoes consist of 2 groups, the low-velocity and high-velocity groups. The low-velocity group had velocities below ~150 m/s, and the authors suggested that these echoes were related to the electrojet instabilities significantly affected by the neutral wind or even generated due to neutral wind-related plasma instabilities (Dimand and Sudan, 1997; Kagan and Kelley, 1998; 2000). In a case of the significant neutral wind effect, one would expect different flow angle variation for the low-velocity component as compared to the high-velocity component. Because of large data spread, see e.g. Fig. 7.7, we cannot make any definitive conclusions in regards to the effect of neutral winds.

Another area of difficulty is the observations of high-velocity components of opposite polarity with respect to the low-velocity components (in high numbered beams). The effect was more pronounced for observations in Fig. 7.7d, beam 14. We think that this feature can be explained by considering the ion motion effect as discussed in Section 2.3.3. For detailed analysis, however, supportive data are needed.

Another explanation for the opposite polarity may be due to vortical structures in the ionospheric electric field. To investigate this possibility, we obtained the DMSP ion drift meter data for two over-passes as shown in Fig. 7.13. The one-second rarefied ion drift measurements are shown for clarity. For the first event (Fig. 7.13a), the satellite crosses just to the east of the region of echoes. In the second event, there is better overlap between the two devices. We present the 8 sample per second component of the ion drift that was measured by DMSP in Fig. 7.14. One notes the absence of fluctuations in the ion drift at magnetic latitudes where double-peaked (DP) echoes occur. The ion drift is smoother than at other magnetic latitudes where double-peaked echoes were not observed (e.g. after 14:33:30 UT in Fig. 7.14a). Hence, from this data set one does not see an indication that the variations in the electric field are the primary cause for the double-peaked spectra.

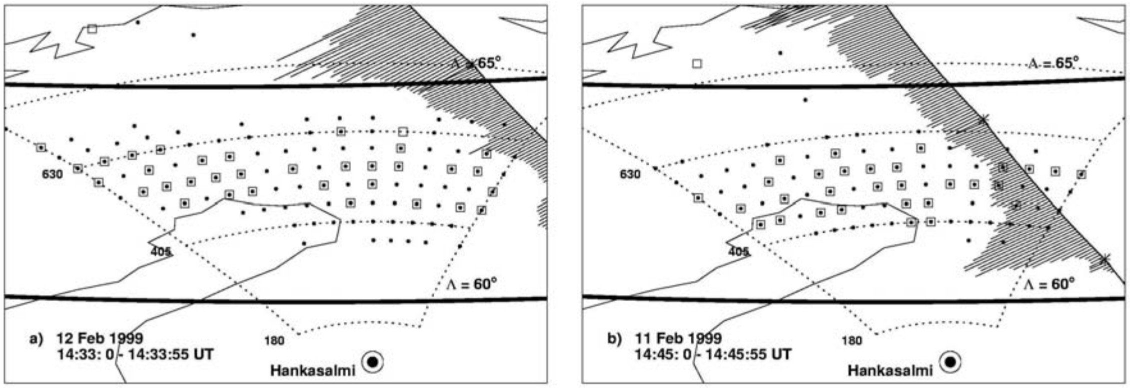

Figure 7.13 DMSP footprint at 110 km and ion drift for the 12 February 1999 (a) and 11 February 1999 (b) passes. The location of double-peaked HF echoes is denoted by a square. HF ionospheric echo occurrences are denoted by dots.

The interpretation of double peaks as scatter from two E-region heights is applicable to any HF radar observations. However, detection of double-peak spectra, especially with the pattern reported in this chapter, is not simple. We expect that such echoes are more difficult to see with radars that have poor geometric aspect angles and whose aspect angles quickly change with the range. The Saskatoon radar is an excellent example of such a case. To detect E-region echoes here, some precipitation is required which is often a highly varying phenomenon in time and space. Double-peak HF echoes should be observed for the low-latitude HF radar locations. Reviewing published data we discovered that double-peaked spectra at the far edge of the E-region band have been reported (but not discussed) by Haldoupis et al. (1996) at mid latitudes.

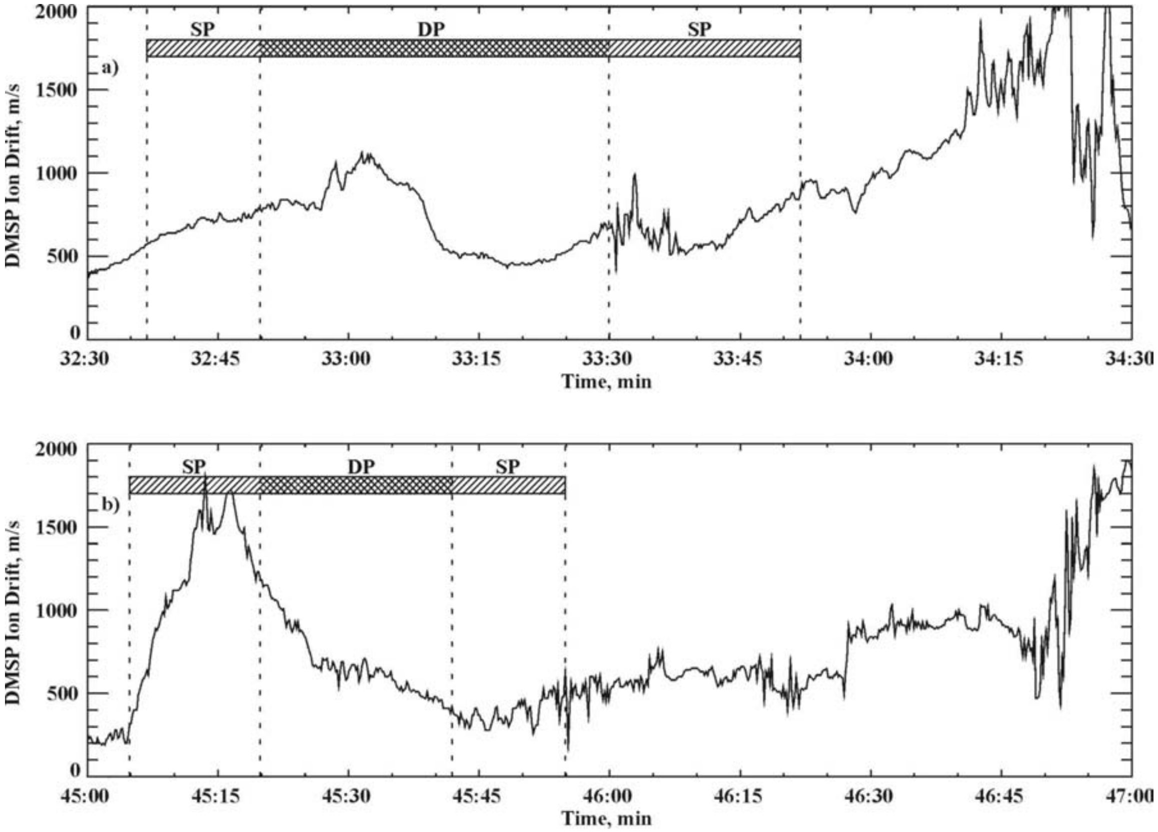

Figure 7.14 The ion drift perpendicular to the track of the satellite is depicted for (a) 12 February 1999 and (b) 11 February 1999. The horizontal axis is time in minutes after 14 UT. DP (SP) is where double- (single-) peaked HF echoes were observed.

This work has used the assumption that ion contributions to the velocity were not significant. In Chapter 2, the effect of ion drift on the phase velocity of E-region irregularities was discussed in Section 2.3.3. Figs. 2.4c,d showed scenarios where the radar observed more or less along the direction of the electric field. It was demonstrated that the phase velocity determined by the radar could be larger or even of opposite polarity with the expected component of the ExB. The Hankasalmi radar views almost along the direction of the typical northward electric field (within +/- 20^o, see Fig. 4.14b) present during the time of observations. The possibility of ion drift could have easily obscured the comparison of the higher velocity peak with the expected component of ExB.

The obtained results on the microstructure of E-region echoes have two potential implications for SuperDARN–related research. One of the questions is how the velocity of each peak is related to the ExB component. One would expect that the high-shifted component is closer to the ExB component whether it is received from above the electrojet layer or just at its topside. Since typically this component is ~100 m/s larger than the FITACF velocity (Fig. 7.7), an implication is that the currently in use FITACF approach should give underestimation of the convection component.

The other aspect is the contribution of E-region scatter to the F-region echoes at ranges less than 1000 km. According to the understanding gained in this study, the spectra should quite often be double (multi)-peaked in the “transition region” from pure E-region and pure F-region scatter. On width maps this should be seen as a stripe of echoes with enhanced width. The exact range location of such a stripe can vary in accordance with the distribution of the electron density. The effect can also “work” at those ranges where echoes can be received from the E-region by the $1\frac{1}{2}$F propagation mode. Moreover, one can expect some enhancement in the spectral width of pure F-region echoes if they are received from two heights and the electric field is strongly nonuniform. This might happened due to the 45-km range gate of SuperDARN such that echoes at different heights might correspond to different magnetic flux lines and different electric fields. Thus, simultaneous echo reception from several heights can be a reason for broader than usual echoes. The effect should be stronger near the edges of particle precipitation. It is not a surprise then that HF radars can detect some magnetospheric boundaries through imaging the spectral width distribution (Woodfield et al., 2002). More work is needed to assess whether this “radiophysical” effect is really occurring.

In order to improve our knowledge of the microstructure of E region spectra at HF with SuperDARN radars, analysis of more events is needed. This work requires significant data processing and it is in our future plans. Further testing of the proposed interpretation of the double-peak structures can be done if nearly simultaneous data on electric field and neutral winds are available. Unfortunately, it is a very seldom occasion this can be achieved with the EISCAT facility. In the CP-1 mode, observations are performed at ranges where F-region echoes are more typical (Davies et al., 1999).

7.8 Summary

In this chapter several new results regarding the spectra of the E-region coherent echoes were obtained. We showed that while E-region HF echo spectra are single-peaked at shortest and farthest ranges of an echo band, there are quite often 2 (or more) spectral components at the intermediate and farther ranges. This “splitting” of spectra starts near the ranges of the power maximum in the power range profile. The typical separation between the peaks is about 150 m/s and hardly changes with the azimuth of observations. We demonstrated that splitting of HF spectra is accompanied by an increase of the FITACF spectral width. The effect can be seen in range profiles for the width. The range of maximum width is shifted farther away from the range of the power maximum indicating that increased width is resulted from the presence of 2 (and sometimes more) spectral components with different velocities. We also showed that velocities of two components in a double-peak spectrum are typically larger and smaller than the velocity of the unresolved spectrum and single-peaked velocity of echoes at shorter ranges. The high-velocity component is closer to the ExB velocity drift along the radar beam than the velocity of the unresolved spectrum. The low-velocity component has values below 200 m/s, the maximum expected wind velocities at the bottom-side E-region.

The observations presented were interpreted in terms of “radiophysical” effect of signal reception from two different heights. Several features in experimental data supported this interpretation, but we identified the ones that did not. This means that plasma physics of irregularity formation is also important for understanding of double-peaked E-region spectra. Possible importance of strong gradients on the FB instability was mentioned. Clearly, more work is needed first of all to quantitatively estimate the role of plasma physics and radiophysics in the formation of double-peaked echoes.

CHAPTER 8

CONCLUSIONS AND SUGGESTIONS FOR FURTHER RESEARCH

In this thesis, several properties of auroral HF and VHF backscatter have been investigated. The study was based on data collected by the Hankasalmi CUTLASS (SuperDARN) HF radar and by the Hankasalmi/Midtsandan STARE VHF radars in Northern Scandinavia. For several individual events, the coherent echo data were supported by EISCAT with measurements of various ionospheric parameters at one spot within the observational area.

8.1 Conclusions

In the course of analysis, cases of F- and E-region backscatter were considered separately. For each of these, conclusions of general character can be made.

8.1.1 F-region backscatter

1. The presented data indicates that there are several factors that control F-region echo occurrence with all of them contributing in a certain way. With the available data it is impossible to give a quantitative estimate of the relative role of each of these factors.

a) We showed that the ionospheric electric field, important for the onset of the GD instability and thus the F-region irregularity production, should be enhanced if HF echoes are to be observed. The threshold effect for F-region backscatter is not as sharp as that for E-region echoes. F-region backscatter is typically observed for electric field magnitudes in excess of 5-10 mV/m. This conclusion comes from the direct comparison of CUTLASS echo occurrence over the EISCAT spot and electric field magnitudes measured by EISCAT. We also showed the significance of the electric field effect by looking at the statistics of F-region echo occurrence in the midnight sector. Such echoes were much more frequent during the years of the solar cycle maximum when more frequent occurrence of enhanced electric fields in the ionosphere is expected due to preferential conditions for magnetospheric merging. Remarkably, there were signatures in the data that echo occurrence can be enhanced during equinoxes, the best seasons for merging as predicted by Russell and McPherron (1973).

b) We also supported the notion that plasma gradients should exist in the F-region for successful launching of the GD instability and onset of decameter irregularities. We showed that echoes tend to be less frequent during the daytime where the solar radiation reduces the ionization gradients within the ionosphere. We showed that duration of the midnight echoes depends on the season, with longer periods of echo occurrence during winter.

c) The evaluation of the role of the E-region conductance on the generation of F-region irregularities by comparing HF data and EISCAT measurements of the electron density did not lead to a firm conclusion. This effect was apparently important for some periods and not so for others.

d) We showed that though F-region echo detection is strongly controlled by the irregularity production factors, it is extremely important to have proper propagation conditions for the radar waves to reach the irregularities. Direct comparison of electron densities over the EISCAT spot and echo occurrence clearly indicated that "optimal" density of the order of $2x10^{11}$ m^{-3} should be established in the F region to detect echoes. We expect that weaker (stronger) densities provide radio wave focusing at larger (shorter) ranges where the irregularity production conditions might be not good. For example, we showed that for the years of solar cycle maximum, the typical F-region densities support echo observations at lower than usual latitudes where the enhanced electric fields might not exist. Also, the electron density distribution with height dictates the altitudes at which echoes can be detected. For low densities, relatively large altitudes are accessible to the radio waves though irregularity production is favored on the bottom side of the F region. This could be the reason why echoes are sometimes absent even if the electric field is strong.

The other effect which clearly exposes the importance of the electron density factor is the observed change over the solar cycle in the character of the seasonal effect. Echoes were more frequent during the summer for the years of the solar cycle minimum and during the winter for the years of the solar cycle maximum. Ray tracings showed that this effect could be explained by changes in the amount of refraction.

e) For the considered events it was found that HF radio wave absorption in the D region was not a factor for echo occurrence, but this conclusion is valid only for the specific conditions of these observations. The comparison needs to be extended to a wider range of ionospheric conditions, including strong precipitation events.

2. The comparison of CUTLASS F-region velocity measurements with EISCAT data confirmed that, to a first approximation, the Doppler velocity of HF echoes is the cosine component of the ExB bulk plasma flow. This conclusion, once again, supports the SuperDARN approach to the convection monitoring. In this validation work, we showed, for the first time, that the Map Potential technique (currently in use for SuperDARN convection estimates) performs reasonably well even for those areas of the high-latitude ionosphere in which data from only one radar were available. Such evaluation has been done for short ranges of ~1000 km (direct propagation mode) and large ranges ~2000 km (probably $1\frac{1}{2}$ F propagation mode). On a finer scale, we showed that CUTLASS HF velocities were often slightly smaller than the ones expected from the EISCAT measurements (10-30%) though the azimuth estimates agree with EISCAT azimuth within $\pm 20^{o}$. No definitive reason for the minor differences was found.

8.1.2 E-region backscatter

1. It was found that the STARE (VHF) Doppler velocity at large flow angles can be well below the ExB component derived from simultaneous EISCAT measurements. The effect was obvious in the afternoon/evening sector of observations. Despite the discovered strong STARE velocity depression effect, the STARE convection azimuths obtained from simple merging of Norwegian and Finland radar data were reasonably good. To explain the observations, it was assumed that STARE echoes originate from irregularities produced by the FB and GD plasma instabilities in a broad range of electrojet heights. Since the aspect angles of observations are non-zero at most heights, the resultant velocity of VHF echoes is decreased as compared to the ExB component. One implication of such interpretation is that quality of STARE convection predictions is worse at the equatorward and eastern parts of the radars' fields of view.

2. It was found that the Doppler velocity of the E-region HF echoes can be smaller than the cosine component of the ExB plasma drift. This conclusion was made by comparing the SuperDARN (CUTLASS) (HF) and STARE (VHF) velocities at various slant ranges (500-700 km) for ~2-hour event under investigation. We discovered that the HF velocity can be smaller than, equal to, or larger than the VHF velocity, depending on the range of the comparison. At short (far) ranges, the HF (VHF) velocity magnitude was typically larger than the VHF (HF) velocity magnitude. For intermediate ranges, where the HF power and velocity magnitude were at maxima, the HF and VHF velocities were comparable. For all ranges of HF/VHF comparison it was expected that the VHF velocity would be well below the ExB component because of the non-zero aspect angles of STARE observations. The effect was expected to be especially strong at the shortest ranges of the comparison ~ 500 km. To interpret the VHF/HF velocity results, it was suggested, that contrary to the pure electrojet origin of the VHF echoes, the HF echoes were perhaps strongly influenced by scatter from heights of less than 100 km, where the irregularity phase velocity is strongly depressed due to collisions and where neutral winds might be contributing to irregularity excitation and to their velocity.

3. To further investigate the potential effect of scatter from various heights, the Burg spectrum technique was applied to study the E-region HF spectra with better than the standard FFT resolution. It was discovered that ~30-40% of the echoes were double-peaked with typical peak separation of ~150 m/s. Double peaks were observed at all flow angles with very little difference in terms of separation, implying that the micro-structure of the spectra indeed very likely associated with echo convolution in height rather than in flow angle (due to reception of Type 1 and Type 2 backscatter). Other features of the double-peak morphology supported this conclusion. For example, it was discovered that double-peaked spectra were more frequent at the middle ranges of an echo band, at ranges farther than the maximum in echo power. These are exactly the ranges where one might expect echo reception from both the top and the bottom of the electrojet layer. Ray tracings with EISCAT electron density profiles confirmed the possibility of such a scenario for several moments of measurements. It was also shown that the FITACF spectra of double peak echoes are broader.

We also demonstrated that the FITACF velocity typically lies between the velocities of the peaks within the spectrum. If one peak of a double-peaked spectrum indeed originates from the top of the electrojet where its velocity should be close to the ExB convection component, the observations imply that the FITACF velocities currently in use for SuperDARN convection estimates at short ranges give an underestimate of the convection velocity component. Some indications of this effect for very limited data sets were reported (but not discussed) in literature (Milan et al., 2003).

8.2 Suggestions for future research

Every project considered in this thesis needs further expansion to go deeper into the nature of the phenomena studied. Here we would like to outline the most beneficial areas for future research.

8.2.1 On the reasons for F-region echo occurrence

a) It is obvious that study of seasonal variations of echo occurrence needs to be expanded to all SuperDARN radars available since each of the radar locations is quite different when both the geographic and geomagnetic latitudes are considered for a site (see Table 3.3 and Fig. 3.2). This means that relative role of irregularity production factors and propagation conditions should depend on both radar location and long-term variations (seasonal, solar cycle). Of special interest are observations of conjugate radars, such as Pykkvibaer and Syowa East. One of the issues is the hemispherical asymmetry in echo occurrence. We showed that northern hemisphere midnight echoes are more frequent during local winter (December-February). Does this mean that southern hemisphere echoes are more frequent during their local winter (June-August)? One might think that the irregularity polarization electric field in one hemisphere could be shorted out through the highly conducting ionosphere of the opposite hemisphere. Is this scenario realistic? One way to assess this possibility is to look at the character of seasonal variations in echo occurrence for conjugate radars since during equinoxes there is not much of a difference between the conductances of conjugate hemispheres.

b) The cases considered in this study of HF/EISCAT measurements corresponded to the periods of fairly low precipitation. As a result, the assessment of the role of the radio wave absorption for the F-region echo detection was not comprehensive. In this sense it is highly desirable to perform more systematic comparisons of D-region riometer absorption and F-region echo occurrence. For the SuperDARN radars in Saskatoon and Kapuskasing, riometer data at a number of CANOPUS stations are available, and the above task seems to be fairly straightforward.

c) Our analysis showed that electron density in the ionosphere is crucial for the propagation of the radar rays to the echo locations. Knowledge of the optimal densities for propagation to the echo region would greatly assist in the selection of operating frequencies for the radar to maximize the amount of desired scatter (E region, F region, or groundscatter). Though we interpreted the results in terms of changes in the amount of refraction, it is clear that more than that needs to be considered. One issue is the height of F-region backscatter. Our ray tracings showed that for typical ionospheric electron density profiles, echoes should be more frequently observed at relatively low heights of ~200 km. These are the heights where the GD instability occurs preferentially. Does this mean that the F-region echo heights are close to 200 km? Here we should note that the SuperDARN mapping procedures assume the heights of scatter to be above 300 km. If echoes do occur at lower heights, appropriate changes in the SuperDARN software would need to be made. For this kind of study, information on the electron density profiles along one of the SuperDARN radar beams is needed. With planned new installations of CADI digital ionosondes in the Canadian sector, such a project seems to be very realistic. One should also seek new common EISCAT-CUTLASS observations.

8.2.2 Refinements of the Map Potential method

To improve the quality of the Map Potential technique, further validation work is needed. One of the concerns arising from this thesis is the indication that the phase velocity of the E-region HF echoes can be well below the ExB convection component. The Map Potential approach uses data from E-region echoes under the assumption that their Doppler velocity is exactly the cosine component of the flow. This means that Map Potential predictions at low latitudes may sometimes underestimate the real flow velocities. To progress further in this area one can try compare HF E-region velocities with DMSP satellite drift data, as was done by Xu (2002). Of course, new coordinated measurements with EISCAT are very desirable. Finally, addition of new SuperDARN radars at mid-latitudes (as currently planned) creates a unique opportunity to observe echoes in the F and E regions simultaneously on the same magnetic flux lines. Such observations would be very beneficial for studying the physics of decameter irregularity production in the E region.

8.2.3 E-region studies

a) Clearly more work needs to be done with respect to the spectra of HF SuperDARN echoes with the Burg method. This thesis showed that E-region echoes are quite frequently double (multiple) peaked. However, data from only one radar were considered. It is required to study data of other radars to investigate the morphology of double peaks. Preliminary work indicates that double peaks are more frequent on zonal-oriented radars, such as Syowa East and Stokkseri. The primary issue to be considered is whether the double-peak nature of E-region SuperDARN echoes is simply the result of the altitude convolution of signals as assumed in this thesis, or is a plasma physical effect such as echo reception from various flow angles. Clearly more knowledge of the propagation conditions is needed for this kind of study, so that joint observations with ionosondes need to be performed. Also, it is desirable to combine this work with simultaneous convection measurements. Involvement of DMSP drift data is desirable since apparently there is very little chance to obtain E-region CUTLASS echoes at a range where EISCAT is measuring F-region convection. The question that can be studied is whether one of the double peaks is related to the electric field and the other one to the scatter from lower altitudes.

b) It is important to continue the STARE/CUTLASS comparisons since these systems are sensitive to different wavelengths of electrojet irregularities. The phase velocity dependence on the wavelength could differentiate between the effects of the FB and GD instabilities. Of special interest are Syowa observations with new 112-MHz Communications Research Laboratory radar that is currently under construction.

8.2.4 Further F- and E-region studies on Canadian soil

The research performed in this thesis was entirely based on observations over northern Europe. Some aspects could have been studied using Canadian radars. For example, the University of Saskatchewan radar group has installed a Canadian Advanced Digital Ionosonde (CADI) in Rankin Inlet that is capable of measuring the maximum electron density in the ionosphere and the mean plasma drift overhead of the station. One possibility is to investigate the optimal densities required for optimal echo reception in Saskatoon and Kapuskasing. The data comparison is especially interesting in view that the diurnal variations of echo occurrence are slightly different for these radars.

Another potential investigation is a velocity comparison between CADI and SuperDARN. The CADI method of velocity estimate is based on the assumption that flow is uniform over its large field of view. This assumption can easily be violated during strong disturbances. Preliminary assessment of joint sets is currently under way.

During the preparation of this thesis, news has arrived about the chances for the University of Saskatchewan to receive funding for two new HF radars at Rankin Inlet and Inuvik, Northwest Territories. This pair of radars is commonly referred to as PolarDARN. The main objective of the PolarDARN pair is to eliminate the gap in coverage of the current SuperDARN network. Indeed, Figure 3.2 shows that the entire Northern Hemisphere polar cap is not accessible to current radars. Though the main advantage of PolarDARN is to improve the quality of the convection maps, these radars will provide invaluable information on processes occurring near the north magnetic pole.

Another wonderful news is that the Stanford Research Institute (SRI) has received funding for an incoherent scatter radar (ISR) at Resolute Bay, Nunavit. This radar will allow the determination of ionospheric parameters in the middle of the PolarDARN FoV. The combination of PolarDARN and ISR will expand significantly the capabilities of Canadian scientists to explore high latitude phenomena in Canada.

These new developments on the instrumental side of observations in Canada will certainly provide numerous opportunities to expand the research initiated in this thesis.

REFERENCES

André, R., Hanuise, C., Villain, J.-P., and Cerisier, J.-C.: HF radars: multifrequency study of refraction effects and localization of scattering, *Radio Sci., 32*, 153-168, 1996.

André, R., Villain, J-P., Krassnosel'skikh, V., and Hanuise, C.: Super Dual Auroral Radar Network observations of velocity-divergent structures in the F region ionosphere, *J. Geophys. Res., 105*, 20,899-20,908, 2000.

Baker, K.B., Greenwald, R.A., and Tsunoda, R.A., Very high latitude F region irregularities observed by HF radar backscatter, *Geophys. Res. Lett., 10*, 904-907, 1983.

Baker, K.B., Greenwald, R.A., Ruohoniemi, J.M., Dudeney, J.R., Pinnock, M., Newell, P.T., Greenspan, M.E., and Meng, C.-I.: Simultaneous HF-radar and DMSP observations of the cusp, *Geophys. Res. Lett., 17*, 1869-1872, 1990.

Bates, H.F., Some effects of dense Es clouds on high-latitude HF backscatter*, J. Geophys. Res., 70*, 5895-5905, 1965.

Ballatore, P., Villain, J.-P., Vilmer, N., and Pick, M.: The influence of the interplanetary medium on SuperDARN radar scattering occurrence, *Ann. Geophys., 18*, 1576-1583, 2001.

Beynon, W.J.G., and Williams, P.J.S.: Incoherent scatter of radio waves from the ionosphere, *Rep. Prog. Phys., 41*, 909-955, 1978.

Brekke, A.: Physics of the Upper Polar Atmosphere, Wiley Press, New York, 1997.

Chaturvedi, P. K., Keskinen, M.J., Ossakow, S. L., and Fedder, J.A.: Effects of field line mapping on the gradient-drift instability in the coupled E and F region high-latitude ionosphere, *Radio Sci., 29*, 317-335, 1994.

Coffey, H.: Geomagnetic and solar data, *J. Geophys. Res., 104*, 22,819-22,820, 1999.

Danskin, D.W., Koustov, A.V., Nozawa, S., Ogawa, T., and Nishitani, N.: HF echo occurrence and parameters of F-region plasma. DASP Winter Workshop. Saskatoon, Canada, 2001a.

Danskin, D.W., Koustov, A.V., Ogawa, T., Nozawa, S., and Nishitani, N.: On the factors controlling the power of F-region coherent echoes. 10th International EISCAT Workshop. Tokyo, Japan, 2001b.

Danskin, D.W., Koustov, A.V., Ogawa, T., Nishitani, N., and Nozawa, S.: Are SuperDARN convection maps compatible with EISCAT electric field measurements?, Space Environment Workshop, Banff, Alberta, November 8-10, 2001c.

Danskin, D.W., Koustov A.V., Ogawa, T., Nozawa, S., Nishitani, N., Milan, S., Lester, M., and André, D.: On the factors controlling the occurrence of F-region coherent echoes, *Ann. Geophys., 20*, 1399-1413, 2002.

Davies, J.A., Lester, M., Milan, S.E., and Yeoman, T.K.: A comparison of velocity measurements from the CUTLASS Finland radar and the EISCAT UHF system, *Ann. Geophys., 17*, 892-902, 1999.

Davies, J.A., Yeoman, T.K., Lester, M. and Milan, S.E.: A comparison of F-region ion velocity observations from the EISCAT Svalbard and VHF radars with irregularity drift velocity measurements from the CUTLASS Finland HF radar, *Ann. Geophys, 18*, 589–594, 2000.

Davies, K., A nomenclature for oblique ionospheric soundings and ray tracing, *Radio Sci., 2*, 1395-1396, 1967.

Davies, K.: Ionospheric Radio, IEE Electromagnetic Waves Series 31, Peter Peregrinus Ltd., London, UK, 1990.

Dimant, Ya.S., and Sudan, R.N.: Kinetic theory of low-frequency cross-field instability in a weakly ionized plasma. 1, *Phys. Plasma, 2*, 1157-1168, 1995a.

Dimant, Ya.S., and Sudan, R.N.: Kinetic theory of low-frequency cross-field instability in a weakly ionized plasma. 2, *Phys. Plasma, 2*, 1169-1191, 1995b.

Dimant, Ya.S., and Sudan, R.N.: Kinetic theory of the Farley-Buneman instability in the E-region of the ionosphere, *J. Geophys. Res., 100*, 14,605-14,623, 1995c.

Dimant, Ya.S., and Sudan, R.N.: Physical nature of a new cross-field current-driven instability in the lower ionosphere, *J. Geophys. Res., 102*, 2551-2563, 1997.

Ecklund, W.L., Balsley, B.B., and Carter, D.A.: A preliminary comparison of F region plasma drifts and E region irregularity drifts in the auroral zone*, J. Geophys. Res., 82*, 195-197, 1977.

Evans, J.V., and Lowenthal, M.: Ionsopheric backscatter observations, *Planet. Space Sci., 12,* 915-944, 1964.

Farley, D.T., and Fejer, B.G.: The effect of the gradient drift term in Type 1 electrojet irregularities, *J. Geophys. Res., 80*, 3087-3090, 1975.

Farley, D.T.: Theory of equatorial electrojet plasma waves: new developments and current status, *J. Atmos. Terr. Phys., 47*, 729-744, 1985.

Fejer, B.G., and Kelley, M.C.: Ionospheric irregularities*, Rev. Geophys., 18*, 401-454, 1980.

Foster, J. C., and Tetenbaum, D.: High-resolution backscatter power observations of 440-MHz E region coherent echoes at Millstone Hill, *J. Geophys. Res., 96,* 1251-1261, 1991.

Fukumoto, M., Nishitani, N., Ogawa, T., Sato, N., Yamagishi, H., and Yukimatu, A.S.: Statistical analysis of echo power, Doppler velocity and spectral width obtained with the Syowa South HF radar, *Advances in Polar Upper Atmosphere Research, 13*, 37-47, 1999.

Fukumoto, M., Nishitani, N., Ogawa, T., Sato, N., Yamagishi, H., and Yukimatu, A. S.: Statistical study of Doppler velocity and echo power around 75^0 magnetic latitude with the Syowa East HF radar, *Advances in Polar Upper Atmosphere Research, 14*, 93-102, 2000.

Grant, I.F., MacDougall, J.W., Ruohoniemi, J.M., Bristow, W.A., Sofko, G.J., Koehler, J.A., Danskin, D., and André, D.: Comparison of plasma flow velocities determined by the ionosonde Doppler drift technique, SuperDARN radars, and patch motion, *Radio Sci., 30,* 1537-1549, 1995.

Greenwald, R.A., Ecklund, W.L., and Balsley, B.B.: Diffuse radar aurora: spectral observations of non-two-stream irregularities, *J. Geophys. Res., 80*, 131-139, 1975.

Greenwald, R.A., Weiss, W., Nielsen, E., and Thomson, N.R.: STARE: A new radar auroral backscatter experiment in Northern Scandinavia, *Radio Sci., 13*, 1021-1039, 1978.

Greenwald, R.A., Baker, K.B., and Villain, J.-P.: Intial studies of small-scale F region irregularities at very high latitudes, *Radio Sci., 19,* 1122-1132, 1983.

Greenwald, R. A., Baker, K.B., Dudeney, J.R., Pinnock, M., Jones, T.B., Thomas, E.C., Villain, J.-P., Cerisier, J.-C., Senior, C., Hanuise, C., Hunsucker, R.D., Sofko, G.J., Koehler, J., Nielsen, E., Pellinen, R., Walker, A.D.M., Sato, N., and Yamagishi, H.: DARN/SuperDARN: A global view of the dynamics of high-latitude convection, *Space Sci. Rev., 71*, 761-796, 1995.

Gurevitch, A.V., and Karashtin, A.N.: Small-scale thermal diffusion instability in the lower ionosphere, *Geom. Aeron., 24*, 733-738, 1984.

Gurevitch, A.V., Borisov, N.D., and Zybin, K.P.: Ionospheric turbulence induced in the lower part of the E region by the turbulence of the neutral atmosphere, *J. Geophys. Res., 102*, 379-388, 1997.

Haldoupis, C., Sofko, G.J., Koehler, J.A., Prikryl, P., and McNamara, A.G.: High resolution Doppler spectrum measurements of 3-meter auroral irregularities at large magnetic aspect angles, *Phys. Scripta, 35*, 910-916, 1987.

Haldoupis, C., and Schlegel, K.: Direct comparison of 1-m irregularity phase velocity and ion-acoustic speeds in the auroral E-region ionosphere, *J. Geophys. Res., 95*, 18,989 -19,000, 1990.

Haldoupis, C., Bourdillon, A., Six, M., and Delloue, J.: Midlatitude E region coherent backscatter observed simultaneously at two radar frequencies, *J. Geophys. Res., 101*, 7961-7971, 1996.

Hall, G.E., MacDougall, J.W., Moorcroft, D.R., and St.-Maurice, J.-P.: Super Dual Auroral Radar Network observations of meteor scatter, *J. Geophys. Res., 102*, 14,603-14,614, 1997.

Hamza, A., and St-Maurice, J.-P.: Large aspect angles in auroral E region echoes: A self-consistent turbulent fluid theory, *J. Geophys. Res., 100*, 5723-5732, 1995.

Hanuise, C., Villain, J.-P., and Crochet, M.: Spectral studies of F region irregularities in the auroral zone, *Geophys. Res. Lett., 8*, 1083-1086, 1981.

Hanuise, C.: High-latitude ionospheric irregularities: a review of recent results, *Radio Sci., 18*, 1093-1121, 1983.

Hanuise, C., Villain, J.-P., Cerisier, J.C., Senior, C., Ruohoniemi, J.M., Greenwald, R.A., and Baker, K.B.: Statistical study of high-latitude E-region Doppler spectra obtained with SHERPA HF radar, *Ann. Geophys., 9*, 273-285, 1991.

Hanuise, C., and Villain, J.-P.: How does HF propagation make possible and disturb SuperDARN observations: A tutorial., SuperDARN Annual Workshop, May 19-23, Kiljava, Finland, 2003.

Hargreaves, J.K.: The Solar-Terrestrial Environment, Cambridge University Press, Cambridge, UK, 1992.

Hosokawa, K., Iyemori, T., Yukimatu, A.S., and Sato, N.: Source of field aligned irregularities in the subauroral F region as observed by the SuperDARN radars, *J. Geophys. Res., 106*, 24,713-24,731, 2001.

Hosokawa, K., Woodfield, E.E., Lester, M., Milan, S.E., Sato, N., Yukimatu, A.S., and Iyemori, T.: Statistical characteristics of spectral width as observed by the conjugate SuperDARN radars, *Ann. Geophys., 20,* 1213-1223, 2002.

Huber, M.: HF radar echo statistics and spectral studies using SuperDARN, M.Sc. Thesis, Univ. of Saskatchewan, Saskatoon, Can., 1999.

Huber, M., and Sofko, G.J.: Small-scale vortices in the high-latitude F region, *J. Geophys. Res., 105*, 20,885-20,897, 2000.

Jayachandran, P.T., St-Maurice, J.-P., MacDougall, J.W., and Moorcroft, D.R.: HF detection of slow long-lived E region plasma structures, *J. Geophys. Res., 105*, 2425-2442, 2000.

Kagan, L.M., and Kelley, M.C.: A wind-driven gradient drift mechanism for mid-latitude E-region ionospheric irregularities, *Geophys. Res. Lett., 25*, 4141-4144, 1998.

Kagan, L.M., and Kelley, M.C.: A thermal mechanism for generation of small-scale irregularities in the ionospheric E region, *J. Geophys. Res., 105*, 5291-5303, 2000.

Kay, S.M.: Modern Spectral Estimation: Theory and Application, Prentice Hall, New Jersey, 1988.

Kelly, J.D., Heinselman, C.J., Vickrey, J.F., and Vondrak, R.R.: The Sondrestrom radar and accompanying ground-based instrumentation, *Space Sci. Rev., 71*, 797-813, 1995.

Kelly, M.C.: The Earth's Ionosphere, The Academic Press, San Diego, 1989.

Keskinen, M.J., Ossakow, S.L., and McDonald, B.E.: Nonlinear evolution of diffuse auroral F region ionospheric irregularities, *Geophys. Res. Lett., 7*, 573-576, 1980.

Keskinen, M.J., and Ossakow, S.L.: Nonlinear evolution of plasma enhancements in the auroral ionosphere. 1. Long wavelength irregularities, *J. Geophys. Res., 87*, 144-150, 1982.

Keskinen, M.J., and Ossakow, S.L.: Nonlinear evolution of convecting plasma enhancements in the auroral ionosphere, 2. Small scale irregularities, *J. Geophys. Res., 88,* 474-482, 1983a.

Keskinen, M.J., and Ossakow, S.L.: Theories of high-latitude ionospheric irregularities: A review, *Radio Sci., 18,* 1077-1091, 1983b.

Koehler, J.A, Sofko, G.J, André, D., Maguire, M., Osterried, R., McKibben, M., Mu, J., Danskin, D., and Ortlepp, A.: The SAPPHIRE auroral radar system, *Can. J. Phys., 73*, 211-226, 1995.

Kohl, H., Nielsen, E., Rinnert, K., and Schlegel, K.: EISCAT results during the ROSE campaign and comparison with STARE measurements*, J. Atmos. Terr. Phys., 54*, 733-739, 1992.

Koustov, A.V., Igarashi, K., André, D., Ohtaka, K., Sato, N., Yamagishi, H. and Yukimatu, A.S.: Observations of 50- and 12-MHz auroral coherent echoes at the Antarctic Syowa station, *J. Geophys. Res., 106*, 12,875-12,887, 2001a.

Koustov, A.V., Makarevitch, R.A., Ogawa, T., Nishitani, N., Igarashi, K., Ohtaka, K., Sato, N., Yamagishi, H., and Yukimatu, A.: Characteristics of 12- and 3-m E-region irregularities as observed at Syowa, Antarctica, Abstracts of 2001 Asia-Pacific Radio Science Conference, August 1-4, Chuo University, Tokyo, Japan, p. 349, 2001b.

Koustov, A.V., Danskin, D.W., Uspensky, M. V., Ogawa, T., Janhunen, P., Nishitani, N., Nozawa, S., Lester, M., and Milan, S.: Velocities of auroral coherent echoes at 12 and 144 MHz, *Ann. Geophys., 20,* 1647-1662, 2002a.

Koustov, A.V., Sofko, G.J., André, D., Danskin, D.W., Benkevitch, L.V.: Seasonal variation of F-region echo occurrence in the midnight sector. American Geophysical Union Fall Meeting. San Francisco, USA, December 6-10, 2002b.

Koustov, A.V., Sofko, G.J., André, D., Danskin, D.W., and Benkevitch. L.: Solar radiation effects in the SuperDARN F-Region echo occurrence. Canadian Association of Physicists Annual Congress. Charlottetown, PEI, Canada, June 7-11, 2003.

Kustov, A.V., Uspensky, M.V., Kangas, J., Huuskonen, A., and Nielsen, E.: Effect of the altitude profile of auroral scattering on electric field measurements in the STARE experiment, *Geom. Aeron., 30*, 384-388, 1990.

Kustov, A.V., and Haldoupis, C.: Irregularity drift velocity estimates in radar auroral backscatter, *J. Atmos. Terr. Phys., 54*, 415-423, 1992.

Kustov, A.V., Uspensky, M.V., Sofko, G.J., Koehler, J.A., and Mu, J.: Aspect angle dependence of the radar aurora Doppler velocity, *J. Geophys. Res., 99*, 2131-2144, 1994.

Kustov, A.V., Koehler, J.A., Sofko, G.J., Danskin, D.W., and Schiffler, A.: Relationship of the SAPPHIRE-North merged velocity and the plasma convection velocity derived from simultaneous SuperDARN radar measurements, *J. Geophys. Res., 102*, 2495-2501, 1997.

Lacroix, P. J., and Moorcroft, D. R.: Ion acoustic HF radar echoes at high latitudes and far ranges, *J. Geophys. Res., 106*, 29,091-29,103, 2001.

Leadabrand, R.L., Baron, M.J., Petriceks, J., and Bates, H.F.: Chatanika, Alaska, auroral zone incoherent scatter facility, *Radio Sci., 7*, 747-752, 1972.

Liou, K., Newell, P.T., and Meng, C.-I.: Seasonal effects on auroral particle acceleration and precipitation, *J. Geophys. Res., 106*, 5531-5542, 2001.

Makarevitch, R.A., Ogawa, T., Igarashi, K., Koustov, A.V., Sato, N., Ohtaka, K., Yamagishi, H., and Yukimatu, A.S.: On the power-velocity relationship for 12- and 50-MHz auroral coherent echoes, *J. Geophys. Res., 106*, 15,455-15,469, 2001.

Makarevitch, R.A., Koustov, A.V., Sofko, G., André, D., and Ogawa, T.: Multi-frequency measurements of HF Doppler velocity in the auroral E region, *J. Geophys. Res., 107*(8), 10.1029/2001JA000268, 2002a.

Makarevitch, R.A., Koustov, A.V., Igarashi, K., Sato, N., Ogawa, T., Ohtaka, K., Yamagishi, H., and Yukimatu, A. S.: Comparison of flow angle variations of E-region echo characteristics at VHF and HF, *Adv. Polar Upper Atm. Res., 16*, 59-83, 2002b.

McNamara, A.G., McDiarmid, D.R, Sofko, G.J., Koehler, J., Forsyth, P.A., and Moorcroft, D.R.: BARS - A dual bistatic auroral radar system for the study of electric fields in the Canadian sector of auroral zone, *Adv. Space Res., 2, N7*, 145 -148, 1983.

Milan, S.E., Yeoman, T.K., Lester, M., Thomas, E.C., and Jones, T.B.: Initial backscatter occurrence statistics from the CUTLASS HF radars, *Ann. Geophys., 15*, 703-718, 1997a.

Milan, S.E., Jones, T.B., Robinson, T.R., Thomas, E.C., and Yeoman, T.K.: Interferometric evidence for the observation of ground backscatter originating behind the CUTLASS coherent HF radars, *Ann. Geophys., 15*, 29-39, 1997b.

Milan, S.E., and Lester, M.: Simultaneous observations at different altitudes of ionospheric backscatter in the eastward electrojet, *Ann. Geophys., 16*, 55-68, 1998.

Milan, S.E., Yeoman, T.K., and Lester, M.: The dayside auroral zone as a hard target for coherent HF radars, *J. Geophys. Res., 25,* 3717-3720, 1998.

Milan, S., and Lester, M.: Spectral and flow angle characteristics of backscatter from decameter irregularities in the auroral electrojet, *Adv. Space Res., 23*(10), 1773-1776, 1999.

Milan, S.E., Davies, J.A., and Lester, M.: Coherent HF radar backscatter characteristics associated with auroral forms identified by incoherent radar techniques: A comparison of CUTLASS and EISCAT observations, *J. Geophys. Res.*, *104*, 22,591-22,604, 1999.

Milan, S.E., and Lester, M.: A classification of spectral populations observed in HF radar backscatter from the E region auroral electrojets, *Ann. Geophys., 19*, 189-204, 2001.

Milan, S.E., Lester, M., Sato, N., and Takizawa, H.: On the altitude dependence of spectral characteristics of decametre-wavelength E region backscatter and the relationship with optical auroral forms, *Ann. Geophys., 19*, N2, 205-217, 2001.

Milan, S.E., Lester, M., and Sato, N.: Multi-frequency observations of E-region HF radar aurora, *Ann. Geophys., 21*, 761-777, 2003.

Mishin, E.V., Burke, W.J., Huang, C.Y., and Rich, F.J.: Electromagnetic waves structures within subauroral polarization streams, *J. Geophys. Res.*, *108*(A8), 1309, 10.1029/2002JA009793, 2003.

Moorcroft, D. R., and Schlegel, K.: Height and aspect sensitivity of large aspect angle coherent backscatter at 933 MHz, *J. Geophys. Res., 95,* 19,011-19,021, 1990.

Naidu, P.S.: Modern Spectrum Analysis of Time Series, CRC Press, Florida, 1996.

Nielsen, E., Guttler, W., Thomas, C.E., Stewart, C.P., Jones, T.B., and Hedberg, A.: A new radar auroral backscatter experiment, *Nature, 304, N5928*, 712-714, 1983.

Nielsen, E., and Schlegel, K.: Coherent radar Doppler measurements and their relationship to the ionospheric electron drift velocity, *J. Geophys. Res., 90*, 3498-3504, 1985.

Nielsen, E.: Aspect angle dependence of mean Doppler velocities of 1-m auroral plasma waves, *J. Geophys. Res., 91*, 10173-10177, 1986.

Nielsen, E.: Coherent Radar Technique, World Ionosphere/Thermosphere Study, WITS Handbook, v.2, eds. C.H. Liu, ICSU/SCOSTEP, U of Illinois, 1989.

Nielsen, E., del Pozo, C.F., and Williams, P.J.S.: VHF coherent radar signals from the E region ionosphere and the relationship to electron drift velocity and ion-acoustic velocity, *J. Geophys. Res.,107*, N1, 10.1029/2001JA900111, 2002.

Ogawa, T., Balsley, B.B., Ecklund, W.L., Carter, D.A., and Johnston, P.E.: Auroral radar observations at Siple Station, Antarctica*, J. Atmos. Terr. Phys., 44*, 529-537, 1982.

Oppenheim, M.M., Dyrud, L.P., and Ray, L.: Plasma instabilities in meteor trails: Linear theory, *J. Geophys. Res., 108*, 10.1029/2002JA009548, 2003a.

Oppenheim, M.M., Dyrud, L.P., and vom Endt, A.F.: Plasma instabilities in meteor trails: 2-D simulation studies, *J. Geophys. Res., 108*, 10.1029/2002JA009549, 2003b.

Ossakow, S.L., and Chaturvedi, P.K.: Current convective instability in the diffuse aurora, *Geophys. Res. Lett., 6*, 332-334, 1979.

Parkinson, M.L., Devlin, J.C., Ye, H.,Waters, C.J., Dyson, P.L., Breed, A.M., and Morris, R.J.: On the occurrence and motion of decameter-scale irregularities in the sub-auroral, auroral, and polar cap ionosphere, *Ann. Geophys.,* accepted, 2003.

Providakes, J.F., Farley, D.T., Fejer, B.G., Sahr, J., Swartz, W.E., Haggstrom, I., Hedberg, A., and Nordling, J.A.: Observations of auroral E-region plasma waves and electron heating with EISCAT and a VHF radar interferometer, *J. Atmos. Terr. Phys., 50*, 339-356, 1988.

Reinleitner, L.A., and Nielsen, E.: Self-consistent analysis of electron drift velocity measurements with the STARE/SABRE system, *J. Geophys. Res., 90*, 8477-8486, 1985.

Rich, F.J., and Hairston, M.: Large-scale convection patterns observed by DMSP, *J. Geophys. Res., 99*, 3827-3844, 1994.

Risbeth, H., and Williams, P.J.S.: The EISCAT ionospheric radar: the system and its early results, *Q. J. Astron. Soc., 26*, 478-512, 1985.

Rino, C.L., Livingston, R.C., Tsunoda, R.T., Robinson, R.M., Vickrey, J.F., Senior, C., Cousins, M.D., Owen, J., and Klobuchar, J.A.: Recent studies of structure and morphology of auroral zone F-region irregularities, *Radio Sci., 18*, 1167, 1983.

Robinson, T.R.: Simulation of convection flow estimation errors in VHF bistatic auroral radar systems, *Ann. Geophys., 11*, 1033-1050, 1993.

Robinson, T.R., and Schlegel, K.: The generation of non aspect sensitive plasma density irregularities by field-aligned drifts in the lower ionosphere, *Ann. Geophys., 18*, 799-806, 2000.

Ruohoniemi, J.M., Greenwald, R.A., Baker, K.B., and Villain, J.P.: Drift motions of small-scale irregularities in the high-latitude F region: An experimental comparison with plasma drift motions, *J. Geophys. Res., 92*, 4553-4564, 1987.

Ruohoniemi, J.M., Greenwald, R.A., Villain, J.-P., Baker, K.B., Newell, P.T., and Meng, C.-I.: Coherent HF radar backscatter from small-scale irregularities in the dusk sector of the subauroral ionosphere, *J. Geophys. Res., 93,* 12,871-12,882, 1988.

Ruohoniemi, J.M., and Greenwald, R.A.: Rates of scattering occurrence in routine HF radar observations during solar cycle maximum, *Radio Sci., 32*, N3, 1051-1070, 1997.

Ruohoniemi, J.M., and Baker, K.B.: Large-scale imaging of high-latitude convection with Super Dual Auroral Radar Network HF radar observations, *J. Geophys. Res., 103*, 20,797- 20,811, 1998.

Russell, C.T., and McPherron, R.L.: Semi-annual variation of geomagnetic activity*, J. Geophys. Res., 78*, 92-108, 1973.

Ruster, R., and Schlegel, K.: Non-magnetic aspect sensitive auroral echoes from the lower E region observed at 50 MHz, *Ann. Geophys., 17*, 1284-1292, 1999.

Sahr, J.D., and Fejer, B.G.: Auroral electrojet plasma irregularity theory and experiment: A critical review of present understanding and future directions, *J. Geophys. Res., 101*, 26,893-26,909, 1996.

Satyanarayana, P., Chaturvedi, P.K., Keskinen, M.J., Huba, J.D., and Ossakow, S.L.: Theory of the current-driven ion cyclotron instability in the bottomside ionosphere, *J. Geophys. Res., 90*, 12,209-12,218, 1985.

Schiffler, A.: SuperDARN measurements of double-peaked velocity spectra, M.Sc. Thesis, Univ. of Saskatchewan, Saskatoon, Can., 1996.

Schiffler, A., Sofko, G., Newell, P.T., and Greenwald, R.: Mapping the outer LLBL with SuperDARN double-peaked spectra, *Geophys. Res. Let., 24*, 3149-3152, 1997.

Schlegel, K.: Interpretation of auroral radar experiments using a kinetic theory of the two-stream instability*, Radio Sci., 18,* 108-118, 1983.

Schlegel, K., and Thomas, E.C.: Reply, *J. Geophys. Res., 93*, 5987, 1988.

Schlegel, K., and Gurevich, A. V.: Radar backscatter from plasma irregularities of the lower E region induced by neutral turbulence, *Ann. Geophys., 15,* 870-877, 1997.

Shue, J.-H., and Kamide, Y.: Effects of solar wind density on auroral electrojets, *Geophys. Res. Lett. 28*, 2181, 2001.

Starkov, G.V., Oksman, J., Uspensky, M.V., and Kustov, A.V.: On the dependence of radar aurora amplitude on ionospheric electron density, *J. Geophysics, 52*, 49-52, 1983.

St.-Maurice, J.-P., and Schlegel, K.: A theory of coherent radar spectra in the auroral E region, *J. Geophys. Res., 88*, 4087-4095, 1983.

St-Maurice, J.-P., Prikryl, P., Danskin, D.W., Hamza, A.M., Sofko, G.J., Koehler, J.A., Kustov, A., and Chen, J.: On the origion of narrow non-ion-acoustic coherent radar spectra in the high latitude E region, *J. Geophys. Res., 99*, 6447-6474, 1994.

Sudan, R.N.: Unified theory of Type 1 and Type 2 irregularities in the equatorial electrojet*, J. Geophys. Res., 88*, 4853-4860, 1983.

Tsunoda, R.T., Presnell, R.I., and Leadabrand, R.L.: Radar auroral echo characteristics as seen by a 398 MHz phased array radar operated at Homer, Alaska, *J. Geophys. Res., 79*, 4709-4724, 1974.

Tsunoda, R.T.: High latitude irregularities: A review and synthesis, *Rev. Geophys., 26*, 719-760, 1988.

Uspensky, M.V., Kustov, A.V., Sofko, G.J., Koehler, J.A., Villain, J.-P., Hanuise, C., Ruohoniemi, J. M., and Williams, P.J.S.: Ionospheric refraction effects in slant range profiles of auroral HF coherent echoes, *Radio Sci., 29*, 503-517, 1994.

Uspensky, M.V., Koustov, A.V., Eglitis, P., Huuskonen, A., Milan, S.E., Pulkkinen, T., and Pirjola, R.: CUTLASS HF radar observations of high-velocity E-region echoes, *Ann. Geophys., 19*, 411-424, 2001.

Uspensky, M., Koustov, A., Janhunen, P., Pellinen, R., Danskin, D., and Nozawa, S.: STARE velocities: Importance of off-orthogonality and ion motion, *Ann. Geophys., 21,* 729-743, 2003.

Vickrey, J.F., and Kelley, J.D.: The effects of a conducting E layer on classical F region cross-field plasma diffusion, *J. Geophys. Res., 87*, 4461-4468, 1982.

Villain, J.-P., Greenwald, R. A. and Vickrey, J. F.: HF ray tracing at high latitudes using measured meridional electron density distribution, *Radio Sci., 19*, 359-374, 1984.

Villain, J.P., Caudal, G., and Hanuise, C.: A SAFARI-EISCAT comparison between the velocity of F region small-scale irregularities and the ion drift*, J. Geophys. Res., 90*, 8433-8443, 1985.

Villain, J.P., Greenwald, R.A., Baker, K.B., and Ruohoniemi, J.M.: HF radar observations of E region plasma irregularities produced by oblique electron streaming, *J. Geophys. Res., 92*, 12,327-12,342, 1987.

Villain, J.-P., André, R., Pinnock, M., Greenwald, R.A., and Hanuise, C.: A statistical study of the Doppler spectral width of high-latitude ionospheric F-region echoes recorded with SuperDARN coherent HF radars, *Ann. Geophys., 20*, 1769-1781, 2002.

Voronkov, I., Friedrich, E., and Samson, J.C.: Dynamics of the substorm growth phase as observed using CANOPUS and SuperDARN instruments, *J. Geophys. Res., 104*, 28,491-28,505, 1999.

Walker, A.D.M., Greenwald, R.A., and Baker, K.B.: Determination of the fluctuation level of ionospheric irregularities from radar backscatter measurements, *Radio Sci., 22*, 689-705, 1987.

Whitehead, J.D., Ierkic, H.M. and Nielsen, E.: Splitting and divergence of STARE auroral radar velocities, *J. Geophys. Res., 88*, 2147-2154, 1983.

Williams, P.J.S., Jones, B., Kustov, A.V., and Uspensky, M.V.: The relationship between E-region electron density and the power of auroral coherent echoes at 45 MHz, *Radio Sci., 34*, 449-457, 1999.

Woodfield, E.E., Davies, J. A., Eglitis, P., and Lester, M.: A case study of HF radar spectral width in the post midnight magnetic local time sector and its relationship to the polar cap boundary, *Ann. Geophys., 20*, 501–509, 2002.

Xu, L., Koustov, A.V., Thayer, J., and McCready, M.A.: SuperDARN convection and Sondrestrom plasma drift, *Ann. Geophys., 19*, 749-759, 2001.

Xu, L.: SuperDARN-derived plasma convection: Comparison with other data and applications to field-aligned current measurements, Ph.D. Thesis, Univ. of Saskatchewan, Saskatoon, Can., 2002.